Surface properties of electrospun polymer nanofibres

Li, Shuangwu

Surface Properties of Electrospun Polymer Nanofibres

Shuangwu Li

This thesis is submitted for the degree of
Doctor of Philosophy (PhD)

Supervised by Dr A.H. Barber

School of Engineering and Materials Science,
Queen Mary, University of London,
Mile End Road, London, E1 4NS, UK

January 2010

Declaration

"*I certify that this thesis, and the research to which it refers, are the product of my own work, and that any words or ideas and the figures from the work of other people, published in books and papers or otherwise, are fully acknowledged in accordance with the standard referencing. I acknowledge the helpful guidance and support of my supervisor, Dr. Asa H. Barber.*"

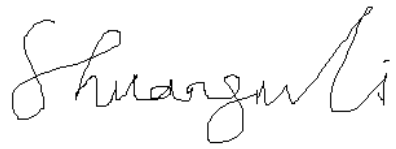

Shuangwu Li

January 2010

Abstract

Fibrous materials are used in a variety of applications due to their relatively high surface area to volume ratio as well as anisotropic behaviour. Electrospinning is a popular fabrication technique which produces polymer nanofibres with a potentially high molecular orientation. The surface of polymer fibres plays a significant role in many applications thus measurement of their surface properties is essential but challenging due to their relatively small size. In this thesis, ultrafine nanofibres have been produced by electrospinning with their nanofibre morphology controlled by varying different processing parameters. Atomic force microscopy (AFM) adhesion contact mechanics and individual nanofibre wetting measurements have been conducted to explore surface properties of the produced electrospun polymer fibres. Results using traditional Owens-Wendt plots applied to our nanomaterials show electrospun nanofibres have a higher dispersive surface free energy compared to bulk polymer film but a lower polar contribution, giving a total surface free energy in excess of bulk equivalents. A novel proposed model indicates that this nanofibre dispersive surface free energy is intimately linked to density of the polymer and ultimately the molecular spacing or orientation for the polymer chains. Comparisons are made with bulk polymer films to show that a high degree of molecular orientation is present at least at the surface of the polymer nanofibre. Structure investigations on electrospun fibres of polyvinyl alcohol using FTIR and XPS surface techniques explore how an increase in hydrogen bonds formed within nanofibres rather than on the fibre surface enhance

this dispersive contribution but lowers the polar contribution. The wetting behaviour of electrospun fibre is extended to assemblies at length scales above individual fibres to highlight how superhydrophobic surfaces can be produced from nanofibre networks with defined spacings and geometries. This superhydrophobicity was adequately described by a Cassie-Baxter model modified to account for the fibrous geometry.

Acknowledgements

It is a great pleasure to express my deep and sincere gratitude to my project supervisor, Dr Asa H. Barber, who gave me solid support, valuable suggestions, constant encouragement, patient guidance and helpful criticism on the entire work. I express my sincere regards to my second supervisor Professor Ton Peijs for his help and suggestions. I would like to thank Nanoforce Technology Limited, Department of Materials at Queen Mary University of London for their financial support. I am grateful to all the faculties in Department of Materials, for various supports they have given.

I would like to thank Dr Mark Baxendale in Department of Physics (QMUL) for allow me using ultrasonic processing equipment. I am thankful to Dr Monisha Philips for the density measurement, Dr Nima Roohpour in Departmet of Materials for the FTIR study and Dr Kate Smith in Department of Engineering for the contact angle measurement. I thank Dr David Morgan from Department of Chemistry (Cardiff University) for the help with XPS.

I wish to thank Dr. Zofia Luklinska and Mr Mick Willis at Nanovision Centre (QMUL) for their help with electron microscopes. I thank Mr John Caulfield, Mr Vince Ford and Mr Bill Godwin at Department of Materials for their help on the electrospinning facilities built and machining. I also would like to thank Mr Christopher T Reynolds, Dr Guogang Ren and Dr Zhujuan Wang who provided

part of the materials for this research.

Thanks are also given to Mr Jonathon Hills, Mrs Sandra Wells, Miss Vicky Wells, and all my research group mates for their helps and friendship.

On the personal side, I am extremely grateful to my mother Weijie Yu, my father Yi Li, my sister Shuangwen Li and my boyfriend Fuyou Zhu for their abundant love, financial support and moral encouragement throughout my study. I'm grateful to all my friends, who gave me supports in my daily life in this period. All their supports are the source of my progress.

SWL, Jan.

2010

Table of Contents

Abstract……..…...…..3

Acknowledgement……..…….5

Table of Contents……...……..7

List of Tables……...…...14

List of Figures……...…….15

Chapter 1. Background and Motivation……..……...23

1.1 Background ……..……..……...……23

1.1.1 Surface Free Energy….…….....23

1.1.2 Polymers……...…….....26

1.1.2.1 Polymer Background……26

1.1.2.2 Classification of Polymers……...…27

1.1.3 Polymer Fibres ……...……..……...…29

1.1.3.1 Structure of Fibre-Forming Polymers……..29

1.1.3.2 Conventional Polymer Fibre Processing Method……30

1.1.3.3 Fibre Properties……..…...32

1.1.3.4 Fibre Types……...32

1.1.3.5 Applications of Fibres……..33

1.1.4 Polymer Nanofibres……...……..……36

1.1.4.1 Electrospinning and Electrospraying……...38

1.1.4.2 Applications of Electrospun Nanofibres Electrospinning....42

1.1.5 Surface Properties…….....45

1.1.6 Scanning Probe Microscopy (SPM)…….....46

1.2 Motivation and Aims……..……...…...47

1.2.1 Motivation……..……...……..47

1.2.2 Aims……..……...48

Chapter 2. Literature Review……..……49

2.1 Introduction……..…….49

2.2 Nanofibres……..……49

2.2.1 Nanotechnology and Nanofibres……..….49

2.2.2 Fabrication of Nanofibres…….....50

2.2.2.1 Overview……..……50

2.2.2.2 Drawing……...……50

2.2.2.3 Template Synthesis……..….51

2.2.2.4 Phase Separation……..……52

2.2.2.5 Self-Assembly……..……....53

2.2.2.6 Electrospinning…….……...54

2.3 The Electrospinning Process……57

2.3.1 Electrospinning Mechanism…….....57

2.3.2 Electrospinning Core-Shell Fibres and Hollow Fibres……..58

2.3.2.1 Core-Shell Fibres…….……..…58

2.3.2.2 Hollow Fibres…….……60

2.3.3 Processing Parameters and Resultant Fibre Morphology.....62

2.3.3.1 Overview……..……..……62

2.3.3.2 Viscosity and Molecular Weight……...…63

2.3.3.3 Solution Concentration…….……64

2.3.3.4 Surface Tension……..……....65

2.3.3.5 Applied Voltage……..…66

2.3.3.6 Flow Rate……..…….66

2.3.3.7 Needle to Target Distance……..……67

2.3.3.8 Conductivity……..…….67

2.3.3.9 Environmental Conditions……..…68

2.3.4 Control of Bead Formation in Electrospinning……...69

2.3.5 Fibre Alignment Methods……..……...71

2.3.5.1 Overview……..……...71

2.3.5.2 Cylinder Collector……..……72

2.3.5.3 Auxillary Electrical Field……...72

2.3.5.4 Rotating Disk Collector……..……73

2.3.5.5 Split Electrodes Collector……..……74

2.4 Surface Properties ……..…….76

2.4.1 Introduction……..…...…76

2.4.2 Surface Tension……...…76

2.4.2.1 Introduction……..…...76

2.4.2.2 Origin of Surface Tension……...77

2.4.2.3 Young's Equation…….…….79

2.4.2.4 Zisman Plot…….……...81

2.4.3 Dispersive and Polar Forces……..…..82

2.4.3.1 Dispersive forces ……..……..…82

2.4.3.2 Polar Forces……..……83

2.4.4 Owens-Wendt Theory……..……...84

2.4.5 Contact Mechanics in Adhesion: Hertz and

Johnson–Kendall–Roberts (JKR) Theory……87

2.4.5.1 Adhesion Measurement Based on JKR Theory……..…..92

2.4.6 Wetting Measurements……..……93

2.4.6.1 Contact Angle Measurement……..…...93

2.4.6.2 Wilhelmy Balance Method.……..…….……94

2.4.6.3 Wetting Measurement Based on Owens-Wendt Theory……96

2.4.7 Hydrophobic Surface……...….98

2.4.7.1 Wenzel Model.……..……99

2.4.7.2 Cassie-Baxter Model…….....…102

2.4.7.3 Superhydrophobic Surfaces…….....104

2.4.8 Summary……...……..……105

2.5 Outline for Following Chapters…….106

Chapter 3. Investigation of Electrospinning Processing Parameter and Resultant Fibre Morphology……..107

3.1 Introduction……..……..107

3.2 Experimental Details……..……...….107

3.2.1 Materials……..……...…107

3.2.1.1 Polyethylene oxide (PEO)……108

3.2.1.2 Polyvinyl alcohol (PVA)…….....108

3.2.2 Polymer Solution Preparation……..…..……...109

3.2.2.1 Polyethylene oxide (PEO) Solution.……109

3.2.2.2 Polyvinyl alcohol (PVA) Solution……...…….110

3.2.3 Electrospinning Polymer Fibres……...…….111

3.2.3.1 Single Needle Electrospinning……..……..111

3.2.3.2 Coaxial Needle Electrospinning……..……112

3.2.4 Characterization Techniques for Electrospun Fibres…….....113

3.2.4.1 Scanning Electron Microscopy (SEM)…….……....113

3.2.4.2 Transmission Electron Microscopy (TEM)……..…....114

3.3 Results and Discussion……..…….115
3.3.1 Electrospun PEO Nanofibre Morphology……..…….....…115
3.3.1.1 Effect of Concentration……..……...115
3.3.1.2 Effect of Applied Voltage……..……....117
3.3.1.3 Effect of Flow Rate……..……120
3.3.1.4 Effect of Molecular Weight……..……121
3.3.1.5 Effects of Conductivity and Surface Tension……..….123
3.3.1.6 Effects of Distance between Tip and Collector……..…...125
3.3.2 Electrospun PVA Nanofibre Morphology…….……126
3.3.2.1 Effect of Solution Concentration……..……...…….126
3.3.2.2 Effect of Flow Rate and DTC…….……127
3.3.2.3 Effect of Applied Voltage……..……...……129
3.4 Electrospun Nanofibre Alignment……..……130
3.5 Electrospinning of Polymer Nanofibres from Organic Solvent…….....131
3.5.1 Polycarbonate……132
3.5.2 Experimental Parameters Governing PC Nanofibre Morphology.133
3.6 Conclusions…….……...135

Chapter 4. Surface Properties of Electrospun Polymer Fibre Aggregates……....137

4.1 Introduction……...…….137
4.2 Background and Aims……..……...138
4.3 Experimental Details……..……141
4.3.1 Materials Manufacturing Process……..…141
4.4 Characterization Techniques…….……142
4.4.1 Optical Microscopy……...…..……..142
4.4.2 Contact Angle Measurement…….....143

4.5 Results and Discussion……..…….145

4.5.1 Vertically Aligned PC Fibre Networks……..…..…..145

4.5.2 Electrospun PC Fibre Network…….……147

4.6 Conclusions……....……...154

Chapter 5. Measurement of Individual Electrospun Fibre Surface Free Energy using Contact Mechanics……..…..…156

5.1 Introduction……..…...……..156

5.2 Experimental……..……157

5.2.1 Sample Preparation…….…….157

5.2.2 Methods……..……...159

5.2.2.1 Atomic Force Microscopy (AFM)……...…159

5.2.2.2 AFM Adhesion Tests……..…….164

5.2.2.3 Density Measurement……..…….……169

5.3 Results and Discussion……..……170

5.3.1 PVA Surface Free Energy……..……170

5.3.2 PC Nanofibre Surface Free Energy……..…….177

5.4 Conclusions……185

Chapter 6. Individual Electrospun Polymer Nanofibre Wetting…….187

6.1 Introduction……..……...187

6.2 Experimental Details……..……..188

6.2.1 Sample Preparation…….……188

6.2.1.1 Short Fibres Formed by Ultrasonic Processor……...188

6.2.1.2 Short Fibres Formed by Razor Blade Cutting……...191

6.2.1.3 Electrospraying Water Droplets onto Nanofibres…….…192

6.2.1.4 Electrospinning of Nanofibres onto Conductive Metal Particles……..……...…….193

6.2.1.5 Short Fibres Formed by FIB (Focused Ion Beam) Cutting……..194

6.2.1.6 PVA Nanofibre Attachment……..…..…….197

6.2.2 Methods……...……200

6.2.2.1 Wilhelmy Balance Measurements to Measure Capillary Forces using AFM……200

6.2.2.2 Fourier Transform Infrared (FTIR) Spectroscopy….……206

6.2.2.3 X-ray Photoelectron Spectroscopy (XPS)……..……208

6.3 Results and Discussion……..……...209

6.4 Conclusions……..……217

Chapter 7. Conclusions and Future Work……...……219

7.1 Conclusions……..……...……219

7.2 Future Work……..……222

7.2.1 Electrospinning Hollow Polymer Fibres…….…222

7.2.1.1 Materials……..…….……..222

7.2.1.2 Coaxial Needle Electrospinning……..…...……224

7.2.1.3 Preliminary Results……..……..225

7.2.1.4 Future Work……...……...227

7.2.2 Individual Hollow Fibre Wetting……..……...227

References……230

List of Tables

1.1 Surface free energy for some solid materials……..……25

1.2 Some polymer surface free energies……...……26

1.3 Engineering Fibres Used in Biomedical Applications…… ……...…33

1.4 Fibre surface area per mass of fibre material for different fibre diameter…37

2.1 Polymer solvent systems for electrospinning……..……55

2.2 Comparison of processing techniques for obtaining nanofibres…….....56

2.3 Advantages and disadvantages of various processing techniques…….56

2.4 Solid surface energy data for common polymers…….……...86

3.1 Different concentration and molecular weight PEO solutions……..…110

3.2 Different concentration PVA solutions……..……110

3.3 Different concentration and molecular weight PC solutions……....134

4.1 Contact angle values for water, PC film and PC fibre networks.....151

6.1 Physical parameters for various liquids wetting individual PVA Nanofibres……....211

List of Figures

1.1 (a) Typical metal structure (b) Typical polymer structure (c) Typical liquid structure…….....……24

1.2 Representive skeletal structures of linear and non-linear polymers……..…26

1.3 Classification of polymers……29

1.4 Schematic diagram of a typical gel spinning production line……...…31

1.5 Scheme of electrospinning experimental setup……33

1.6 Schematic representation of the electrohydrodynamic atomization equipment set-up……..….41

1.7 (a) Stable cone–jet mode atomization of the aspirin solution. The needle exit is indicated by a dotted line. (b) Optical micrograph of droplets soon after EHDA…….....…….42

2.1 Drawing method to obtain nanofibres……...51

2.2 Template synthesis method to produce nanofibres……....52

2.3 Generic schematics of phase separation to produce nanofibrous structure…...53

2.4 Self-assembly for obtaining nanofibre……..54

2.5 Photographs illustrating the instability region of a liquid jet from electrospun PEO solution……58

2.6 (a) Schematic of co-electrospinning of PMMA/PAN blend in DMF using a single circular nozzle. The PMMA/DMF droplets are shown in yellow, while the PAN/DMF liquid is shown in blue. (b) PMMA/PAN fibre with clear core-shell structure. (c) Heat treatment in a nitrogen atmosphere converted

core-shell PMMA/PAN fibres into carbon tubes. The defects in these tubes were caused by handling, and are shown to demonstrate the hollow character of the heat-treated tubes……...59

2.7 (A) Schematic example of the setup for electrospinning core/sheath structure nanofibres. The spinneret was made from two coaxial needles, through which heavy mineral oil and a solution containing PVP and $Ti(OiPr)_4$ were simultaneously ejected to form a continuous coaxial jet. (B) TEM image of two as-spun hollow fibres after the oily cores had been extracted with octane. The walls of these tubes were made of a composite containing amorphous TiO_2 and PVP. (C) TEM image of TiO_2 (anatase) hollow fibres that were obtained by calcining the composite nanotubes in air at 500 °C. (D) SEM image of uniaxially aligned hollow fibres that were deposited across the gap between a pair of electrodes. These fibres were fractured using a razor blade to expose their cross-sections……..……..61

2.8 PLLA nanofibres with different diameters and pores……..64

2.9 Beaded PEO nanofibres……...69

2.10 A schematic rotating collector for electrospun ultrafine fibres……...72

2.11 Knife-edged bar and blade attached to needle to change the electric field during electrospinning……..……73

2.12 (a) Setup to produce aligned nanofibrous scaffold by electrospinning using a disk collector. (b) Image of a PEO nanofibre attracted to the edge of the disk. (c) SEM image showing the electrospun fibre yarns obtained. The individual fibre yarns are parallel to each other with a gap of 1 to 2 μm……..74

2.13 (A) Schematic example of the setup for electrospinning that used to produce uniaxially aligned nanofibres. The ground electrodes contained two pieces of conductive silicon stripes separated by a gap. (B) Calculated electric field strength vectors in the area between the needle and the collector. The arrows

indicate the direction of the electrostatic field lines. (C) Electrostatic force analysis of a charged nanofibre spanning across the gap. The electrostatic force (F_1) resulted from the electric field and the Coulomb interactions (F_2) between the positive charges on the nanofibre and the negative image charges on the two grounded electrodes……...……..75

2.14 Scheme of attractive forces among the molecules of water……....77

2.15 Water breaks up into droplet……78

2.16 Overpressure inside a drop of oil "o" in water "w"……....79

2.17 Young's equation for a flat solid surface……80

2.18 Zisman plot to determine γ_c ……..82

2.19 Sphere on flat contact geometry with (a) no load and (b) load = L. (c) The distribution of contact pressure across the contact zone of (b)…….…….88

2.20 Deformation and contact radius of an elastic sphere contacting a rigid flat. Solid line: Johnson-Kendall-Roberts (JKR) contact with adhesion. Dashed line: Hertzian contact without adhesion……89

2.21 Comparison of contact areas predicted by the Johnson-Kendall-Roberts (JKR) theory, and Hertz theory…….……91

2.22 The contact angle of a liquid on a flat solid surface……...94

2.23 Liquid surface tension determination by the Wilhelmy plate method. A rectangular plate of length, *l*, width, *w*, and thickness, *d*, of material is immersed to a depth of *h* in a liquid, θ is the contact angle forming between the liquid and the plate……..……..95

2.24 ESEM images of PEG wetting surfaces on: (a) Carbon fibre; (b) Carbon nanofibre; (c) MWCNT, from which the contact angle can be measured…..97

2.25 Owens-Wendt plot for carbon fibre, carbon nanofibres and multiwall Nanotubes……...98

2.26 Effect of Roughness for a hydrophobic surface (a) a liquid droplet in contact with a smooth surface; (b) a liquid droplet in contact with a

rough surface……101

2.27 A liquid droplet sitting on a rough surface (a) Wenzel Model (b) Cassie-Baxter Model……..103

2.28 SEM photographs of microstructured water-repellent leaf surfaces. (a) Nelumbo nucifera adaxial leaf surface; (b) Colocasia esculenta leaf surface.....105

3.1 Synthesis of polyethylene oxide (PEO)…….……...108

3.2 PVA with fully hydrolyzed grades and partially hydrolyzed grades…...…..109

3.3 Single needle electrospinning experimental set-up……...112

3.4 Coaxial needle electrospinning experimental set-up…….113

3.5 (a) Jeol JSM-6800, (b) Jeol JSM-6300……..114

3.6 Transmission Electron Microscopy……...115

3.7 (a) S1: Concentration 0.25 wt/v%, (b) S2: Concentration 0.5 wt/v%, (c) S3: Concentration 0.75 wt/v%, (d) S4: Concentration 1.0 wt/v%, (e) S5: Concentration 1.25 wt/v%, (f) S6: Concentration 1.5 wt/v%.....116

3.8 (a) S3: Applied Voltage 6.6 kV, (b) S3: Applied Voltage 8.5 kV, (c) S3: Applied Voltage 11.1 kV, (d) S3: Applied Voltage 13.5 kV……..119

3.9 (a) S5: Flow rate 0.2 ul.min^{-1}, (b) S5: Flow rate 1.0 ul.min^{-1}…....120

3.10 (a) S8: M_w 200,000 g.mol^{-1}, (b) S8: M_w 200,000 g.mol^{-1}, (c) S7: M_w 1,000,000 g.mol^{-1}, (d) S6: M_w 8,000,000 g.mol^{-1}…….121

3.11 (a) S2: Before adding salt, (b) S2: After adding 1 wt. % salt, (c) S8: Before adding salt, (d) S8: After adding 1 wt. % salt, (e) S6: Distilled water 25 %, (f) S9: Distilled water: 35 %.....123

3.12 (a) S5: DTC = 10 cm, (b) S5: DTC = 25 cm……....126

3.13 (a) S10: Concentration 6 wt/v%, (b) S11: Concentration 7 wt/v%, (c) S12: Concentration 8 wt/v%, (d) S13: Concentration 13 wt/v%.....127

3.14 (a) S12: Flow rate 1.0 ul.min^{-1}, DTC = 15 cm; (b) S12: Flow rate 9.0 ul.min^{-1} DTC = 15 cm; (c) S12: Flow rate 1.0 ul/mn, DTC = 13 cm, (d)

S12: Flow rate 1.0 ul/mn, DTC = 20 cm……..128

3.15 (a) S12: Voltage 11.2 kV, (b) S12: Voltage 13.5 kV, (c) S12: Voltage 15.8 kV, (d) S12: Voltage 17.2 kV……..……..129

3.16 (a) PVA: 1 minute deposition, (b) PVA: 5 minutes deposition……..131

3.17 Polycarbonate chemical structure……..133

3.18 Electrospun Polycarbonate nanofibres……..135

4.1 SEM images of carbon nanotube forests. (a) As-grown forest with nanotube diameter of 50 nm and a height of 2 μm, (b) PTFE-coated forest after HFCVD treatment, and (c) an essentially spherical water droplet suspended on the PTFE-coated forest……..…139

4.2 (a) Water contact angle of a PVA film with a smooth surface; (b) Water contact angle of synthesized PVA nanofibers with a rough surface..140

4.3 Optical Microscopy (a) Meiji Binocular; (b) Olympus BX60……...143

4.4 KSV CAM 100 contact angle meter……..144

4.5 KSV CAM Software Image of water droplet on a sample surface……...145

4.6 (a) Water Droplet sit on the top of nanofibre forest; (b) Water droplet penetrate into the voids of nanofibre forest…….….146

4.7 (a) Aligned PC fibre ends; (b) Some PC fibre cross sections……..……..147

4.8 (a) Optical image of PC fibre network with 30 seconds deposition……..148

(b) Optical image of PC fibre network with 15 seconds deposition……148

4.9 (a) SEM image of PC fibre network with 30 seconds deposition…….148

(b) SEM image of PC fibre network with 15 seconds depositon…….148

4.10 Water contact angle on glass…….…149

4.11 Optical images of (a) Water droplet on a smooth PC film, (b) Water droplet on electrospun PC fibre network with 30 seconds deposition, (c) Water droplet on electrospun PC fibre network with 15 seconds deposition……..150

4.12 Plot of experimental data relationship between f_1 and *Cos* θ. Two theoretical lines are shown representing the contact angle θ expected for a range of fibre

fractions (f_l) using equation 4.1. The two lines differ by considering that the contact angle on the flat surface θ_0 of a continuous PC film or glass slide...154

5.1 (a) A schematic illustration of a typical AFM device and its principle; (b) Lennard-Jones curve showing the expected force experienced by an AFM tip approaching a sample's surface……...……162

5.2 Pull-off force related with cantilever bending……164

5.3 (a) Scanning Probe Microscopy (b) SEM image of an AFM tip……165

5.4 Cantilever deflection versus distance curve in adhesion measurement…...168

5.5 Micromeritics AccuPyc 1330 He Pycnometer……...169

5.6 AFM semi-contact topography imaging shows (a) how the nanofibres are of uniform diameter and continuous, (b) electrospinning for short amounts of time gives a lower density of nanofibres on the substrate, allowing simple visualization of individual nanofibres……..…170

5.7 (a) AFM image for an individual PVA Nanofibre, (b) Individual PVA nanofibre diameter measurement from AFM Nova software……171

5.8 Force-distance curve for the separation of the AFM tip from the surface of a PVA nanofibre shown in the AFM semi-contact image (insert) and an undrawn film……172

5.9 PVA nanofibre dispersive surface free energy related to fibre diameter….174

5.10 PVA Films dispersive surface free energy related to draw ratio……..175

5.11 Force-distance plot for the separation of an AFM tip from polycarbonate film surfaces with differing draw ratios (λ) and an electrospun fibre surface. The adhesion force F is shown for a film with λ=1 only for clarity……..178

5.12 Dispersive surface free energy for different draw ratio PC films……179

5.13 Optical micrographs of a polyethylene glycol droplet on polycarbonate films with different draw ratio (λ=1, 1.25, 1.5, 1.75, 2) and smaller droplet contact angle for the higher draw ratio film……..…..180

5.14 Plot of calculated dispersive free energy versus polycarbonate density for a

variety of drawn films and electrospun fibres……....181

5.15 Intermolecular forces across an interface……..….182

5.16 Plot of the dispersive free energy γ^{d}_{polym} of various drawn films and electrospun fibre surfaces against the polymer density/average chain distance ρ / r_{11}. The fit line gives πA/32 resulting in a Hamaker constant (A) of 1.2 x 10^{-19} J……185

6.1 (a) Ultrasonic Processor (Sonics&Materials, Inc, USA)……..…..189

(b) Probe of the ultrasonic processor……...…….189

6.2 Mastersizer 2000 for particle analysis……...190

6.3 Length distribution of short electrospun PVA nanofibres……....190

6.4 SEM images of short PVA nanofibres after sonication……..……191

6.5 Short PVA nanofibres obtained through razor blade cutting……..……191

6.6 Short PVA nanofibres obtained after electrospraying water droplets onto electrospun PVA nanofibres……192

6.7 Optical images of PVA nanofibres deposited on aluminium particles……..194

6.8 SEM images of PVA nanofibres deposited on copper particles……194

6.9 Quanta 3D FEG instrument……...196

6.10 (a) Before FIB cutting, (b) after FIB cutting……196

6.11 PVA nanofibre attachment process……...……198

6.12 Attachment of PVA nanofibre onto an AFM tip before FIB cutting…….198

6.13 Single PVA nanofibre attached onto an AFM tip after FIB cutting …….199

6.14 ESEM pictures of PVA nanofibres attached on a manipulator arm was removed dynamically from (a) Glycerol; (b) PEG; and (c) Formamide…..201

6.15 Cantilever deflection signal versus time curve during liquid (glycerol) approaching an individual PVA nanofibre-AFM tip. A sharp drop in the AFM deflection signal indicates bending of the AFM cantilever towards the liquid surface indicating PVA nanofibre jump-in to glycerol probe liquid due to capillary forces……..……...204

6.16 (a) Force-distance curve with fibre attached onto the AFM tip……..206
(b) Force-distance curve of fibre has been removed from the AFM tip….206

6.17 Nicolet 8700 FTIR spectrometer…….207

6.18 The Kratos Axis Ultra-DLD system at Cardiff University……..209

6.19 Force profiles for individual electrospun PVA nanofibre contacting liquids of Glycerol, PEG and formamide. A sudden change in the force with time during the fibre approach to the liquid surface is indicative of the fibre jump-in into the liquid. The negative force represents attraction between the PVA nanofibre and each probe liquid. The small bumps seen at 3.6, 3.9 and 3.3 s, respectively, can be related to environmental noise, and are not reproducible…….....….210

6.20 Owens and Wendt plot for single PVA nanofibre. The y axis value Y represents $[\gamma_l(1+\cos\theta)]/2\sqrt{\gamma_l^d}$, and the x axis value X is $(\sqrt{\gamma_l^p}/\sqrt{\gamma_l^d})$. Each point is an average of at least five measurements……....212

6.21 FTIR spectrum of PVA nanofibres and bulk PVA film……...213

6.22 Possible conformation modes of the PVA molecules at the air/solid Interface……..215

6.23 X-ray photoelectron spectra illustrating the dependence of the detection angle for O(1s) of PVA nanofibres…….217

7.1 Polyvinylpyrrolidone Synthesis……..223

7.2 Coaxial needle electrospinning experimental set-up……..225

7.3 (a) Electrospun PVP nanofibre filled with mineral oil; (b) Hollow PVP nanofibre after octane extraction……226

7.4 (a) PVA hollow fibres with traces of mineral oil left inside; (b) PEO nanofibre with traces of mineral oil left inside……..227

7.5 PVP hollow fibres with 1 μm diameter after razor blade cutting……..228

7.6 FIB melts the end of the electrospun hollow fibre……229

Chapter 1

Background and Motivation

1.1 Background

1.1.1 Surface Free Energy

Atoms on a solid surface have an environment which is different from that of atoms in the bulk of the solid. This difference is attributed to the lower number of neighbouring atoms at the surface compared to the bulk. To increase the surface area of a solid, we have to bring atoms from the bulk of a solid or liquid to the surface and move the atoms which are already on the surface along the surface in order to accommodate the new surface atoms. Under conditions of equilibrium at constant temperature T and pressure P, the reversible surface work δW^S required to increase the surface area a by an amount da of a one-component system is given by [1]

$$\delta W^S_{T,P} = \gamma da \qquad (1.1)$$

Where γ is the two-dimensional analogue of the pressure and is called the "surface tension" (liquids) or "surface energy" (solids), or "surface free energy" (solids), while the volume change is replaced by the change in surface area. Equation 1.1

can be compared with the reversible work needed to increase the volume of a one-component system at constant pressure, $P\,dV$ where P is always perpendicular to the surface and γ is always parallel to the surface. The pressure P is the force per unit area [dynes /cm^2 (N/m^2)], while the surface tension γ has units of force per unit length [dynes /cm (N/m)]. The usual units of surface tension or surface energy, N/m or J/m^2, are dimensionally the same. γ can be considered as a pressure along the surface plane that resists the creation of more surface [1]. An approximation of the magnitude of surface energy can be made by assuming that the surface work is equal to the magnitude as the heat of sublimation, since sublimation continually creates a new surface. For metals [2] there is a strong experimental correlation between the heat of sublimation ΔH_{subl} and the surface energy γ, empirically stated as:

$$\gamma \approx 0.16\Delta H_{subl} \qquad (1.2)$$

Importantly, solids have surface energy that is dependent on the chemical composition. Surfaces are discontinuous and chemical bonding between atoms has to stop at a surface, therefore atoms at a surface have missing bonds. If we consider a crystal solid, away from the surface, typically known as the 'bulk', each atom forms 6 bonds with its neighbouring atoms, but the atoms at the surface only make 3, 4 or 5 chemical bonds, such as metal which is shown in Figure 1.1 (a). Metals have large thermodynamic drive to lower the energy of the surface because of these free chemical bonds. The surface free energies of metals are therefore high.

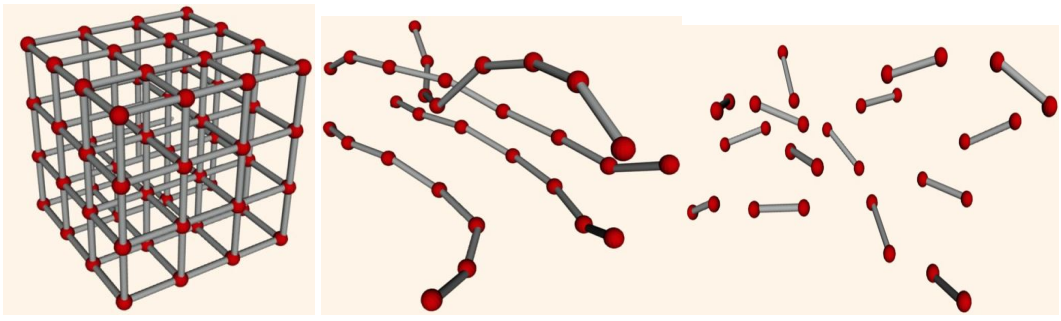

Figure 1.1 (a) Typical metal structure (b) Typical polymer structure (c) Typical liquid structure

Polymers consist of long chains of molecules and the atoms in the polymers are all chemically bonded to neighbours, as shown in Figure 1.1 (b). Polymer chains at a surface are therefore much more stable than discontinuities in metals where atoms are missing neighbours. Therefore polymer solids have a much lower surface free energy comparing to metals. Similar for liquids, atoms in liquids are all chemically bonded to their neighbours as shown in Figure 1.1 (c), therefore liquids have similar surface free energy with polymers. Table 1.1 shows surface free energy values for some solid materials.

Table 1.1 Surface free energy for some solid materials [3]

Material	Surface free energy ($mJ.m^{-2}$)
Sodium	190
Copper	1550
Silver	910
Iron	1880
Tungsten	2500
Aluminium	700
Silicon	750
Ice	75
Polyethylene	38
Polystyrene	40
Polyvinyl chloride	42
Polydimethyl siloxane	20

Polymer surface free energy is dependant on the intermolecular forces between the chains. Polymer surface free energy is therefore dependant on the chemical composition of the polymer chains. This is a similar concept to liquids i.e. increasing number of electronegative atoms in polymer chains increase the inter-molecular forces. More polar groupings in polymer chains give larger surface free energies, this is due to increased polar interactions between polymer chains. Table 1.2 shows some polymer surface free energies.

Table 1.2 Some polymer surface free energies

Name	Surface free energy at 20 °C (mJm^{-2})
Polydimethylsiloxane (PDMS)	19.8
Polypropylene-isotactic (PP)	30.1
Polycarbonate (PC)	34.2
Polyvinylacetate (PVA)	36.5
Polyamide 12 (PA-12)	40.7
Polyvinylchloride (PVC)	41.5
Polyetheretherketon (PEEK)	42.1
Polyethylene oxide (PEO)	42.9

1.1.2 Polymers

1.1.2.1 Polymer Background

A polymer is a substance composed of molecules which have long sequences of one or more species of atoms or groups of atoms linked to each other by primary, usually covalent bonds [4]. Many macromolecules have a linear skeletal structure which may be represented by a chain with two ends. There are also many with non-linear skeletal structures shown in Figure 1.2.

Linear polymer molecule | Branched polymer molecule | Network polymer (crosslinked)

Figure 1.2 Representive skeletal structures of linear and non-linear polymers [4]

Polymerization or crosslinking pre-existing chains can form non-linear polymers [4]. Different skeletal structures give different physical properties. For example, linear polyethylene has a melting point about 20 ^{o}C higher than that of branched polyethylene. Network polymers do not melt when heating and will not dissolve; they may only swell slightly in compatible solvents [4].

1.1.2.2 Classification of Polymers

Polymers can be separated into three groups: thermoplastics, elastomers and thermosets as shown in Figure 1.3. Thermoplastics are linear or branched polymers which can be melted upon heating, often named as plastics. They can be moulded and remoulded into nearly any shape using injection moulding and extrusion techniques [4]. They make up by far the largest proportion of polymers used in industry. Thermoplastics also form distinct structures by molecular ordering. This includes crystalline thermoplastics, with high molecular ordering, amorphous thermoplastics and semi-crystalline thermoplastics where there are both amorphous and crystalline domains [4].

Thermoplastics normally do not crystallize easily when cooling to the solid state because this needs considerable ordering of the highly entangled and coiled macromolecules in the liquid state [4]. Most thermoplastics that crystallize do not usually produce perfectly crystalline materials but are instead semi-crystalline with both crystalline and amorphous domains [4]. The crystalline phases of thermoplastic polymers are characterized by their melting temperature (T_m) during which a substance changes its state from solid to liquid. Amorphous polymers or amorphous phases of semi-crystalline polymers are characterized by the temperature at which they transform suddenly from the glassy state (hard) to the rubbery state (soft), known as the glass transition temperature (T_g). If we consider completely amorphous polymers, these polymers don't crystalline even when cooled slowly from the melt. The aim of cooling is to decrease the thermal motion of the molecular segments. In the melt condition, the molecular segments change place by thermally activated jumps. If cooling continues, a temperature will be

reached when the segmental movement rate is reduced considerably, which defines glass transition temperature. The structure of the polymer below this temperature consists of molecules tangled in a liquid like condition but without significant molecular motion, resulting in a glassy state [5]. The melting and glass transition temperatures are found to increase when the physical properties of the polymer such as chain stiffness and intermolecular attraction forces increase [4].

A thermoset plastic is a polymer that can be produced to experience a chemical linking reaction to create a network polymer, also called a thermoset polymer [6]. Thermoset polymers such as epoxy can be shaped with the application of heat and pressure, but the number of such cycles is strictly limited. Heating thermoplastic polymers cause viscous flow, thus thermoplastic polymer can be subsequently heated and cooled reversibly with time. For thermoset polymers, their precursors can be heated to a proper temperature for a short time, so they can flow as a viscous liquid; after this a chemical cross linking reaction will happen and cause the liquid to solidify. The precursor materials for thermoset polymers may have low molecular weight, and some will flow and cross-link at room temperature after mixing [5, 6].

An elastomer is a polymer which shows significant elastic deformation when loaded. It usually can be interchanged with the term of rubber. Elastomers are crosslinked rubbery polymers exhibit good strength and elongation properties. For example rubbery networks that could easily be stretched to high extensions and which rapidly recover their original dimensions when releasing applied stress [4]. This particularly important and useful property is an indication of their molecular structure in which the network is of low crosslink density. The polymer chains of elastomers become extended when they deformed [4].

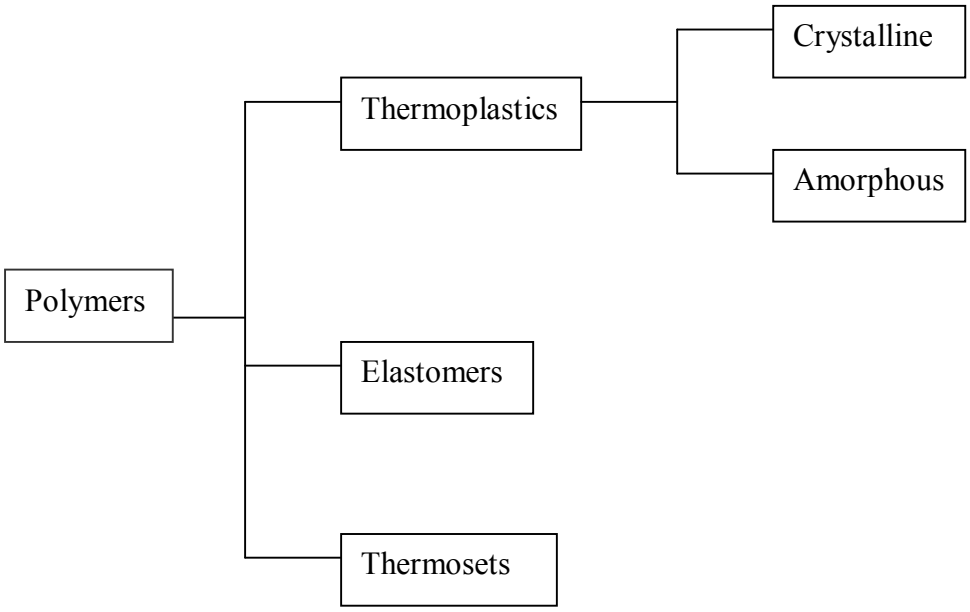

Figure 1.3 Classification of polymers.

1.1.3 Polymer Fibres

1.1.3.1 Structure of Fibre-Forming Polymers

One important class of polymer is the form of fibres. Polymeric fibres are distinguishable from other type of processed polymers by their characteristic high aspect ratio and physical properties which are particularly dominated by anisotropic structural organization [7]. Molecular organization within the fibre structure can be described at three levels and each related to certain characteristics of fibre behaviour and properties. The first important level is the organochemical structure which defines the chemical composition and molecular structure of the repeating unit in the polymer. This primary level of molecular structure is directly related to chemical properties, moisture sorption, swelling characteristics, and not directly related to all physical properties. The macromolecular level of structure describes the chain length, length distribution, stiffness and molecular size and shape. The supramolecular organization is the arrangement of the polymer chains in three-dimensional space. The physical properties of polymer fibres are directly influenced by the organization of polymeric chains into crystalline and

noncrystalline domains, and the disposition of these domains relating to each other. This morphology is complicated, with fibrils, microfibrils, and similar structural subunits frequently surrounded by a matrix material in a composite composition. [7]

All useful polymeric fibres in textile applications are semicrystalline where the polymeric chains are ordered into crystalline and amorphous regions in a two phase structure (crystalline-amorphous model) [7]. Moreover, other models describe a fibre as a polymeric substance with a high degree of three-dimensional structural regularity, and bring about the concept of the degree of crystallinity, for example: the fractional crystalline content of a partially crystalline polymeric material [7]. The requirement of at least partial crystallinity, the extent of which is described by the fractional degree of crystallinity, controls the number of polymers suitable for forming fibres. Significantly a fibre forming polymer is in fact a "crystallisable" polymer. Some structural characteristics of polymers such as chain directionality, chain stiffness and single chain conformation allow them to crystallize under suitable conditions [7].

Interest has also focused on the noncrystalline regions with many important properties of fibres directly related to the noncrystalline or amorphous regions. Examples include absorption of dyes, moisture, and other penetrants occur into these amorphous regions. Although adsorption on crystallite surfaces has been postulated, these penetrants are not expected to diffuse into the crystalline domains. [7]

1.1.3.2 Conventional Polymer Fibre Processing Method

Spinning is manufacturing process to produce polymer fibres and is a specialized extrusion method that uses a spinneret to form multiple continuous filaments. There are four types of spinning: wet, dry, melt, and gel spinning. Wet spinning is the most conventional of the four processes. This process is used for polymers that need to be dissolved in a solvent to be spun. The spinneret contains the polymer in

solution and is submerged in a chemical bath allows the fibre to precipitate and solidify upon contact with the bath. Therefore this process is called wet spinning. Dry spinning also uses polymers dissolved in a solvent to be spun but differs from wet spinning as the solidification of the fibre is achieved through rapid solvent evaporation which can be achieved by a stream of air or inert gas. Melt spinning uses a heated spinneret to induce a phase change of the polymer to the liquid state before spinning. The polymer typically solidifies by cooling with air after being extruded from the spinneret, finally collected on a take-up wheel. Common fibres of nylon and polyester are commercially produced from this process. Gel spinning is used to obtain high strength fibres or other improved fibre mechanical properties along the principle fibre axis. The polymer contained in the spinneret is not in a true liquid state but a "gel" state. Extruding of the gel allows the polymer chains to align due to a critical number of entanglement points between the chains. Therefore the polymer chains within the fibres have a high degree of alignment, which increases strength. The fibres are air dried after extrusion to remove the solvent from the gel and then cooled in a liquid bath. Some high strength polyethylene and aramid fibres are produced through this process. While extruded fibres are solidifying, or sometimes even after they have hardened, the fibres may be drawn further to pull the molecular chains together and align them along the fibre axis in order to produce a considerably stronger yarn. Figure 1.4 shows the schematic diagram of a typical gel spinning production line. [8]

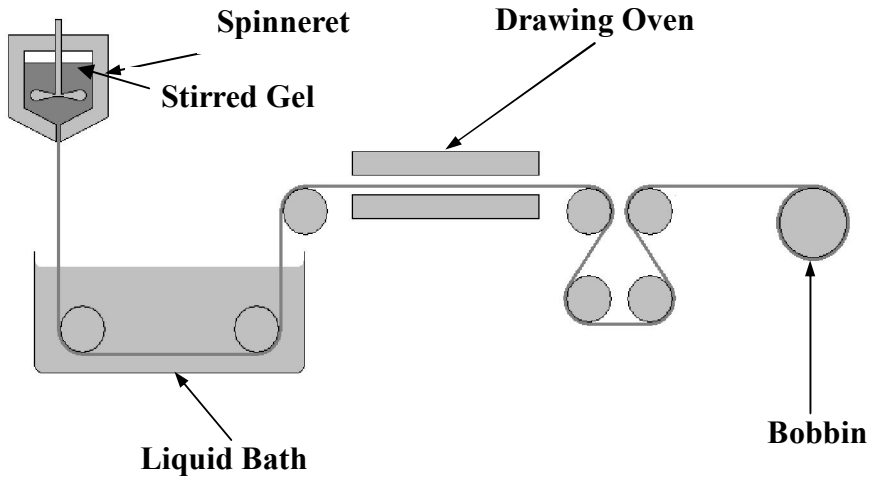

Figure 1.4 Schematic diagram of a typical gel spinning production line [8].

It should be pointed out that the drawability of the as spun polymer fibres is strongly dependent on the molecular weights of the polymers used. Generally, the drawing of melt spun fibres is difficult when using larger molecular weight polymers as the high melt viscosity of these polymers can lead to frequent blocking of the drawing die [8]. This can be overcome by solution/gel spinning techniques where a polymer with large molecular weight is dissolved by the solvents and the entanglement density is reduced by mechanical stirring. Since the larger molecular weight polymer chains become aligned in the drawing direction, the drawability of solution/gel spun fibres is much improved comparing to that of the melt spun fibres [8].

1.1.3.3 Fibre Properties

Fibres have advantages which can be used in biomedical areas, especially a large surface to volume ratio which is important in surface directed applications. Engineering fibre can also be processed into woven or hollow structures that provide the different porosity and strength needed in biomedical applications for example artificial ligaments, synthetic blood vessels and controlled drug delivery. [9]

A number of biocompatible engineering fibres have been used within the body due to their excellent mechanical properties, long term stability, and low toxicity. Biocompatibility of the fibres depends on the type of polymer which they are made from, on processing conditions, and on the surface properties of the fibres. Woven fibres may approximate the stress strain behaviour of nature tissue more than other structures and therefore offer better compatibility. This is important especially in applications such as the natural blood vessels replacement. [9]

1.1.3.4 Fibre Types

Natural and synthetic engineering fibres are both used in the biomedical field which shown in Table 1.3. Natural fibres such as collagen and silk have been used

for many years by physicians but synthetic polymer fibres have found increased use in biomedical applications due to higher production volumes. Some high performance fibres such as carbon have been used in tissue engineering where high strength and improved tissue compatibility is required. [9]

Table 1.3 Engineering Fibres Used in Biomedical Applications [9]

Type	Examples
Natural fibres	collagen, silk, cellulose, chitin
Synthetic organic fibres	polyester, polyamide, polypropylene, polyurethane Polytetrafluoroethylene, polyethylene, poly (vinyl alcohol), polyacrylonitrile, poly (glycolic acid), poly (lactic acid), regenerated cellulose, polydimethylsiloxane, aramid
Inorganic fibres	carbon, graphite, alumina, glass

1.1.3.5 Applications of Fibres

Fibre-Reinforced Composites

Fibre-reinforced composites are used for a number of mechanical functions and contain two main components: high strength and modulus fibres and a matrix which performs as a binder for the fibres. In this manner, both fibres and matrix maintain their physical and chemical character but the resultant composite has properties not achievable from each constituent. Generally fibres are the major component for carrying load, whilst the surrounding matrix holds fibres together in a desired orientation and location, functioning as a load transfer medium between fibres and matrix [10]. A common result is the production of a composite of high strength and stiffness but lacking the brittleness of the fibres. Different types of glass and carbon fibres and Kevlar 49 are the basic fibres in commercial

use. These fibres can be embedded into a matrix either in continuous or discontinuous lengths. The matrix material could be a polymer, a metal, or a ceramic [10]. The properties of fibre-reinforced composites can be controlled by the fibre volume fraction which is often a critical parameter in defining the mechanical properties of the composite. Generally, the higher the fibre volume fraction, the higher the strength and modulus of the fibre-reinforced composite [10]. Critically, the adhesion between the fibre and matrix dictates the mechanical properties of the composite.

Fibre-reinforced composites can be used for industrial and commercial applications where their mechanical performances are the main importance. As such, composites have been used in the area of military and commercial aircrafts, for which weight reduction is essential for increased payloads and higher speeds. Fibre-reinforced composite materials are increasingly being used in aerospace applications, electronics applications and automotive applications which include: body components, chassis components and engine components. For example, body parts of race cars and some automobiles are composites made of glass fibres. Sports equipment, such as a racing bicycle frame consists of carbon fibres embedded in a thermoset polymer matrix.

Biomedical Applications

Fibres have been used in medical applications for many years such as tapes, sanitary pads, operating-room apparel and dressings. Engineering fibres have many applications including medical equipment, surgical implants, prosthetic devices and sutures. Engineering fibres also have been used for separations and purifications for example substrates for large scale cell culture. These fibres help in maintaining and improving the quality of life. [9]

Engineering fibres also have been used in surgical implants. One purpose is in synthetic replacements for diseased or non-functioning blood vessels, such as segments of the aorta or other large diameter arteries. Synthetic materials for these applications include polytetrafluoroethlene (PTFE) and polyester fibre. Polyester

fibres produced from poly (ethylene terephthalate) are woven into a porous tube with a lightly napped and smooth surface. The PTFE is manufactured as a continuous microporous tube with a noncrimped and smooth flow surface. [9]

Tensile strength, toughness, biocompatibility and porosity are requirements of the woven fibre used in arterial replacements. The structure must have adequate strength to withstand the intraluminal blood pressure, and to be suturable. These properties must be maintained adequately to prevent rupture or aneurysm formation for many years after implantation. The fibrous structure must also have enough porosity to allow tissue in-growth and a thin fibrin-based thromboresistant neointima forming on the tubing inner surface. Alternatively, the pores must be small enough to prevent the outflow of blood. Ultimately the fibre must not bring out an unfavourable tissue response that would lead to rejection. [9]

Typical structures derived from polyester fibres and PTFE have been acceptable in large diameter, high-blood-flow applications. Smaller diameter synthetic arteries substitutes require new elastic fibrous structures that are more thromboresistant. [9]

Damaged tendons and ligaments could be replaced by orthopaedic implants fabricated from engineering fibres. Natural tendons and ligaments are fabricated primarily of collagen fibres; ligaments connect two or more bones while tendons connect muscle to bone. Engineering fibres are candidate replacements for these structures and are near their biological and mechanical properties. Polytetrafluoroethylene, polypropylene, polyester, and carbon fibres also have been investigated. [9]

Carbon is a high performance fibre material and most commonly used in polymer-matrix composite reinforcement [11]. Carbon fibres have the highest specific modulus and specific strength in all reinforcing fibre materials [11]. It is because of these mechanical properties that carbon fibres have gained interest for both tendon and ligament replacements. Carbon fibres can be used as scaffolds to allow

the growth of new, oriented collagenous fibrous tissue. Unfortunately, carbon fibres are known to be brittle and are thus typically coated with poly (lactic acid) to contain potential carbon fragments which may be produced when the fibres fracture. Composites of carbon fibre with polysulfone resin and carbon fibre reinforced carbon have been evaluated in orthopaedic devices such as artificial hips. The potential advantage of these composites is a closer modulus to bone, otherwise it will cause shear. [9]

1.1.4 Polymer Nanofibres

Nanofibres can be defined as fibres with diameters on the order of 100 nm size or less. Polymer nanofibres have many potential applications such as in biomaterials, composites, filtration and energy storage because of their very large surface area to volume ratio and their porosity.

The fibres are often structurally anisotropic and can sometimes be extremely highly ordered, such as in Kevlar fibres. These polymer fibres have excellent mechanical properties due to high molecular alignment, giving an optimal elastic modulus. It has been suggested that the ultimate strength of highly oriented UHMW-PE fibres [12-15] and carbon fibres [16, 17] depends on the diameter of the fibres, which is consistent with Griffith theory [18]. The size effect for a series of entirely oriented UHMWPE fibres with different fibre diameters has been analyzed [13, 14] and the data showed a suitable fit to a modified Griffith equation:

$$\frac{1}{\sigma} = K_1 D^{1/2} + K_2 \qquad (1.3)$$

where K_1 and K_2 are constants, D is the fibre diameter and σ is the fibre's tensile strength.

The improvements in mechanical properties of polymer fibres also make them suitable as reinforcements in composite materials, with the adhesion between the

surface of the fibres and surrounding polymer matrix critical in defining overall composite performance. The production of polymer nanofibres may improve the mechanical performance of polymers even further through the reduction in critical defects as well as a highly confined volume in which to give highly ordered molecular orientation. In this case, the utilization of the potential mechanical improvement of nanofibres in composites materials is again critically dependent on the adhesion at the nanfibre-matrix interface. Because of their large surface area to volume ratio and light weight, nanofibres have the potential to be used in numerous applications. Table 1.4 shows the fibre surface area per mass of nanofibres compared with another two fibre production methods: wet spinning and melt spinning [19].

Table 1.4 Fibre surface area per mass of fibre material for different fibre diameter [19]

Fibre Type	Fibre diameter (μm)	Fibre surface area per mass of fibre material (m^2g^{-1})
Nanofibres	0.05	80
Wet Spun fibre	20	0.2
Melt Spun fibre	2.0	2

The potential for unique surface properties of nanofibres due to a polymer structural organization within a confined volume, as well as the large surface area per mass, may make them suitable for a variety of applications from medical to consumer products and from industrial to high tech applications in energy storage, fuel cells, aerospace, transistors, capacitors, battery separators, drug delivery systems and information technology. [19]

The most promising route to make polymer nanofibres is using the electrospinning process which will be described in sections below. The advantages of electrospinning are the flexibility of technique and relatively simple equipment required. Many techniques to produce nanofibres exist such as drawing [20], phase separation [21], template synthesis [22, 23], self-assembly [24] and electrospinning [25, 26]. However, all of these techniques have some disadvantages including multi-step discontinuous processes, limited range of polymers used and jet instability. Compared to conventional fibres, the process of

producing nanofibres is relatively expensive because of low production rate and high technology cost. Additionally potentially toxic solvent evaporation during electrospinning process needs to be controlled in an environmental friendly approach. This also involves additional equipment and cost. Eventually the challenges faced for nanofibres include cost, safety, solvent vapour, handling, packaging and shipping, etc. Overall electrospinning seems a cost effective technique which can produce long, continuous nanofibres. Critically the physical properties and molecular structure of electrospun polymer nanofibres is not well understood. [19]

1.1.4.1 Electrospinning and Electrospraying

Electrospinning and electrospraying are two popular techniques based on the same principle of electrostatic hydrodynamics, which use an electric field to generate a liquid jet from a nozzle. Higher viscosity solutions can form continuous fibres which is called electrospinning whereas lower viscosity solution will break up into droplets, which is called electrospraying. Both techniques will be discussed in the following sections.

Electrospinning

Electrospinning is a simple and popular method used to produce ultrafine fibres from many different materials which include polymers, composites and ceramics [27]. The electrospinning process can be considered as an alteration of the well known electrospray process. This method is similar to the commercial processes for drawing out microscale fibres except an electrical field is used rather than a mechanical or shear force to continuously draw out a jet to form different diameter fibres [28, 29]. Electrospinning can generate relatively small fibre diameters when compared to conventional drawing methods. Similar to mechanical drawing, electrospinning is also a continuous process and should have a high production rate and volume. Electrospinning also can be considered as a variant of electrohydrodynamic atomization (or electrospray) process [30] and will be discussed in next section.

Solution viscosity is higher in electrospinning process comparing to the electrospray process and the solution droplet will be charged by the high voltage and thus induce the ejection of a liquid jet throughout a spinneret to form nanofibres. The electrical potential is applied between a droplet of a polymer solution, or melt, held at the end of the capillary needle and a grounded target. A charged jet of the polymer solution is ejected and the route of the charged jet will be controlled by the applied electric field once the applied voltage overcomes the surface tension of the droplet [31]. The jet shows bending instabilities due to repulsive forces between the charges carried with the jet. The jet expands through spiralling loops of increasing diameter, where the jet gets longer and thinner until it solidifies to form nanofibres on the ground electrode [31]. A typical electrospinning setup has been shown in Figure 1.5. A detailed overview of the electrospinning process will be given in Chapter 2.

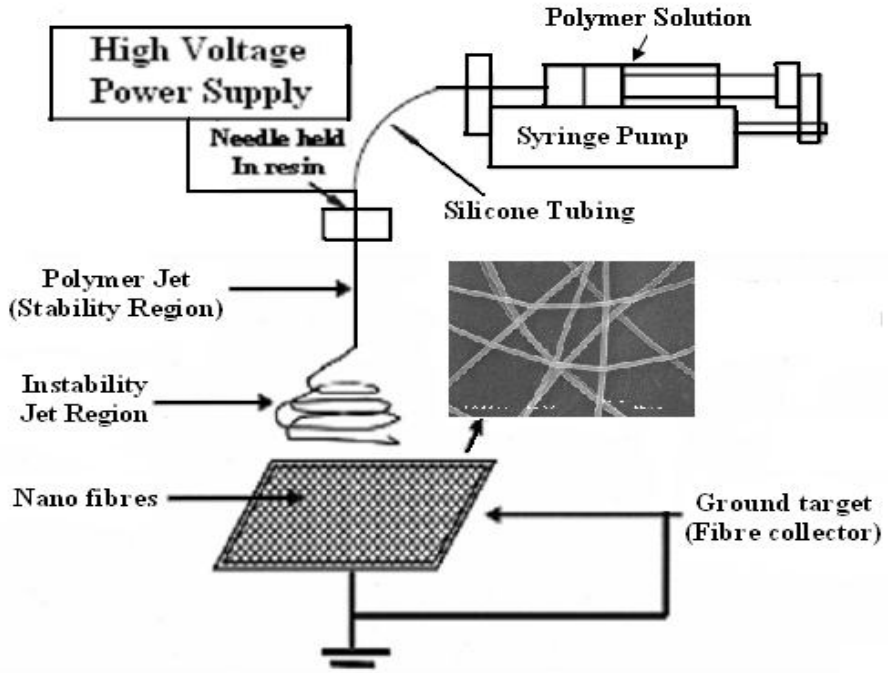

Figure 1.5 Scheme of electrospinning experimental setup

Electrospraying

The field of drug delivery is advancing swiftly. Accurate control over the dosage and targeting of the drug within the human anatomy is known to reduce side effects and gives rise to new therapies [32]. Inhalation systems, predominantly used for transporting particles, can only be successfully used for delivering fine particles, which are airborne, or droplets below a certain size (3–4 μm). However, if either of these is too large, continuously suspending in air is extremely difficult, and therefore inhalation cannot be used [33]. Several routes have been adopted for processing biomedicines. These can essentially be categorized as dry powder inhalation [34], aerosol delivery [35] and breath-activated guidance [36]. The first is predominantly based on particle aerodynamics and requires the patient to take a deep breath, hence transporting the powder into the lungs. Aerosol delivery offers a route for inhaling biomedicines, e.g. insulin, as a therapeutic treatment for diseases like diabetes. The breath-activated system of delivery is assisted by electronic components in a device triggering operation of features such as dose titration, breath actuation and coordination, inhaled air temperature and electronic storage of dosing information. Aspirin, acetylsalicylic acid, is one of the most popular drugs in the world [37]. It is a white, crystalline, weakly acidic substance, with a melting point of 137 ◦C. It is useful in the relief of headaches, muscle and joint aches. Aspirin is also effective in reducing fever, inflammation, swelling, and thus has been used for treatment of rheumatoid arthritis, rheumatic fever and mild infection. Electrospray is a droplet generation route uses an electric field to draw out a jet, which later narrows down to detach droplets, hence leading to form a spray [30]. This route is referred to as electrohydrodynamic atomization (EHDA) or electrospraying (Figure 1.6). There are several different modes of electrohydrodynamic atomization, namely spindle, multi-jet, rim emission, together with their numerous manifestations [38-44], and the technique has been used for processing proteins [45-48], manipulating DNA within organisms using the gene gun [49]and in the treatment of asthma and similar lung diseases [50]. In this process, the imposed electric field draws the liquid medium to form a stable

jet from a conical base and subsequently breaks the liquid into a narrow distribution of droplets [41]. This spray morphology is referred to as the cone–jet mode of electrohydrodynamic atomization, hence generating a near-monodispersed distribution of droplet relics (Figure 1.7). The crucial parameters for achieving a stable cone–jet mode of electrohydrodynamic atomization are density, surface tension, viscosity, electrical conductivity and relative permittivity [51-54] of the solution.

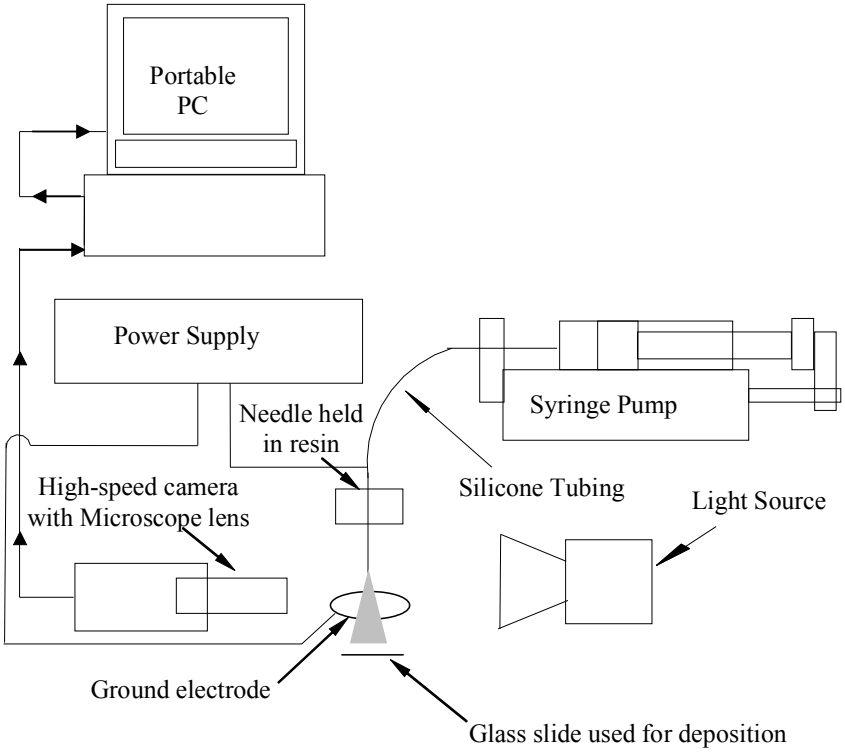

Figure 1.6 Schematic representation of the electrohydrodynamic atomization equipment set-up.

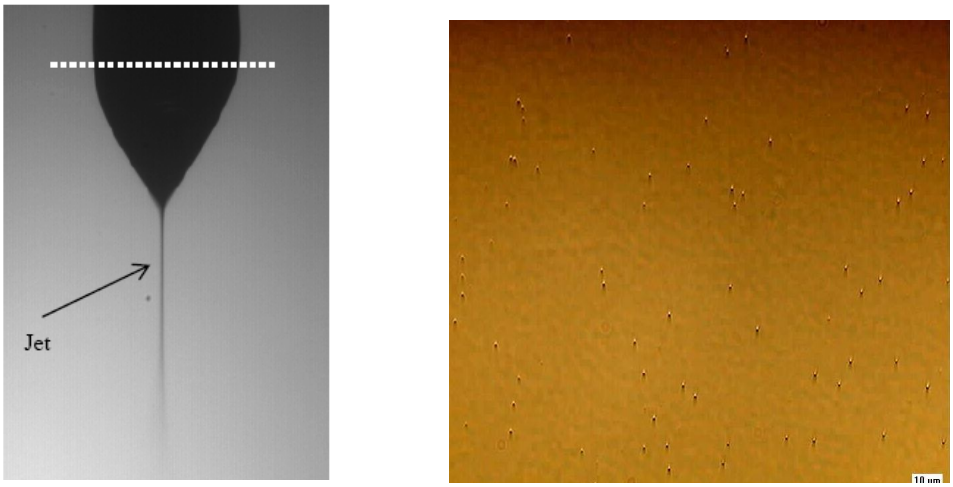

(a) (b)

Figure 1.7 (a) Stable cone–jet mode atomization of the aspirin solution. The needle exit is indicated by a dotted line. (b) Optical micrograph of droplets soon after EHDA.

1.1.4.2 Applications of Electrospun Nanofibres

Nanofibre Reinforced Composites

Engineering fibres such as carbon fibres, glass fibres and Kevlar fibres are the most widely used together with resin substrates in the application of recent composites, with consideration of the strength to weight ratio. However, nanofibres may bring an evolution to this field with better mechanical properties than micro-scale fibres and superior structural properties. Because nanofibre has large surface area to volume ratio, using nanofibre as components in composite can efficiently increase the interaction between nanofibres and matrix materials and lead to better reinforcement or potentially higher toughness composites if the composite failure occurs at the nanofibre-matrix interface. A significant amount of literature examines a wide variety of fibrous nanomaterials reinforcing polymers, with carbon nanotubes often selected as a reinforcing phase due to their high elastic modulus. For electrospun nanofibres reinforcements, several researchers

have successfully studied resultant polymer composites. The reinforced effect of electrospun nanofibres of polybenzimidazole (PBI) in an epoxy matrix and in a rubber matrix was studied by Kim and Reneker [55]. They observed that mechanical properties such as Young's modulus of a rubber film can be significantly increased by reinforcing with electrospun poly(benzimidazole) nanofibres [55]. Bergshoeh and Vancso also found with addition of electrospun Nylon nanofibres to an epoxy resin could significantly increase the composite mechanical strength and stiffness [56]. These observations suggest that electrospun polymer fibres may become viable, and cheaper, alternatives to other nanomaterial reinforcements in composites.

Biomedical Applications

Electrospun nanofibres have biomedical applications particularly in tissue engineering as scaffolds [57]. This is because mats consisting of many electrospun nanofibres have a relatively large surface area and interconnected three dimensional porous structures which are conductive to tissue ingrowth. In addition, many biopolymers and biodegradable polymers have been electrospun as nonwoven membranes. Another example of biomedical application of electrospun nanofibres is the use of electrospun nanofibres as drug carriers for drug delivery system [58]. Various drugs have been successfully introduced (i.e., maintain their structure and bioactivity) into nanofibre scaffolds, which can potentially be used as drug delivery vehicles. Electrospun polymer nanofibres have been attempted as cosmetic skin care masks for the skin healing, skin cleansing treatment and other therapeutically or medical properties with or without various additives [59]. Other examples such as electrospun nanofibres can be used for wound dressing because of their fibrous structures can protect the wound from bacteria penetration through aerosol particle capturing mechanism and provide a path for vapour transport [60, 61].

Catalytic Nanofibres

Electrospun nanofibres are regarded as excellent supports for enzyme immobilization in application such as fine-chemical/pharmaceutical synthesis, food processing, and biosensors fabrication [62, 63]. The use of electrospun nanofibres results in enzyme immobilization which can overcome the limitations of enzyme such as instability and nonreusability [62]. Wang et al (2009) suggested three aspects of the qualification of electrospun nanofibres were the reasons behind this application of electrospun nanofibres. Firstly, they suggested that there are a variety of polymers which can be electrospun and meet different requirements as supports. Secondly, the hindrance for mass transfer of electrospun supports was low. This is because of the high porosity and the interconnectivity of electrospun supports. Thirdly, the nanofibre surfaces can be modified to benefit enzyme activity.

Filtration

Electrospun nanofibres are used in filtration in many engineering fields. As we know, electrospun nanofibres have very high surface area to volume ratio and good interconnectivity of pores which results in high surface cohesion. Qin et al. have investigated the filtration properties of electrospun nanofibres [64]. Because of the high surface area to volume ratio and the resulting high surface cohesion, electrospun nanfibrous filters can easily trap tiny particles of the order <0.5 μm and have the potential to incorporate active chemistry on a nanoscale [64], also polymer low surface free energy can stop things sticking together. Barhte et al. have investigated the structural and transport properties of electrospun nanofibrous membrane related with the experimental processing parameters attempting to understand the deposition, distribution and orientation of nanofibres in the nanofibrous filtering media [65]. They can achieve the controlled pore size distribution by coordinating the drawing and collection rates [65].

1.1.5 Surface Properties

Electrospinning is effective at producing a wide range of polymer nanofibres. Some of the physical properties for electrospun nanofibres such as mechanical properties indicate that polymer structure has played an important role for the final properties. However, surface properties of electrospun nanofibres and how it relates to polymer structure has not been extensively investigated.

In this thesis we are aiming to investigate the adhesion and wetting properties of electrospun polymer nanofibres. These two surface properties are both related to surface tension or surface energy.

Surface tension is a direct demonstration of the cohesive forces that hold liquids together. The skin of the water surface allows a needle to float on the surface of pure water and can be used by insects to walk across the surface of pool. It has been seen that a fluid surface behaves like a taut membrane; if such a membrane has been cut then it must need to apply a given force per unit length of cut to hold the surface together. Thus surface tension has the measurement of a force per unit length and this must be equal to the energy of the surface [66].

Surface tension is due to the attraction between the molecules of a liquid caused by intermolecular forces. In a liquid body, each molecule is attracted uniformly in all directions by its neighbor liquid molecules and leading to a zero net force. At the liquid surface, the molecules are attracted by other molecules inside the liquid and are not strongly attracted by the neighbor medium molecules (either vacuum, air or other liquid). As a result all of the molecules at the surface experience an inward molecular attraction force and this driving force will diminish the surface area, so from this point a liquid surface looks like a stretched elastic membrane. Eventually the liquid will compress itself together until it reaches the lowest surface area, such as a spherical shape. [67]

Wetting is the capability of a liquid to keep contact with a solid surface because of intermolecular interactions when the liquid and the solid are brought together.

Wettability can be determined by surface energy or surface tension. Generally a high surface energy material has better wettability comparing to a material with low surface energy. Wetting is essential in the bonding of two materials as the adhesive needs to spread and wet both of the surfaces involved. Wetting and the surface forces that influence wetting are also responsible for other related phenomena such as capillary effects [68]. A low contact angle is a sign of good wetting [69].

Adhesion and surface energy are also closely related. Adhesion is the force needed to separate two surfaces. Interfacial surface energy is the work used to separate these two surfaces. Therefore adhesion is depending on the surface energy. Surface energy is usually quantified by contact angle measurement from a goniometer. For a bulk surface contact angle can be easily measured and surface energy can be calculated from Young's equation. Little work on polymer nanofibre surface energy has been investigated from literature [70-72] because of difficulties in performing modified experiments at the nanoscale. Surface contact angle of electrospun nanofibrous membranes was measured by a water contact angle machine [73]. A distilled water pendent droplet was injected from a syringe onto the membrane was imaged through an image analyzer and the angle between the surface and the water droplet was measured [73]. A hydrophilic material could show a low contact angle (water spreading across a surface) and a hydrophobic material could show a high contact angle (minimal contact between a surface and a water droplet) [73]. More information about surface properties will be discussed further in Chapter 2.

In this thesis we will use scanning probe microscopy (SPM) technique and contact mechanics to examine adhesion and wetting properties of electrospun polymer nanofibre surfaces.

1.1.6 Scanning Probe Microscopy (SPM)

In the last twenty eight years the microscopy field has experienced a revolution with the development of a new family of techniques based on scanning probe

microscopes (SPM). There are several types of scanning probe microscope. This microscope will generate a topographical map on an atomic scale, an image of surface features and characterisation of the examined specimen [11]. Comparing to other microscopic techniques, SPM shows a number of advantages: is particularly useful for obtaining the following:

1) Examine a specimen on the nanometer scale and high resolution imaging [11].
2) Generate three dimensional topographical information [11].
3) Operate in different environments such as air, vacuum, air and liquid, so a particular specimen can be examined in its most favorable environment [11].
4) SPM is suitable for understanding and measuring adhesion force and surface energy.

1.2 Motivation and Aims

1.2.1 Motivation

Fibrous materials are used in a variety of applications due to their relatively high surface area to volume as well as potential structural anisotropic organization. Polymers are widely employed as fibres because they are easy to process, lightweight and have a range of properties that can be tailored to a particular function. The properties of polymers are critically dependent on their structure and chemical composition. Numerous studies into polymer structure-property relationships have been extensively carried out on polymers ranging from the macroscopic level to the microscopic. New processing techniques based on electrospinning have recently been developed which allow the manufacture of polymer fibres with unique structural organization at the nanoscale [74]. However, understanding the properties of polymer fibres at the nanoscale is not yet fully developed.

The surface of polymer fibres plays an important role in many applications. Composites require good adhesion between the fibre and surrounding matrix to

allow efficient stress transfer for mechanical reinforcement. Other examples include filters, made of polymer fibres, being critically dependent on the interaction between the polymer surfaces and filtrate. As the dimensions of polymer fibres become smaller, potential property differences may occur due to changes in structure. It can be indicated that:

Processing ⟶ Structure ⟶ Properties ⟶ Performance

Electrospinning is therefore an effective technique for producing fibres with relatively small dimensions in order to study any different or unique structures, and thus physical properties, which can occur relative to bulk polymer materials.

1.2.2 Aims

The aims of this project are to develop and understand the surface properties of polymer fibres at the nanoscale using experimental techniques. More specifically, there are three aims as described below:

- To produce polymer nanofibres using electrospinning techniques. Size effects will be examined by controlling different processing parameters such as solution concentration, applied electric field strength, flow rate and a few other parameters to define the nanofibre morphology.
- Experimentally measure the surface properties of electrospun polymer nanofibres by scanning probe techniques (SPM) and contact mechanics, in order to understand wetting and adhesion.
- Relating surface property measurement to polymer structure to evaluate how the material structure from electrospinning affects the surface properties.

Chapter 2

Literature Review

2.1 Introduction

Section 1.1.4 highlighted how polymer nanofibres have advantages over bulk polymer materials such as large surface area to volume ratio and anisotropic behaviour, but their surface properties have not been fully understood. In addition, there are challenges in manufacturing of these nanofibres. The literature review below details the various processes used to manufacture polymer nanofibres and highlights the applicability of electrospinning as a principle method. The review then examines the surface behaviour of electrospun nanofibres and the feasibility of measuring their surface properties directly.

2.2 Nanofibres

2.2.1 Nanotechnology and Nanofibres

The prefix "nano" is used to technically signify physical quantities within the scale of a billionth of the reference unit, therefore nanometer describes a billionth of a meter [75]. Nanotechnology signifies the science and engineering of materials, structures and devices where at least one of the dimensions is l00 nm or even less

[75]. Polymer fibres can be considered as nanomaterials if their diameters are sub-100 nm, although length scales approaching a few hundreds of nanometres have also been defined as nanomaterials [1]. Potential advantages have been found when producing materials at smaller length scales. For example, the elastic modulus of polymeric nanofibres is found to increase when the fibre diameter decreases below 350 nm [76, 77].

2.2.2 Fabrication of Nanofibres

2.2.2.1 Overview

There are various processing technologies for nanofibres including drawing [78], phase separation [79], template synthesis [80, 81], self-assembly [82] and electrospinning [83, 84], etc. These techniques will be introduced in the following sections.

2.2.2.2 Drawing

Nanofibres have been produced with citrate molecules through a drawing process [85]. A micropipette with a few micrometers diameter was dipped into the droplet by using a micromanipulator as shown in Figure 2.1.

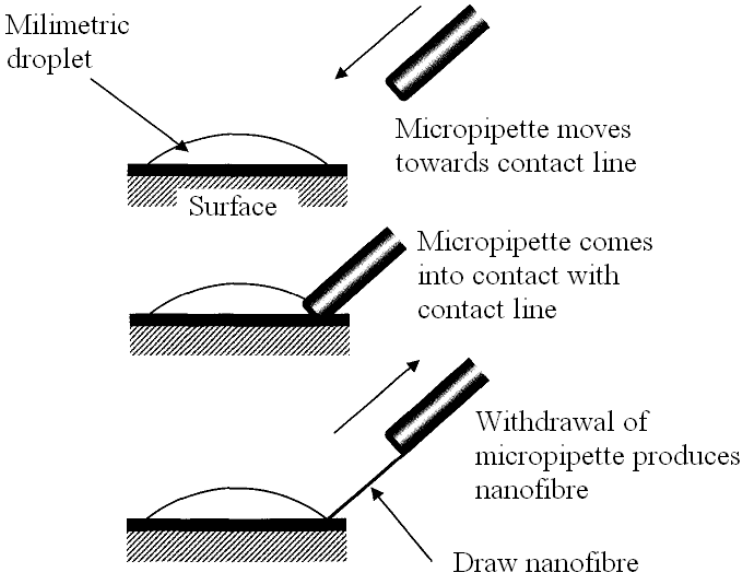

Figure 2.1 Drawing method to obtain nanofibres [85]

A nanofibre will be drawn after the micropipette was withdrawn from the liquid and moving at a speed of about 1 x 10^{-4} $m.s^{-1}$. By touching the drawn fibre with the micropipette end, the fibre will be deposited on the surface. The nanofibres drawing can be repeated on a single droplet to produce numerous fibres. [85]

2.2.2.3 Template Synthesis

Template synthesis process uses a mould to produce the desired nanofibre as shown in Figure 2.2. The principle for template synthesis is the incorporation of a polymer solution within pores on a membrane. For nanofibre production [86] the template is an aluminium oxide membrane with nano-scale diameter pores of uniform thickness. The polymer solution will experience water pressure on one side and restrain from the porous membrane, extrusion and contact with a solidifying solution. In this process the nanofibre diameters will be determined by the pores. [86]

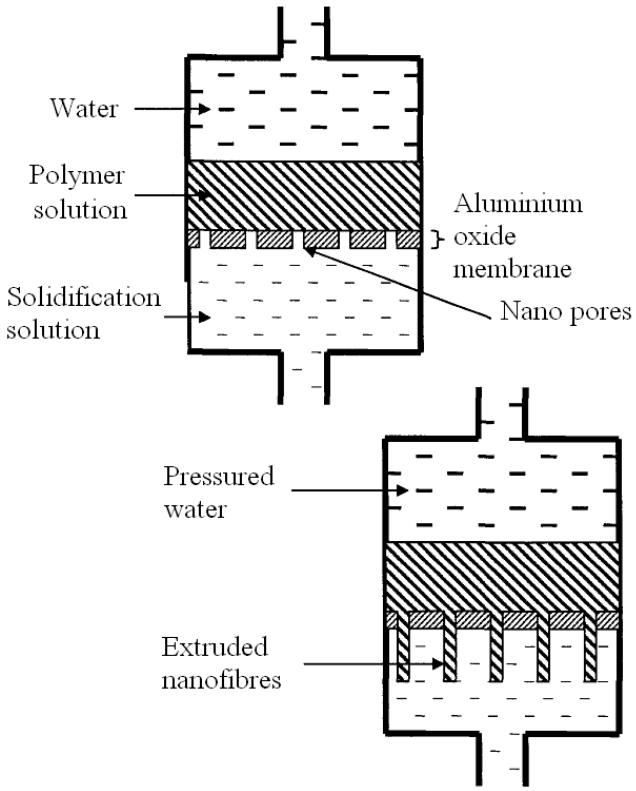

Figure 2.2 Template synthesis method to produce nanofibres [86]

2.2.2.4 Phase Separation

Phase separation is a common concept encountered in polymer science and been applied to the production of polymer nanofibres. The concept of phase separation relies on a mixture of two or more mobile components separating into distinct phases due to differences in their surface tension. This phase separation has been successfully employed to produce fibres by first mixing a polymer with a solvent to give a gel network with solvent regions [75]. The solvent is extracted, leaving behind strands of a solid phase [75]. Nanofibrous poly(L-lactic) acid (PLLA) has been produced by using this procedure [79], with the main steps which include polymer dissolution, gelation and solvent extraction, shown in Figure 2.3.

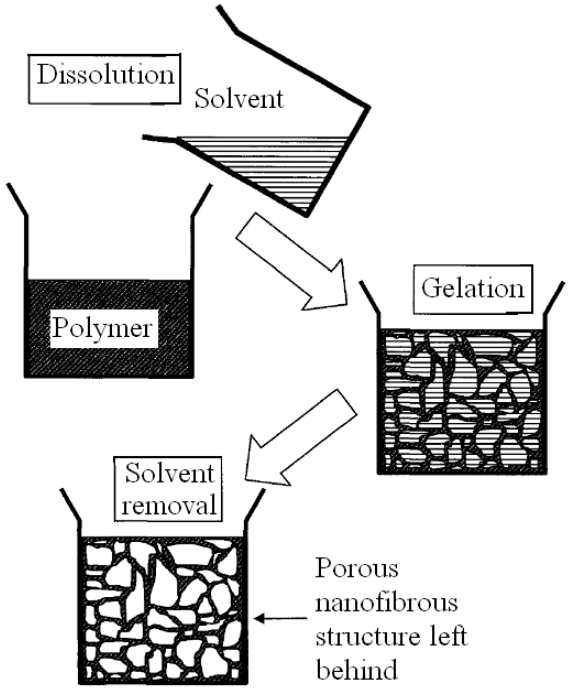

Figure 2.3 Generic schematics of phase separation to produce nanofibrous structure [79]

2.2.2.5 Self-Assembly

Self-assembly is becoming a popular method of building structures from the controlled combination of molecules. This self-assembly can therefore be used to produce nanofibres from smaller molecules. Figure 2.4 is a simple schematic for nanofibre self-assembly method [87]. A small molecule (Figure 2.4 (a)) is assembled in a concentric way, so bonds can form between the concentrically assembled small molecules (Figure 2.4(b)), which upon extension in the plane's normal gives the longitudinal axis of a nanofibre, is shown in Figure 2.4 (c). The mechanism for self-assembly is the intermolecular forces bring the smaller molecules together. The shape of the smaller molecules determines the shape of the macromolecular nanofibre.[87]

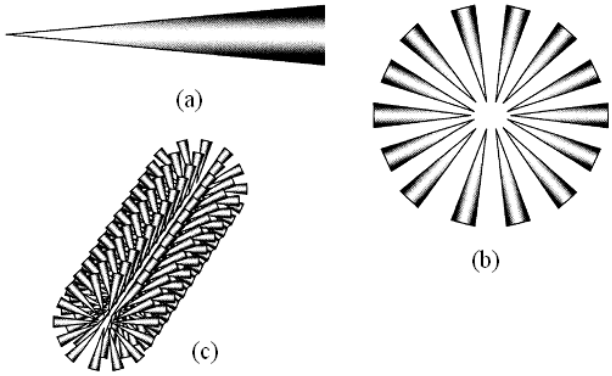

Figure 2.4 Self-assembly for obtaining nanofibre [87]

2.2.2.6 Electrospinning

The final technique to produce nanofibres discussed in this review is electrospinning. The first case of electrospinning fibres from a molten sealing wax was shown in the 1900s. However sealing wax is brittle, and no viable commercial development of this process for making fibres has resulted until recently [88]. Current research is focussed on the mechanism of liquid jets created by electric fields, the deformation of liquid droplets in an electric field, the breakdown of liquid jets into droplets, and the development of processes for electrospraying paint and other liquids [88].

A process to produce polymer filaments using electrostatic force was patented in 1934 and is referred to as electrospinning. Generally electrospinning produce nanofibres through an electrically charged jet of polymer melt or polymer solution. Suitable solvent should be selected to dissolve the polymer for electrospinning and also needs to evaporate quickly enough. The surface tension and viscosity of the solution must be in a range to form electrospun fibres.

Polymers were dissolved in some suitable solvents before electrospinning. Table 2.1 gives list of some of polymer solvents used during electrospinning process. Polymers which can melt at high temperatures can also be electrospun into nanofibres [89-91].

Table 2.1 Polymer solvent systems for electrospinning [92]

POLYMER	SOLVENTS
Nylon 6 and nylon 66	Formic Acid
Polyacrylonitrile	Dimethyl formaldehyde
PET (Polyethylene terephthalate)	Trifluoroacetic acid/Dimethyl chloride
PVA (Polyvinyl alcohol)	Water
Polystyrene	DMF/Toluene
Nylon-6-co-polyamide	Formic acid
Polybenzimidazole	Dimethyl acetamide
Polyramide	Sulfuric acid
Polyimides	Phenol

Among all the techniques for processing of nanofibres described above, the electrospinning process is the only successful method which can be further developed for mass production of continuous nanofibres from various polymers. It produces much smaller diameter fibres because of a high electrical force applied on the polymer solution, thus the nanofibrous structure have extremely large surface area to volume ratio [93]. Table 2.2 and 2.3 respectively compares the various nanofibre processing techniques. These tables highlight the flexibility of electrospinning and electrospinning was therefore selected as our nanofibre production method. Thus further studies of the electrospinning process have been carried out in the next section.

Table 2.2 Comparison of processing techniques for obtaining nanofibres [93]

Process	Technological advances	Can the Process be Upscaled ?	Repeatability	Convenient to process?	Control of fibre dimensions
Drawing	Laboratory	X	√	√	X
Template Synthesis	Laboratory	X	√	√	√
Phase Separation	Laboratory	X	√	√	X
Self-Assembly	Laboratory	X	√	X	X
Electro-spinning	Laboratory (with potencial for industrial processing)	√	√	√	√

Table 2.3 Advantages and disadvantages of various processing techniques [93]

Process	Advantages	Disadvantages
Drawing	Minimum equipment requirement	Discontinuous process
Template Synthesis	Fibres of different diameters can be easily achieved by using different templates	Can not make continuous fibres
Phase Separation	Minimum equipment requirement. Process can directly fabricate a nanofibre matrix. Batch-to-batch consistency is achieved easily. Mechanical properties of the matrix can be tailored by adjusting polymer concentration.	Limited to specific polymers
Self-Assembly	Good for obtaining smaller nanofibres	Complex process
Electrospinning	Cost effective. Long, continuous nanofibres can be produced	Jet instability

2.3 The Electrospinning Process

2.3.1 Electrospinning Mechanism

The mechanism behind the electrospinning phenomenon is complicated despite the simple electrospinning experimental set-up in Figure 1.5. A number of researchers have investigated the mechanism for electrospinning [89-91, 94-102]. The electrospinning setup consists of a syringe to hold the polymer solution, a DC voltage power supply in the kV range and a grounded electrode. The polymer solution was fed into a capillary and the high voltage power supply was connected between the tip of the capillary and the ground electrode. When the electric charge overcomes the surface tension of the polymer solution droplet, a charged jet will be ejected. The route of the charged jet is controlled by the electric field strength. The jet demonstrates bending instabilities caused by repulsive forces between the charges carried with the jet [103]. Figure 2.5 (a) shows a spinning jet recorded using high speed optical photography. The jet is shown to be ejected from the needle tip with an initially straight pathway and then became unstable. The unstable pathway is cone-shaped. The unstable pathway can be easily mistaken as multiple jets but imaging using a high speed camera proves that there is only a single, rapidly whipping or bending jet as shown in Figure 2.5 (b) [103]. The jet whipping frequency is relatively high and gives the impression that the original jet splits into multiple jets when it moving towards the collector [103]. The jet extends through spiralling loops; as the loops increase in diameter the jet becomes longer and thinner. Evaporation of the solvent in the jet occurs during this process resulting in solidification of fibres which are collected on the ground electrode [104-108]. The distance between the needle and grounded electrode should be large enough for solvent evaporation but not too small to create sparking [75]. For a melt polymer solution the discharged jet solidifies when it passes through the air and is collected on the ground electrode target. The fibres with fine diameters is mainly achieved by the stretching and the acceleration of the fluid filament during the instability region [103].

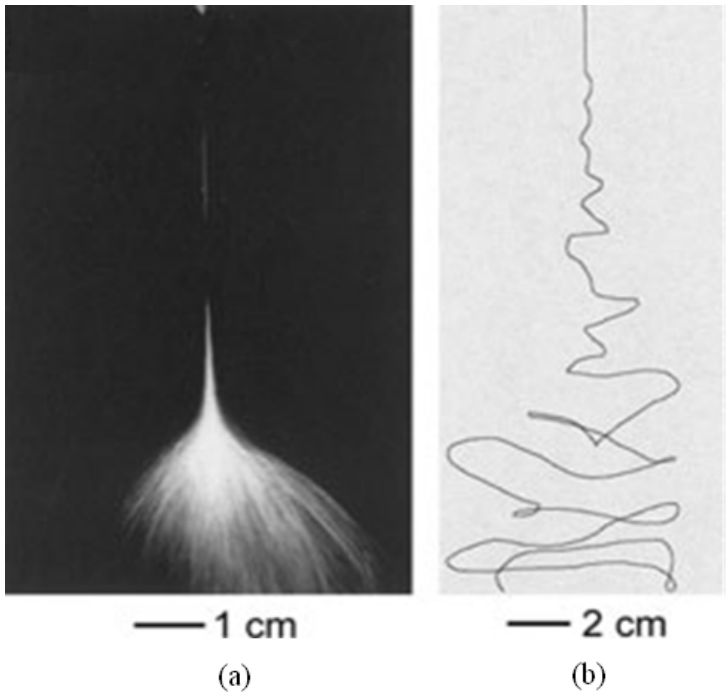

Figure 2.5 Photographs illustrating the instability region of a liquid jet from electrospun PEO solution [103].

2.3.2 Electrospinning Core-Shell Fibres and Hollow Fibres

2.3.2.1 Core-Shell Fibres

Recently core-shell structured material have gained great interest in many applications as core-shell structures can further enhance material property profiles for different applications such as encapsulation in drug delivery system [109] and core-shell fibres used for semiconductor [110]. Electrospinning technique has been demonstrated for the fabrication of core-shell structure polymer nanofibres [111]. For example, Sun et al have produced core-shell structures by co-electrospinning of two materials [111]. They used a co-axial needle which included an inner needle and an outer needle. Two liquids of polymer solutions or combination of polymer solutions have been supplied into the inner needle and the outer needle individually. A compound droplet suspended at the edge of the co-

axial needle would be then stretched into a compound jet through applied electric field. The compound jet solidified after solvents evaporation, resulting in compound core-shell structure nanofibres [111].

One interesting aspect of the core-shell method mentioned above is the effective production of materials, which cannot be spun on their own, as the core. The shell polymer is therefore acting as a template for the core material and results in a core-shell structure [111]. The shell acting as a template has been used to produce a highly spinnable PEO shell with a core of a low molecular weight poly(dodecylthiophene) (PDT, core) [111]. The PDT cannot be electrospun on its own due to its low molecular weight and less viscosity [111].

Additional core-shell structures have been obtained using a single needle setup and an immiscible phase in a secondary phase. Bazilevsky et al first demonstrated this from blends of poly(methyl methacrylate) (PMMA)/polyacrylonitrile (PAN) solutions in dimethylformamide (DMF) [112] as shown in Figure 2.6 (a). This work suggested that theoretically the outer shell jet was adequately strong to stretch the inner droplet into a Taylor cone during electrospinning to form a core-shell jet. The fibres produced had an outer diameter range from 0.5 μm to 5 μm and have similar core-shell structure comparing to the fibres attained from two needles, as shown in Figure 2.6 (b). Subsequent processing converted the core PAN into carbon tubes by heat treatment in nitrogen atmosphere as shown in Figure 2.6 (c).

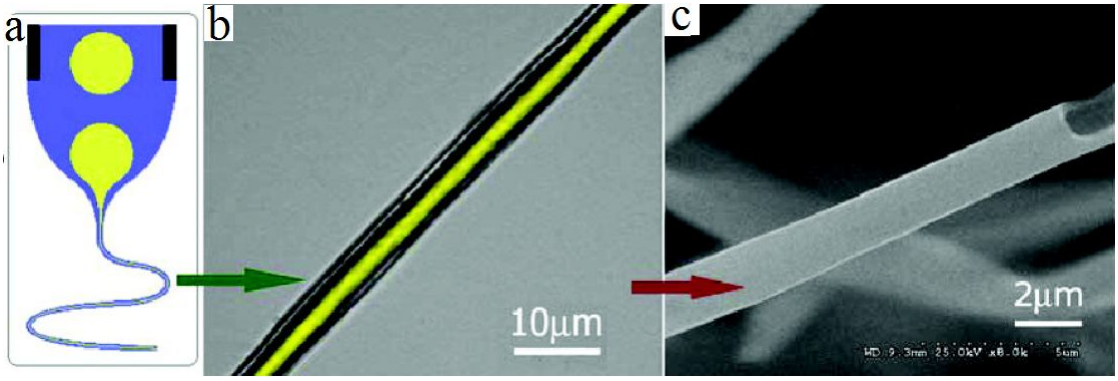

Figure 2.6 (a) Schematic of co-electrospinning of PMMA/PAN blend in DMF using a single circular nozzle. The PMMA/DMF droplets are shown in yellow, while the PAN/DMF liquid is shown in blue. (b) PMMA/PAN fibre with clear core-shell structure. (c) Heat treatment in a nitrogen atmosphere converted core-shell PMMA/PAN fibres into carbon tubes. The defects in these tubes were caused by handling, and are shown to demonstrate the hollow character of the heat-treated tubes. [112]

2.3.2.2 Hollow Fibres

Tubular nanostructures made of polymers, ceramics, metals, and carbon have been attractive in many applications such as nanofluidic channels, optical waveguides [113], energy conversion, catalysis, purification, separation, gas storage, drug release, sensing, and environmental protection, etc [85]. Many kinds of fabrication methods to produce nanotubes from different materials have been carried out. Electrospinning has been shown to be an effective method for the production of such nanostructures.

Li and Xia produced inorganic/polymer composites and ceramics hollow nanofibres by electrospinning two immiscible liquids through a coaxial needle which was followed by a core removal [113]. A sol-gel precursor consisting 0.3 g PVP (Mw ≈ 1 300 000), 3 g Ti(O*i*Pr)$_4$), 2 ml acetic acid, and 5 ml ethanol has been used as a shell liquid, and heavy mineral oil has been used as the core liquid [113] as shown in Figure 2.7 (A). These two liquids were supplied into two individual capillary spinneret. A stable coaxial jet was formed after applying high voltage. By controlling experimental parameters, they achieved different core-shell thickness. All experiments were carried out at room temperature in air, and the obtained electrospun nanofibres were left in air for about one hour to allow the Ti(O*i*Pr)$_4$ precursor to hydrolyze completely [113]. Finally the inner mineral oil was extracted by immersing the nanofibres into octane overnight [113]. Figure 2.7 (B) shows TEM image of two as-spun hollow fibres after the oily cores had been extracted with octane. The walls of these tubes were made of a composite

containing amorphous TiO_2 and PVP. Pure titania hollow fibres have been achieved by calcining the as-spun fibres in air at 500 °C for one hour [113] as shown in Figure 2.7 (C). By using a pair of electrodes with a gap to collect these fibres, uniaxially aligned hollow fibres can be achieved. These fibres can be fractured using a razor blade to expose their cross-sections as shown in Figure 2.7 (D).

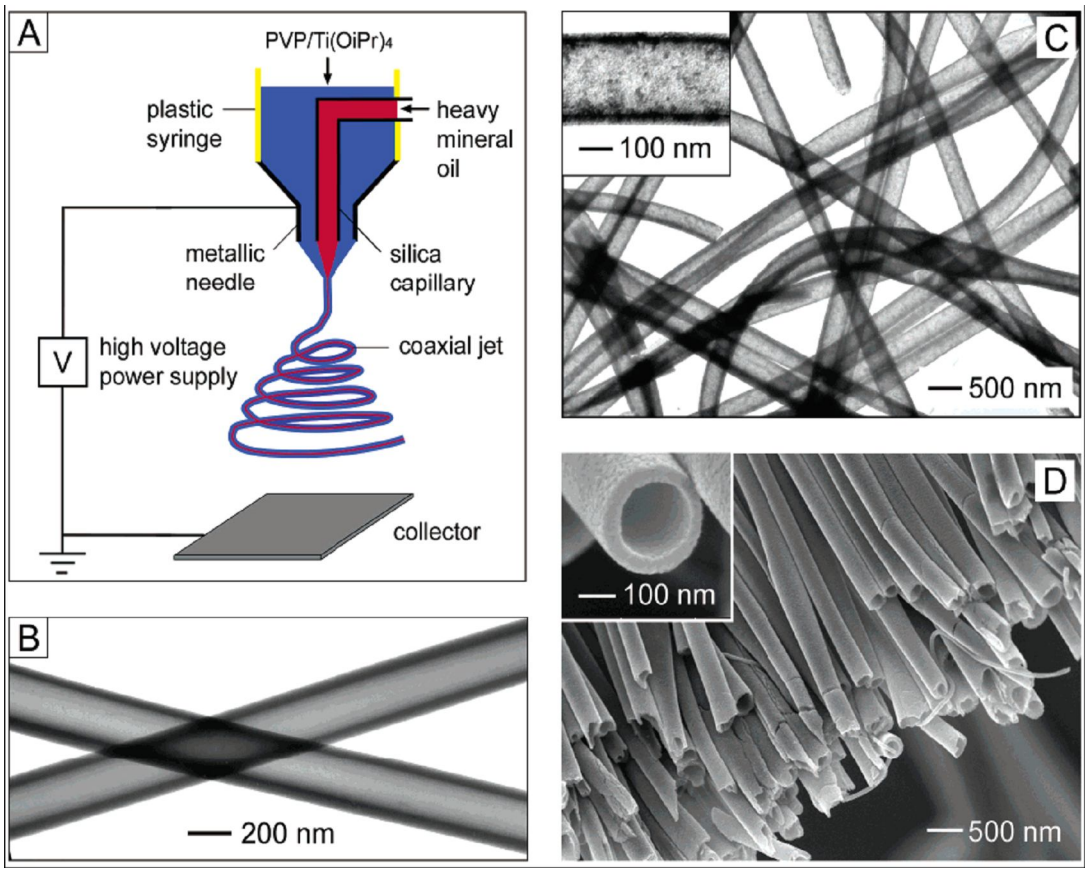

Figure 2.7 (A) Schematic example of the setup for electrospinning core/sheath structure nanofibres. The spinneret was made from two coaxial needles, through which heavy mineral oil and a solution containing PVP and Ti(O*i*Pr)$_4$ were simultaneously ejected to form a continuous coaxial jet. (B) TEM image of two as-spun hollow fibres after the oily cores had been extracted with octane. The walls of these tubes were made of a composite containing amorphous TiO_2 and PVP. (C) TEM image of TiO_2 (anatase) hollow fibres that were obtained by calcining the composite nanotubes in air at 500 °C. (D) SEM image of uniaxially aligned hollow fibres that were deposited across the gap between a pair of electrodes. These fibres were fractured using a razor blade to expose their cross-sections. [113]

So far it can be concluded that long, continuous, circular cross section, uniform size and well oriented hollow fibres can be fabricated using electrospinning process with two immiscible liquids through a coaxial spinneret. These hollow fibres can be easily transferred to other substrates. It is believed that this method can also be applied to many other materials leading to more applications. For example, this method can be applied to produce hollow nanofibres made of various oxides by replacing titanium alkoxide with other sol-gel precursors [114, 115]. In addition, this method suggests liquids with low electrical conductivities which are not suitable for electrospinning can be stretched into thin jets by coelectrospinning with another solution which is spinnable. This will greatly expand the scope of the materials that can be processed.

2.3.3 Processing Parameters and Resultant Fibre Morphology

2.3.3.1 Overview

This section will detail the parameters that influence the electrospinning process during transformation of polymer solutions into nanofibres and nanofibre morphology. These parameters include: (a) the solution properties such as concentration, viscosity, surface tension, conductivity, etc. (b) experimental setup parameters such as solution flow rate, applied voltage at the needle tip, and the distance between the tip and the collecting target, and (c) ambient parameters such as solution temperature, humidity, and air velocity in the electrospinning chamber [116]. It should be noted that the effects of some parameters mentioned above on the electrospinning process and fibre morphology are mutual-dependent rather than isolated.

2.3.3.2 Viscosity and Molecular Weight

Polymer chains are connected through entanglements and their length must be sufficient enough to form a network where polymer chains can not flow independent of each other. Moreover, longer the polymer chains are, higher the molecular weight and viscosity is. A spinnable polymer must be generally with relatively high molecular weight, resulting in a highly viscous solution after being dissolved with solvent [117]. This presence of polymer entanglements can prevent the charged liquid jet breaking up during the electro-drawing [118]. Thus, varying the molecular weight of polymer can result in different fibre morphologies. Viscoelastic force prevents rapid changes in the shape of the jet [88] and more viscous solutions are less likely to form beads or beaded fibres during electrospinning process [88]. Beads structure will be formed when solutions are less viscous, the beads diameter become larger and the average distance between beads on the fibres become longer if the viscosity increases. In the mean time the shape of the beads steadily changes from spherical like to spindle like [88] but high viscosity may result in failure of electrospinning process due to the flow instability caused by high polymer solution cohesiveness. For example, literature suggests that electrospinning poly(ethylene oxide) (PEO) can only proceed from a corresponding solution with a viscosity that varies from 1 to 20 poises and surface tension in the range from 35 to 55 dynes.cm^{-1} were suitable for fine nanofibre formation [88]. When viscosities were over 20 poises, the electrostatic force generated from the applied voltage was insufficient for electro-drawing. Droplets were formed when the viscosity was lower than 1 poise due to the spinning jet rapidly breaking down into spherical droplets to reduce the liquid's surface area. Another example of viscosity effects was demonstrated in electrospinning cellulose acetate (CA) dissolved in 2:1 acetone/DMAc (dimethylacetamide) solvent. Viscosities between 1.2 and 10.2 poises were found to be suitable for electrospinning [119]. If outside this range, the solutions could not be electrospun into fibres at room temperature. Only few fibres can be processed from an even higher viscosity solution or the liquid jet broke up to droplets because of a low solution viscosity less than 1.2 poise [100]. The above two cases clearly indicate

that for different polymer solutions which can be electrospun into fibres the usable viscosity ranges are different. [100]

The fibre diameter is usually required to be controlled in electrospinning. Since nanofibres are achieved from evaporation or solidification of polymer liquid jets, the fibre diameters will mostly depend on the jet sizes. During the travelling of a solution jet onto a ground target, the primary jet may [120-122] or may not [97, 107, 108, 123-125] split into multiple jets, resulting in different size for fibre diameters (Figure 2.8). If no splitting occurs, one of the most important parameters affecting the fibre diameter is the polymer solution viscosity. A higher viscosity results in a highly viscous liquid jet can reduce the solvent evaporation rate and results in larger fibre diameter size [88, 94, 116].

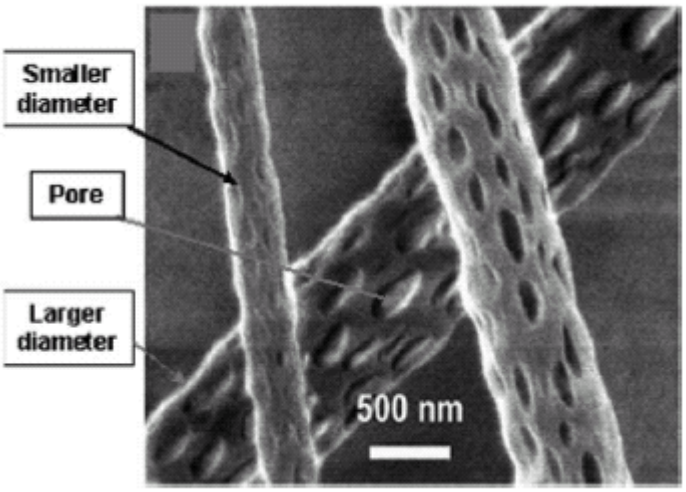

Figure 2.8 PLLA nanofibres with different diameters and pores [126]

2.3.3.3 Solution Concentration

Solution concentration is directly related to the viscosity of the spinning polymer solution and thus dictates resultant fibre diameter. Increasing polymer concentration gives an increased viscosity due to the enhancement in the number of polymer chain entanglements. These entanglements therefore allow ejection of more polymer material into the jet to give larger electrospun nanofibre diameters

[122]. Demir et al [127] suggested that the fibre diameter was proportional to the cube of the polymer concentration. A relatively higher polymer concentration in solution results in fewer bead-type structures being formed during electrospinning, with the bead shape changing from spherical-like to spindle-like if the polymer solution varied from low concentration to high concentration [128]. The reason for these different morphologies is principally the effect of increasing the solution viscosity as the fraction of polymer within the solution increases. This proves that the effects of solution concentration and solution viscosity on the electrospinning process and fibre morphology are closely related.

2.3.3.4 Surface Tension

As discussed in section 1.1.5, surface tension always tries to decrease the surface area per unit mass, so the jets will change their shape into spheres [88, 129]. The formation of the beads and beaded nanofibres can be considered as the break-up of the electrospinning jets by surface tension, adjusted by the applied electrical force presence [88]. Fibres can be formed without beads by reducing polymer solution surface tension [116]. For example, it has been observed that the surface tension of PEO solution can be reduced by changing the solvent from pure water to water and ethanol mixture and keeping the PEO concentration constant which will result in smooth electrospun fibres [88]. In addition, increasing the concentration of ethanol allows more solvent evaporate and increases the viscosity to prevents the rate of bead formation [88]. While low surface tension is favoured for electrospinning fibres, decreasing the surface tension of a spinnable solution will result in increasing fibre diameter. The mechanism for this diameter increase is expected to be because the formation of additional surface, which occurs as the fibre diameter increases, is less unfavoured as the solution surface tension decreases [88].

While the effects of solution concentration and solution viscosity on the electrospinning process and fibre morphology are closely related, as discussed in 2.3.3.3, the effects of solution concentration and surface tension on the electrospinning process and fibre morphology are not always related. This is

because the surface tension of polymer solution is more related to the function of solvent compositions, rather than related to the polymer concentration [119, 128].

2.3.3.5 Applied Voltage

In electrospinning, a DC voltage is applied between the polymer solution droplet and an electrically grounded substrate. Increasing this voltage gradually until a critical value is reached causes the droplet to deform into conical shape known as the Taylor cone [116]. When voltage passes the critical value, the distributed charges on the surface interact, overcoming the surface tension of the solution and a charged liquid jet emitted from the Taylor cone. The route of the charged jet is controlled by the electric field strength. The forces from the applied electric field try to increase the surface area, preventing the formation of beads and favours thinner diameter jets. Previous work has investigated the influence of voltage on electrospun fibre diameters spun from polystyrene (PS) solutions. The PS fibre diameter was found to decrease from 20 μm to 10 μm when increasing the voltage from 5 kV to 12 kV [130] and this phenomena was also observed for other polymers such as synthetic silk [131]. However, higher applied voltages have been shown to eject more solution in the jet, resulting in a larger fibre diameter [127]. This complication can be explained by considering electric field strength, and not electric potential, applied at the spinneret tip, with high electric field strengths resulting in a larger ejection of solution [132].

2.3.3.6 Flow Rate

The polymer solution flow rate is a significant processing parameter because it affects the jet speed and the solution transfer rate. The volume of polymer being spun dictates the fibre diameter, consequently a higher feeding rate leads to the formation of thicker fibres [133]. The flow rate of the ejected solution from the spinneret also follows the same principles. For example, when electrospinning polystyrene fibres, it was found that the fibre diameter and the pore diameter increased when increasing the polymer solution flow rate. Fibres had distinct

beaded morphologies and the mean pore size increased from 90 to 150 nm while increasing the flow rate [130]. In general, it was found that lower flow rates produced fibres with smaller diameters. Flow rates that were too high resulting in beading since fibres did not have a chance to dry prior to reaching the collector.

2.3.3.7 Needle to Target Distance

The morphology and structure of electrospun fibres is simply affected by the needle to ground electrode distance because they depend on the deposition time, evaporation rate, and whipping or bending instability period. It has been observed that during the electrospinning process of silk like polymer fibre with fibronectin functionality (SLPF) if not concerning the concentration of the solution, less needle-collector distance fabricates wet fibres and beaded structures. SLPF fibre shape changed from round to flat when decreasing the needle and ground target distance from 2 cm to 0.5 cm [131]. It has also been observed that aqueous polymer solutions need more distance to form dry fibre than solutions that use more volatile solvents [131]. In addition, bead structure formation has been seen for electrospun PS fibres when reducing the distance between the needle and collecting target, while forming the ribbon shaped fibre morphology with decreasing the distance between the needle to ground target distance [130].

2.3.3.8 Conductivity

Solvent conductivity is an important factor to affect the electrospun nanofibre morphology. Fong et al. suggests that increase in the solution conductivity causes higher electric net charges on the liquid jet, resulting in an increase in the force exerted on the jet to allow smaller fibres to be produced [88]. It was reported that solution with high conductivity can form fibres with bead free from even lower concentration solution [134]. A polymer solution by adding some filler material also can form fibres which are bead free. It was found that electrospun biodegradable PLDA polymers, with 1 wt.% salt addition, the obtained nanofibres were bead free [135]. Pham et al. have demonstrated that conductivity also can be

increased by the addition of alcohol into the polymer solvent, resulting in smoother poly (hydroxybutyrate-co-valerate) (PHBV) fibres with fewer beads presented [136].

2.3.3.9 Environmental Conditions

Electrospun fibre structure and morphology also can be influenced by environmental conditions such as the surrounding air, vacuum conditions, relative humidity, temperature etc. For example, it has been observed that acrylic fibres electrospun in an atomosphere with relative humidity over 60 % can not dry completely and appear entangled structure on the ground target surface [94]. It also been realized that the fibre diameters achieved from higher temperature (about 70 °C) polymer solution were much more uniform than the fibres obtained at room temperature.

Sometimes, environmental conditions can affect the effect of other parameters on electrospinning process and morphology such as viscosity. For example, polyurethane polymer solution viscosity with the same concentration but at higher temperature was much lower than that at room temperature. The highest concentration of electrospun polymer solution for polyurethane is 12.8 wt.% at room temperature, but the concentration can go up to 21.2 wt.% at a higher temperature [127].

Various parameters affecting the electrospinning process and fibre morphology have been reviewed. The aim of this review is to form a robust understanding of the electrospinning process. Thus an electrospinning process with the following characteristics can be achieved:

1. Diameters of the electrospun fibres are uniform and controllable;
2. Continuous single fibres are collectable;
3. The fibre surface is defect controllable or defect free. [100]

2.3.4 Control of Bead Formation in Electrospinning

Electrospun fibres often have beads and the formation of beaded fibres has been observed extensively [137]. For example, Figure 2.9 shows the beads in electrospun PEO fibres. Fang et al (1997) [138] also observed electrospun beaded DNA nanofibres. Control of bead formation is important issue in electrospinning process and involves selection of the correct parameters affecting electrospinning process mentioned in sections above such as viscosity, applied voltage and the solution surface tension.

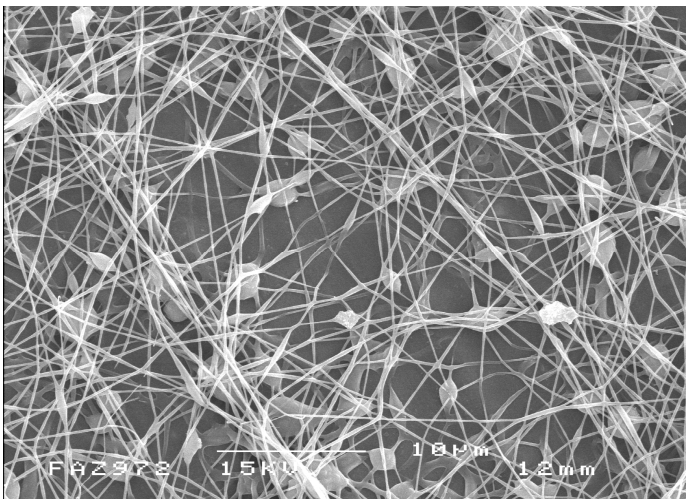

Figure 2.9 Beaded PEO nanofibres

The electrospun beaded fibres are related to the jet instability of the polymer solution, which was studied by Yarin [139] and Entov [140]. They developed a mathematical model for the jets break-up of polymer solutions, which did not include the effects of applied voltage. In 1962, it has been found that the breakup of water jets dependent on the electrical current [141]. Huebner found an electrical phenomena that the jet carried with more electrical current seems less likely to form droplets [142].

Fong et al (1999) [88] characterized the formation of electrospun beaded nanofibres and suggested that solution viscosity, net charge density of the

electrospinning jet and surface tension of the solution are the main factors. According to their findings, the net charge density carried by the moving liquid jet can be defined using equation 2.1 where C is jet current, t is collecting time, s is PEO concentration, ρ is the solution density and m is the mass of dry polymer. They suggested that higher viscosity, higher net charge density and lower surface tension favour the formation of bead-free fibres. More specifically, when the solution viscosity is increased, the beads become bigger, the fibre diameter become larger, the average distance between beads become longer, and the beads changes from spherical shape to spindle shape [139]. When increasing the net charge density, the beads will become smaller and more spindle shape, and the diameters of fibres become smaller [139]. Higher surface tension results in the reduction of the radius of the jet, which in turn causes the solution to form beads [139]. If decreasing the surface tension the beads will disappear gradually.

$$\text{Net charge density} = \frac{C.t.s.\rho}{m} \qquad (2.1)$$

Applied external electric field strength can affect the net charge density carried by the jet during the electrospinning process [88]. Thus increasing applied voltage will have more net charges flowing into the liquid jet, but this net charge is not distributed uniformly through the jet [88]. From literature, the addition of NaCl to a PEO/water solution is observed to increase the net charge density carried by the electrospinning jet. When the jet shape is changing quickly, most of the net charge is near to the jet surface [143].

In summary, electrospun nanofibre diameter and morphology can be controlled by a series of processing parameters including solution properties (for example: concentration, viscosity, surface tension, conductivity), applied voltage, flow rate, tip to target distance and needle diameter etc. Additionally humidity and temperature of the surrounding environment also play a very important role for the nanofibre morphology. There is a common problem that beads will form within the final nanofibre structure due to the solution concentration. Some experiments for electrospinning poly (ethylene oxide) (PEO) have been carried

out and the influence of solution properties on the density of obtained beads in the electrospun fibres have been investigated [88]. Some fibres obtained from electrospinning are ribbon-like structure with rectangular cross sections due to rapid evaporation of solvent [120]. The major factor influencing fibre diameter is the concentration and electrical conductivity of the polymer solution, applied electric field and flow rate. Generally high concentration polymer solutions will produce thicker electrospun fibres. Increasing electrical conductivity by adding salts can reduce the diameter of fibres. A higher feeding rate of the solution into the syringe will always lead to the formation of thicker fibres due to more volume polymer being spun. However the influence of applied voltage on fibre morphology seems to be poorly established. Some literature shows the fibre diameter decreases with increasing the applied voltage but some shows the opposite effect where fibre diameter increases with increasing the voltage [144].

2.3.5 Fibre Alignment Methods

2.3.5.1 Overview

The nanofibres are mostly collected as nonwoven mats and the fibres are randomly oriented. This can be used for a few applications such as implant coating film [131], filtration [145, 146], tissue scaffolds [147], and wound dressing [148]. From traditional fibre and textile industry, if we can get continuous single nanofibres or uniaxially aligned nanofibres then their applications will expand more areas. However this objective is not easy to be achieved for electrospun nanofibres, because the polymer jet path is in a complicated three dimensional ‘‘whipping’’ system due to bending instability rather than in a straight line [100]. The following techniques are some possible methods which have been tried to get uniaxially aligned electrospun nanofibres.

2.3.5.2 Cylinder Collector

If we use a rotating cylinder surface instead of the fibre collecting device in electrospinning, and if the speed of the rotating cylinder matches the depositions of polymer solution jet, the fibres will be collected on the cylinder surface tightly and in a circumferential way, leading to a fine alignment [100], see Figure 2.10. This speed can be named as an alignment speed. If the speed of the rotating cylinder is slower than the fibre alignment speed, randomly fibres will be collected, this is due to the fast and instable motions of jets determine the ultimate collection [100]. Conversely, there must be a limit speed and above this speed continuous fibres can not be collected because the over fast collection speed will break the fibre jet [100]. So a perfect alignment is not easy to achieve due to the fact that the chaos motions of polymer jets seems not like to be consistent and are not very controllable [100]. This method has been used to electrospin aligned poly(glycolic acid) (PGA) fibres at a rotating speed of 1000 rpm and collagen fibres at a rotating speed of 4500 rpm [149, 150].

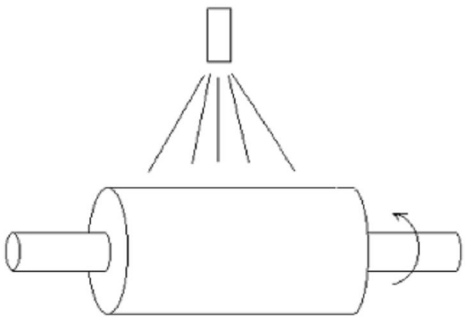

Figure 2.10 A schematic rotating collector for electrospun ultrafine fibres [100].

2.3.5.3 Auxillary Electrical Field

In electrospinning process, the electrospinning jet can be controlled by manipulating electric field [151]. Thus the alignment of fibres can be controlled by manipulating electric field. An example can be found in the work of Teo et al.

They used a knife-edged conducting bar to manipulate electric field as shown in Figure 2.11. The knife-edged assisting electrode was given a charge and this is opposite to the charge given to the needle to create an electric field which could support fibre aligning on the tube collector [151]. This aluminium bar was tilted 45^{o} so that its body will give less influence on the electric field between the needle tip and its edge [151]. This method can produce nanofibres with potential applications such as blood vessel scaffold [151].

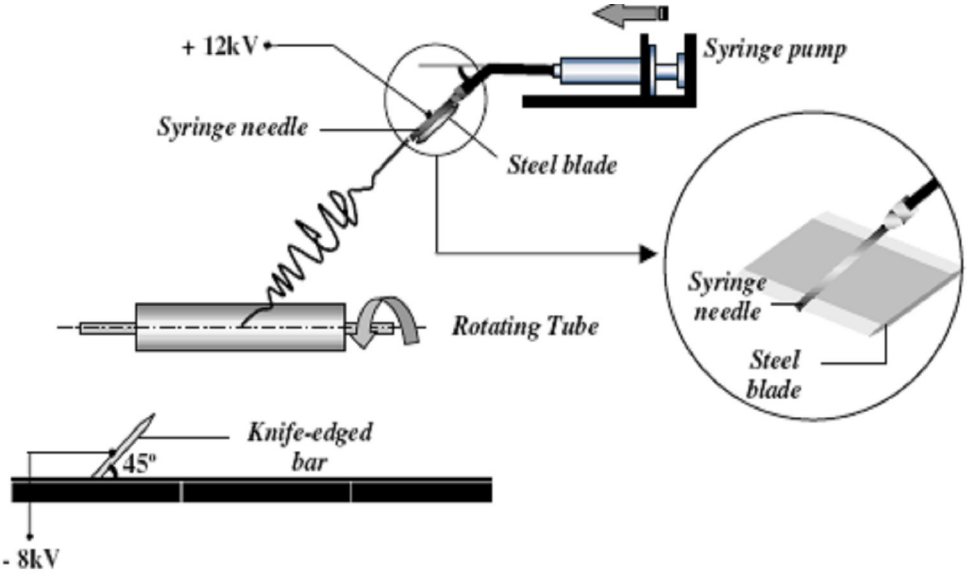

Figure 2.11 Knife-edged bar and blade attached to needle to change the electric field during electrospinning [151].

2.3.5.4 Rotating Disk Collector

Aligned nanofibres can be produced by electrospinning process by using a rotating disk collector which has a sharp edge. Nanofibrous scaffolds have been produced by this method which the disk has a 200 mm diameter with a sharp edge and is shown in Figure 2.12 (a) [152, 153]. The sharp edge of the rotating disc will affect the electric field and the jet will be stretched by this electric force. The speed of the rotating disk at the edge was set at 11 m/s [152]. From literature most of the nanofibres were collected on the sharp edge. Experiments were carried out

in a constant disk rotation speed and the collected nanofibres show a highly ordered alignment [152]. Figure 2.12 (b) shows that when the polymer jet approaches the collector, it was pulled toward the tip of the disk [152, 153]. The disk rotation has an effect on the nanofibres when they were collected on the wheel. The nanofibre density increases with increase the nanofibre collection time [152, 153]. Figure 2.12 (c) shows fibre aligned and parallel to each other with a gap of 1 to 2 μm due to high electric field strength. It has been explained that these gap formations were caused by the residual charges, retained by nanofibres, repelling each other [153].

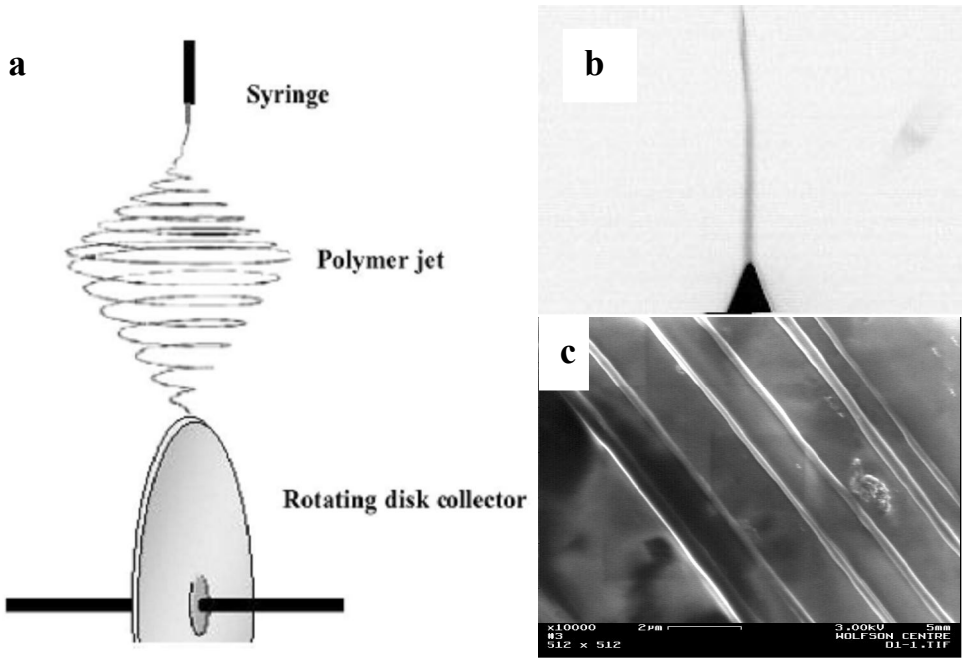

Figure 2.12 (a) Setup to produce aligned nanofibrous scaffold by electrospinning using a disk collector [152]. **(b)** Image of a PEO nanofibre attracted to the edge of the disk [153]. **(c)** SEM image showing the electrospun fibre yarns obtained. The individual fibre yarns are parallel to each other with a gap of 1 to 2 μm [153].

2.3.5.5 Split Electrodes Collector

Nanofibres can be uniaxially aligned by introducing an insulating gap into the conductive collector, i.e. using split electrodes collector. The width of the gap can

be varied from hundreds of micrometers to a few centimetres. An example of split electrodes collector was shown in Figure 2.13 (A). The split of electrodes results in changes in electric fields as shown in Figure 2.13 (B). The electric fields near the split electrodes collector were split which resulting an electrostatic force F_1 as shown in Figure 2.13 (C). F_1 is in the same direction as the electric field lines and should pull the fibre two ends towards the two grounded electrodes [154]. When charged nanofibres have moved to the area near to the electrodes, charges of the nanofibre will induce opposite charges on the surfaces of the electrodes because of Coulomb interaction. The induced opposite charges are called image charge. The presence of image charge results in a second electrostatic force F_2 as shown in Figure 2.13 (C). The two ends of the nanofibre will generate strongest electrostatic force F_2. F_2 caused the nanofires being stretched across the insulating gap and form a parallel array [115]. Additionally, fibres directly deposited on the top of the ground electrodes will be discharged immediately, but the fibres suspended between the two electrodes will still remain the charges. The electrostatic repulsion force between the deposited fibres and the upcoming fibres will further enhance the nanofibre alignment [154]. Thus from this method electrode pattern can be designed for control both the alignment and assembly of electrospun nanofibres [115, 154]

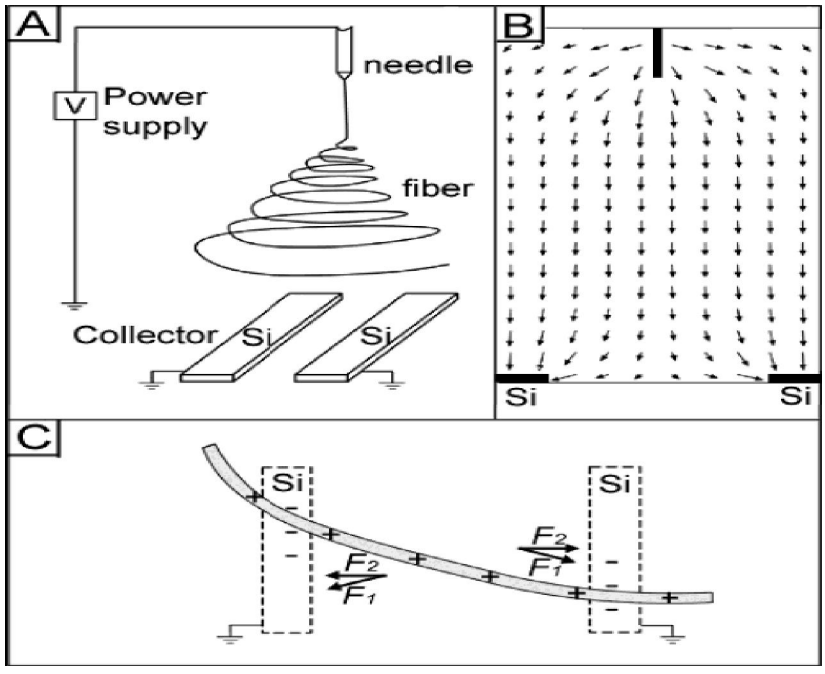

Figure 2.13 (A) Schematic example of the setup for electrospinning that used to produce uniaxially aligned nanofibres. The ground electrodes contained two pieces of conductive silicon stripes separated by a gap. **(B)** Calculated electric field strength vectors in the area between the needle and the collector. The arrows indicate the direction of the electrostatic field lines. **(C)** Electrostatic force analysis of a charged nanofibre spinning across the gap. The electrostatic force (F_1) resulted from the electric field and the Coulomb interactions (F_2) between the positive charges on the nanofibre and the negative image charges on the two grounded electrodes. [115]

2.4 Surface Properties

2.4.1 Introduction

Surface properties of polymer fibres are important in most applications, as discussed in section 1.1, and are critically dependent on the processing conditions, which dictate the resultant fibre structure. Theories of surface behaviour through considerations of wetting and adhesion are considered in the sections below. These theories have been developed essentially for macroscopic objects but supporting measuring techniques are potentially limited when considering relatively small materials such as the electrospun fibres of this work. Therefore, this section reviews the background of surface properties and considering measuring techniques applicable to our electrospun fibres.

2.4.2 Surface Tension

2.4.2.1 Introduction

Surface tension is a phenomena observed in everyday life. Our raincoats need to have specific surface properties so that droplets slide of them, leaves of the lotus

flower have high water repellence and even modern glasses have their surfaces modified so that water rolls off their surface. Glues applied between two materials are sometimes required to spread to give a better join. Surface tension is therefore important and this section will describe the origin of surface tension and its measurement.

2.4.2.2 Origin of Surface Tension

Surface tension arises from unequal forces acting on molecules. Considering a molecule in a liquid, attractive forces exist between all molecules within the liquid. Therefore, a molecule within the liquid will have forces acting on it in all directions. This results in a net zero force acting on the molecule in the liquid, as shown in Figure 2.14. If we now consider a molecule at the surface of the liquid, the forces of attraction will originate from other liquid molecules but not above the surface of the liquid. The net force acting on this surface molecule will not be zero and, as a result, this non-zero surface force is characterized by the surface tension. Solids also experience these conditions and are characterized by surface energy. For liquids, surface tension is commonly denoted by γ_L and is usually given in units of tension per unit length: mNm^{-1} (the same as dyn cm^{-1}). For solids, surface energy is commonly denoted by γ_s and is given in units of energy per unit area: mJm^{-2} (the same as erg cm^{-2}) [155], although mNm^{-1} can also be encountered.

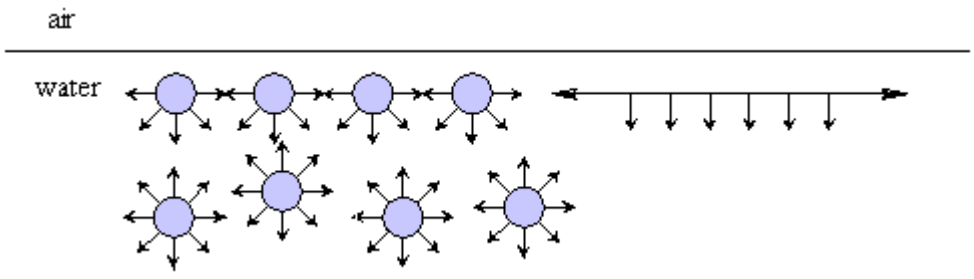

Figure 2.14 Scheme of attractive forces among the molecules of water.

The magnitude of this surface tension or surface energy is critically dependent on the chemical composition of the liquid or solid considered. If the attractive force between liquid molecules is large then the net asymmetric forces acting at the

surface of the liquid will also be large, resulting in a large surface tension. For example, a simple mineral oil and water have significantly different surface tensions. Water has considerable intermolecular forces of attraction which gives a surface tension of 73 mJm^{-2}. However, the molecules in oil weakly interaction with one another and therefore surface tension values of around 20 mJm^{-2} are common. The energy required to maintain these surfaces is described by the surface tension. Water requires a large energy per unit area to maintain its surface and will therefore try to reduce its surface where possible. An example of this is in water and can be observed during flow. At low water flows we can clearly see that water break up into droplets as shown in Figure 2.15. Droplets are favoured as this is the geometry which gives the smallest surface area for a particular volume. A comparison with oils is also useful as oils have a low surface tension so is relatively easy to produce a large surface area for a given volume. This is why oils are often used in cooking where the spreading of a finite liquid volume over a large area is required.

Figure 2.15 Water breaks up into droplet.

The thermodynamic drive for liquids to reduce their surface area is not continuous and must be balanced by the pressure build up within the liquid droplet. This consideration of pressure is termed as Laplace pressure and it describes the difference in pressure between the inside and outside of a droplet due to surface tension. We take an example of a drop of oil (o) inside water (w), in Figure 2.16, p_0 and p_w are the pressure in the oil and water respectively, and γ is the interfacial

tension between oil and water, then equation 2.2 can be given. Therefore, the smaller the drop, the greater its inner pressure.

$$\Delta p = p_0 - p_w = \frac{2\gamma}{R} \qquad (2.2)$$

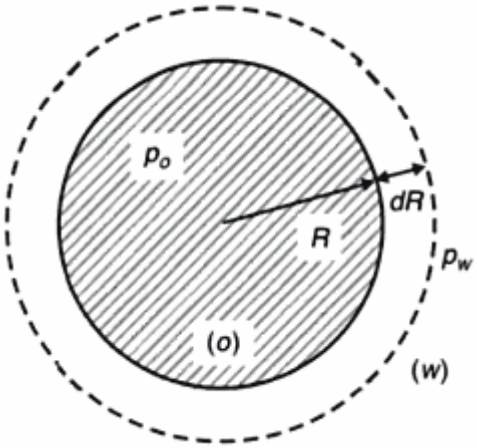

Figure 2.16 Overpressure inside a drop of oil "o" in water "w" [156].

The above discussions have focussed on liquid surfaces exclusively without the consideration of other interactions. In particular, liquids in contact with solid surfaces to produce a solid-liquid interface are of particular technological and scientific importance.

2.4.2.3 Young's Equation

The Young's Equation describes the balance of forces when a liquid droplet contacts a solid surface to form a solid-liquid interface. Contact angle describes the shape of a liquid droplet sitting on a flat solid surface and is useful for understanding the surface properties of the solid and its relationship with the liquid's surface tension. After drawing a tangent line from the droplet to the touch of the solid surface, the contact angle is the angle between the solid surface and the tangent line [92]. In an ideal gas-liquid-solid system, if the solid surface is smooth, flat and nondeformable, the contact angle θ is related to the surface tension and to the interfacial energies by Young's equation [92]. Figure 2.17

shows Young's equation for a flat solid surface. Young's equation can be described as equation 2.3 where θ_0 is the Young's angle or the contact angle, γ_s is the solid surface energy in the presence of the liquid vapour, γ_l is the liquid surface tension and γ_{sl} is the solid and liquid interfacial energy. A parameter called the spreading coefficient S can be defined using equation 2.4 and is able to describe the thermodynamic driving force for the droplet to cover the solid's surface [92]. When S >0, the liquid is said to 'wet' the surface completely in order to lower its surface energy resulting in a contact angle θ = 0. This wetting is also termed as full wetting. When S <0, the liquid is said to be partially wetting [92] if the contact angle $0 < \theta \leqslant 90^{\circ}$ or "non-wetting" if $\theta \geqslant 90^{\circ}$.

$$Cos\theta_0 = (\gamma_s - \gamma_{sl})/\gamma_l \quad (2.3)$$

$$S = \gamma_s - \gamma_{sl} - \gamma_l \quad (2.4)$$

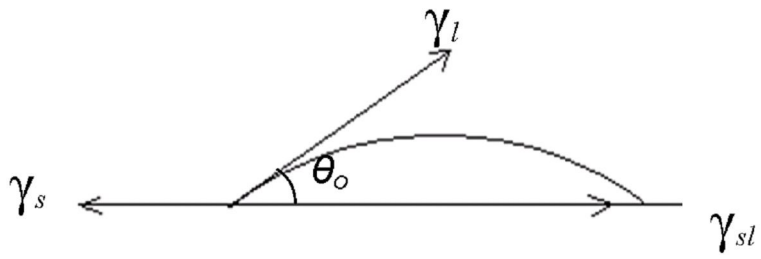

Figure 2.17 Young's equation for a flat solid surface

The contact angle measurement is extremely useful in characterizing the surface free energy of the solid if the surface tension of the liquid is known. However, direct measurements of contact angles cannot be used to calculate this solid surface free energy as the solid-liquid interface energy γ_{sl} is typically unknown and, therefore, contact angle measurements tend to be qualitative. For example, a small water contact angle on a solid's surface will suggest hydrophilicity whereas an increasing contact angle indicates more hydrophobic behaviour.

2.4.2.4 Zisman Plot

Zisman plots have advantages over Young's equation as the solid-liquid interface energy γ_{sl} does not need to be known. Zisman plots are useful as a quantitative critical surface tension γ_c where a liquid will wet a surface is defined. In 1950s, Dr. William Zisman developed this method in which a series contact angle measured from different liquids on the same solid surface can be plotted to determine the surface wetting which is called the critical surface tension, γ_c. A more specifically example is shown in Figure 2.18 where a plot was drawn from the cosine of a series of contact angles versus the surface tension of each liquid. This kind of plot is called Zisman plot. The critical surface tension value is the surface tension at the plot when the cosine is equal to 1 as shown in Figure 2.18 [157]. Critical surface tension, γ_c is different to regular "surface tension" as the value is essentially empirical. However, the critical surface tension of a solid surface can describe its hydrophobic or hydrophilic character depending on if the critical surface tension value is relatively small or large respectively. In addition, the critical surface tension (γ_c) suggests that liquid surface tensions below this value will fully wet the solid surface and therefore defines the highest value of surface tension of the test liquid that will fully wet the solid surface. The solid surface should be a flat and non porous when using Zisman plot to determine the critical surface tension.

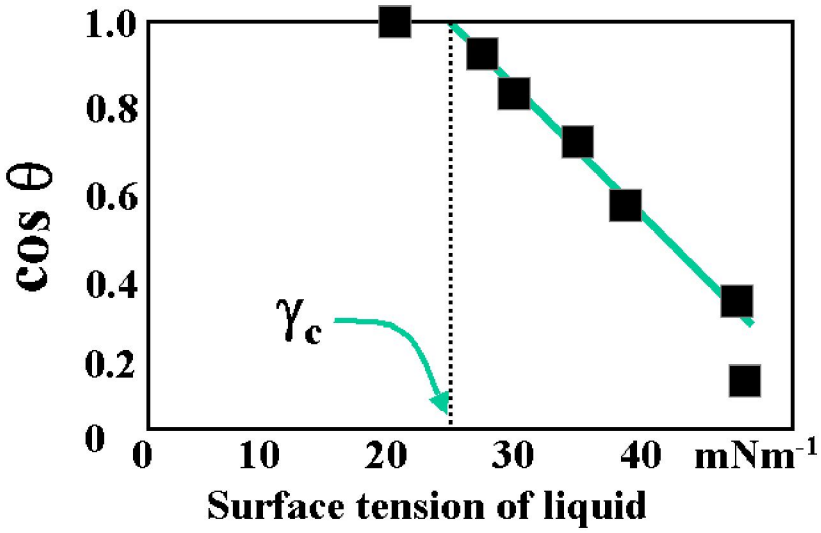

Figure 2.18 Zisman plot to determine γ_c

A relative weakness of both Zisman plot and Young's equation is the lack of a suitable description of hydrophobicity or hydrophilicity. An improvement is to consider the surface tension in terms of molecular structure which gives rise dispersive and polar interactions. The surface tensions used in Young's equation and Zisman plot are the summation of these interactions.

2.4.3 Dispersive and Polar Forces

2.4.3.1 Dispersive Forces

When two atoms in a molecule share electrons unequally, a dipole is formed. An atom or molecule which is normally electrically symmetric, i.e. the overall spatial distribution of the electrons is symmetric with respect to the positively charged nucleus [158], can induce dipole on another atom or molecule. This is because of the fact that atoms are experiencing constant vibrational motion that can cause instantaneous and short-lived distortions of this electrical symmetry for one of the atoms or molecules [158]. The instantaneous dipole can in turn produce a displacement of the electron distribution of an adjacent molecule or atom, which

induces the second one also to become a dipole that is then weakly attracted or bonded to the first. This type of bonding contributes to dispersive forces [158]. Dispersive forces are also called London dispersion forces, London forces or London van der Waals forces. Therefore we can conclude that London forces are due to instantaneous dipoles occurring within molecules, which induce a dipole within a neighbouring molecule. London forces may exist between large numbers of atoms or molecules, where forces are temporary and fluctuate with time [158].

2.4.3.2 Polar Forces

In general an intermolecular potential has a repulsive part and an attractive part. The attractive part consists of electrostatic interactions between permanent dipoles which is called Keesom force. Another source of attraction is induction. It is caused by the fact that a permanent dipole on one molecule can induce dipole on another molecule. Induction is the interaction between the permanent dipole and the induced dipole. This interaction is called Debye force. Polar forces results from intermolecular forces which is due to permanent and induced dipoles (Keesom and Debye forces) and hydrogen bonding. Hydrogen bonding, the strongest secondary bonding type, is found to exist between some molecules that have hydrogen as one of the constituents [158]. A special case of polar molecule bonding and occurs between molecules in which hydrogen is covalently bonded to fluorine (as in HF), oxygen (as in H_2O), and nitrogen (as in NH_3). For each H-F, H-O, or H-N bond, the single hydrogen electron is shared with the other atom. Thus, the hydrogen end of the bond is essentially a positively charged bare proton that is unscreened by any electrons. This highly positively charged end of the molecule is capable of a strong attractive force with the negative end of an adjacent molecule. In essence, this single proton forms a bridge between two negatively charged atoms. The magnitude of the hydrogen bond is generally greater than that of the other types of secondary bonds and may be as high as 51 kJ/mol (0.52 eV/molecule). Melting and boiling temperatures for hydrogen fluoride and water are unusually high in light of their low molecular weights, as a consequence of hydrogen bonding [158].

Dispersive forces and polar forces which include London, Keesom and Debye forces, and hydrogen bonding are all belong to van der Waals forces. Van der Waals forces exist between atoms and molecules. Van der Waals bonds, i.e. secondary or physical bonds are weak in comparison to the primary or chemical ones; bonding energies are typically on the order of only 10 kJ/mol (0.1 eV/atom). There are three types of primary bonds, i.e. covalent bond, ionic bond and metallic bond. Secondary bonding exists between virtually all atoms or molecules, but its presence may be obscured if any of the three primary types is present [158]. Secondary bonding is evidenced for the inert gases, which have stable electron structures, and, in addition, between molecules in molecular structures that are covalently bonded [158]. Secondary bonding forces arise from atomic or molecular dipoles. The bonding results from the columbic attraction between the positive end of one dipole and the negative region of an adjacent one. Dipole interactions occur between induced dipoles (London forces), between induced dipoles and polar molecules which have permanent dipoles (Debye forces), and between polar molecules (Keesom forces). In chemistry van der Waals forces sometimes can be used as synonym for non-covalent or intermolecular forces [158]. In some texts, van der Waals force means the totality of forces (including repulsion), others mean all the attractive forces, and some texts use van der Waals force only as a synonym for the London dispersion force [158]. The Lennard-Jones potential is often used as an approximate model for the isotropic part of a total (repulsion and attraction) van der Waals force as a function of distance [158].

In summary of dispersive and polar forces, we note that these interactions are physical and do not consider primary chemical bonds. These interactions are weaker than chemical but often act over large areas, meaning the total magnitude of the interaction can be large.

2.4.4 Owens-Wendt Theory

For two materials in contact, the work of adhesion is the energy it takes to separate these two pieces of material with an interface of unit area and bring the

pieces to infinite separation. In the special case, when the two materials are the same, the work of adhesion becomes the work of cohesion. In 1964, Fowkes [159] had proposed that the work of cohesion W_c, and the work of adhesion W_a, can be separated into their dispersion *d*, polar *p*, induction *i*, and hydrogen bonding *h* components as following [160]:

$$W_c = W_c^d + W_c^p + W_c^i + W_c^h + \ldots \qquad (2.5)$$

$$W_a = W_a^d + W_a^p + W_a^i + W_a^h + \ldots \qquad (2.6)$$

The dispersion component of the work of adhesion between a solid and a liquid can be described as:

$$W_a^d = 2\sqrt{\left(W_c^d\right)_s \left(W_c^d\right)_l} = 2\sqrt{\gamma_s^d \gamma_l^d} \qquad (2.7)$$

And the interface energy between the solid and the liquid interacting by London dispersion forces can be described as:

$$\gamma_{sl} = \gamma_s + \gamma_l - 2\sqrt{\gamma_s^d \gamma_l^d} \qquad (2.8)$$

Combining this equation and Young's equation, it gives:

$$\gamma_l \cos\theta = -\gamma_l + 2\sqrt{\gamma_s^d \gamma_l^d} \qquad (2.9)$$

In 1969, Owens-Wendt proposed a new expression based on Fowkes equation and divided the surface energy into two components, dispersive component γ_i^d and polar component γ_i^p. They assumed that the free energy of adhesion of a polymer in contact with a liquid can be described as:

$$W_a = 2(\sqrt{\gamma_s^d \gamma_l^d} + \sqrt{\gamma_s^p \gamma_l^p}) \qquad (2.10)$$

Base on the assumptions:

$$\gamma_i = \gamma_i^d + \gamma_i^p \qquad (2.11)$$

Therefore the total surface energy can be considered as the sum of dispersive surface energy and polar surface energy. Combining equation 2.9, 2.10 and 2.11, we can conclude Owens-Wendt equation:

$$\frac{\gamma_l(1+\cos\theta)}{2\sqrt{\gamma_l^d}} = \sqrt{\gamma_s^p}\left(\frac{\sqrt{\gamma_l^p}}{\sqrt{\gamma_l^d}}\right) + \sqrt{\gamma_s^d} \qquad (2.12)$$

where the γ^p and γ^d represent polar and dispersive surface energy respectively, and θ is the contact angle of the droplet. Owens-Wendt theory is advantageous as the measured contact angle can be used to define the polar and dispersive contributions of a solid if the corresponding liquid values are known. Equation 2.12 has the linear equation form of $y = mx + b$ where $y = \frac{\gamma_l(1+\cos\theta)}{2\sqrt{\gamma_l^d}}$, $m = \sqrt{\gamma_s^p}$, $x = \frac{\sqrt{\gamma_l^p}}{\sqrt{\gamma_l^d}}$, $b = \sqrt{\gamma_s^d}$. This has led to Owens-Wendt plots where a linear relationship between x and y can be defined when the liquid dispersive and polar surface energy are known. Therefore m and b can be calculated from the intercept and slope respectively of the linear plot and results can give the solid polar and solid dispersive surface energy values. The application of Owens-Wendt plots is discussed in section 2.4.6.3. Table 2.4 gives the surface energy of some common polymers.

Table 2.4 Solid surface energy data for common polymers [161]

Name	Surface free energy (SFE) at 20 °C (mNm^{-1})	Dispersive contrib. of SFE (mNm^{-1})	Polar contrib. of SFE (mNm^{-1})
Polyethylene-linear PE	35.7	35.7	0
Polyethylene-branched PE	35.3	35.3	0
Polypropylene-isotactic PP	30.1	30.1	0
Polyisobutylene PIB	33.6	33.6	0
Polystyrene PS	40.7	34.5	6.1
Poly-α-methyl styrene PMS (Polyvinyltoluene PVT)	39.0	35	4
Polyvinyl fluoride PVF	36.7	31.2	5.5
Polyvinylidene fluoride PVDF	30.3	23.3	7
Polytrifluoroethylene P3FEt/PTrFE	23.9	19.8	4.1
Polytetrafluoroethyle PTFE	20	18.4	1.6

Polyvinylchloride PVC	41.5	39.5	2
Polyvinylidene chloride PVDC	45.0	40.5	4.5
Polychlorotrifluoroethylene PCTrFE	30.9	22.3	8.6
Polyvinylacetate PVA	36.5	25.1	11.4
Polymethylacrylate (Polymethacrylic acid) PMAA	41.0	29.7	10.3
Polyethylacrylate PEA	37.0	30.7	6.3
Polymethylmethacrylate PMMA	41.1	29.6	11.5
Polyethylmethacrylate PEMA	35.9	26.9	9.0
Polybutylmethacrylate PBMA	31.2	26.2	5.0
Polyisobutylmethacrylate PIBMA	30.9	26.6	4.3
Poly(t-butylmethacrylate) PtBMA	30.4	26.7	3.7
Polyhexylmethacrylate PHMA	30.0	27.0	3
Polyethylene oxide PEO	42.9	30.9	12.0
Polytetramethylene oxide PTME (Polytetrahydrofurane PTHF)	31.9	27.4	4.5
Polyethyleneterephthalate PET	44.6	35.6	9
Polyamide 6,6 PA-66	46.5	32.5	14
Polyamide 12 PA-12	40.7	35.9	4.9
Polydimethylsiloxane PDMS	19.8	19.0	0.8
Polycarbonate PC	34.2	27.7	6.5
Polyetheretherketon PEEK	42.1	36.2	5.9

2.4.5 Contact Mechanics in Adhesion: Hertz and Johnson–Kendall–Roberts (JKR) Theory

An important application of surface free energy considerations is within the area of contact mechanics. Contact mechanics is particularly useful in relating

adhesion between bodies and the surface theories described in the sections above. Hertz theory describes contact mechanics between a spherically shaped ball and a flat geometry when the former is brought into contact with the later. In Hertz theory, it is assumed that there is no adhesion between the ball and the flat geometry and only the flat geometry deforms during the whole process. As shown in Figure 2.19, when a ball was brought into contact with a flat surface, a contact zone with radius of a was created. The contact radius a is given by equation 2.13 where E_c is related to the elastic modulus of the materials of both the ball and the flat surface, and is given by equation 2.14. The real area of contact A is shown by equation 2.15. The distribution of the contact pressure L is illustrated in Figure 2.19 (c). It can be seen that the pressure has a maximum at the centre and falls into zero at the edge of the contact zone. The mean pressure p_m is given by equation 2.16, and the maximum pressure p_0 is calculated as 3/2 times p_m. The distribution of contact pressure in the contact zone is given by equation 2.17 where $-a \leq r \leq a$ as shown in Figure 2.19 (c). The amount of elastic deformations of the flat surface in the normal direction is given by equation 2.18.

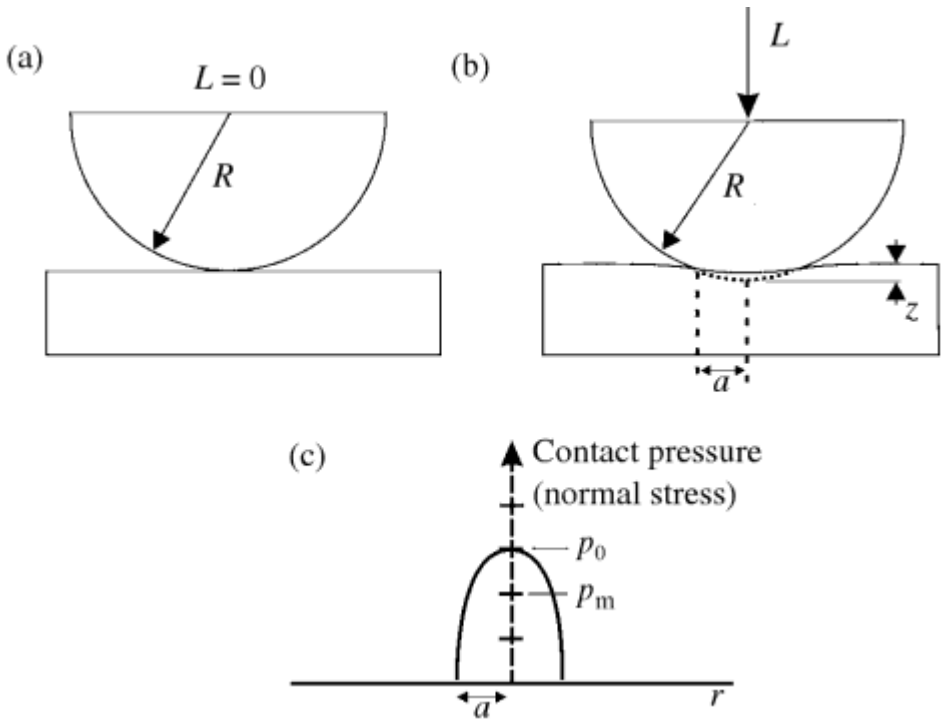

Figure 2.19 Sphere on flat contact geometry with (a) no load and (b) load = L. (c) The distribution of contact pressure across the contact zone of (b) [162].

$$a = (\frac{3RL}{4E_C})^{1/3} \qquad (2.13)$$

$$\frac{1}{E_C} = \frac{1-\nu_1^2}{E_1} + \frac{1-\nu_2^2}{E_2} \qquad (2.14)$$

$$A = \pi a^2 = \pi(\frac{3RL}{4E_c})^{2/3} \qquad (2.15)$$

$$P_m = \frac{L}{A} = \frac{1}{\pi}(\frac{4E_c}{3R})^{2/3} L^{1/3} \qquad (2.16)$$

$$p = p_0\{1-(r/a)^2\}^{1/2} \qquad (2.17)$$

$$\Delta z = \frac{a^2}{R} = (\frac{9L^2}{16RE_c^2})^{1/3} \qquad (2.18)$$

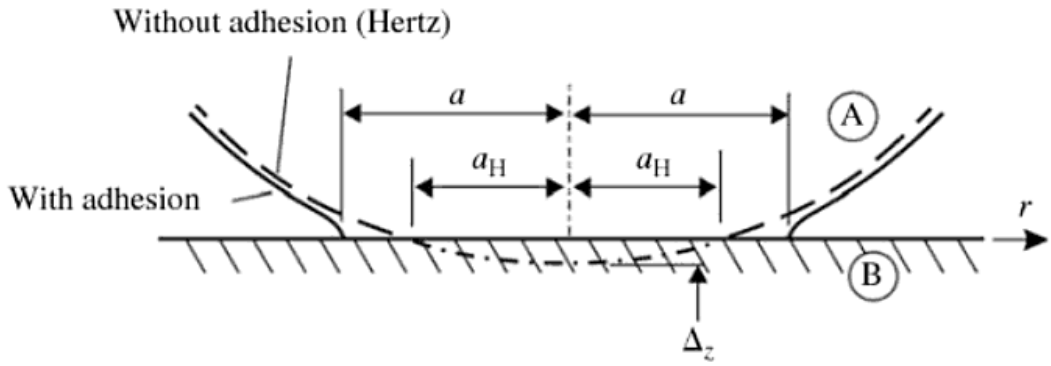

Figure 2.20 Deformation and contact radius of an elastic sphere contacting a rigid flat. Solid line: Johnson-Kendall-Roberts (JKR) contact with adhesion. Dashed line: Hertzian contact without adhesion [162] .

In Hertz theory, the adhesion between the two bodies was ignored. Johnson et al [163] extended the Hertz theory to include the elastic deformations caused from the adhesive forces. They modified equation 2.17 for contact pressure in Hertz theory by adding a range of tensile adhesive stress as shown in equation 2.19. Figure 2.20 illustrated that the tensile adhesive force elastically deformed the edge of the contact zone, and caused the increase of the size of the contact zone. Johnson et al [163] build JKR theory based equation 2.20 where U_T is the total energy of the sphere-on-flat geometry, U_S is the surface energy loss due to

formation of a finite contact area, and U_E is the energy stored in elastic deformations. They suggested that the equilibrium contact radius a corresponds to the balance of the two energies, i.e. $\left[\frac{\partial U_T}{\partial a}\right]_{\Delta Z} = \left[\frac{\partial U_S}{\partial a}\right]_{\Delta Z} + \left[\frac{\partial U_E}{\partial a}\right]_{\Delta Z} = 0$ when the overall elastic deformation (Δa) is kept constant. They defined $\left[\frac{\partial U_E}{\partial a}\right]_{\Delta Z}$ and $\frac{\partial U_S}{\partial a}$ using equation 2.21 and equation 2.22 respectively where E_C is the composite modulus in equation 2.14 and W_{AB} is work of adhesion between A and B and the minus sign comes from surface energy being lost as the contact area grows [162]. Combing equation 2.21 and 2.22 and $\left[\frac{\partial U_T}{\partial a}\right]_{\Delta Z} = \left[\frac{\partial U_S}{\partial a}\right]_{\Delta Z} + \left[\frac{\partial U_E}{\partial a}\right]_{\Delta Z} = 0$ gives an expression of $p_0^{'}$ as shown in equation 2.23. They calculated the external applied force (L_{ext}) by integrating *p(r)* in equation 2.19 over the contact area as shown in equation 2.24. In Hertz theory described above, the compressive force p_0 is expressed by equation 2.16 and 2.17. Thus both p_0 and $p_0^{'}$ in equation 2.24 can be substituted to give equation 2.25. Equation 2.25 can be transformed into different form for different purpose. For example, equation 2.25 can be changed into equation 2.26 to highlight the contact radius. It can be seen that if W_{AB}=0, equation 2.26 becomes equation 2.13 in Hertz theory mentioned above.

$$p = p_0\{1-(r/a)^2\}^{1/2} + p_0^{'}\{1-(r/a)^2\}^{1/2} \quad (2.19)$$

$$U_T = U_S + U_E \quad (2.20)$$

$$\left[\frac{\partial U_E}{\partial a}\right]_{\Delta Z} = \frac{\pi^2 a^2}{E_C} p_0^{'2} \quad (2.21)$$

$$\frac{\partial U_S}{\partial a} = -2W_{AB}\pi a \quad (2.22)$$

$$p_0^{'} = -\left(\frac{2W_{AB}E_C}{\pi A}\right)^{1/2} \quad (2.23)$$

$$L_{ext} = \int_0^a 2\pi r p(r) dr = \left(\frac{2}{3} p_0 + 2p_0^{'} \right) \pi a^2 \qquad (2.24)$$

$$\left(L_{ext} - \frac{4E_C a^3}{3R} \right)^2 = 8\pi W_{AB} E_C a^3 \qquad (2.25)$$

$$a^3 = \frac{3R}{4E_C} \left(L_{ext} + 3\pi R W_{AB} + \sqrt{6\pi R W_{AB} L_{ext} + (3\pi R W_{AB})^2} \right) \qquad (2.26)$$

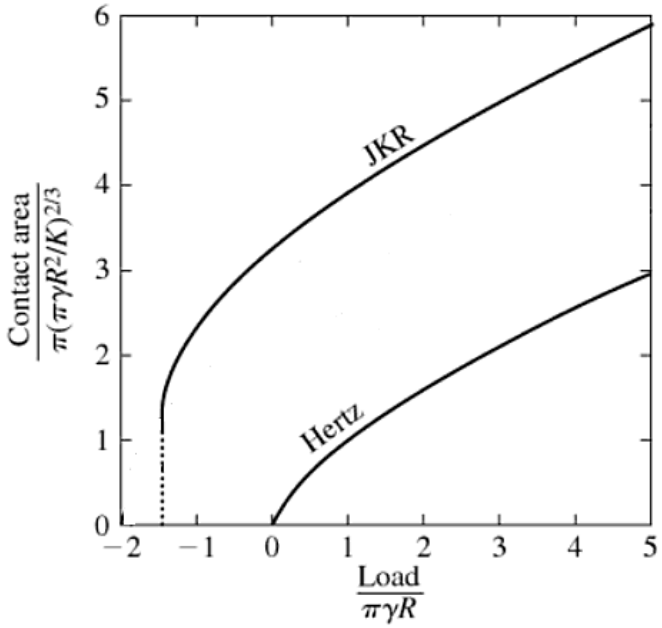

Figure 2.21 Comparison of contact areas predicted by the Johnson-Kendall-Roberts (JKR) theory, and Hertz theory. (Redraw from [162])

Figure 2.21 plots the relationships between the contact area and the external force of both JKR theory and Hertz theory. It can be seen that when the external force is equal to 0 surface separations doesn't occur in JKR theory. The surface separation occurs at a critical point where the loading was negative. Johnson et al [163] suggests that at this critical point, the magnitude of the external loading force corresponded to an adhesive force in following equation:

$$L_{adh} = \frac{3}{2} \pi W_{AB} R \qquad (2.27)$$

Although JKR theory is better than Hertz theory in predicting the contact areas, it has two main shortcomings. Firstly, JKR theory assumes perfectly smooth surface.

Secondly, it only works well for materials with relatively low elasticity [162] where adhesion between the two bodies is finite and measurable. Thus it can be concluded that JKR theory should be used to predict contact area when there is strong adhesion and the elastic modulus of the material is low.

2.4.5.1 Adhesion Measurement Based on JKR Theory

JKR theory can be applied to measure surface properties of nanomaterials. It has been found that adhesion measurements at the nanoscale can be conducted by combining AFM (atomic force microscopy) and JKR theory. For example, Zhang et al. used AFM and JKR theory to measure the surface energies of crystalline and amorphous lactose [164]. As mentioned in section 2.4.5, JKR theory describes the force required to remove a sphere from a surface. This force F required to remove the sphere is related to the radius of the sphere and the work of adhesion W_A by

$$F = \frac{3}{2}\pi R W_A \qquad (2.28)$$

The work of adhesion can be calculated using equation 2.29 where γ_1 and γ_2 are the dispersive components of the surface energy of the silicon tip and lactose material respectively [164] and:

$$W_A = 2\sqrt{\gamma_1}\gamma_2 \qquad (2.29)$$

The typically values of a silicon sphere used to describe the material of an AFM tip is given as 42 mJ m^{-2} by Zhang et al. This value is considered to be γ_1 as there is only a dispersive contribution for silicon [164]. However, AFM usually measures the sum of all forces interacted between the tip and specimen surface, which may include London forces, electrostatic, and capillary forces [164]. In order to minimize electrostatic and capillary forces, Zhang et al demonstrated all the experiments at low humidity (1% RH) and removed electrostatic charges [164].

Importantly, Zhang et al calculated the surface energy of crystalline and amorphous lactose using equation 2.30 which is based on equation 2.28 and equation 2.29:

$$\gamma_2 = (\frac{F}{3\pi R})^2 \frac{1}{\gamma_1} \qquad (2.30)$$

Here, F is unknown, and can be measured by AFM adhesion force measurement. The another unknown, R, which is the geometry of the tip contacting apex was examined by scanning a porous aluminium film with ultra sharp spikes with radius about 2 to 3 nm [164]. The prepared smooth specimen surface and sphere shaped silicon tip were suitable for the application of the JKR theory [164, 165]. We also used this above equation 2.30 for our adhesion force measurements.

2.4.6 Wetting Measurements

2.4.6.1 Contact Angle Measurement

The previous section detailed processes in which surface free energies of contacting materials could be measured from adhesion. A second method, referred to as contact angle, is examined herein which is also suitable for the determination of surface properties. Importantly, contact angle has advantages over contact mechanics as the hydrophilic or hydrophobic nature of a material can be determined [166]. Contact angle measurements use the principles of Young's equation, described in section 2.4.2.3. A solid surface is hydrophobic when the contact angle of a water droplet will be larger than 90° [92]. Hydrophilicity of a surface is indicated by a smaller contact angle and higher surface energy of the solid. The hydrophilic or hydrophobic nature of a substrate has a direct impact for its applications. For example, in membrane distillation, where water must not enter the membrane, so a hydrophobic membrane has to be used [166]. In order to separate of protein solutions, hydrophilic membranes can be used to minimize protein adsorption [166]. Similarly hydrophilic scaffolds are preferred for tissue-engineering scaffolds. For measuring these hydrophobic or hydrophilic

characteristics, the most direct method is contact angle measurements [166]. Contact angle can be illustrated using Figure 2.22 where α is the contact angle [92] . If $\alpha < 90^o$ the liquid wets the surface, for example, water on glass. If $\alpha > 90^o$ the liquid does not wet the surface, for example, mercury on glass. If $\alpha = 0^o$ the liquid perfectly wet the surface [92]. Goniometer devices are typically employed to view the droplet from the side in order to observe the contact angle value with a camera [167], this technique will be detailed in experimental sections.

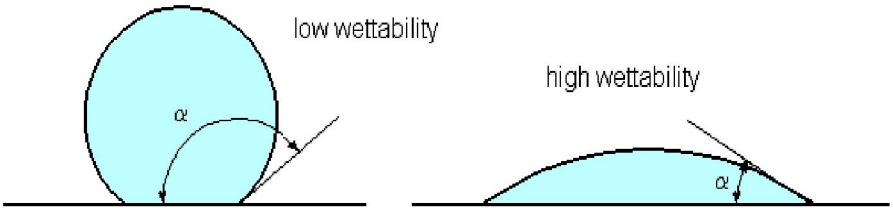

Figure 2.22 The contact angle of a liquid on a flat solid surface [92].

Generally it is easy to measure contact angle for large scale materials such as polymer films. However, difficulties occur when conducting contact angle measurements for nanometer size material such as nanofibres due to the difficulty in producing a small enough stable liquid droplet on the nanomaterial surface and then observing the resultant contact angle. Contact angle measurements can be carried out within an electron microscope in order to observe these small droplets but the vacuum conditions within the microscope chamber can potentially cause rapid evaporation of the probe liquid. The next section will review the technique and method used to characterize the wetting properties of nanoscale materials.

2.4.6.2 Wilhelmy Balance Method

Wilhelmy balance method has been shown to be effective in characterizing contact angle of single carbon nanotubes [168]. In 1863, Wilhelmy used a thin plate, which was suspended from a balance, partially and vertically immersed into

a liquid to determine the liquid surface tension. A meniscus formed around the perimeter of the suspended thin plate. If the contact angle between the liquid and the thin plate is zero, the liquid surface is oriented almost vertically upwards, as shown in Figure 2.23 [169]. The liquid surface tension present in the meniscus applies a downward force, which is equal to the weight of the meniscus arisen on the perimeter of the thin plate [169]. If the weight of the plate probe is zeroed in the device before the liquid surface is moved up to the contact position, the imbalance that occurs on contact will be due to the weight of the arisen meniscus. Wilhelmy was the first person to use this simple surface tension method by using a lever balance to measure the force acting on the plate. These thin plates were named as Wilhelmy plates and are usually made of roughened platinum, glass, steel, plastic or mica [169].

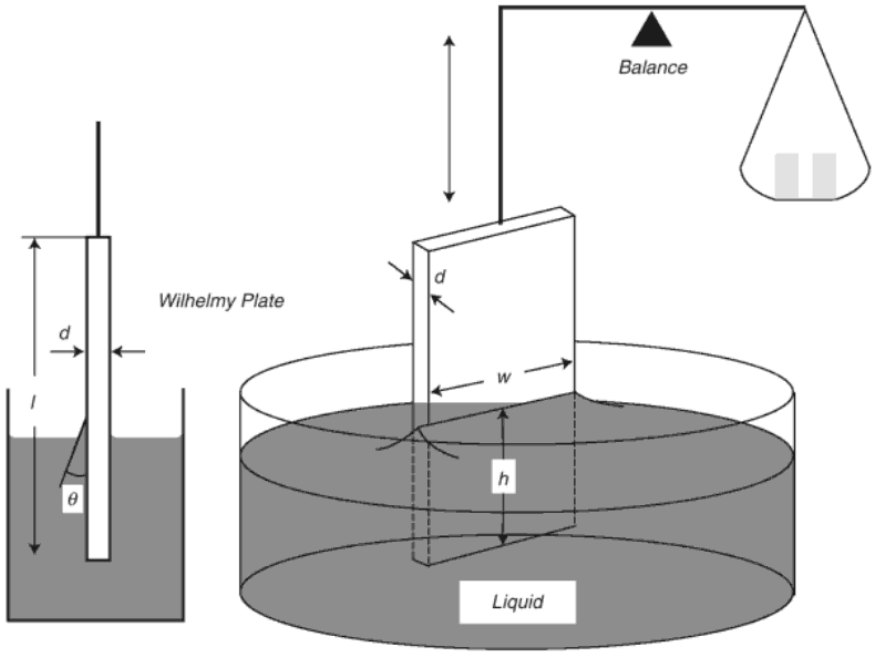

Figure 2.23 Liquid surface tension determination by the Wilhelmy plate method. A rectangular plate of length, l, width, w, and thickness, d, of material is immersed to a depth of h in a liquid, θ is the contact angle forming between the liquid and the plate [169].

The Wilhelmy balance method has been used to measure contact angles for different probe liquids wetting plates. Barber et al. have accurately measured the contact angle between various organic liquids and single carbon nanotube surface

by immersing and removing carbon nanotubes from liquids using atomic force microscopy [168]. They have also developed an approach to accurately monitor and record the forces acting on individual carbon nanotubes during their immersion into and retraction from different probe liquids in air [168]. They used the recorded force profiles to calculate the equilibrium liquid contact angle for each probe liquid through the Wilhelmy balance method by using this equation [168]:

$$F_r = \pi d \gamma_l \cos\theta \qquad (2.31)$$

where F_r represents the restoring force of the AFM cantilever, d is diameter of the nanotube, γ_l is the probe liquid surface tension, and θ is the liquid-nanotube contact angle [168]. Therefore this Wilhelmy balance method can be used to characterize contact angle of materials down to nanoscale level.

2.4.6.3 Wetting Measurement Based on Owens-Wendt Theory

Wilhelmy balance method has been used to characterize the contact angle of a nanoscale material but it couldn't give the surface energy value of the nanomaterial. Here Owens-Wendt theory has been used to calculate the dispersive and polar contribution for the surface energy of a nanomaterial. For example, Barber et al. have also measured the contact angle between multiwall carbon nanotubes, carbon nanofibre and carbon fibres, and polypropylene (PP) and polyethylene glycol (PEG) liquids using electron microscopy, as shown in Figure 2.24 [170]. They used Owens–Wendt theory to obtain the dispersive, polar component and total surface energy for these three types of carbon materials[170]. The Owens-Wendt equation they have used in their study [171] is described as equation 2.12 in section 2.4.4. Figure 2.25 shows the Owens-Wendt plot for carbon fibre, carbon nanofibres and multiwall nanotubes wetted by two polymer liquids Polyethylene glycol (PEG) and polypropylene (PP) [171].

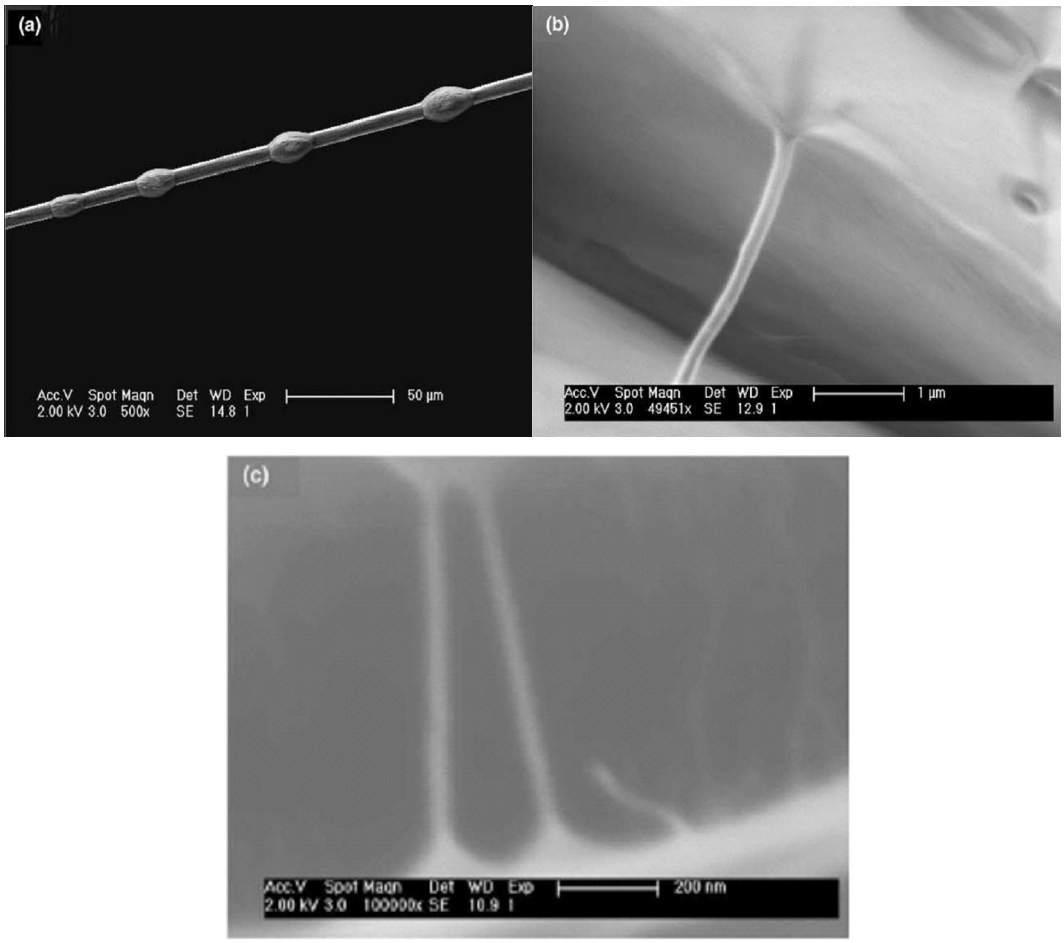

Figure 2.24 ESEM images of PEG wetting surfaces on: **(a)** Carbon fibre; **(b)** Carbon nanofibre; **(c)** MWCNT, from which the contact angle can be measured. [171]

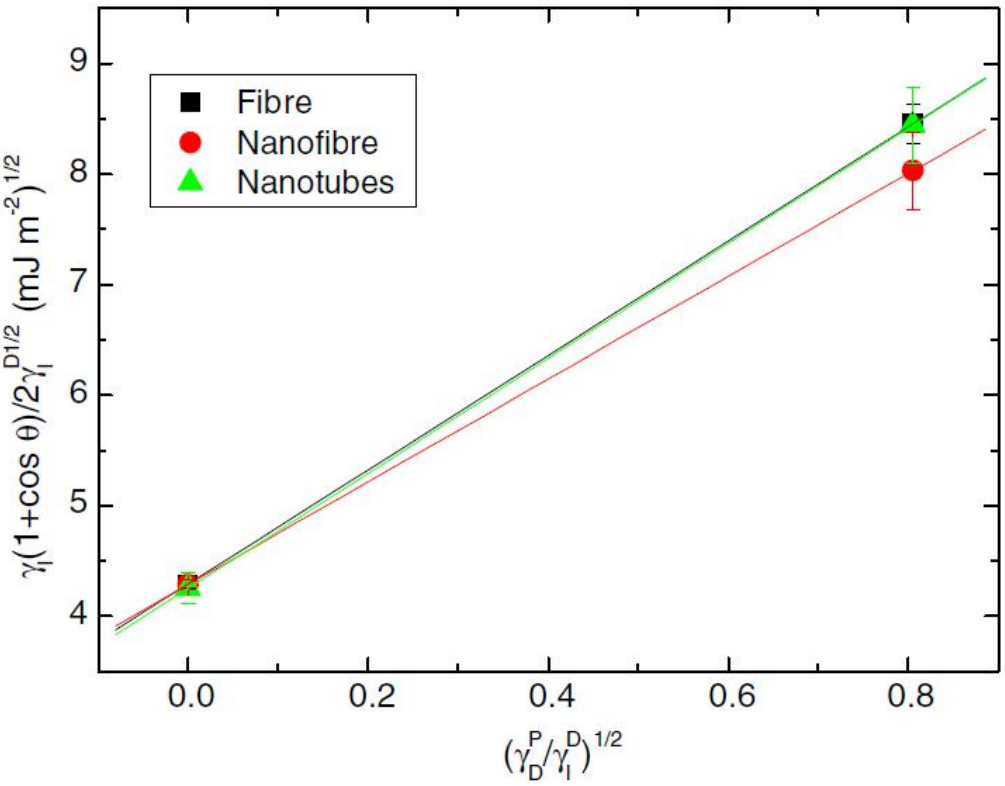

Figure 2.25 Owens-Wendt plot for carbon fibre, carbon nanofibres and multiwall nanotubes [171].

As the dispersive and polar components of the surface tension are known for many liquids, the contact angle then allows determination of the dispersive and polar components of the solid surface from the intercept and slope respectively of the line indicated by equation 2.12 [170]. Hence it can be concluded that the solid's surface energy can be determined by the resulting Owens-Wendt plot [171]. The Owens-Wendt plot method for a range of solid and liquid combinations has been shown to be accurate when compared with other surface free energy measurements and standards [172].

2.4.7 Hydrophobic Surface

Previous discussions examined surface properties at a molecular level and did not consider any larger microscopic effects. However microscopic effects in terms of the organization of a material are well documented in changing surface behaviour.

The simplest consideration is that of a rough solid surface which is being partially wetted by a liquid. Thus it is necessary to study the relationship between roughness and contact angle. Nosonovsky and Bhushan carried out work which was focused on a detailed model for roughness effect on contact angle and an optimised local roughness distribution for wetting [173, 174]. The Wenzel model [173] and Cassie Model [174] was used to explain the effect of contact area, solid-liquid-air composite interface and sharp edges of asperities on wetting behaviour [175, 176]. The Wenzel model [173] and Cassie Model [174] are the two most well known models regarding the effect of roughness on surface wetting behaviour. Thus in the sections below, the details of these two models will be studied.

2.4.7.1 Wenzel Model

The Wenzel model is based on the net energy decrease during a droplet spreading on a rough surface [173]. A larger solid-liquid interface area is obtained on a rough surface, resulting in larger net energy. Therefore, the liquid has no preference to be adhesive to the surface due to the tendency to decrease the net energy. The result of the system attempting to lower the net energy will be to decrease the liquid contact angle with the solid surface, thus decreasing the total solid-liquid interface. When a liquid contacts with a solid surface, the energy of the whole system will be decreased due to the attraction between solid molecules and liquid molecules on the interface. This can be expressed by equation 2.32 where W_{sl} is the work of adhesion per unit area between two surfaces; γ_s is the surface energy of the solid against air; γ_l is the surface tension of the liquid against air; γ_{sl} is the surface energy of the solid against liquid [155, 175, 176].

$$W_{sl} = \gamma_s + \gamma_l - \gamma_{sl} \qquad (2.32)$$

$$E_{tot} = \gamma_l (A_l + A_{sl}) - W_{sl} A_{sl} \qquad (2.33)$$

$$\gamma_l (dA_l + dA_{sl}) - W_{sl} dA_{sl} = 0 \qquad (2.34)$$

$$dA_l / dA_{sl} = \cos\theta_0 \qquad (2.35)$$

When a liquid droplet sitting on a solid surface to form a static contact angle θ_0 at the equilibrium condition, this contact angle can be determined when the system net surface free energy is minimum [155, 176, 177]. The total energy E_{tot} can be described using equation 2.33 where A_l is the contact area of the liquid with the air, and A_{sl} is the contact area of the solid with the liquid by assuming the droplet volume and pressure are constant [176]. At the equilibrium condition, dE_{tot} =0, and equation 2.34 can be derived from equation 2.33. Therefore for a droplet with constant volume, the contact angle can be defined as equation 2.35 by using geometrical consideration [176].

Finally, combining equation 2.32, 2.34 and 2.35, the Young's equation for the contact angle can be obtained as shown in equation 2.36.

$$\cos\theta_0 = \frac{\gamma_s - \gamma_{sl}}{\gamma_l} \qquad (2.36)$$

In the case of a rough solid surface, the Young's equation 2.36 is not sufficient to describe the contact angle as the roughness can give an increased contact area A_{sl} between the liquid droplet and solid surface [173]. If a droplet is in contact with a rough surface without air pockets, the interface is called a homogeneous interface. Wenzel et al developed equation 2.37 based on equation 2.35 for homogeneous interface [173] where θ is the contact angle for the rough surface, A_{sl} is the actual surface area of solid with liquid, and A_f is the geometric flat solid-liquid contact area which is also equal to the A_{sl} onto the horizontal plane. R_f is referred to as roughness factor and can be defined as equation 2.38 [175].

$$\cos\theta = dA_l / dA_f = (\frac{A_{sl}}{A_f})(dA_l / dA_{sl}) = R_f \cos\theta_0 \quad (2.37)$$

$$R_f = \frac{A_{sl}}{A_f} \quad (2.38)$$

As the actual solid-liquid contact area A_{sl} is always greater than the geometric flat solid-liquid contact area A_f due to roughness, so R_f is always more than one (R_f > 1) [173]. From equation 2.37, it is apparent to see that if a liquid wets a solid surface with contact angle θ_0, where $\cos\theta_0$ > 0, it will also wets the same solid with a rough surface with a contact angle $\theta < \theta_0$. Also if the smooth surface of a solid is nonwetted by a liquid, where $\cos\theta_0$ < 0, the rough surface will also be nonwetted with an even higher contact angle $\theta > \theta_0$. Figure 2.26 shows the effect of roughness for a hydrophobic surface, $\theta > \theta_0$ [175].

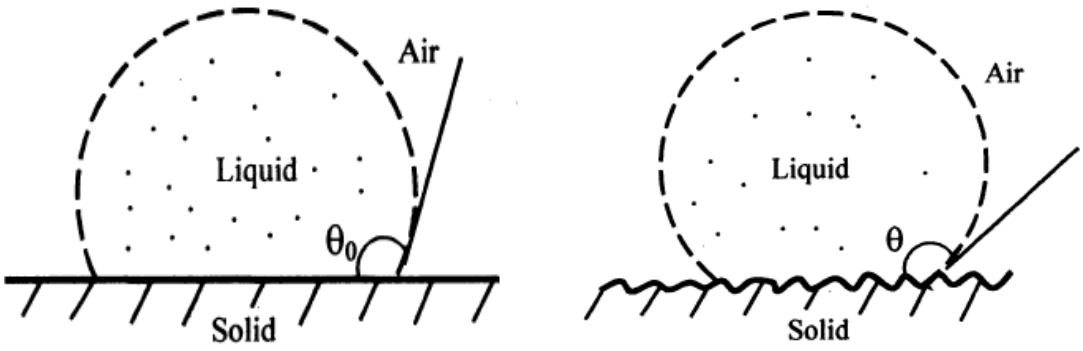

(a) Smooth Surface **(b) Rough Surface**

Figure 2.26 Effect of Roughness for a hydrophobic surface **(a)** a liquid droplet in contact with a smooth surface; **(b)** a liquid droplet in contact with a rough surface. [175].

The roughness of surface affects the contact angle according to the Wenzel model has been verified experimentally. Yost [178] found that roughness can enhance wetting of a copper surface with Sn–Pb eutectics solder, which has a contact angle of 15–20° for smooth surface. Shibuichi et al. [179] measured the contact angle of a variety of liquids on alkyl ketene dimer (AKD) substrate. All these study have found out that the roughness has a positive effect on enhancing the wetting for the surface that can be wetted by liquids. Erbil [180] measured the contact angle of polypropylene (contact angle of 104° for smooth surface) and found out that the roughness has a positive influence on increasing the hydrophobicity of the surface.

2.4.7.2 Cassie-Baxter Model

The Wenzel model of equation 2.37 is limited as the roughness factor R_f cannot be high as the condition $-1 \leq R_f \cos\theta_0 \leq 1$ must be achieved. For high roughness, the surface seems to become porous, and some air pockets can be formed in the cavities of the surface. Thus a wetting liquid will be completely absorbed by the cavities of the rough surface [175] but a non wetting liquid will not penetrate into the rough surface cavities, resulting in a composite solid-liquid-air interface [175]. As the solid-liquid contact area can be only exist at the peaks of asperities for high roughness surface, so the solid-liquid contact area will not further increase with increasing surface roughness [175].

Cassie and Baxter extended Wenzel's model which was originally developed for the homogeneous solid-liquid interface to the solid-liquid-air composite interface and defined an equation for a porous surface as [175]:

$$\cos\theta = R_f f_{sl} \cos\theta_0 - f_l \qquad (2.39)$$

Where f_{sl} is the fractional flat geometrical area of solid-liquid interface under the liquid droplet, f_l is the fractional flat geometrical area of liquid-air interface under the liquid droplet [175].

If the surface is moderate rough rather than porous, the liquid completely contact with the solid surface without forming a composite solid-liquid-air interface, then f_{sl} and f_l is one and zero, respectively. Hence equation 2.39 is converted to Wenzel's equation: $\cos\theta = R_f \cos\theta_0$ [173]. As R_f increases to its maximum, f_{sl} will approaches zero, and f_l approaches one, resulting in a contact angle θ approaches 180° [173, 175]. Figure 2.27 simply shows the two models for a liquid droplet sitting on a rough surface.

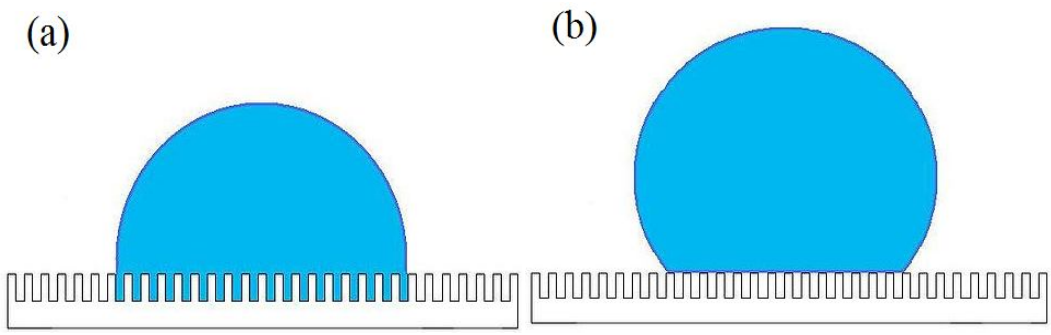

Figure 2.27 A liquid droplet sitting on a rough surface **(a)** Wenzel Model **(b)** Cassie-Baxter Model

The Cassie–Baxter model does not show how f_{sl} and f_l depend on R_f or conditions for the formation of the composite interface [175]. Johnson and Dettre et al. showed a droplet have two states, which are homogeneous and composite interfaces. Although it may geometrically possible for a system to be composite, it is energetically favourable for the liquid to penetrate into pores between asperities to form a homogeneous interface [181]. Marmur demonstrated experiments and expressed geometrical conditions for a surface to minimise the energy of local system, under which the composite interface could be formed [182]. Patankar

found out that the existence of the homogeneous or composite interface was dependent on the system history, which the liquid droplet was deposited or formed on the solid surface [183]. However, all above analyses did not give the conditions for the formation of a homogeneous or composite interface.

Bhushan et al recently proposed conditions where a homogenous interface would be formed [175]. In this work, the spacing between asperities was assumed to be the controlling parameter, with relatively large distances between asperities causing the formation of a homogenous interface [175, 176].

2.4.7.3 Superhydrophobic Surfaces

Contact angle can be used to identify the hydrophilic or hydrophobic nature of a substrate. The surface is considered as being superhydrophobic when the contact angle is approaching 180°. Superhydrophobic surfaces have several interesting properties such as self-cleaning, antisticking or low adhesion, and low friction [177].

Several factors can affect contact angle such as surface preparation, cleanliness and roughness [155, 176, 177]. Thus the hydrophilic or hydrophobic nature of a substrate was also affected by these factors. For example, surface preparation using low surface energy materials or by chemically treating materials like wax, silicon or polytretafluoroethylene can form hydrophobic surfaces [155, 177]. In addition, increasing roughness increases hydrophobicity of a surface. It should be noticed that this is only true for hydrophobic surface. For a hydrophilic surface, it will become more hydrophilic when increase the surface roughness [155, 175].

In the last decade, hydrophobic surface has been produced according to the study of nature surfaces, such as Nelumbo nucifera (lotus), which leaves are water-repellent or superhydrophobic, and have high contact angle [175, 184-186]. This phenomenon is also called lotus effect. Figure 2.28 shows SEM images of microstructured water-repellent leaf surface of Nelumbo nucifera and Colocasia

esculenta [187]. It is obvious to see that both surfaces are covered by papillae or bumps that provide a high level of roughness and air pockets [185, 187]. The surfaces were also covered with different sorts of wax, which are made of some hydrocarbon molecules that have a strong hydrophobicity [185, 187]. Hence the combination of bumps and wax give a high contact angle, for example, lotus leaf has a contact angle of 162° [184].

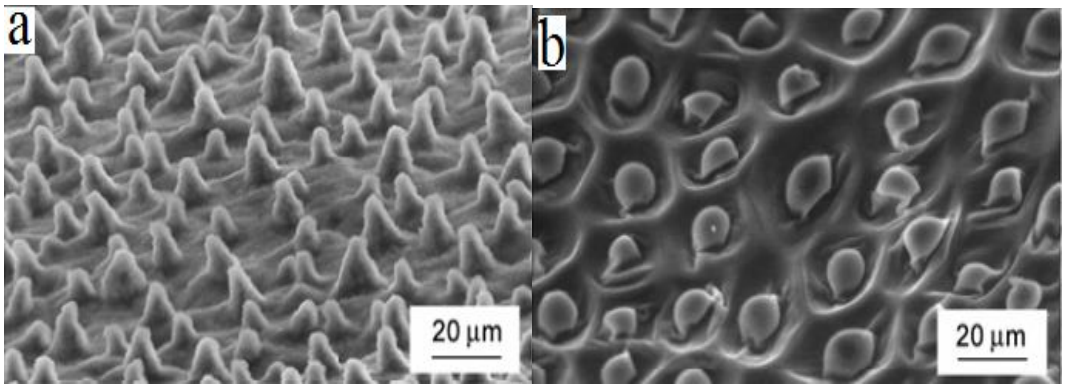

Figure 2.28 SEM photographs of microstructured water-repellent leaf surfaces. (a) Nelumbo nucifera adaxial leaf surface; (b) Colocasia esculenta leaf surface. [187]

2.4.8 Summary

This section 2.5 highlights how the chemical composition of a material is correlated with surface properties. The surface energy of materials has been commonly measured in a number of ways based on wetting and adhesion studies. The techniques used to determine these surface properties are sometimes difficult to translate to smaller length scales. Therefore, measuring the surface properties of electrospun nanofibres becomes challenging as new methods need to be developed.

2.5 Outline for Following Chapters

The surface properties of electrospun polymer fibres are unknown. This thesis is to investigate the surface behaviour of electrospun polymer fibres at two scales; that of the fibre itself and the second at the level of networks of many electrospun fibres. In Chapter 3, the preparation of polymer (PEO, PVA, PC) nanofibres with well controlled geometric morphology by electrospinning will be discussed in detail. This is carried out by experimental investigation of electrospun polymer solution properties and processing parameters.

A range of methods to measure the surface properties of these electrospun fibres are proposed, some of which are novel. In particular, wetting behaviour of electrospun networks are important as the liquid response on the network can lead to potential applications. This is especially relevant for superhydrophobic surfaces where a droplet contact angle with a solid surface needs to be large (greater than 150º). In Chapter 4, electrospun superhydrophobic polymer networks will be investigated and results will be discussed based on different models. Chapter 5 of this thesis introduces the surface free energy investigation of individual electrospun fibre itself from AFM contact mechanics adhesion tests. Comparisons are made for different draw ratio bulk polymer films and a relationship between polymer intermolecular distance and its dispersive surface free energy will be proposed in this chapter. Chapter 6 describes wetting measurements of individual electrospun polymer fibres using Wilhelmy balance method combining Owens-Wendt theory, and other surface property measurement techniques are employed in this chapter to understand the difference of the surface molecular structure between electrospun polymer fibres and bulk polymer film. Chapter 7 includes the conclusions of this thesis, electrospinning of hollow polymer nanofibres and recommendations for the future work.

Chapter 3

Investigation of Electrospinning Processing Parameters and Resultant Fibre Morphology

3.1 Introduction

This chapter details the experimental work carried out in order to manufacture electrospun polymer fibres for subsequent investigations of their surface properties. Resultant electrospun fibre morphology can be influenced by many parameters such as solution concentration, surface tension, viscosity, conductivity, applied voltage, flow rate, and distance between needle tip and ground electrode collector (DTC), as reviewed in section 2.3.3. Effects of these solution properties and processing parameters on resultant electrospun fibre morphology will be characterized and investigated experimentally herein. The ordering and alignment of electrospun polymer nanofibres will also be investigated.

3.2 Experimental Details

3.2.1 Materials

Polyethylene oxide (PEO), polyvinyl alcohol (PVA) are all water soluble polymers

and therefore easy to electrospin from non-toxic solvents. These polymers were selected in our experimental work due to their low toxicity, widespread usage. More importantly, PEO and PVA were used as model polymer systems in order to investigate how changing the processing parameters influence the resultant ability to electrospun fibres and their resultant morphology. Understanding the complex relationship between the electrospinning parameters and collected material was important in future studies using other polymers in subsequent chapters.

3.2.1.1 Polyethylene oxide (PEO)

PEO is a nonionic homopolymer of ethylene oxide and can be represented by the formula $(OCH_2CH_2)_n$, Figure 3.1 shows synthesis of polyethylene oxide. It is water soluble and highly hydrophilic; it is the most commercially important type of polyether. In this study, polyethylene oxide (PEO) with molecular weights of 200,000; 1,000,000; and 8,000,000 $g.mol^{-1}$ were used. PEO powders were purchased from Sigma-Aldrich, UK.

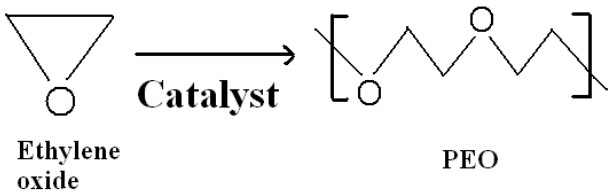

Figure 3.1 Synthesis of polyethylene oxide (PEO)

3.2.1.2 Polyvinyl alcohol (PVA)

Polyvinyl alcohol (PVA) is a semi-crystalline and water-soluble polymer with good chemical and thermal stability. PVA is prepared by polymerization of acetaldehyde through partial or complete hydrolysis of polyvinyl acetate to remove acetate groups, Figure 3.2 shows polyvinyl alcohol (PVA) with fully

hydrolyzed grades and partially hydrolyzed grades. PVA has excellent oil, grease and solvent resistance and film forming, emulsifying and adhesive properties. The melting point is 230 °C for the completely hydrolyzed PVA and 180-190 °C for the partially hydrolyzed PVA. PVA is non-toxic and biodegradable which can be considered as an environmental friendly polymer. In this study, PVA powders with an average molecular weight of 98,000-143,000 g.mol^{-1} and 98 % hydrolyzed were purchased from Sigma-Aldrich, UK.

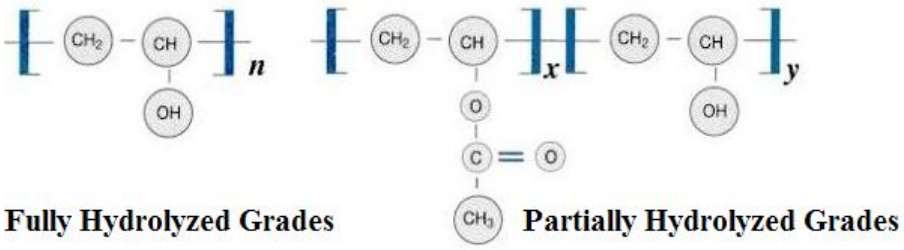

Figure 3.2 PVA with fully hydrolyzed grades and partially hydrolyzed grades

3.2.2 Polymer Solution Preparation

3.2.2.1 Polyethylene oxide (PEO) Solution

Polymers in solution are required for the electrospinning process. Various PEO solutions were prepared by dissolving PEO in ethanol and water mixture solvent at room temperature (22-24 ^{o}C) and gently stirred for about 24 hours. Table 3.1 shows the details of PEO solutions used in this study, including the weight of polymer which was added to the volume of solvent. A range of different PEO solution concentrations and molecular weights were explored in order to determine the suitability of the parameters for spinning fibre geometries, as discussed in section 3.3.1.

Table 3.1 Different concentration and molecular weight PEO solutions

Solution No	PEO Molecular weight (g/mol)	Powder Weight (g)	Ethanol (ml)	Distilled water (ml)	PEO Solution Concentration (wt/v %)
1	8,000,000	0.25	75	25	0.25
2	8,000,000	0.5	75	25	0.5
3	8,000,000	0.75	75	25	0.75
4	8,000,000	1	75	25	1
5	8,000,000	1.25	75	25	1.25
6	8,000,000	1.5	75	25	1.5
7	1,000,000	1.5	75	25	1.5
8	200,000	6	75	25	6
9	8,000,000	1.5	65	35	1.5

3.2.2.2 Polyvinyl alcohol (PVA) Solution

PVA solutions for subsequent electrospinning were prepared by dissolving PVA in distilled water. The solution was heated up to 80-90 ^{o}C and gently stirred for 2-3 hours to obtain a homogenous solution using a stirring hot plate. Table 3.2 shows the details of PVA solutions used in this study.

Table 3.2 Different concentration PVA solutions

Solution No	PVA Molecular weight (g/mol)	Powder Weight (g)	Distilled water (ml)	PVA Solution Concentration (wt/v %)
10	98,000-143,000	6	100	6
11	98,000-143,000	7	100	7
12	98,000-143,000	8	100	8
13	98,000-143,000	13	100	13

3.2.3 Electrospinning Polymer Fibres

3.2.3.1 Single Needle Electrospinning

The electrospinning single needle experimental set up used to produce electrospun nanofibres is shown in Figure 3.3. Polymer solution was fed into a 10 ml syringe, with the flow rate controlled by a pump (Harvard PHD4400, Harvard Apparatus Ltd., UK) to allow a constant flow rate during the electrospinning process. The syringe is connected to one end of a short-length silicone capillary, with the other end of the silicon capillary connected to a 24 gauge (outer diameter = 0.56 mm, inner diameter = 0.305 mm) stainless steel tubing needle. A constant pressure was applied to the syringe tip so that a small stable drop of solution was suspended at the tip of steel needle. A high voltage DC power supplier (Glassman High Voltage Inc., US) was used to supply an electric field up to 30.0 kV. The liquid drop formed a cone shape due to applied electric field and a charged polymer solution jet was ejected from the cone and travelled under bending instability [188-190] when a critical electrical potential, V_c, was applied. During this process, the solvents rapidly evaporate, resulting in ultrafine polymer fibres deposited on the ground collector (such as aluminium foil or silicon), which was placed with a DTC (distance from needle tip to collector) of 8-20 cm in this study. A rotating cylinder with 52.8 cm diameter has been used to align electrospun fibres underneath the needle as shown in Figure 3.3. All the experiments were performed at room temperature (22-24 ºC). PEO and PVA electrospun fibres were produced in this study using different polymer solution compositions as defined in Tables 3.1 and 3.2 above.

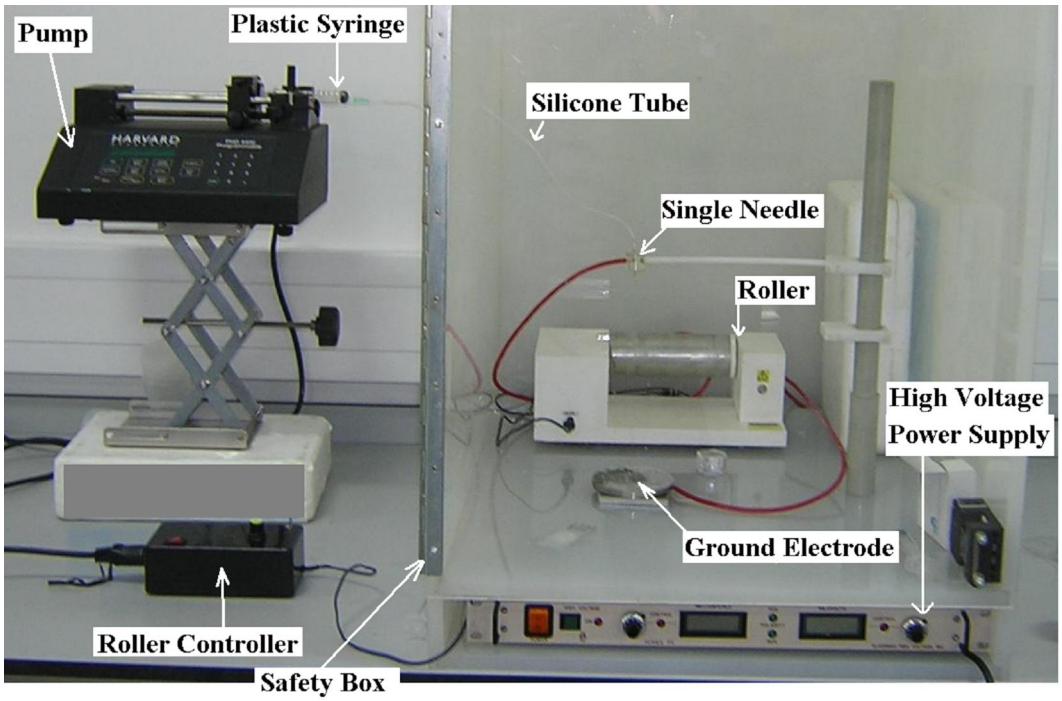

Figure 3.3 Single needle electrospinning experimental set-up.

3.2.3.2 Coaxial Needle Electrospinning

Electrospinning with a coaxial needle was used to demonstrate the production of PVA and PEO hollow fibres. The experimental set-up is similar to the set-up of electrospinning with single needle except that two pumps, two plastic syringes and a coaxial needle were used, as shown in Figure 3.4. The coaxial needle consists of an inner needle and an outer needle. Polymer solutions defined in Tables 3.1 and 3.2 were fed into outer needle with mineral oil or vegetable oil introduced into the inner needle. This experimental procedure followed the work of Li and Xia [191]. After electrospinning, octane was used to extract mineral oil or vegetable oil to form hollow fibres.

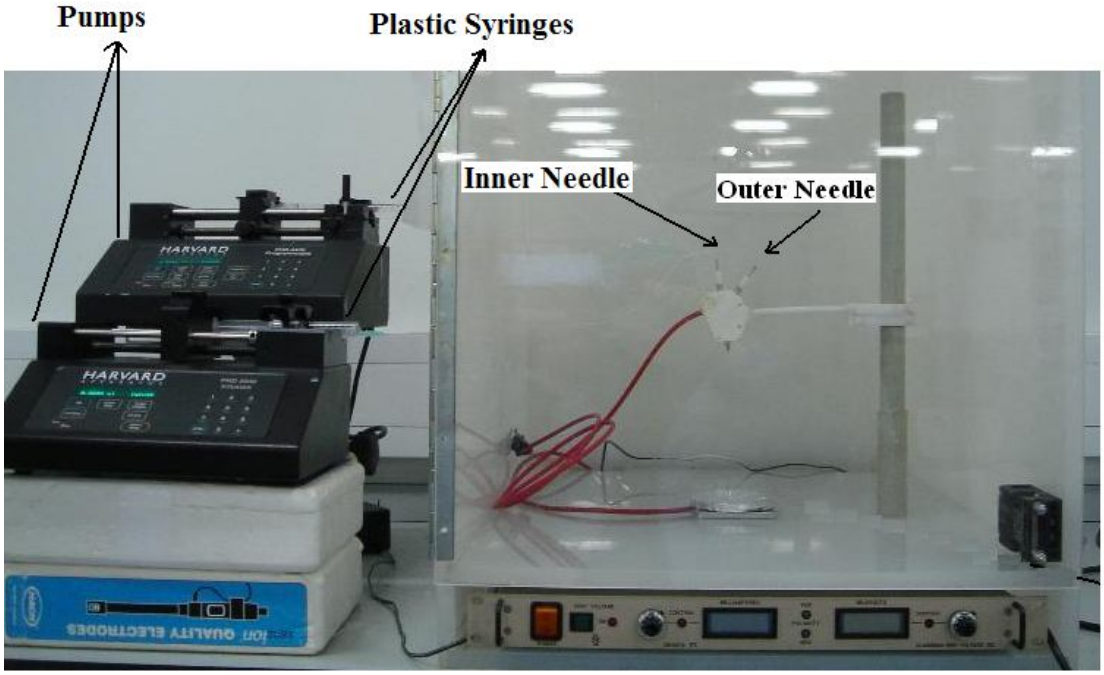

Figure 3.4 Coaxial needle electrospinning experimental set-up.

3.2.4 Characterization Techniques for Electrospun Fibres

3.2.4.1 Scanning Electron Microscopy (SEM)

The morphological and dimensional characterization of nanofibres can be performed by scanning electron microscopy (SEM). SEM uses an electron beam to raster scan over the surface of a sample, with the scattered electrons collected at a detector. The number of electrons scattered depend strongly on the topography of the sample's surface. This form of SEM, known as secondary electron imaging, is therefore suitable for imaging surface topography. Jeol JSM-6300 and Jeol JSM-6800 scanning electron microscopes, as shown in Figure 3.5, have been used to characterize electrospun fibres in this study operating at accelerating voltages of between 0.2 and 30 kV under vacuum environment. Jeol JSM-6300 is an analytical SEM and Jeol JSM-6800 is a high resolution field emission SEM which

can provide superior image resolution. All polymer fibre samples were carbon or gold coated prior to SEM imaging to prevent the accumulation of electron charging from the electron microscope.

Figure 3.5 (a) Jeol JSM-6800 **(b)** Jeol JSM-6300

3.2.4.2 Transmission Electron Microscopy (TEM)

TEM is a technique whereby a beam of electrons is transmitted through an ultra thin specimen, interacting with the specimen when it passes through. Image contrast is provided by the material's composition within the electron beam. Thus, thick or dense specimens do not permit the electron beam to transmit through the sample whereas lighter element or thinner samples allow electron transmission to a detector situated below the specimen. As electrospun polymer fibres can be relatively small, with diameters below 100 nm, TEM is suitable for high resolution imaging purposed. A Jeol JSM 2010 has been used in this study, as shown in Figure 3.6, operating at an electron beam accelerating voltage of 200 kV and is able to obtain a spatial resolution of less than 1 nm. Electrospun polymer fibres in this work were prepared by electrospinning directly onto an electrically conducting TEM grid with a thin carbon support film.

Figure 3.6 Transmission Electron Microscopy

3.3 Results and Discussion

3.3.1 Electrospun PEO Nanofibre Morphology

PEO nanofibres with different concentration and molecular weight have been produced by the electrospinning process. The morphologies of PEO nanofibres can be controlled by different parameters and detailed by the following sections.

3.3.1.1 Effect of Concentration

Figure 3.7 (a)-(f) have shown electrospun PEO nanofibres from different concentration solutions with same molecular weight of 8000,000 $g.mol^{-1}$. A flow rate of 0.8 $\mu l.min^{-1}$, applied voltage of 8.5 kV, and DTC value of 15.5 cm was used in all of the PEO electrospinning investigations. Figure 3.7 (a) clearly indicates the formation of beaded structures when spinning from S1 (solution 1), resulting in nanofibre diameters for S1 of about 100 nm. For other solution concentrations, the average fibre diameter increased from 200 nm to 2 μm as the

solution concentration was increased.

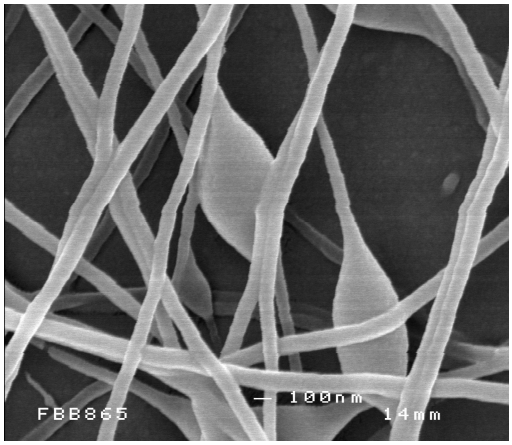

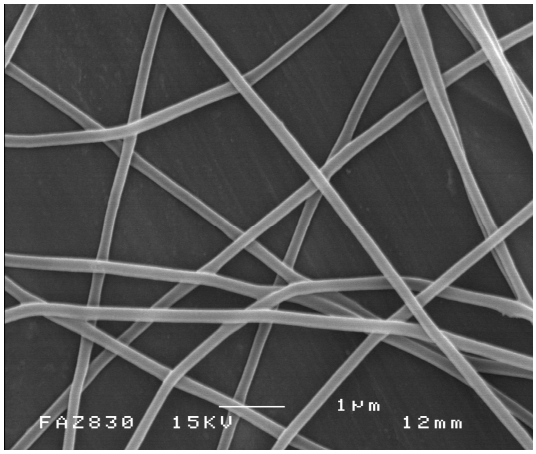

Figure 3.7 (a) S1: Concentration 0.25 wt/v% **(b)** S2: Concentration 0.5 wt/v%

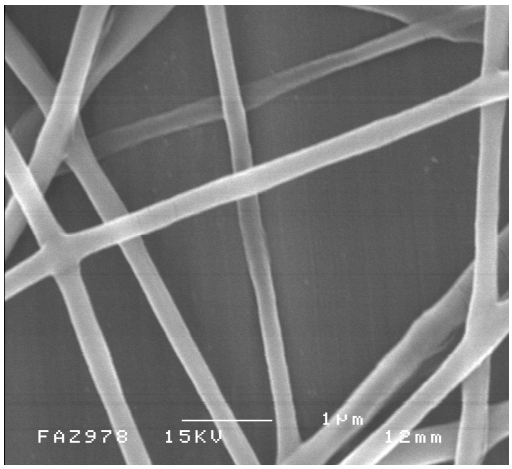

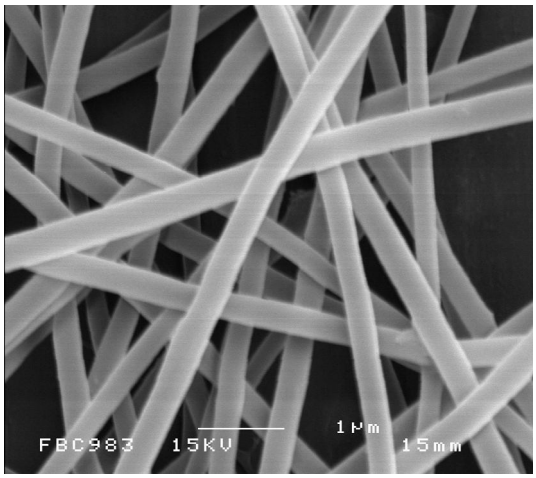

(c) S3: Concentration 0.75 wt/v% **(d)** S4: Concentration 1.0 wt/v%

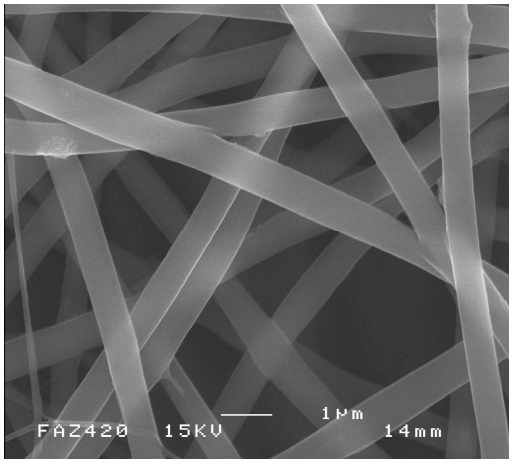

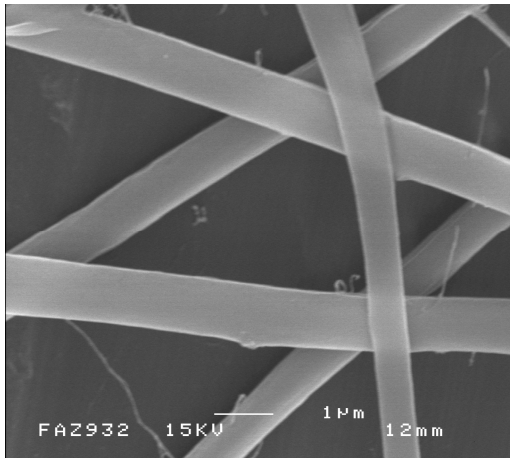

(e) S5: Concentration 1.25 wt/v% **(f)** S6: Concentration 1.5 wt/v%

The increase in fibre diameter with increasing solution concentration can be explained by considering solution viscosity as discussed in section 2.3.3.2. Viscosity of a polymer solution plays a significant role in determining the electrospinning process and the resultant fibre morphology. For PEO-ethanol-water solution, it has been found that the solution viscosity is proportional to the polymer concentration. In electrospinning process, the spinnability of a polymer solution is dependent on the polymer concentration (i.e. viscosity). If polymer concentration is too low, i.e. low viscosity, only beads or beaded-fibres will be formed. If polymer concentration is too high, electrospinning will be prohibited by an inability to control and maintain the flow of the polymer solution to the needle tip due to the electric forces being unable to deform and draw the highly viscose solution. In general, a higher viscosity results in larger fibre diameters due to the reduction of solvent evaporation rate from the liquid jet, so the formation of thicker fibres will be generated from a higher concentrated polymer solution.

3.3.1.2 Effect of Applied Voltage

To experimentally examine the effect of applied voltage, S3 (solution 3) with molecular weight of 8,000,000 $g.mol^{-1}$ and concentration of 0.75 (wt/v)% has been used for this study. The flow rate was held at 1.0 $\mu l.min^{-1}$ and the distance between the needle and the ground electrode was kept at 15.5 cm during the electrospinning process. After applying a voltage to the solution, the liquid droplet held at the needle tip was electrically charged to form a conical shape, known as the Taylor cone. Increasing the applied voltage to 6.1 kV resulted in a thin and stable liquid jet ejected from the Taylor cone. Further increasing the applied voltage to the needle tip caused the size of Taylor cone to decrease and receded to

the edge of needle tip but the liquid jet was still highly stable. This mode is often referred to as cone-jet mode [192]. At 10.9 kV the Taylor cone disappeared and the jet originated from the liquid within the needle tip. Above 10.9 kV, the liquid jet was non-stable at the needle tip and the spinning process was non-continuous. At 12 kV, several mini jets were ejected from the needle (multi-jets spinning) beside the main large liquid jet. Further increasing voltages above 15 kV caused discharge, making the electrospinning process impossible.

Figure 3.8 (a)-(d) show SEM images of electrospun PEO nanofibres generated from different applied voltage. The relationship between fibre diameter and the applied voltage shows two regions, with a transition occurring at an applied voltage of 10.9 kV. In the first region, fibre diameters decrease significantly with increasing voltages from 6.1 kV to 10.9 kV, and very uniform diameter nanofibres were generated (Figure 3.8 (a) and (b)). The Taylor cone became smaller as the applied voltage increased and the charged liquid jet from Taylor cone tip became progressively thinner. Since the ultrafine fibres were mainly formed by the stretching and acceleration in whipping region, higher electric field strength induced more cycles of bending instability and a thinner liquid jet always resulted in thinner electrospun fibres. Therefore, increasing the applied voltages during the cone-jet spinning region will decrease the diameters of electrospun PEO nanofibres.

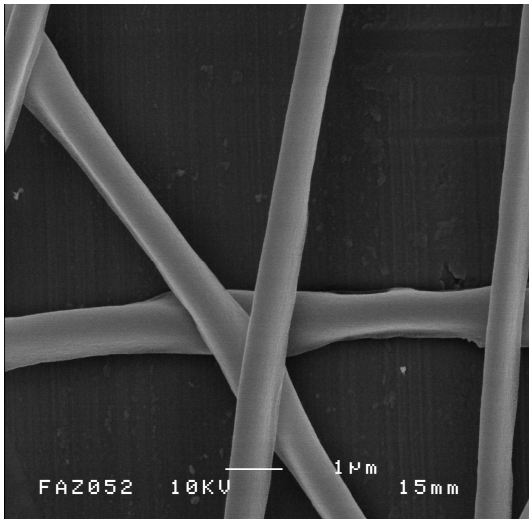

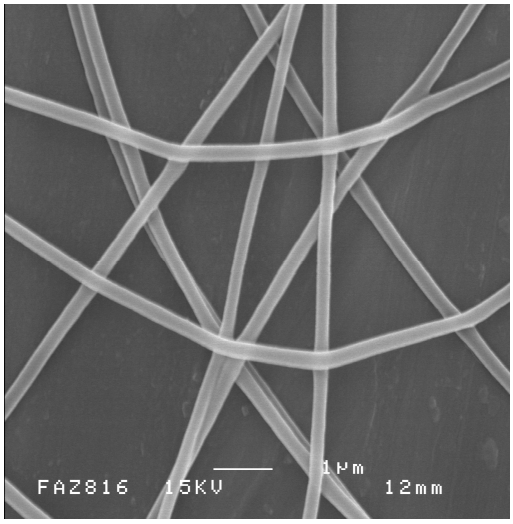

Figure 3.8 (a) S3: Applied Voltage 6.6 kV **(b)** S3: Applied Voltage 8.5 kV

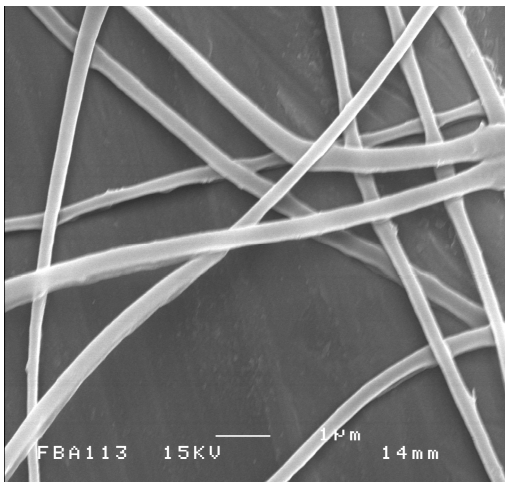

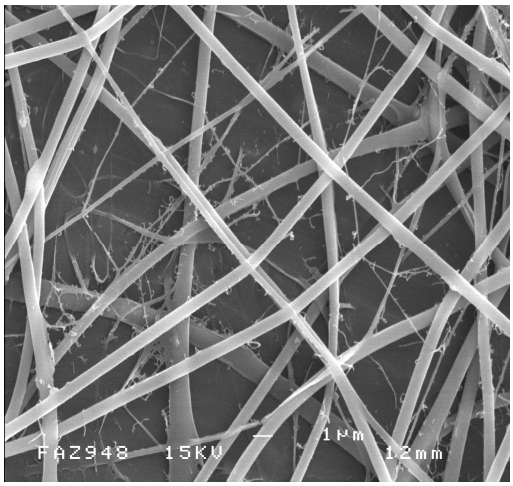

(c) S3: Applied Voltage 11.1 kV **(d)** S3: Applied Voltage 13.5 kV

As shown in Figure 3.8 (c) and (d), a different fibre diameter and applied voltage relationship occurs above 10.9 kV when the fibre diameter increased significantly with the applied voltage. A broad fibre diameter distribution can be seen when using voltages higher than 11.1 kV as shown in Figure 3.8 (d). In this second electrospinning region, the polymer solution jet seems to be ejected from the inside of the needle indicating that there wasn't sufficient fluid for the formation of the Taylor cone. In this region for PEO/ethanol-distilled water system, the higher applied voltage removes more liquid from the solution capillary and ejects

a thicker jet from the needle tip; as a result, the formation of the thicker fibres are obtained. Conversely, increasing the electric field also increases the electrostatic repulsive force on the fluid jet that favours thinner fibre formation. At 13.5 kV, a considerable amount of thin fibres with diameters below 150 nm were found and a broad distribution in the fibre diameter was observed as shown in Figure 3.8 (d). This was mainly caused by multi-jet spinning.

3.3.1.3 Effect of Flow Rate

The nanofibre morphology can be affected by varying the flow rate. To investigate the effects of flow rate, varying the solution flow rate into the spinning needle while other parameters were kept constant was performed. Investigations of flow rate on fibre morphology were achieved using PEO solution S5 with an applied voltage of 7.9 kV and the distance between the needle and the ground electrode of 19.5 cm. Figure 3.9 (a) and (b) show the electrospun PEO nanofibres for different flow rate. An increase in the flow rate from 0.2 $\mu l.min^{-1}$ to 1.0 $\mu l.min^{-1}$ for S5 (solution 5) gives a nanofibre diameter increase from ~ 200 nm to ~ 2 μm.

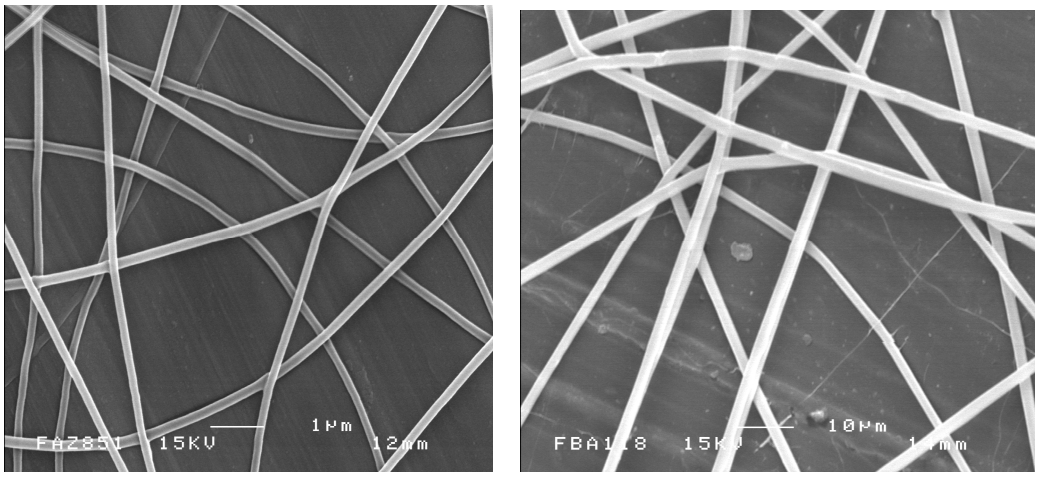

Figure 3.9 (a) S5: Flow rate 0.2 $ul.min^{-1}$ **(b)** S5: Flow rate 1.0 $ul.min^{-1}$

As expected, an increasing flow rate delivers more PEO solution to the Taylor

cone, which increases the size of the cone. Thus, the diameter of the liquid jet initiation from the Taylor cone tip was increased, which results in thicker fibre formation. When the flow rate was further increased to exceed a critical value, the delivery rate of PEO solution to the Taylor cone exceeded the rate at which the solution jet was ejected from the tip by the applied electric force. This shift in the mass-balance resulted in an unstable jet and prevented fibre formation.

3.3.1.4 Effect of Molecular Weight

The PEO average molecular weight (M_w) is a critical processing parameter which dictates fibre morphology. The increased molecular entanglement with M_w causes a corresponding increase in the solution viscosity. This is examined when electrospinning with solution 6 (S6), solution 7 (S7) and solution 8 (S8). Other parameters such as flow rate and applied voltage were all kept constantly during the electrospinning process.

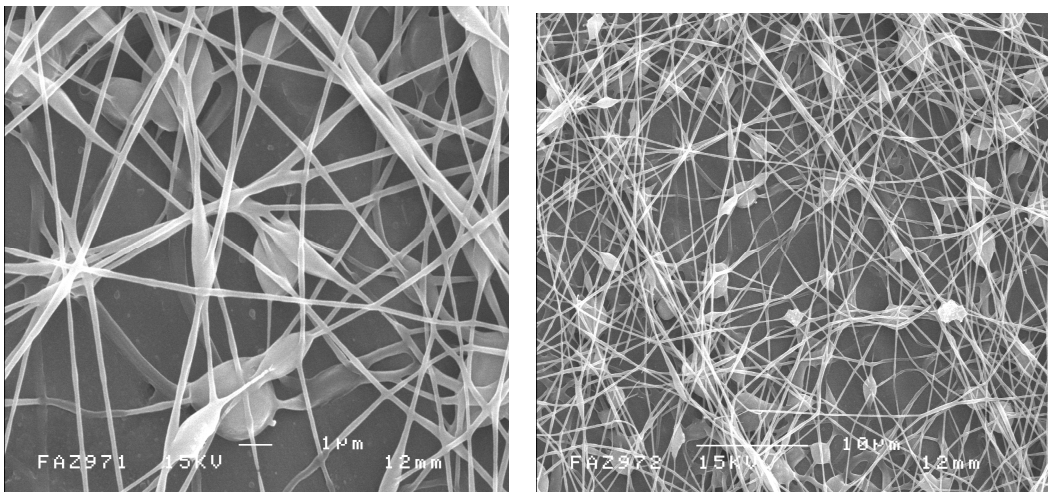

Figure 3.10 (a) S8: M_w 200,000 g.mol^{-1} **(b)** S8: M_w 200,000 g.mol^{-1}

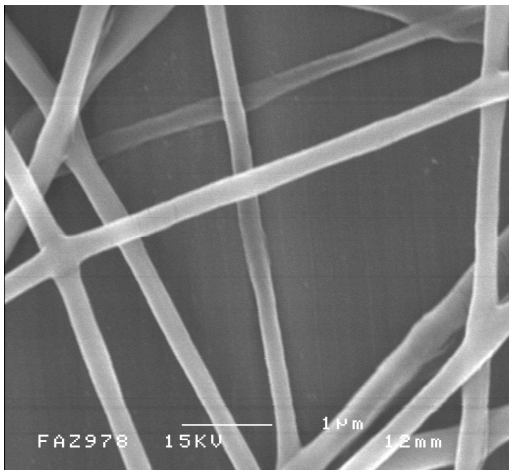

(c) S7: M_w 1,000,000 g.mol^{-1}

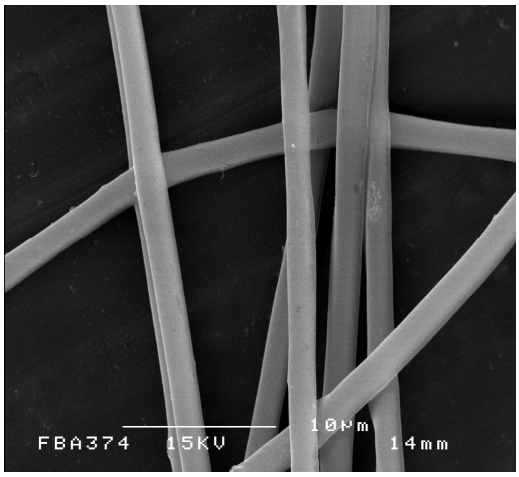

(d) S6: M_w 8,000,000 g.mol^{-1}

PEO solution with molecular weight (M_w) of 200,000 g.mol^{-1} and high concentration of 6 wt/v% cannot achieve regular fibrous geometries after electrospinning process, highlighted by the beaded structures as shown in Figure 3.10 (a) and (b). The preparation of a low M_w in solution shows that the surface tension driven collapse of the spinning jet to form spherical bead features along the fibre length occurs even when using a relatively high wt/v %. When increasing molecular weight (M_w) to 1,000,000 g.mol^{-1}, nanofibres were obtained with average diameter about 350 nm, as shown in Figure 3.10 (c). Further increasing molecular weight (M_w) to 8,000,000 g.mol^{-1} caused a large fibre diameter distribution with fibre diameters of over one micron, as shown in Figure 3.10 (d). Since the viscosities of PEO solutions could be significantly increased by increasing molecular weight, the resultant PEO fibre morphology changed from beads structure (S8), to fibres with small diameters (S7), and further large fibre diameters (S6). Thus varying the molecular weight of polymer can result in different fibre morphologies. This morphology change is because viscoelastic force prevents rapid changes in the shape of the jet and more viscous solutions are less likely to form beads or beaded fibres during electrospinning process, as discussed in section 2.3.3.2.

3.3.1.5 Effects of Conductivity and Surface Tension

Solution properties such as conductivity and surface tension can also influence the electrospun fibre morphology, as detailed in section 2.3.3.4 and 2.3.3.8. Increase in the solution conductivity causes higher electric net charges on the liquid jet, resulting in an increase in the force exerted on the jet to allow smaller fibres to be produced. Conductivity of a solution can be simply increased by the addition of a small amount of salt. Solution 2 (S2) with concentration of 0.5 wt/v% and molecular weight of 8,000,000 $g.mol^{-1}$ has been used for this investigation, and the average fibre diameter decreased from 250 nm to 200 nm after adding 1 wt.% salt as shown in Figure 3.11 (a) and (b). In addition, the formation of beads can also be decreased or further prohibited with increasing solution conductivity. Solution 8 (S8) with concentration of 6 wt/v% and molecular weight of 200,000 $g.mol^{-1}$ has been used for this study. Fibres without beads were formed when adding 1 wt. % salt into this PEO solution 8 (S8), as shown in Figure 3.11 (d).

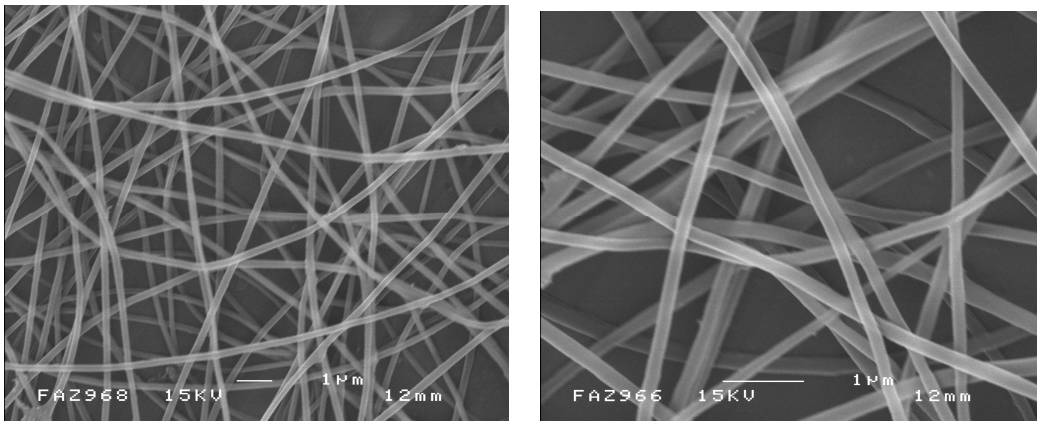

Figure 3.11 (a) S2: Before adding salt **(b)** S2: After adding 1 wt. % salt

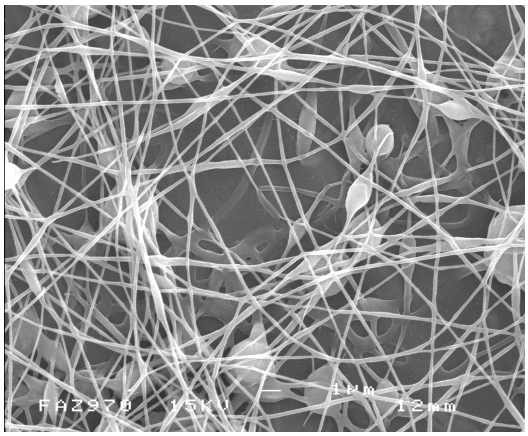

(c) S8: Before adding salt

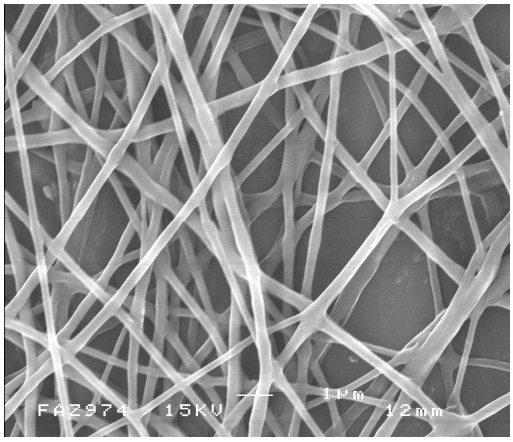

(d) S8: After adding 1 wt. % salt

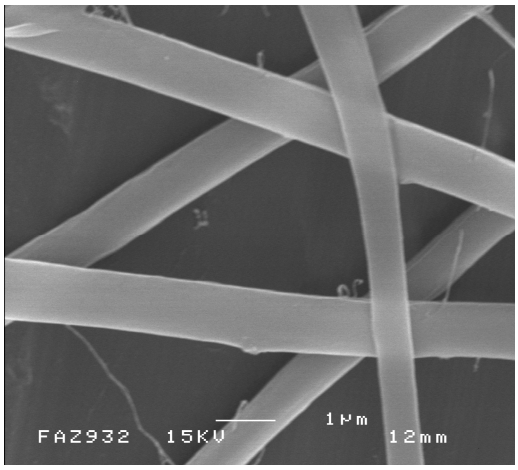

(e) S6: Distilled water 25 %

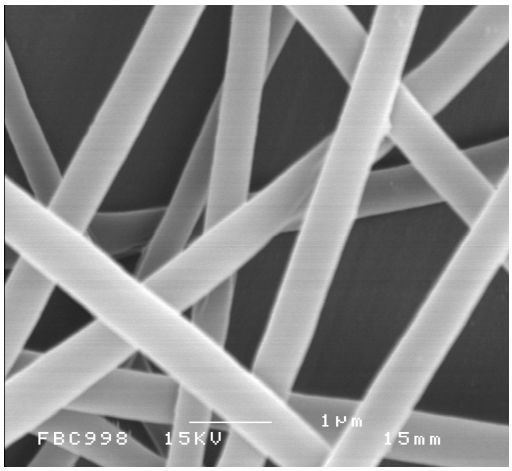

(f) S9: Distilled water: 35 %

Thinner electrically charged jets could be generated by increasing the solution surface tension. Water has a surface tension of 73 dyn.cm^{-1}, which is higher than that of ethanol (22 dyn.cm^{-1}). In PEO/ethanol-distilled water system, surface tension of solution can be increased by increasing the volume fraction of distilled water in the solvents mixture. In this study, PEO solution 6 (S6) with ethanol/distilled water volume fraction ratio of 75/25 and solution 9 (S9) with ethanol/distilled water volume fraction ratio of 65/35 were investigated. By increasing the volume fraction of water from 25 % (solution 6) to 35 % (solution 9), surface tension was increased, and the average fibre diameter was decreased from ~ 1 μm to ~ 700 nm, as shown in Figure 3.11 (e) and (f). Therefore

increasing the surface tension of a spinnable solution will result in decreasing fibre diameter. The mechanism for this diameter decrease is expected to be because the formation of reduced surface area, which occurs as the fibre diameter decreases, is favoured as the solution surface tension increases.

3.3.1.6 Effects of Distance between Tip and Collector

The effect of distance between needle tip to ground electrode collector (DTC) on electropun fibre morphology could be easily experimentally achieved by physically moving the needle tip closer or further away from the ground electrode collector. A 1.25 wt/v % PEO solution with M_w of 8,000,000 $gmol^{-1}$ (S5) was used for this study. A series of experiments were carried out in which the distance of needle tip to target collector was varied from 10 to 25 cm while other parameters were kept constant. The DTC is expected to be critical in determining if the fibres on the grounded collector still contain solvent, with a large DTC allowing more time for the solvent to evaporate during spinning when compared to a small DTC. A distance of needle tip to target of 10 cm gave relatively flat, tape-like fibres, due to the collected nanofibres still possessing solvent that allows some polymer mobility. Thus, these wet fibres collected on the substrate will spread to wet the substrate, causing the tape-like geometries observed in Figure 3.12 (a). Some nanofibres adhere together and bundles of nanofibres were collected, as shown in Figure 3.12 (a) because this tape-like geometry causes better geometric packing. At the distances of tip to target of 15 cm and longer, the nanofibres exhibited a straight, cylindrical morphology indicating that the nanofibres are mostly dry when they have reached the target, as shown in Figure 3.12 (b).

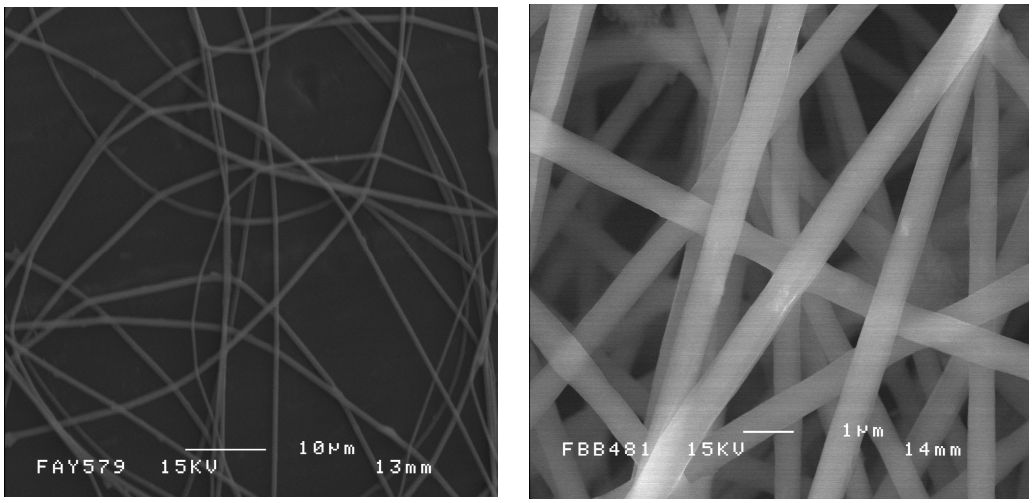

Figure 3.12 (a) S5: DTC = 10 cm **(b)** S5: DTC = 25 cm

3.3.2 Electrospun PVA Nanofibre Morphology

3.3.2.1 Effect of Solution Concentration

The effects of changing the electrospinning parameters on the resultant fibre morphology are examined in this section, and in the same way as for PEO. A series of PVA polymer solutions with different concentrations were electrospun. An applied voltage of 15.0 kV, flow rate of 1.0 $\mu l.min^{-1}$ and the distance between the tip and the collector of 15 cm were maintained during these experiments. Various nanofibre morphologies were characterized and are shown in Figure 3.13 (a)-(d). Solution 10 (S10) with 6 wt/v % concentration exhibited a number of large, spherical-like beads formed within fibres, as shown in Figure 3.13 (a). Increasing the PVA solution concentration to 7 wt/v % (solution 11), the number of the beads in the electrospun fibres were reduced and the beads structure changed from spherical-like to the spindle-like, as shown in Figure 3.13 (b). Further increasing the PVA solution concentration to 8 wt/v % (solution 12) causes the nanofibre morphology to change from a beaded structure to the

uniform fibre structure with an average fibre diameter of about 200 nm, as shown in Figure 3.13 (c). For solution 13 (S13), PVA with concentration of 13 wt/v %, the average fibre diameter increases to 1 μm due to an increase in solution viscosity allowing a reduction of solvent evaporation rate from the liquid jet and ejection of more polymer material into the jet to give larger electrospun nanofibre diameters.

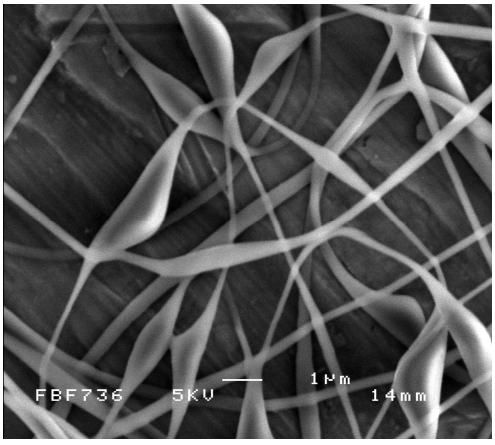

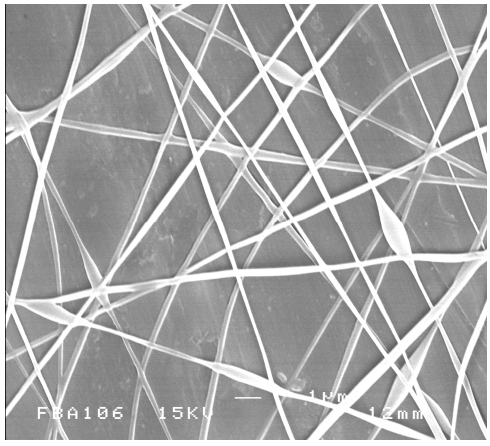

Figure 3.13 (a) S10: Concentration 6 wt/v% **(b)** S11: Concentration 7 wt/v%

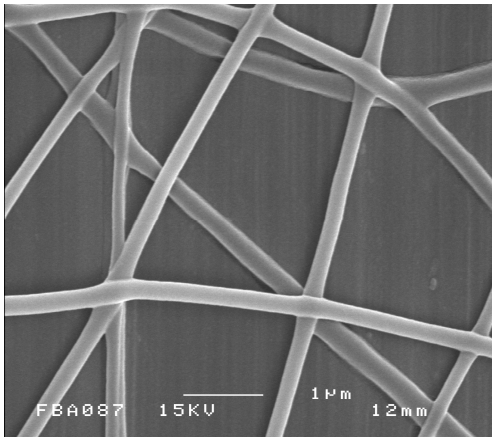

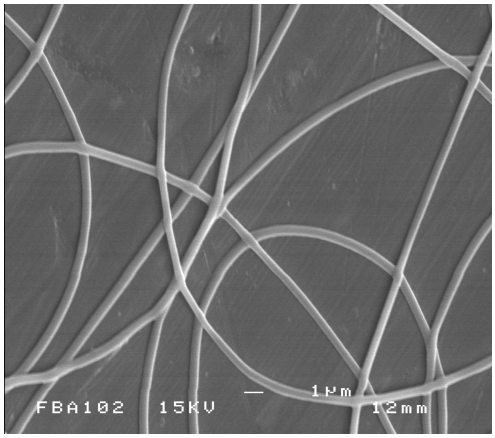

(c) S12: Concentration 8 wt/v% **(d)** S13: Concentration 13 wt/v%

3.3.2.2 Effect of Flow Rate and DTC

8 wt/v% PVA solution (S 12) was used for the investigation of the flow rate and the DTC influence on PVA fibre morphology. A constant voltage of 15 kV was

applied to this PVA solution (S12) while varying the solution flow rate and the DTC. As shown in Figure 3.14 (a)-(b), a slight increase in the electrospun PVA fibre diameter is observed when increasing the flow rate from 1.0 µl.min^{-1} to 9.0 µl.min^{-1}. The solution jet was assumed to elongate and deposit rapidly during this electrospinning process because of the high conductivity of the fully hydrolyzed PVA used. The diameter of the electrospun fibre became slightly larger as the DTC increased. When increasing the distance between the needle and collecting target from 13 cm to 20 cm, dry fibres were formed in Figure 3.14 (c), rather than the ribbon shaped fibre morphology in Figure 3.14 (d), as discussed in section 2.3.3.7.

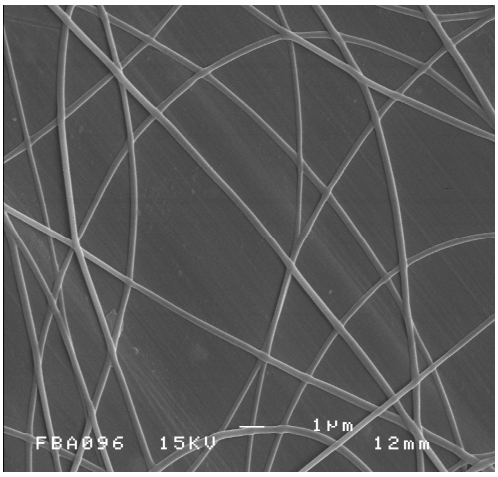

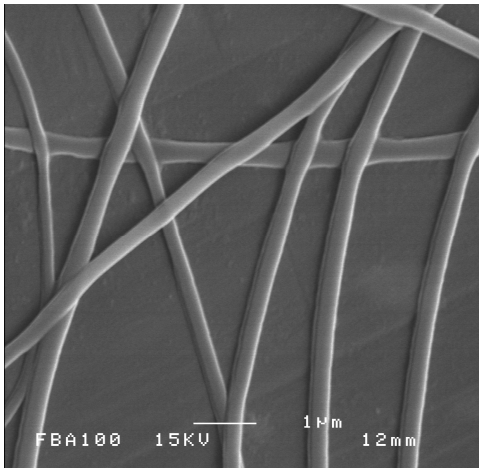

Figure 3.14 (a) S12: Flow rate 1.0 ul.min^{-1} DTC = 15 cm **(b)** S12: Flow rate 9.0 ul.min^{-1} DTC = 15 cm

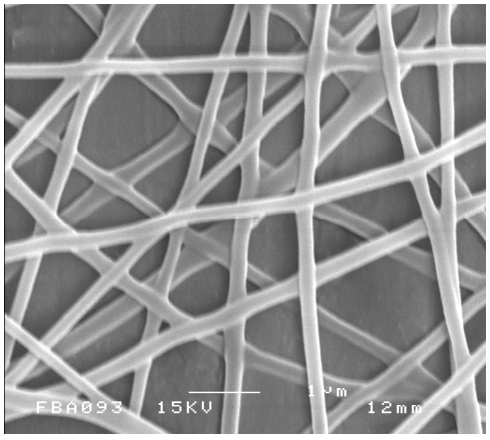

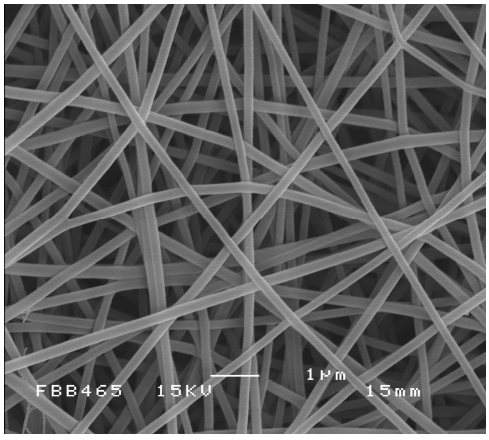

(c) S12: Flow rate 1.0 ul/mn DTC = 13 cm **(d)** S12: Flow rate 1.0 ul/mn DTC = 20 cm

3.3.2.3 Effect of Applied Voltage

Solution 12 (S12) with 8 wt/v% PVA solution was used for this study. The solution flow rate was kept at 1.0 $\mu l.min^{-1}$ constantly and the distance between the needle tip and the collector was controlled as 15 cm. When the applied voltage exceeded a critical value of 10.5 kV, the charged liquid jet was ejected from the tip of the cone, thus a cone-jet spinning mode was formed. The applied voltage was adjusted between 10.5-17.2 kV to keep the whole electrospinning process in a stable cone-jet mode. Results show a decrease in the average fibre diameter from 400 nm to 200 nm when increasing the applied electric field from 11.2 kV to 17.2 kV, as shown in Figure 3.15 (a)-(d). This increase is because higher electric field strength induces a thinner liquid jet and results in thinner electrospun PVA fibres during the cone-jet spinning region.

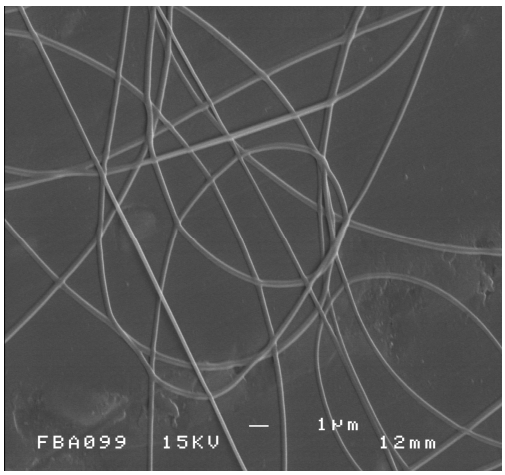

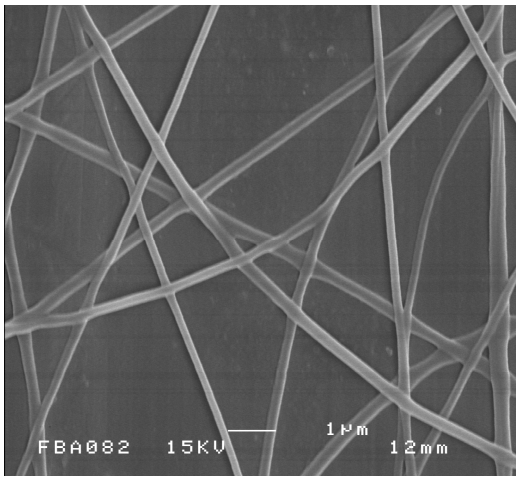

Figure 3.15 (a) S12: Voltage 11.2 kV **(b)** S12: Voltage 13.5 kV

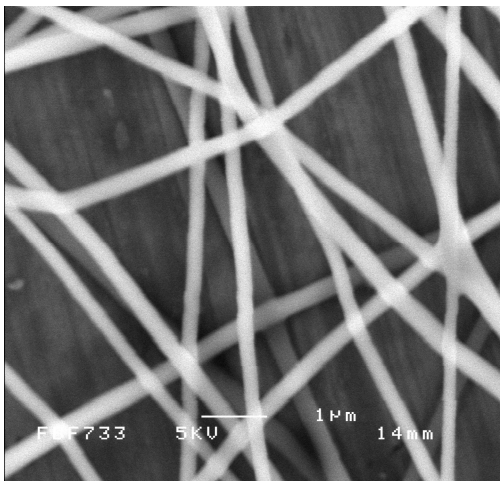

(c) S12: Voltage 15.8 kV

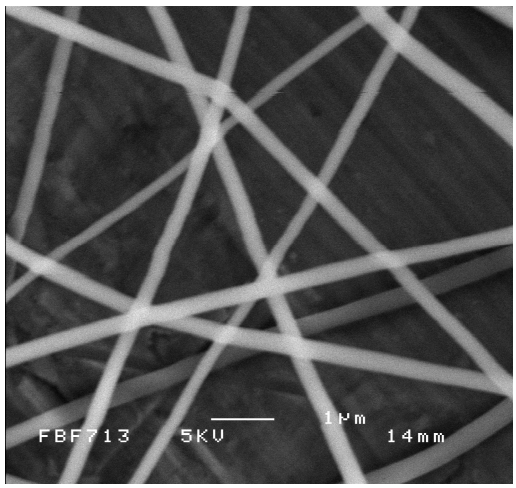

(d) S12: Voltage 17.2 kV

3.4 Electrospun Nanofibre Alignment

Uniaxially aligned PVA nanofibres have been produced by using rotating cylinder collection method. Fibre alignment using this method relies on the matching of the rate of fibre deposition onto the rotating target, and the linear velocity of the target, as discussed in section 2.3.5.2. Therefore, in the case of electrospinning PVA, aligned fibres were achieved due to the matching of velocities. The rotating cylinder diameter is 52.8 mm and nanofibres were collected on a piece of aluminium foil fixed onto the rotating cylinder surface. The PVA solution concentration used for this study was 8 wt/v % and the distance between the tip and the rotating cylinder was 20 cm. The applied voltage for this electrospinning process was 15 kV, the flow rate was 6 $\mu l.min^{-1}$ and the deposition time was 1 and 5 minutes respectively. Figure 3.16 (a) and (b) are the SEM images of the uniaxially aligned PVA nanofibres. Fibres collected after 1 minute of electrospinning show a relatively large separation distance, as shown in Figure 3.16 (a) whereas an increase electrospinning time reduces the average fibre spacing in Figure 3.16 (b). The results clearly show that the distance between the uniaxially aligned fibres is dependent on the deposition time with longer

deposition times giving larger density of aligned electrospun PVA fibres.

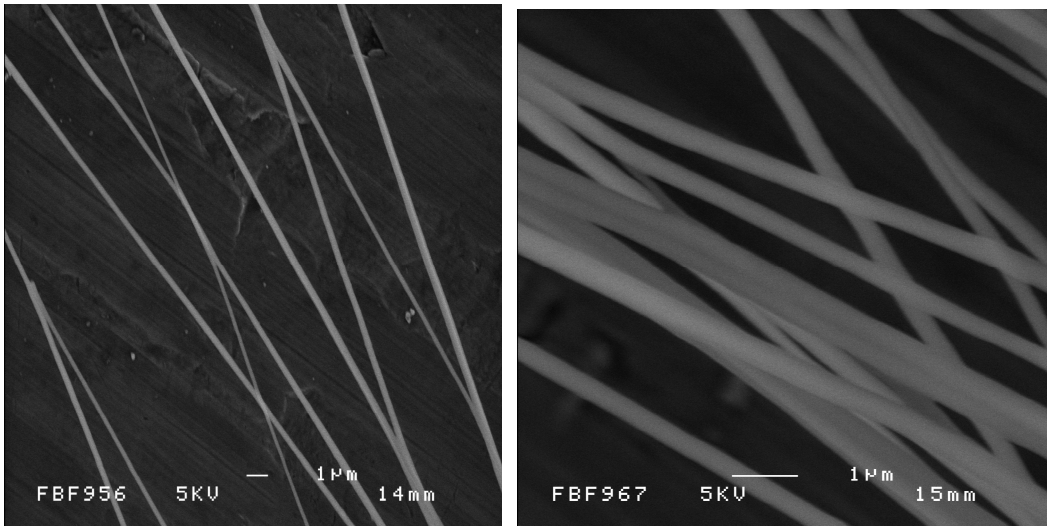

Figure 3.16 (a) PVA: 1 minute deposition **(b)** PVA: 5 minutes deposition

The distance between the needle tip and the rotating cylinder is critical because this is related to the level of the electrospun nanofibre drying. A small DTC value will not allow enough time for the solvent to evaporate for dry nanofibres. Therefore wet nanofibres produced with small DTC values may adhere with each other. Furthermore, the rotating speed will affect the amount of fibre entanglement for wet fibres. Electrospun PVA nanofibres entanglement at low rotating speeds as the fibres are not aligned preferentially in one direction. However, if the rotating speed is too high, the electrospun nanofibres will be stretched and can sometimes break. Therefore the rotating speed should be optimized and was estimated to be 4000 rpm in our work [193, 194].

3.5 Electrospinning of Polymer Nanofibres from Organic Solvent

Electrospinning of PVA and PEO has been successfully carried out by

optimization of solution concentration, applied voltage, flow rate and DTC. In particular, the flow rate and DTC appear to be almost material independent i.e. a flow rate of 1 $\mu m.min^{-1}$ and a DTC of 20 cm is effective at producing continuous electrospun fibres of regular diameter using both PVA and PEO solutions. However, all of the previous solvents used were inorganic, with the resultant fibres electrospun from semi-crystalline polymers. An additional polymer is defined here which is both soluble in organic solvents as well as having an amorphous structure to contrast with the previous partially crystalline PVA and PEO materials. Polycarbonate (PC) is selected as the final polymer electrospun and subsequent work in the following chapters contrast its low solubility in water and amorphous structure with the semi-crystalline PVA examined. The electrospinning parameter optimizations defined above for PEO and PVA are thus examined for PC, with applied voltage and solution concentration the only variables.

3.5.1 Polycarbonate

In 1898, German chemist Einhorn discovered polycarbonate when preparing cyclic carbonates using hydroquinone reacting with phosgene. This work was expanded later in 1902 when researchers Bischoff and Hedenstrom found out a similar cross-linked, high molecular weight polycarbonate [195]. Bayer Lab made the first linear thermoplastic polycarbonate of high molecular weight in 1953. Commercial production of PC (polycarbonate) by Bayer Lab and General Electric [195] followed soon after. Polycarbonates are thermoplastic polymer, having long molecule chains which are composed by linked carbonate groups (-O-(C=O)-O-). Figure 3.17 shows the chemical structure of polycarbonate. Polycarbonate has a good resistance against water with very low water absorption of 0.1 wt. % over 24 hours. In this study, polycarbonate with a typical molecular weight 11,000 $g.mol^{-1}$

has been used.

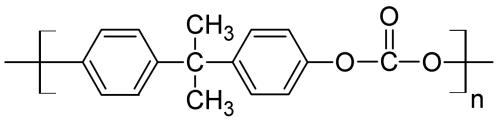

Figure 3.17 Polycarbonate chemical structure

3.5.2 Experimental Parameters Governing PC Nanofibre Morphology

A single needle electrospinning experimental set-up was used to produce PC nanofibres. Polycarbonate solutions were prepared by dissolving PC in chloroform. The solution was heated up to 60 ^{o}C and gently stirred for 8 hours to obtain various homogenous solution concentrations from 12 to 20 wt/v% using a stirring hot plate. These polycarbonate solutions were fed into a 10 ml syringe using a constant flow rate of 1 $\mu l.min^{-1}$ with a DTC of 20 cm. The applied voltage between the end of the syringe containing the PC solution and the grounded electrode was increased, as with the processing parameter investigations for electrospinning PEO and PVA, until expulsion of solution from the end of the syringe occurred. Electrospinning was typically observed to occur at applied voltages of 25 kV. Table 3.3 below summarizes the solutions used and the resultant material collected on the ground electrode.

Table 3.3 Different concentration and molecular weight PC solutions

Solution No	**PC Molecular weight (g/mol)**	**Pellet Weight (g)**	**Chloroform (ml)**	**PEO Solution Concentration (wt/v %)**	**Fibre Morphology**
14	11,000	12	100	12	Only Beads Structure
15	11,000	16	100	16	Fibres with Beads
16	11,000	20	100	20	Uniform Fibres

The solution that was most suitable for electrospinning PC fibres was found to be 20 wt/v% of the concentration. The solvents evaporate rapidly, resulting in polycarbonate fibres deposited on the ground collector (glass slide or silicon substrate), therefore an electrospun PC fibre network can be easily achieved after this process. Aligned electrospun PC fibres can also be achieved by using a rotating cylinder underneath the electrospinning needle. All the experiments were performed at room temperature (22-24 ^{o}C). SEM images confirmed these morphological results, with the optimal continuous fibres of regular diameter highlighted in Figure 3.18.

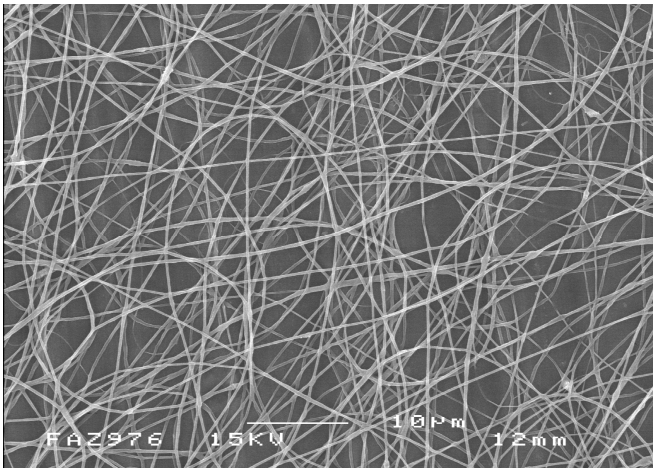

Figure 3.18 Electrospun Polycarbonate nanofibres

3.6 Conclusions

The electrospinning process and the electrospun fibre morphology is dependent on a number of experimental parameters, which include solution concentration, applied voltage, flow rate, conductivity, surface tension, polymer molecular weight and distance between the needle tip and the collector (DTC). Ultra fine polymer nanofibres have been produced by electrospinning a series of PEO and PVA polymer solutions. The results show that increasing the polymer concentration changes the resultant electrospun material from beaded structures, through nanofibres to progressively larger diameter fibres. Applied voltage also played a significant role for determining fibre morphology. For both PEO and PVA nanofibres, the average fibre diameters decreased with increasing applied voltage when electrospinning was in a stable cone-jet mode region, since the high electric field strength favours the formation of a thinner liquid jet in this mode. The study of electrospinning PEO further showed that the average fibre diameters can be increased if increasing the applied voltage above the cone-jet mode value. This diameter increase is due to the charged liquid jet being ejected from the

inside of the needle tip, allowing the removal of more liquid from the needle tip. The average electrospun fibre diameters could also be slightly increased with increasing the flow rates and the DTC. A DTC adjusted to a suitable value allows the nanofibres to dry sufficiently upon deposition. Finally, the solution composition is shown to be valuable in dictating the electrospun fibre diameter. An increase of water volume fraction will increase the polymer solution surface tension, resulting in a decrease of electrospun fibre diameter. Increasing solution viscosity decreases the beads density and further prevents bead formation. Therefore, the solution properties such as concentration, viscosity, conductivity and surface tension are the main factors influencing the electrospinning process.

The alignment of electrospun nanofibres can be achieved by using a rotating cylinder collector. The rotating cylinder speed should match the nanofibre production speed to optimize the alignment process. Density and separation distance of the uniaxially aligned nanofibres will depend on the deposition time. The separation of electrospun fibres is particularly useful in future experiments where isolation of individual fibres is required for direct fibre surface property measurements.

Chapter 4

Surface Properties of Electrospun Polymer Fibre Aggregates

4.1 Introduction

This chapter details the surface properties of electrospun fibre aggregates using conventional, and macroscopic, contact angle wetting measurements using water. Complex surface geometries often related to material roughness is used to evaluate the wetting behaviour of electrospun fibre aggregates, also referred to as fibre mats. Indeed, considerable research has focussed on the formation of superhydrophobic surfaces utilizing both the chemical composition of surfaces and geometric effects. The surface properties of electrospun fibres are therefore examined with the potential to exploit the fibres through enhancing hydrophobic behaviour. While the previous chapter examined how a range of polymer fibres can be produced from electrospinning, this chapter focuses on the use of polycarbonate (PC) fibres due to i) the insolubility of PC in water that allows standard wetting measurements with water to be performed without changing the fibre geometry and ii) the chemical structure of PC is generally expected to be more hydrophobic than the other polymers of PEO and PVA that are also routinely produced. In this study, a surface was produced by electrospinning a network of

polycarbonate fibres in order to produce a surface that can be considered as rough. Characterization and analysis of PC electrospun fibre and PC film surfaces were carried out to compare surface roughness with wetting contact angle. Analytical models are then used to describe hydrophobicity in terms of this roughness.

4.2 Background and Aims

A number of works within the literature have examined surface geometry in order to explain the resultant wetting behaviour with water droplet. To achieve a superhydrophobic surface, Lau et al. have demonstrated the creation of a superhydrophobic surface in a vertically aligned carbon nanotube forest with a hydrophobic polytetrafluoroethylene (PTFE) coating on the nanotube's surface [188]. The PTFE increased the hydrophobicity of the carbon nanotubes, illustrated through the relatively low PTFE surface energy of 18 mJm^{-2}, in addition to the large aspect ratio of the nanotube fibre arrays that approximated to an extremely rough surface [196]. Superhydrophobicity was shown when micrometer sized spherical water droplets were suspended on top of the nanotube forest, as shown with SEM images of carbon nanotube forests in Figure 4.1. Figure 4.1 (a) shows the as-grown carbon nanotube forest with nanotube diameter of 50 nm and a height of 2 μm, Figure 4.1 (b) shows PTFE-coated forest after HFCVD treatment, and Figure 4.1 (c) shows an essentially spherical water droplet suspended on the top of the PTFE-coated forest [196]. The same principle was demonstrated by Huang et al using a superhydrophobic surface of aligned carbon nanotubes coated with a thin layer of zinc oxide (ZnO) film [197].

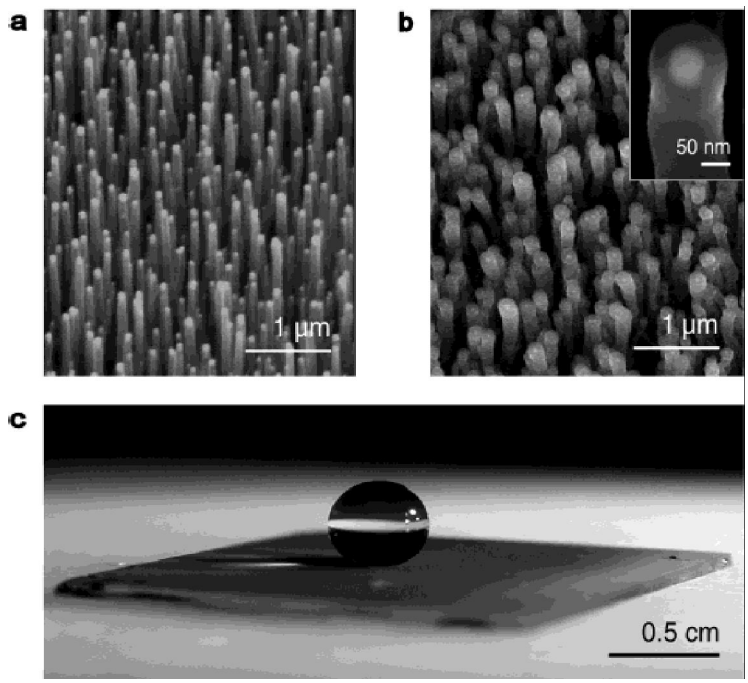

Figure 4.1 SEM images of carbon nanotube forests. **(a)** As-grown forest with nanotube diameter of 50 nm and a height of 2 μm, (b) PTFE-coated forest after HFCVD treatment, and (c) an essentially spherical water droplet suspended on the PTFE-coated forest. [196]

Nanofibre networks of other materials as opposed to carbon nanotubes have also been used to create superhydrophobic surfaces. Han et al have demonstrated a coaxial electrospinning process with poly(ε-caprolactone) (PCL) as a core material and a low surface free energy Teflon AF fluoropolymer as a shell material [198]. The PCL provided a structural fibre whereas the Teflon shell, effectively a coating for the PCL, providing the surface layer. Water droplets on these electrospun fibre surfaces effectively formed large contact angles due to the presence of the Teflon. However Feng et al [199] have shown that the production of a nanofibre mesh of PVA using a template extrusion process gives a water contact angle of 171.2 ± 1.6°, as shown in Figure 4.2 (b), when compared to a water contact angle of 72.1 ± 1.1°, as shown in Figure 4.2 (a), on a smooth PVA

film surface. This result is therefore surprising as the PVA is clearly a hydrophilic surface due to the water contact angle being less than 90°. The authors considered that an increase in the surface roughness of a polymer can increase the contact angle using arguments related to Wenzel's equation. However, Wenzel's equation indicates that a hydrophobic surface becomes more hydrophobic with roughness but, conversely, a hydrophilic surface becomes more hydrophilic with increased roughness. The observation by Feng et al is therefore counter to this. The authors examined the chemical structure of the PVA nanofibres and found that the surface of the fibres were actually hydrophobic due to a reorientation of the PVA backbone causing the hydrophilic alcohol groups to point away from the surface. The polymer processing is therefore critical in defining the wetting behaviour of a surface [199].

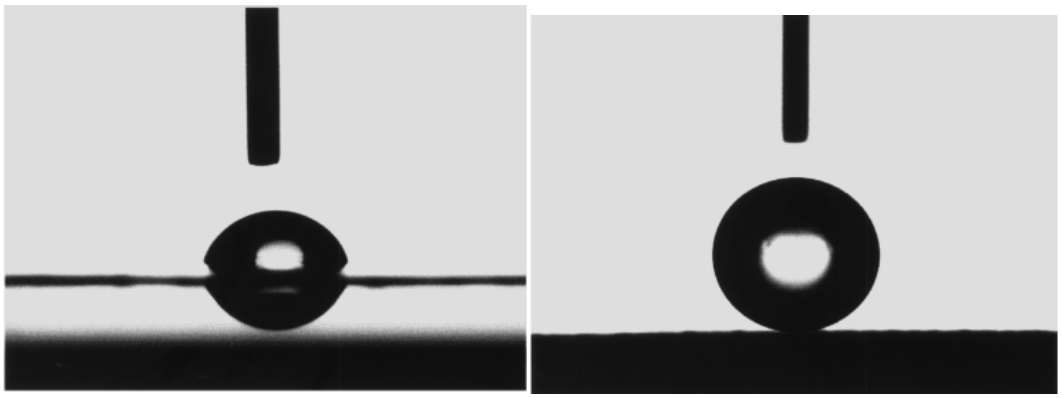

Figure 4.2 (a) Water contact angle of a PVA film with a smooth surface [199] **(b)** Water contact angle of synthesized PVA nanofibres with a rough surface [199]

In order to examine the effects of a triple (composite) interface between a liquid droplet and electrospun fibre network, a range of different fibre geometries are used in this work to examine the wetting properties of electrospun polymer fibres. These geometries consist of electrospun fibres aligned as a forest vertically to the collected substrate, analogous to the carbon nanotubes detailed above, and

electrospun fibres that are parallel to the collector plate. Both of these fibre orientations explore the possibility of a porosity existing between the fibres in order to develop an increased surface roughness to enhance the hydrophobicity of PC.

4.3 Experimental Details

4.3.1 Materials Manufacturing Process

Electrospun fibres of PC were produced from solution number 16 as described in section 3.5.2 in Chapter 3. The PC fibres were collected onto clean glass microscope slides. In order to produce different surface geometries, electrospinning was performed at relatively small spinning times of 15 and 30 seconds. This allowed the deposition of electrospun fibres on the glass slide surface with different fibre spacing. Collection times above 30 seconds tended to increase the fibre mat thickness and not the fibre density. PC films were produced in order to compare the effects of geometry on wetting behaviour of PC. PC is of prime importance in this comparison as the amorphous PC structure will show little structural differences between films and fibres, whereas PVA and PEO will be structurally heterogeneous due to different levels of crystallinity during the processing of films and electrospun fibres.

The PC films were made from Lexan 121R polycarbonate by Sabic Innovative plastics (formerly GE plastics) using a Collin E-20T single screw extruder fitted with a 100 mm wide slot die. The die orifice was adjusted via an adjustable die lip to a thickness of 0.2 mm. The polycarbonate resin was dried for 4 hours at 120˚C prior to extrusion. The extruder from throat to die consists of five heating zones with the hopper being water cooled to prevent bridging. A gradient temperature

profile was used 270˚C, 280˚C, 290˚C, 295˚C 300˚C, where the hottest zone is the die. The extrudate was quenched on Collin CR 52-T chill rolls with temperature controlled rolls. The roll temperature was set to 25˚C. After purging for 30 minutes a clear colourless and consistent extrudate was produced. This was wrapped around the chill rolls to facilitate rapid heat transfer from the melt and solidification. The solid extrudate (PC films) were then spooled onto a roll.

4.4 Characterization Techniques

Electrospun fibrous material was examined using Scanning Electron Microscopy (SEM), with its operation detailed in section 3.2.4.1. Evaluating the wetting behaviour of polymers with water was carried out using optical microscopy and contact angle measurement, which will be introduced in the following sections.

4.4.1 Optical Microscopy

A Meiji binocular microscope and Olympus BX60 microscope have been used for the characterization of electrospun PC fibre network before contact angle measurement, as shown in Figure 4.3. The electrospun fibre networks were prepared by collecting PC fibres onto clean glass slides for 30 seconds and 15 seconds during the electrospinning process. The resolution for this type of microscopy is relatively low and can only examine the sample at the micrometer level.

(a) (b)

Figure 4.3 Optical Microscopy **(a)** Meiji Binocular; **(b)** Olympus BX60.

4.4.2 Contact Angle Measurement

Section 2.4.6.1 described how a goniometer can be used to measure the contact angle of a liquid on a solid surface. A high resolution camera and software capture the contact angle image in this device, which is called contact angle meter or goniometer. In this study, we used a KSV system (KSV Instruments Ltd, Finland) and CAM 100 software, which is window-based and developed by KSV instruments to measure the contact angle, as shown in Figure 4.4 [200]. The system consists of three main components which are syringe, high resolution camera and operation software. The syringe ejects a tiny liquid water droplet onto the specimen surface that is to be measured. An outline of the liquid droplet on the surface is captured by the high resolution camera. All the information obtained by the camera is transferred to the software, which fits a droplet shape to the collected image in order to calculate the contact angle of liquid on the specimen surface. This system contact angle measuring range is from 0 to 180 degrees and contact angle error is +/- 0.1 degrees. The maximum sample size can be unlimited x 150 mm x 50 mm (Length x Width x Height) and the minimum frame interval is 100 ms.

Figure 4.4 KSV CAM 100 contact angle meter [200]

The measurement of a liquid droplet's contact angle with a specimen's surface was achieved by first filling the syringe, which is fixed above the sample stage, with the probe liquid. The camera was adjusted to allow imaging of the droplet along the horizontal plane, giving a 'side view' of the droplet. The specimen was placed on the sample stage and a single droplet of the probe liquid was dispensed from the syringe, which fell onto the sample's surface. The CAM 100 software was used to record the liquid droplet contact angle on the solid surface. In our experimental study, 20 images were taken by the camera for each specimen over a range of times extending from the time when the droplet initially contacted the sample to a few minutes. Contact angles values were determined from the equilibrium droplet contact angle, defined by when the contact angle does not change with time. Figure 4.5 shows image of the software for measuring the liquid droplet contact angle on the specimen surface. The horizontal line, which is

red in Figure 4.5, should be on the plane of the solid-liquid interface. The Windows-based KSV CAM software fits the measured droplet profile with the Young's equation to calculate contact angle and surface tension. Two kinds of electrospun PC fibre network with 15 seconds and 30 seconds deposition respectively and a PC film were characterized by using this technique for comparison of their contact angles.

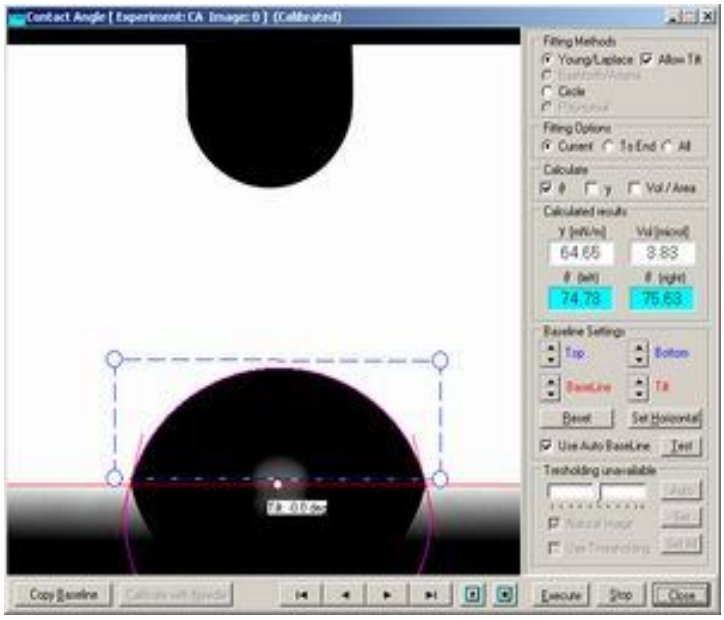

Figure 4.5 KSV CAM Software Image of water droplet on a sample surface [200]

4.5 Results and Discussion

4.5.1 Vertically Aligned PC Fibre Networks

In order to investigate polymer nanofibre wetting properties, an experiment was designed where water was dropped onto the top of a vertically aligned polymer nanofibre 'forest' network. The wetting dictates if the water droplet remains on the top surface of nanofibre forest, indicating hydrophobic or superhydrophobic

behaviour if a composite liquid-air-solid interface forms, as shown in Figure 4.6 (a), or water infiltrates between the fibres of the forest, as shown in Figure 4.6 (b).

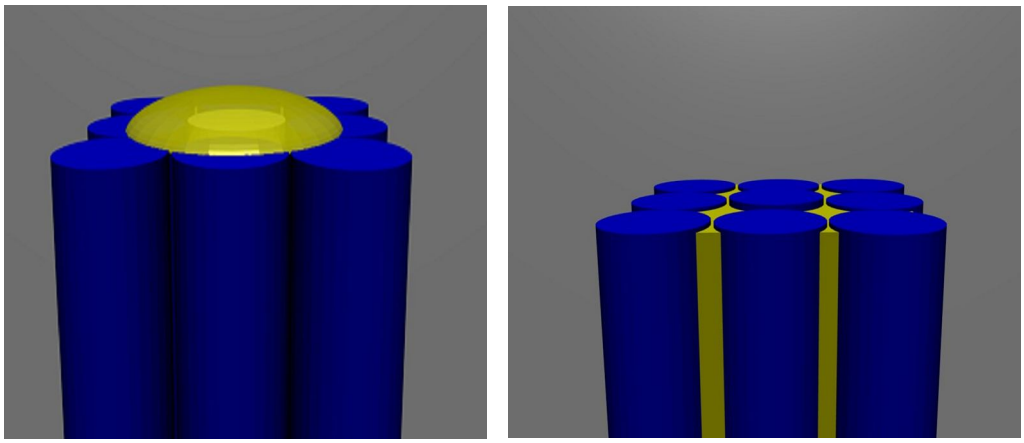

Figure 4.6 (a) Water Droplet sit on the top of nanofibre forest **(b)** Water droplet penetrate into the voids of nanofibre forest

In order to demonstrate the above designed experiment and create a superhydrophobic surface using our electrospun polymer fibres, aligned polycarbonate fibres were used for this study. Initial experiments attempted to recreate the superhydrophobic carbon nanotubes forests using vertically aligned electrospun PC fibres. A cryo-microtome was used to cut the aligned PC fibres after the electrospinning process. Comparing to carbon nanotubes, polycarbonate fibres are more ductile and our SEM results show the fibre ends bend after cutting, as shown in Figure 4.7 (a) and (b). Although we can see the cross sections of the PC nanofibres, their fibre directions changed considerably after cutting and cannot form vertically aligned nanofibre forest successfully. These results indicate that polycarbonate is not suitable for the demonstration of the vertically aligned fibre assemblies due to the much lower elastic modulus of the polymer fibres when compared to carbon nanotubes that causes extensive bending during cutting preparation.

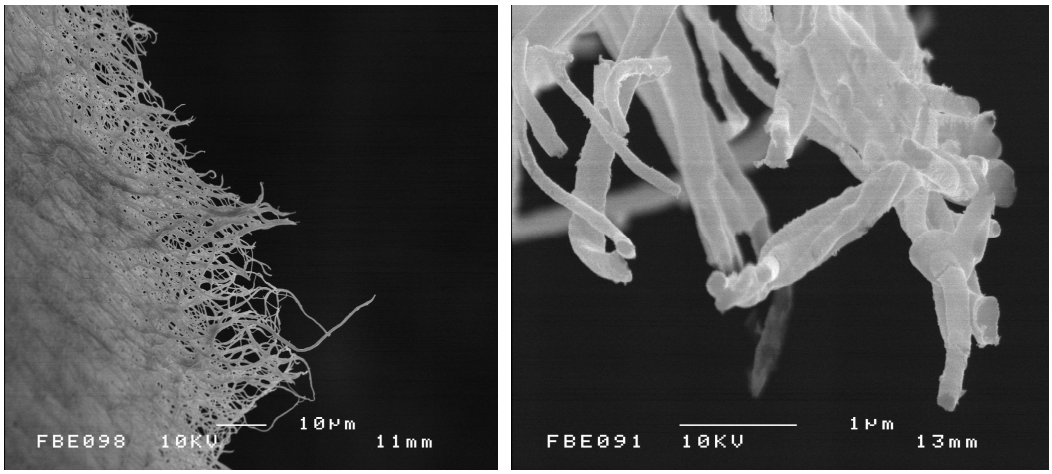

Figure 4.7 (a) Aligned PC fibre ends **(b)** Evidence for considerable damage and bending at the end of the PC fibres during cutting

4.5.2 Electrospun PC Fibre Network

As discussed in section 2.4.7, roughness can affect contact angle, in terms of increasing the area of the solid-liquid interface in Wenzel model, and formation of composite liquid-air-solid interface in Cassie-Baxter model. Therefore roughness has a great influence in producing hydrophobic surfaces. Using this information, electrospun polycarbonate fibre network surfaces have been selected to study their roughness structure and related surface properties. Electrospun PC nanofibre networks with two different deposition times of 30 seconds and 15 seconds are characterized herein by using optical microscope and SEM. The purpose for differing samples by electrospinning time is to obtain different surface roughness and porous structure of the PC fibre network surface. The electrospinning time can influence the porosity of electrospun fibre network which subsequently affects roughness of the surface. From optical image in Figure 4.8 (a) and SEM image in Figure 4.9 (a), the fibre network was achieved by electrospinning deposition time of 30 seconds, and fibre network in Figure 4.8 (b) and 4.9 (b) was achieved by

electrospinng deposition time of 15 seconds. The PC fibre network after electrospinning for 15 seconds has more porous structure comparing to the network obtained from 30 seconds deposition, as expected. Therefore, a smaller deposition time gives surface structure with a relatively large pore size.

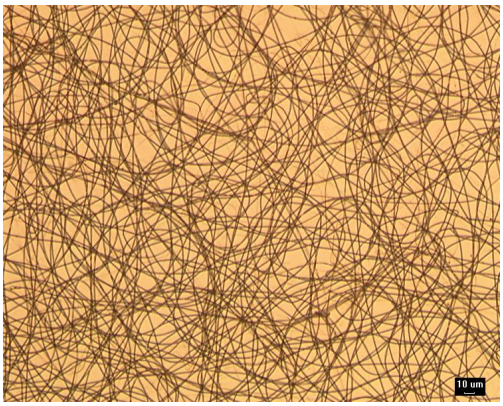

Figure 4.8 (a) Optical image of PC fibre with 30 seconds deposition

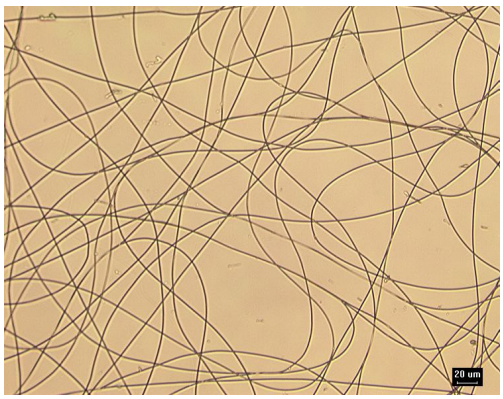

(b) Optical image of PC fibre network network with 15 seconds deposition

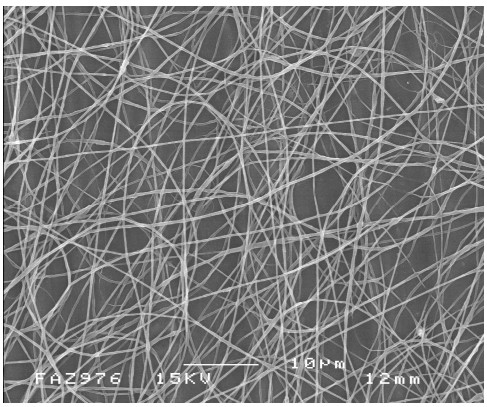

Figure 4.9 (a) SEM image of PC fibre network with 30 seconds deposition

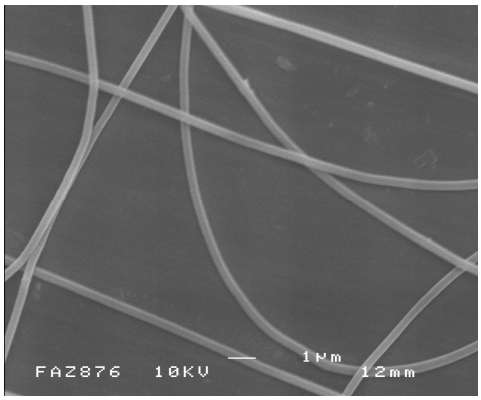

(b) SEM image of PC fibre network with 15 seconds deposition

Representative optical images of water droplets on the two PC electrospun fibre networks and a smooth PC film is shown in Figure 4.11 (a), (b) and (c). The contact angle values for these three samples were calculated by KSV CAM software and 20 values were taken for each of the three samples giving the mean

value of their water-PC contact angle. From our experimental study, water contact angle on smooth PC film surface was calculated as 85 ± 0.6°, as shown in Table 4.1, and this value is in a good agreement with a literature value of 85° [201]. Also from Table 4.1, electrospun PC fibre network with 30 seconds deposition gives a water contact angle of 122 ± 0.7°, and electrospun PC fibre network with 15 seconds deposition gives a water contact angle of 159 ± 0.6°. These results have shown that superhydrophobic polycarbonate fibre surface can be created by the electrospinning process. For comparison, the water contact angle on a glass slide without any PC fibres is also shown in Table 4.1 and indicates a much smaller wetting angle indicative of a hydrophilic glass surface. Qualitatively, these water contact angles suggest that the water droplet is in contact with the PC fibres when spun onto the glass slide due to the large contact angle >90°, with the hydrophilic glass surface contributing little to the surface's wetting behaviour. In order to explore the wetting behaviour of the electrospun PC fibres on the glass surface further, Wenzel and Cassie-Baxter models as introduced in section 2.4.7 are used to describe these surfaces in terms of roughness.

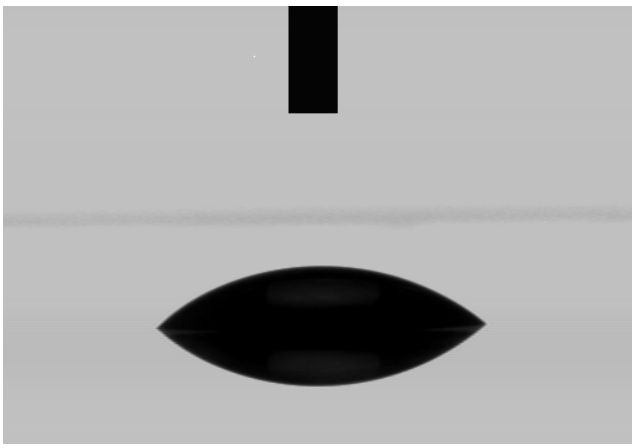

Figure 4.10 Water contact angle on glass

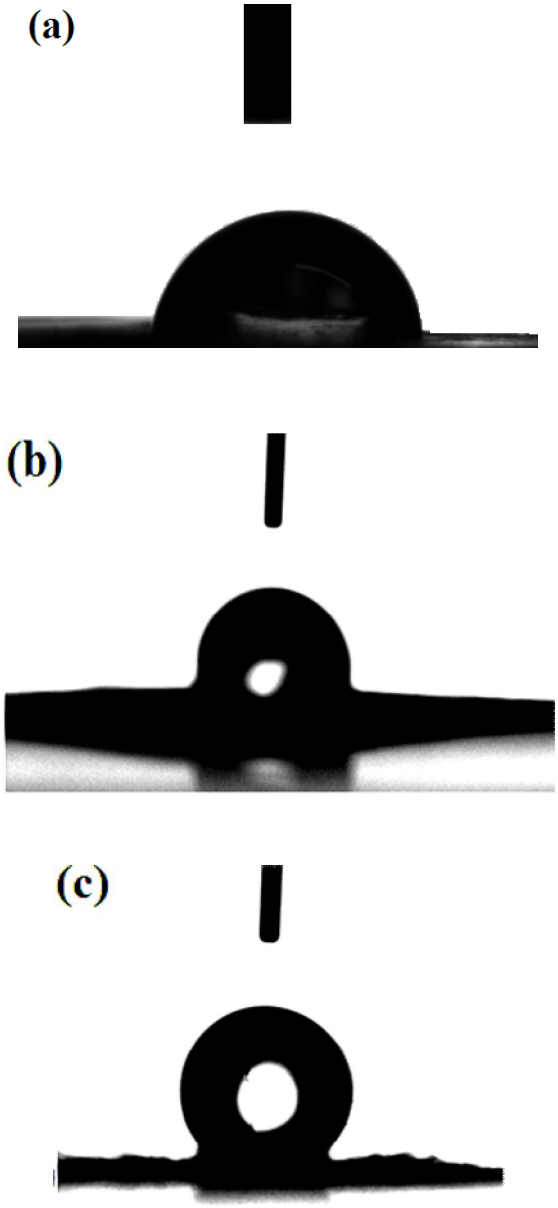

Figure 4.11 Optical images of **(a)** Water droplet on a smooth PC film, **(b)** Water droplet on electrospun PC fibre network with 30 seconds deposition, **(c)** Water droplet on electrospun PC fibre network with 15 seconds deposition.

Table 4.1 Contact angle values for water, PC film and PC fibre networks

	Glass	**Smooth PC Film**	**PC Fibre Network (30 seconds deposition)**	**PC Fibre Network (15 seconds deposition)**
Contact Angle	$32 \pm 0.6^{\circ}$	$85 \pm 0.6^{\circ}$	$122 \pm 0.7^{\circ}$	$159 \pm 0.6^{\circ}$

The Wenzel model considers a liquid droplet contacting completely with a solid surface, excluding the formation of composite interface. The contact angle is determined by equation 2.37 thus:

$$Cos\theta = R_f Cos\theta_0$$

where θ is the contact angle of rough surface, θ_0 is the contact angle of smooth surface and R_f is the roughness factor. As analysed in section 2.4.7.1, the roughness can reduce the contact angle of the rough solid surface if the smooth solid surface is hydrophilic or increase the contact angle of the rough solid surface if the smooth solid surface is hydrophobic. Our experimental results show that the water contact angle for smooth polycarbonate surface is $85 \pm 0.6^{\circ}$. Therefore according to Wenzel model, the roughness can enhance the wetting property for rough surfaces. However, in this experiment, it was shown that the water contact angle for the rough polycarbonate surfaces were increased as shown in Table 4.1, comparing with smooth film surface of $85 \pm 0.6^{\circ}$. Therefore, the Wenzel model is not suitable to explain our experimental results in this study. Figure 4.11 (b) and (c) have also shown that the water droplets did not penetrate into the electrospun fibre cavities but is sitting above the fibre networks with a large contact angle of 122° and 159°.

An improvement over the Wenzel model can be provided by the Cassie-Baxter model, with a composite liquid-air-solid interface increasing hydrophobicity of a rough surface, as discussed in section 2.4.7.2. Figure 4.9 and 4.11 (b) and (c) also show that the electrospun PC fibre network surfaces are rough enough that air can be present in the voids between individual electrospun PC fibres. Therefore, the surface of the electrospun PC fibres network can be regarded as a composite surface consisting of nanofibres and air. To thoroughly understand the hydrophobicity of the PC nanofibre surfaces, theoretical considerations are necessary. The contact angle on a composite interface can be expressed by the Cassie-Baxter model as [202]:

$$Cos\theta = f_1 Cos\theta_0 - f_2 \qquad (4.1)$$

where θ and θ_0 are the water contact angles on a rough surface and smooth surface, respectively, i.e. the PC film and fibrous networks in this study. f_1 and f_2 represent the fractions of the solid surface (i.e. the electrospun fibres) and air in contact with the liquid respectively. Thus $f_1 + f_2 = 1$. Equation 4.1 simply deduces that increasing f_2 increases the contact angle θ, indicating that a large fraction of entrapped air within the PC fibres gives a resultant increase in contact angle. In order to assess the validity of equation 4.1, a method to evaluate the fraction of fibres in contact with the liquid droplet, or the fraction of air gaps in the mesh, needs to be made. If we assume that the spacing between the electrospun fibres is similar across all parts of the electrospun film, a calculation of the areas fraction of PC fibres can be found from Figure 4.8 and Figure 4.9. Image J software was used to evaluate the area fraction of fibres in Figure 4.8 by assuming that all the relatively dark areas in the image correspond to fibres and Figure 4.9 by assuming that all the relatively light areas in the image correspond to our electrospun fibres. This software measures objects in binary or threshold images by scanning the

image until the edge of each fibre are found. The fibres are outlined and filled by the software to make them indistinguishable, then resumes scanning until it reaches the end of the image. The area fraction of fibres from our optical images and SEM images was found to be 0.45 ± 0.02 for 30 seconds of electrospinning and 0.07 ± 0.01 for 15 seconds of electrospinning. The calculated fibre area fraction f_1 were compared to area fraction values calculated from equation 4.1 using contact angle values in Table 4.1. The calculated fibres area fractions are found to be $f_1 = 0.432$ for 30 seconds of electrospinning and $f_1 = 0.061$ for 15 seconds of electrospinning time. These calculated values are similar to the measured values from optical microscopy.

In order to test if the Cassie-Baxter model is sufficient to describe the electrospun fibre mats, a plot was made showing the relationship between f_1 and $Cos\ \theta$ (Figure 4.12). The plot shows two theoretical lines corresponding to the expected contact angle for a glass surface and PC surface containing differing roughnesses, expressed as the solid area fraction f_1 calculated using equation 4.1. Experimental data of the water contact angle on the two different electrospun PC fibre mats is also shown in Figure 4.12. The experimental data shows a good fit to the theoretical line for a rough PC film surface. This fit indicates that the electrospun fibrous PC mat behaviour as a rough surface and is accurately described by the Cassie-Baxter model. The applicability of the water contact angle on the PC film relative to the glass surface indicates that the water droplet is exclusively in contact with the electrospun PC fibres in Figures 4.11 (b) and (c), with the glass slide substrate playing no part in dictating the resultant contact angle. Furthermore, we can conclude that more entrapped air gives more porosity and surface roughness to create a superhydrophobic surface. Our observations and analysis above show that the contact angle values become smaller as the electrospun fibre density increases. This is because the liquid-air interface area f_2 for more porous

surface is relatively larger than the area of less porous surface. Therefore, a superhydrophobic PC fibre surface is created and experimentally proved by increasing the roughness of the electrospun fibre network surface. This method of increasing the hydrophobic behaviour of a surface is highly desirable using electrospun fibres as the surfaces can be rapidly and easily covered, in contrast to other methods such as the production of nanofibre forests that require careful control and growth of fibres in a preferential direction.

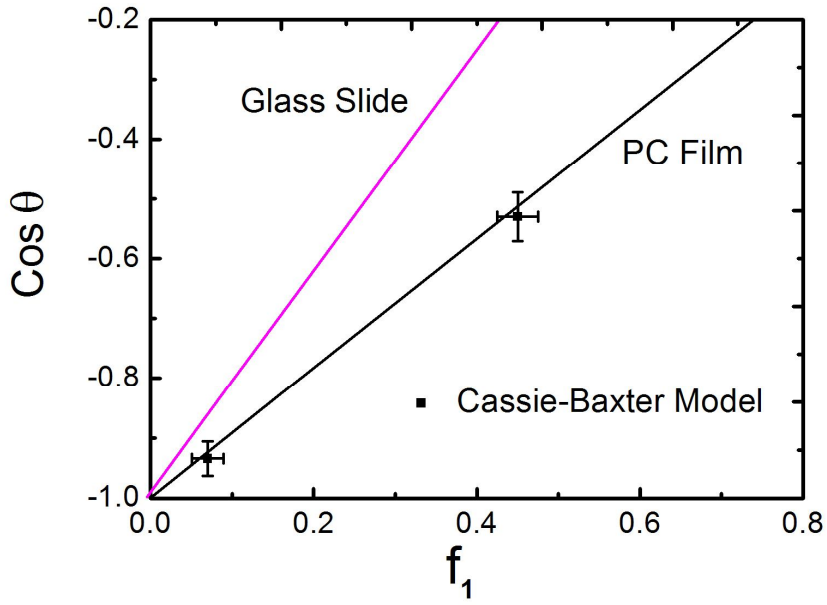

Figure 4.12 Plot of experimental data relationship between f_1 and *Cos* θ. Two theoretical lines are shown representing the contact angle θ expected for a range of fibre fractions (f_1) using equation 4.1. The two lines differ by considering that the contact angle on the flat surface θ_0 of a continuous PC film or glass slide.

4.6 Conclusions

Superhydrophobic polycarbonate fibre surfaces have been successfully created from single needle electrospinning process by increasing the surface roughness and apparent porosity through spacing between the electrospun fibres. The

changes in the surface roughness are therefore geometric rather than a function of a surface treatment applied to the polymer surface. Electrospun PC fibres can produce a superhydrophobic surface, with a relatively high contact angle of 159°. Our experimental results show the water contact angle increases with apparent roughness as described using a Cassie-Baxter model, where composite liquid-air-solid interface was formed and thus enhanced hydrophobicity of the surface. Image J software was employed in this study to calculate the area fractions of fibres in contact with the liquid droplet (f_1) and plot of f_1 vs $Cos\ \theta$ shows that Cassie-Baxter model is the correct for describing the wetting of electrospun PC fibre networks. Therefore nanostructures are applicable in producing superhydrophobic surfaces with high water contact angles.

Chapter 5

Measurement of Individual Electrospun Fibre Surface Free Energy using Contact Mechanics

5.1 Introduction

The properties of solid material surfaces are historically investigated using contact angle measurements. The previous chapter used water contact angles to understand the wetting behaviour of a composite surface notably consisting of electrospun polymer fibres. However, contact angle measurements use a probe liquid, such as water, that covers a considerable surface area relative to the electrospun fibres themselves. Thus, these contact angle measurements cannot examine the surface properties of the polymer fibres themselves. This limitation in contact angle measurements is restrictive as the surface behaviour of polymers processed from electrospinning methods cannot be compared to bulk polymer behaviour. A direct method for understanding the surface properties of individual electrospun fibres is presented in this chapter and comparisons with bulk samples made. Atomic force microscopy (AFM) is a particularly powerful method for examining individual electrospun fibre surface properties as samples can be both imaged and adhesion properties between the AFM tip and sample elucidated. In addition, the surface

properties of electrospun polymer nanofibres and their larger equivalents are related to structural organization. This structural organization is particularly important for electrospinning as potential ordering of polymer chains, as achieved in conventional polymer fibre processing described in section 1.1.3.2, increases anisotropy and may produce significant changes in surface behaviour when compared to bulk isotropic polymers. This chapter introduces contact mechanics adhesion methods to accurately measure the surface free energy of individual electrospun nanofibres of a semicrystalline polymer of PVA and amorphous PC. PEO was not selected as its high solubility in water can potentially form a gel-like layer on the surface of the polymer fibres easily such as in reasonably humid environments, which may influence surface adhesion measurements.

5.2 Experimental

5.2.1 Sample Preparation

The surface properties of electrospun fibres of PVA and PC as well as equivalent bulk films were examined. The bulk films were drawn to a different draw ratio (λ) in order to compare the effects of molecular alignment in a film to the potential orientation that may occur in the electrospinning process. Massardier et al. have found out that the effect of draw ratio on increasing molecular alignment is significant, such as the chain alignment and crystallinity in poly(phenylene vinylene) (PPV) films increase with film draw ratio [203].

Poly(vinyl alcohol) (PVA) with an average molecular weight of 98,000-143,000 $g.mol^{-1}$ was used for producing films and electrospun fibres. PVA solutions were prepared by dissolving the polymer in distilled water 80-90°C and gently stirred for

2-3 hours. The PVA solutions were cast into a Petri dish and degassed in a vacuum oven. Resultant PVA films were dried at room temperature, peeled off the Petri dish and dried in a desiccator. As electrospinning was expected to provide some degree of orientation at the fibre surface, films were drawn in order to induce molecular orientation and provide bulk equivalents to the electrospun fibres. The films of PVA were clamped between two grips on an Instron machine and heated to 130 $^{\circ}$C using an environmental chamber fitted around the sample. The film was then pulled in tension at this temperature in order to induce molecular alignment from the drawing process. The draw ratio (λ) was defined as the ratio of the film length in the drawing direction after and before the drawing. Oriented films of draw ratio from 1 to 5 were prepared by this solid-state drawing, with the PVA film tending to fail above λ values of 5. Thus, a larger draw ratio indicates thinning of the film and more polymer chain ordering along the drawing direction.

The PVA solutions used to generate electrospun fibres in the studies here were prepared following the procedure as described in section of 3.2.2.2. The experiments of electrospinning were carried out according to the previous works in Chapter 3 using solution numbers 12 and 13 to give fibres of varying diameters. For subsequent AFM measurements, pure silicon substrates were used to collect the as-spun fibres and the collecting time was short (~10 s) to obtain individually separated polymer fibres. All the experiments were performed at room temperature.

Polycarbonate (PC, M_w=11000 g.mol^{-1}) was used to produce PC films and electrospun PC fibres. PC was selected because of its amorphous structural homogeneity. Films were manufactured by extruding a PC injection-molding mass through an extrusion die followed by air-cooling as described in section 4.3.1. Polymer chain alignment within the films was achieved by cold drawing as has been shown previously [204]. A series of polymer films with differing draw ratio

were produced up to a maximum draw ratio of 2 achieved before failure of the film. PC electrospun fibres were prepared from a 20 %wt.vol^{-1}mass dissolved in a solvent of chloroform as described for solution number 16 in Chapter 3. Electrospinning gave solid fibres with an average diameter of 750±50 nm, which were collected on the grounded plate of silicon.

5.2.2 Methods

5.2.2.1 Atomic Force Microscopy (AFM)

AFM History

Atomic force microscope (AFM) is the most versatile microscopy in the family of scanning probe microscopes (SPMs). Scanning probe microscope generated in the early 1980s when Binnig and Rohrer developed microscopy from the discovery of the scanning tunnelling microscope (STM) [205], and were subsequently awarded the Nobel Prize in physics in 1986. STM is the first member of the large probe microscopes family and measuring tunnelling current between a material surface and a sharp probe as the probe is scanned over the surface. STM is similar to an earlier instrument called a Topografiner, created by Yong [206], but had much higher resolution than the topografiner due to STM monitoring electron tunnelling especially from one atom at the end of a probe to a conducting surface. Both Topografiner and STM were limited to electrically conducting samples required for electron tunnelling. Therefore Binning and his colleagues replaced the electron tunnelling from a sharp tip of STM with the cantilever approach of atomic force microscopy (AFM), which can image electrically insulating materials, most notably polymers [205]. Commercial AFM instruments have been available from

1988 with many developments and new modes of operation devised for AFM. Additional AFM operation where the measurement of forces and not imaging is sometimes referred to as scanning force microscope (SFM) [205].

AFM Principles

AFM uses a solid probe that is kept in a close contact with material surface through a feedback mechanism while it scans over the surface. Various probes have been used and the most commonly used are microfabricated silicon (Si) or silicon nitride (Si_3N_4) cantilevers, typically 100 μm long, tens of microns in width and a few microns in thickness. An integrated tip at the end of the cantilever is used to scan over and interact with the sample's surface. The AFM tips are usually sharp to provide high lateral imaging resolution, with tip radius describing the sharpness of the tip and often ranging from 5 nm to 20 nm. The probe moves at the same probe-sample surface distance and this is taken to be the surface topography. Forces acting on the AFM tip cause the cantilever to bend, with this cantilever bending commonly monitored by an optical lever [207] as shown in Figure 5.1 (a). The optical lever contains a laser focused on the back of the cantilever and reflected onto a photodetector. This system can significantly magnify the cantilever bending and is sensitive to cantilever bending deflection movement over the order of a nanometer. The operation of the cantilever and subsequent signal used to describe the AFM tip-sample interaction defines the imaging mode used. In the simplest mode, known as contact mode, the AFM probe is in hard contact with the sample so that the cantilever bends away from the surface due to a net repulsion between the probe and sample surface. The repulsion between the probe and the sample is maintained as the probe is scanned over the sample surface in the x-y plane. Controlled movement of the AFM probe or sample in the x-y axis in provided by scanning piezoelectric materials [208]. Maintaining the AFM probe-sample

interaction is also achieved by piezo movement in the z-axis, normal to the samples surface. Thus, a set of 3-dimensional coordinates (x, y, z) is generated to give an image of the sample's surface topography [209, 210]. The action of maintaining the repulsive interaction between the AFM probe and sample is provided by a feedback system. In this feedback, the cantilever deflection signal is set at a required value known as the setpoint. The feedback loop constantly records the cantilever deflection during AFM probe scanning and adjusts the z-piezo in order to maintain the setpoint value. AFM images can be affected by hysteresis of the piezoelectric material scanner especially as the movement of the piezo often suffers from creep. However, AFM closed loop system are designed to have better dynamic performance and significantly reduce piezo hysteresis by monitoring creep of the piezoelectric material positions and correcting for this creep in a feedback system. AFM resolution in z height can be sub-Angstrom, whereas lateral resolution can be of the order of 1 nm. In order to achieve such high resolution, the state of the sample surface, the levels of acoustic and electronic noise, and experimental conditions should be greatly optimised [210].

Oscillation of the cantilever is used to examine attractive interactions between the AFM probe and sample surface, in contrast to contact mode where repulsion is considered. Oscillation of the cantilever at its resonance frequency f_0 produces a resultant amplitude. Monitoring of the amplitude signal can be used to image a surface in a similar manner to that of cantilever deflection for contact mode imaging. Proximity of a sample's surface to the AFM probe at the end of the oscillating cantilever will cause a reduction in the amplitude at f_0. Thus, a setpoint can be defined for selection of a suitable amplitude signal. The oscillating AFM probe typically operates within the attractive regime of a Lennard-Jones type van der Waals interaction curve as shown in Figure 5.1(b) with a relatively low setpoint, corresponding to an increased tip-sample interaction, allowing the tip to

periodically contact with the samples surface in a semi-contact mode. A higher setpoint indicative of a smaller shift in the cantilever oscillation relative to a freely oscillating cantilever causes little or no contact with the sample's surface as is known as non-contact mode. Scanning of the AFM probe or sample in the x-y plane while maintaining the setpoint value can also produce a sample topography image. The dimensions of the AFM cantilever are often critical in the imaging mode, with low spring constant cantilevers used for contact imaging, thus ensuring relatively low contact pressures, whereas higher spring constants with better resonance characteristics used for semi-contact imaging [211, 212]. It is important to note that all of these imaging modes can be conducted in a range of environments such as in air, vacuum, other gases and liquid environments and therefore has distinct advantages over SEM or TEM.

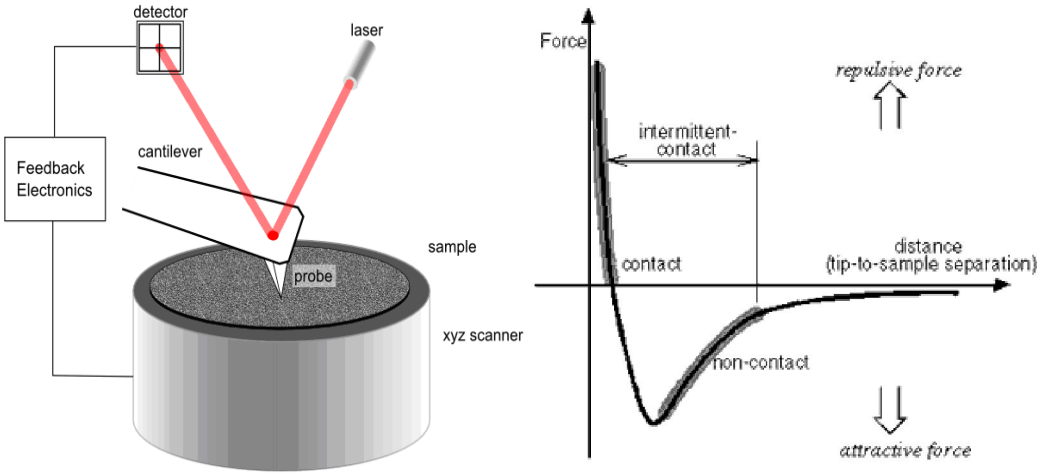

Figure 5.1(a) A schematic illustration of a typical AFM device and its principle; **(b)** Lennard-Jones curve showing the expected force experienced by an AFM tip approaching a sample's surface.

Nontopographic modes

While imaging remains the principle use of AFM, a number of additional modes have been used to measure other sample properties including: Magnetic Force Microscopy (MFM) which measures the distribution of magnetic field in the sample [213], Kelvin Probe Microscopy (KPM) which measures contact potential difference across the sample [214]. Force Spectroscopy can be used to measure interactions between the AFM probe and a contact point on the sample's surface. Nanoindentation is one such example of force spectroscopy to measure softness or hardness of the sample [215]. In force spectroscopy, the AFM tip is brought into contact with the sample surface. The force experienced between the tip and sample causes a deflection of the cantilever according to Hooke's law defined in equation 5.1 where K is the cantilever spring constant, Δy is the maximum deflection of cantilever when a force is applied to the tip

$$F = K\Delta y \qquad (5.1)$$

Figure 5.1 (a) shows that imaging of a sample surface can be achieved by recording the cantilever deflections that are detected by a laser beam reflected from the back of the cantilever to a photodiode, during the tip scanning over a sample. AFM can also be used to perform more complex surface property studies such as adhesion and wetting measurements especially as relatively small cantilever deflections, corresponding to forces of tenths of nN, can be accurately determined using the photodiode setup. Most adhesion measurements using AFM require knowledge of the interaction between the AFM tip and sample, as well as the effective tip-sample interaction area. Van der Waals forces of attraction are always present between atoms and molecules, follow a Lennard-Jones curve. Therefore Lennard-Jones curves are normally used to illustrate the force acting between the AFM tip and the sample surface. In Figure 5.1 (b), the Lennard-Jones curve shows the parts of an approach and retraction cycle of the tip. The distance regions are labelled on the Figure which includes the contact region and the non-contact region.

5.2.2.2 AFM Adhesion Tests

The Lennard-Jones curve is important analysis of the force acting between the AFM tip and the sample surface but cannot be measured directly from AFM experiments. Instead AFM force-distance curve is used to measure the interaction between an AFM tip and a solid sample surface quantitatively [216]. The force-distance curve is achieved by contacting the AFM tip with a solid substrate and then pulling the tip away. The cantilever deflection during this approach and retraction was recorded as shown in Figure 5.2 [216], with adhesion force calculated using Hooke's law as described above. The adhesion force is shown as the force required to remove the AFM tip fully from the substrate's surface as shown in Figure 5.2. Comparisons of surface energies for different sample surfaces can be conducted using this AFM tip removal technique. Generally, the adhesion force is proportional to root square of the surface free energy.

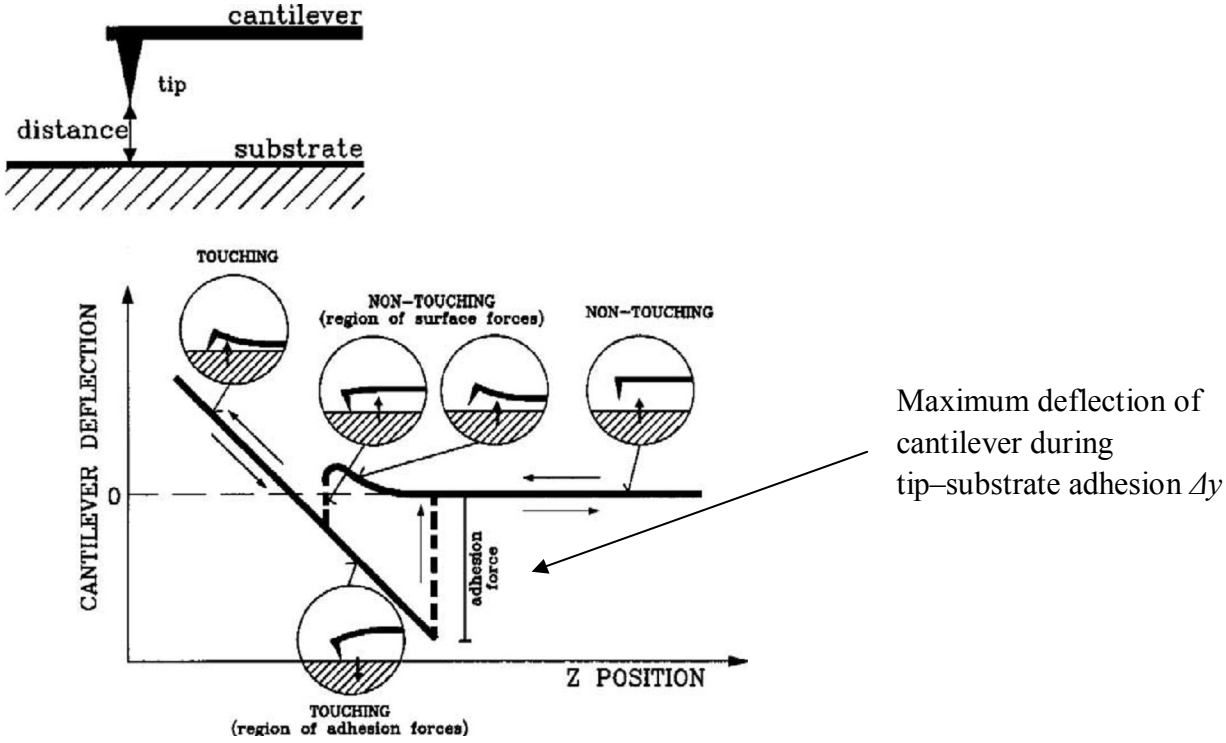

Figure 5.2 Pull-off force related with cantilever bending [216]

In this study, the morphology and dimensions of the collected electrospun nanofibres were investigated using an AFM (NTEGRA Spectra**,** NT-MDT, Russia.) shown in Figure 5.3 (a). Surface property measurements were also carried out using the same AFM. Specimens were prepared as 1cm x 1cm size and were mounted on a sapphire sheet before characterization. Cantilevers (Nanosensors, Windsor Scientific Ltd, UK) with different spring constant have been used in this study. Soft cantilevers with relatively low spring constant about 0.1 Nm^{-1} were used for these adhesion measurements. Figure 5.3 (b) shows SEM image of an AFM tip [216].

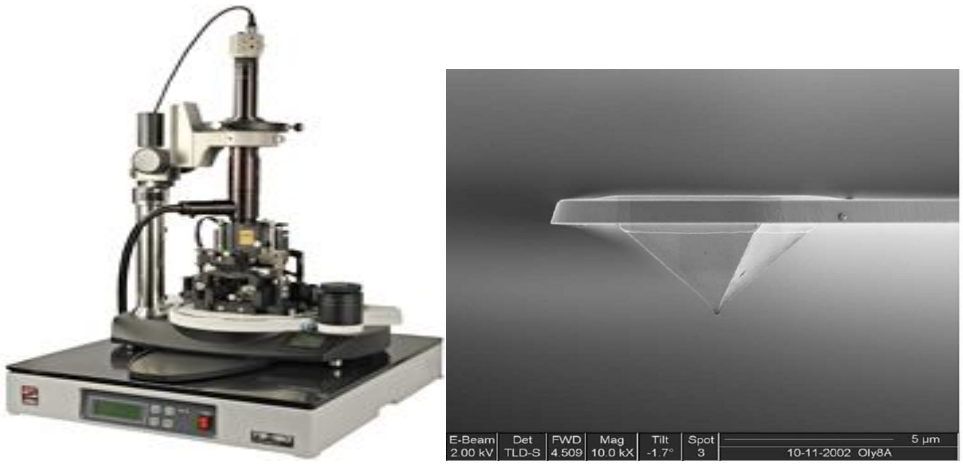

(a) **(b)**

Figure 5.3 (a) Scanning Probe Microscopy**(b)** SEM image of an AFM tip [216]

AFM cantilever spring constant was calibrated every time before measurement. The cantilever's spring constant is important for determining the force required to cause deflection of the cantilever from Hooke's law. The spring constant depends on the cantilever dimensions such as length (L), thickness (t), width (b) and the elastic modulus of the cantilever material (E) by: $K = Ebt^3/(4L^3)$. The elastic modulus of cantilevers, typically made from Si or Si_3N_4, is well documented. However, the dimensions of cantilevers strongly affect the resultant spring constant value. The length and width of a cantilever are many tens of microns and can be measured from SEM. The thickness of the cantilever is normally 1 μm but any

errors in this measurement from SEM imaging will give a large error in the calculated spring constant *K*. Any small errors in the measured cantilever thickness have a significant effect on the calculated *K* value due to the power relationship. Recently, a method for measuring the rectangular cantilevers' spring constant *K* has been reported by Sader et al [217] as:

$$K = 0.1906\rho_f b^2 L Q_f \Gamma_i(f_0) f_0^2 \qquad (5.2)$$

where b and L are the width and the length of the cantilever, respectively, Q_f and f_0 are the quality factor and the resonance frequency of the cantilever in fluid and ρ_f is the fluid density; all of these three parameters are typically used when the cantilever is placed in air, Γ_i is the imaginary part of the hydrodynamic function and only depends on the Reynolds number Re = $\rho_f f_0 b^2/(4\eta)$, where η is the viscosity of surrounding fluid (air), and is independent of the cantilever thickness and density [217]. The quality factor Q_f is related to the damping ratio (δ), which is a measure of how fast the oscillator is losing energy and can be determined experimentally [217].

Therefore Sader's method has been used in this study for determining the rectangular AFM cantilevers' spring constant due to a reported high accuracy of around 5%. This method is attributed to the cantilever thickness not used for the spring constant *K* value calculation. In this study, all AFM cantilevers used were rectangular with their dimensions (b, L) measured from SEM. Nova software (Nova, NT-MDT, Russia) has been used to run this Sader's method cantilever calibration with known width and length of the cantilever from SEM.

Adhesion measurement using AFM and JKR theory has been reviewed in section 2.4.5.1 and has been implemented by other researchers for crystalline and amorphous Lactose solids [218]. In order to minimize capillary forces acting

between a contacting AFM tip and potential water condensation on the sample's surface, all adhesion experiments were conducted in a vacuum chamber to achieve low humidity (<1% RH). In addition, the sample was electronically grounded to remove any electrostatic charge buildup. Adhesion forces were calculated using equation 5.1 and the experimentally measured maximum cantilever deflection Δy_1 taken from cantilever deflection-distance curves as typically shown in Figure 5.4.

This deflection is measured as photodiode which is in nA, and this doesn't give the information on cantilever deflection in terms of nm. Therefore contacting with a non-deformable solid (silicon substrate) is required in order to calibrate the cantilever deflection from nA to nm. When the AFM tip is in contact with the solid sample, z-piezo movement towards the tip by a defined amount will cause a corresponding cantilever bending, therefore the cantilever deflection signal in nA is equal to the z-piezo movement in nm. $\frac{\Delta x'}{\Delta y'} \times \Delta y_1$ will give the maximum cantilever deflection during AFM-tip separation from the sample's surface. Cantilever deflection can then be converted to adhesion force using Hooke's Law (equation 5.1).

The surface free energy of a solid surface can be measured from AFM adhesion force measurements. The calculation of the surface free energy of the solid to be examined requires knowledge of the contact between the AFM tip and solid sample as discussed in section 2.4.5. Equation 2.30 is typically used to calculate surface free energy when retracting a contacting AFM tip but the AFM tip radius R must be known. R was calculated by retracting the AFM tip from an atomically flat solid substrate of silicon and measuring the adhesion force. As the AFM tip and silicon substrate are the same material, the surface free energy of the AFM tip and silicon

substrate (γ_1 and γ_2 in equation 2.30) are equal. The surface free energy of silicon is a dispersive surface energy of 42 mJm^{-2} [218] and this value was used for both $\gamma_1$and γ_2. Thus R is the only unknown parameter and can be calculated after measuring the adhesion force between the AFM tip and silicon substrate. The determination of the surface free energy of samples was carried out in a similar fashion as the R calibration. However, in these adhesion tests, R was known but the surface free energy $\gamma_2$was the unknown. Calibration of R values was carried out before every AFM adhesion test.

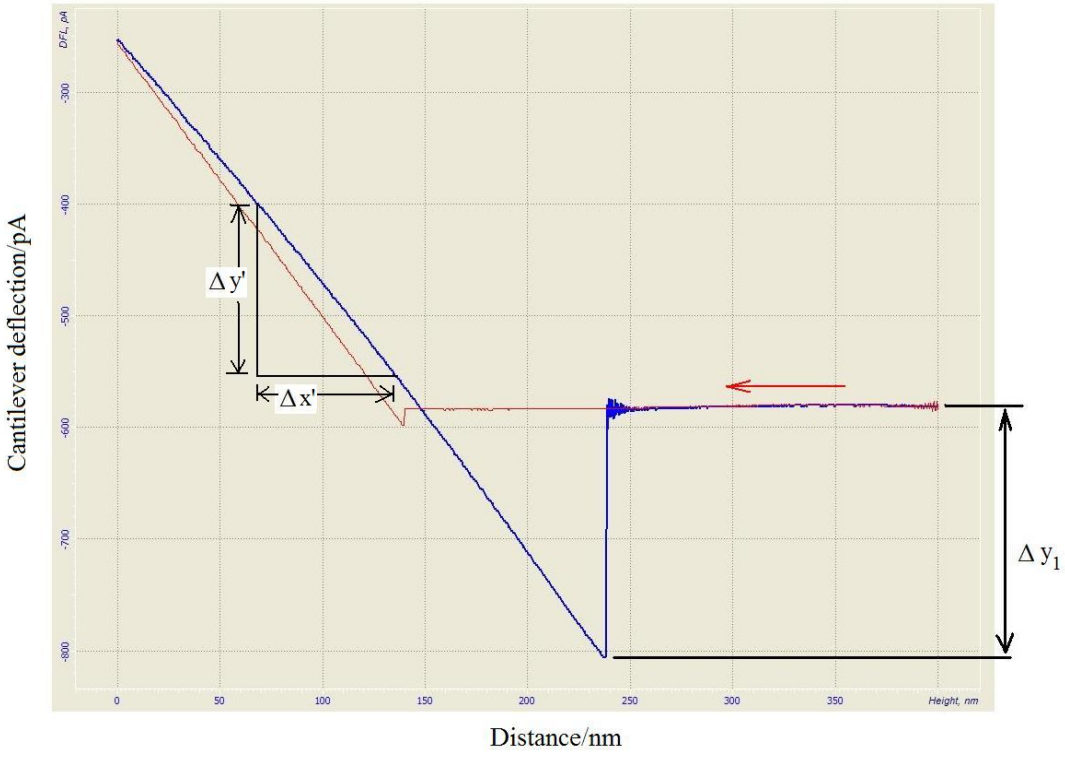

Figure 5.4 Cantilever deflection versus distance curve in adhesion measurements.

Various studies have developed models in order to measure the surface free energy of a polymer surface at the nanoscale using assumptions of the AFM tip-sample contact area [218-224]. Two theories dominate, namely Johnson–Kendall–Roberts (JKR) and Owens-Wendt Theory. The former is used to determine the adhesion properties of polymer surfaces. The later is used to determine wetting properties of

polymer surfaces when combining with a Wilhelmy balance method and will be detailed in Chapter 6.

5.2.2.3 Density Measurement

The relationship between the structural organisation in the polymer samples and their surface free energy can be evaluated by considering the density of the polymer samples. In this study, the densities of polycarbonate films with different draw ratio and electrospun polycarbonate fibres have been measured using a pycnometer (MicromereticsAccuPyc 1330 He Pycnometer,USA.) which uses a gas displacement technique for measurement, as shown in Figure 5.5. This pycnometer is a fast density analyzer which can automatically provide high precision and high speed density measurement on a wide range of materials such as powders and slurries. The specimen volumes can be varied from 0.1 to 100 mL.

Figure 5.5 MicromeriticsAccuPyc 1330 He Pycnometer

5.3 Results and Discussion

5.3.1 PVA Surface Free Energy

A representative SPM topography image of electrospun PVA nanofibres in Figure 5.6 shows continuous fibres of a constant fibre diameter. The fibre diameter as measured from Figure 5.6 (a) is 300±50 nm. Electrospinning for short amounts of time produced more isolated nanofibres in which surface properties could be investigated as shown in Figure 5.6 (b).

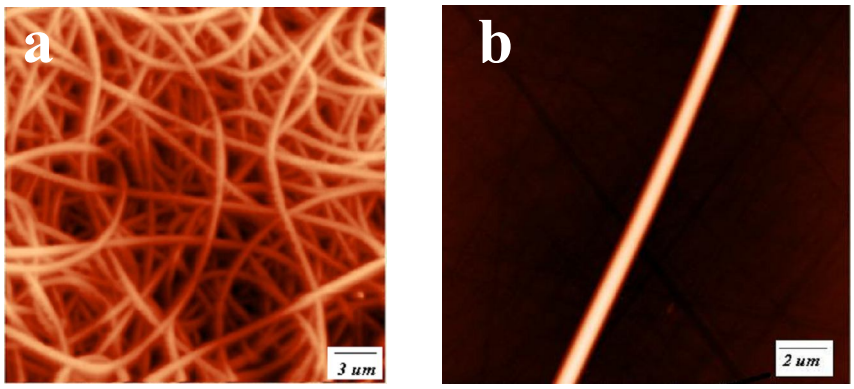

Figure 5.6 AFM semi-contact topography imaging shows (a) continuous nanofibres of uniform diameter, (b) a low density of nanofibres on the substrate when electrospinning for short amounts of time, allowing isolation of individual nanofibres.

The diameter of each nanofibre was accurately measured from AFM topography images as shown in Figure 5.7 (a). A cross-sectional view of an individual electrospun fibre on the substrate is shown in Figure 5.7 (b). The maximum height of the fibre can be easily elucidated and is used to define the fibre diameter.

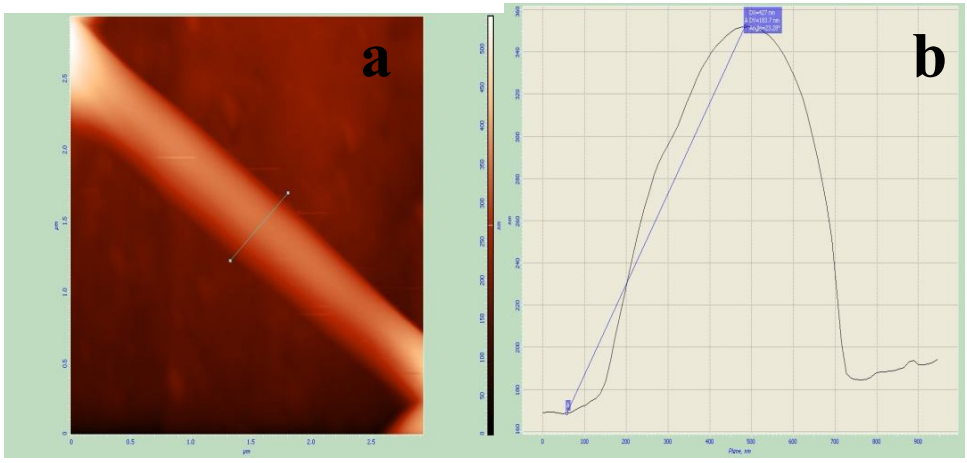

Figure 5.7 (a) AFM topography image of an individual PVA Nanofibre, **(b)** Cross-sectional representation of an individual PVA nanofibre diameter measurement from AFM Nova software.

An isolated PVA nanofibre as shown in Figure 5.6 (b) was selected to determine the contact adhesion force between a tip and a sample surface for the derivation of surface free energy. The AFM tip was moved into contact with the nanofibre's surface using the z-piezo (z-scanner) of the AFM. Spatial drift between the sample and tip was minimal using the AFM's closed loop system. Once in contact, the z-piezo was used to separate the tip from the sample's surface while monitoring the forcing acting on the tip using cantilever bending data. A typical force-distance curve showing the tip pulling away from the sample surface is shown in Figure 5.8. This curve shows the contact point between the AFM tip and the PVA nanofibre surface (1), the maximum adhesion force holding the tip at the sample surface (2) and the separation point (3).

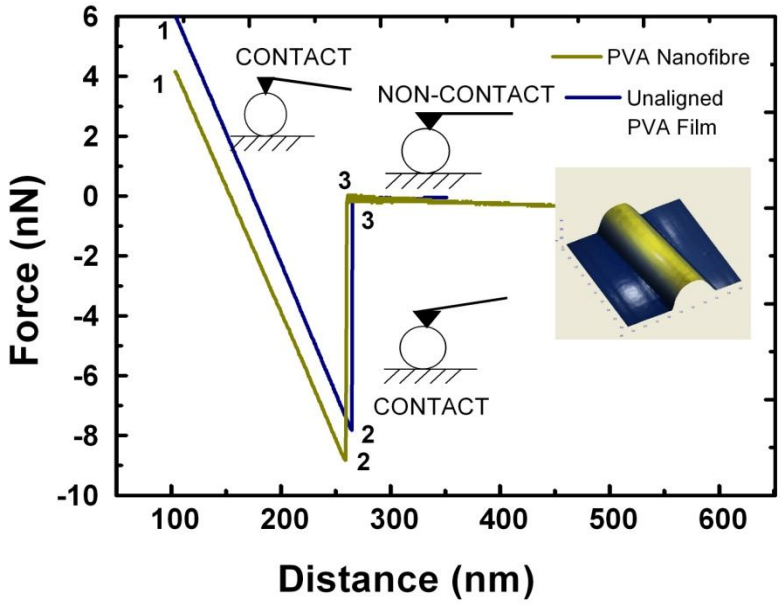

Figure 5.8 Force-distance curve for the separation of the AFM tip from the surface of a PVA nanofibre shown in the AFM semi-contact image (insert) and an undrawn film.

Contact mode cantilevers with a spring constant of 0.1 Nm^{-1} were used so that there was minimal contact pressure between the tip and sample. Large contact pressures increase the tip-sample contact area and are avoided in this study. This was achieved by selecting a suitable set-point so that the cantilever bent back from the sample by less than 1nm upon contact in feedback.

The tip in contact with the sample surface is modelled according to a sphere in contact with a plane. This is reasonable as the tip radius of curvature is almost two orders of magnitude smaller than the nanofibre radius. Johnson-Kendal-Roberts theory is used to correlate the maximum pull-off (adhesion) force F, shown at (2) in Figure 5.8. Equation 5.2 was used to calculate the dispersive component of the surface energy of polymer material. In order to minimize capillary forces, all adhesion experiments were conducted in a vacuum chamber to achieve low

humidity (1% RH). In addition, the experimental facilities were connected to ground (electricity) electrode to remove electrostatic charges. Thus, the relationship between the AFM tip radius of curvature, the dispersive components of the surface energy of the SPM tip and sample (γ^{d}_{tip} and γ^{d}_{polym}) is:

$$\gamma^{d}_{polym} = \left(\frac{F}{3\pi R}\right)^{2} \frac{1}{\gamma^{d}_{tip}} \qquad (5.3)$$

The adhesion force was taken from Figure 5.8 between points (2) and (3). The pull-off force for the PVA nanofibres has an average value of 8.8 nN and an unaligned PVA film has an average value of 7.8 nN. Using equation 5.3 and calibrated R values, the dispersive surface free energy of the PVA nanofibres were calculated as 40.6 ± 3.3 mJm^{-2}. This is interesting as non-electrospun (bulk) PVA polymer film dispersive surface free energy was calculated as 25.5 ± 2 mJm^{-2} which is similar with reported literature values of 25.1 mJm^{-2}[225].

Figure 5.9 shows the dispersive surface free energy for different diameter electrospun PVA nanofibres. The nanofibre surface free energy is around 40 mJm^{-2} and, while there is some scatter in the data, there is no generally perceivable relationship between the PVA nanofibre surface free energy and the fibre diameter. This highlights that the JKR model of a sphere contacting a flat surface is reasonable for this study. The slight increase in the surface free energy with decreasing the PVA fibre diameter is expected to be due to the contact area for the tip and the thinner diameter nanofibre being relatively smaller than the contact area from larger diameter fibres. This indicates that the separation force acts over a smaller area when the fibre diameters are relatively small, giving a higher surface free energy. However, it should be noted that this effect is slight and may only gives changes of 1 mJm^{-2} due to geometric inaccuracies. Importantly, the dispersive

surface free energy for normal bulk PVA polymer is only 25 mJm^{-2}, whereas the results have shown PVA electrospun nanofibre has much higher dispersive surface free energy value of 40 mJm^{-2}. The reason for this increase in the surface free energy of electrospun fibres compared to bulk films might be because the surface molecular structure has been changed after applying high electric field strength during electrospinning process and giving better potential molecular alignment. In order to investigate this further, the surface free energy for PVA films with five different draw ratios have been studied in the next section.

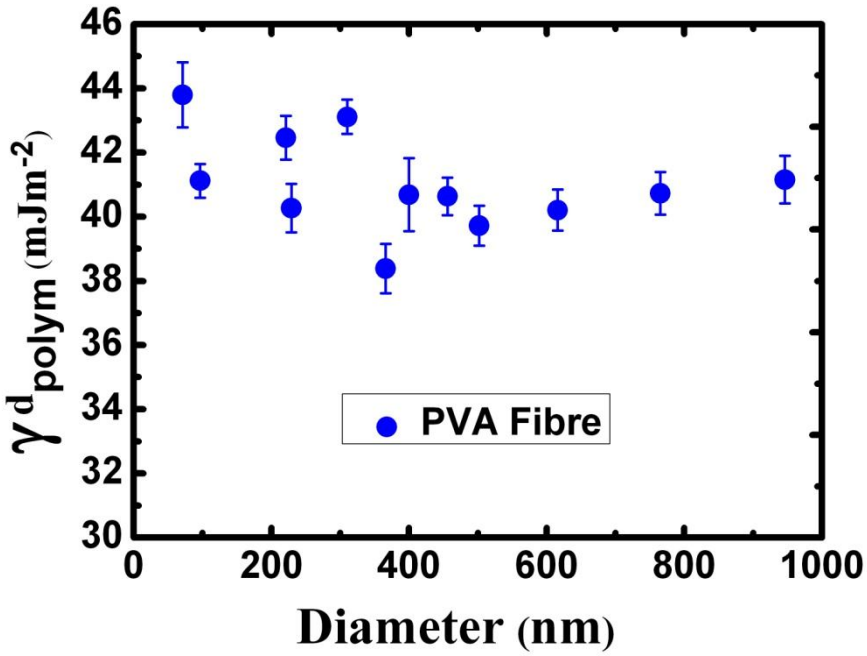

Figure 5.9 PVA nanofibre dispersive surface free energy related to fibre diameter

Five different draw ratio (λ=1, 2, 3, 4, 5) PVA films dispersive surface free energy have been measured from AFM using same method mentioned above. These draw ratio's are used to examine if the surface energy of the polymer changes according. Thus, an indication of the molecular alignment in the electrospun fibres can be found by comparing to the surface free energy of the films to the fibres. Figure 5.10 shows the dispersive surface free energy of PVA films increases with their draw

ratio, with the largest PVA film giving the largest dispersive surface free energy value. Comparisons between these bulk drawn PVA films and electrospun PVA nanofibres suggests that the electrospun fibres have more molecular orientation than both aligned and unaligned bulk polymer films.

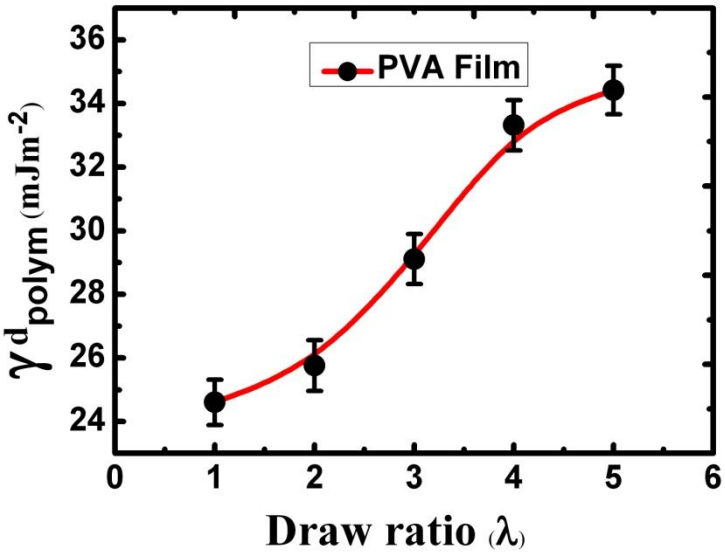

Figure 5.10 PVA films dispersive surface free energy related to draw ratio

The adhesion force used to separate the AFM tip from individual electrospun PVA nanofibres is larger than required for the PVA films (Figure 5.8). The corresponding calculated surface free energies are valid only if the assumption of a sphere contacting a flat surface is true. Surface roughness in the films and fibres can influence the total measured adhesion force. For example, a rough surface will increase the contact area between the AFM tip and sample surface resulting in an increase in the adhesion force relative to a flat surface. Previous researchers have attempted to identify the influence of roughness on adhesion force measurements using AFM [226]. Little success was achieved due to problems in defining a quantity of roughness that influences the adhesion measurement. A method was proposed which used the average RMS roughness within an imaged area as an

indication of how roughness may affect the adhesion force measurement. However, this area was typically 1 μm x 1μm whereas the real contact between the AFM tip and surface is inherently much smaller (of the order to perhaps 10 nm x 10 nm). The authors importantly stress the potential limitations with this methodology and note that RMS roughness values below the radius of curvature of the AFM tip was not influence adhesion force measurements in our study. The RMS roughness of the PVA films and small areas on top of the electrospun PVA fibres was measured from AFM topography images. The average roughness for PVA films is 3.09 nm (dispersive surface free energy is 25.5 mJm^{-2}), and the average roughness for PVA nanofibre is 3.03 nm (dispersive surface free energy is 40.6 mJm^{-2}). As the surface roughness for the films and fibres are similar, the surface energy change is expected to be because of the molecular organization effects, which is principally from molecular alignment.

The increase in surface free energy between electrospun PVA nanofibres and their bulk equivalents suggests that the two molecular structures are quite different. Previous literature [227, 228] has suggested that electrospinning provides high molecular alignment when compared with polymer films. Consideration of the electrospinning process would support this; ejection of the polymer from the needle involves rapid stretching of an electrified jet and evaporation of the solvent. The polymer chains are expected to experience an extremely strong shear force during the electrospinning process. This shear force and rapid solidification could prevent polymer chains from relaxing back to their equilibrium conformations and resulting in better molecular orientation. From our measurements it is clear that the unique polymer morphology in electrospun polymer nanofibres influences and increases the surface free energy relative to bulk polymer.

PVA is a semi-crystalline polymer thus it has both amorphous and crystalline

regions. From the above results, we can obtain that larger surface free energy which may be from improved molecular orientation. However, this origin of any potential alignment is complicated by the presence of a heterogeneous structure consisting of amorphous and crystalline regions. In order to simplify this problem, surface energy measurements are carried out on a homogenous amorphous polycarbonate material in order to better understand the relationship between molecular structure and surface free energy.

5.3.2 PC Nanofibre Surface Free Energy

The dependence of surface free energy on molecular orientation in two diverse amorphous polycarbonate forms of drawn films and electrospun fibres are examined. Equation 5.3 was used to calculate the dispersive component of the surface energy of polycarbonate films and fibres. In order to minimize capillary forces, all adhesion experiments were conducted in a vacuum chamber to achieve low humidity (1% RH). In addition, the experimental facilities were connected to ground (electricity) electrode to remove electrostatic charges. The dispersive surface free energy of polycarbonate in the form of drawn solid films and electrospun fibres was calculated from AFM adhesion force measurements as carried out for PVA. Results show how increasing the molecular orientation of the film through drawing increases the dispersive surface free energy of the film and highlighted the significant molecular orientation in electrospun fibres unachievable using mechanical drawing methods. A mechanism for increased dispersive surface free energy with molecular spacing is proposed.

The surface free energy of the electrospun PC fibres and drawn films were measured experimentally using AFM and applying JKR contact mechanics theory. A closed loop AFM with low spatial drift was first used to image samples and then

contact the AFM tip with the sample's surface. Subsequent separation of the AFM tip from the surface of the sample causes a corresponding bending of the AFM cantilever away from the sample until, at a critical force, the bending of the cantilever overcomes the adhesion between the AFM probe and surface. Figure 5.11 shows a typical plot of the force applied to the sample surface, with negative values defining attractive forces measured between the AFM tip and sample, as the sample is separated from the tip. The adhesion force F is defined by the change in force from its most negative value to a zero force during the 'snap-off' point.

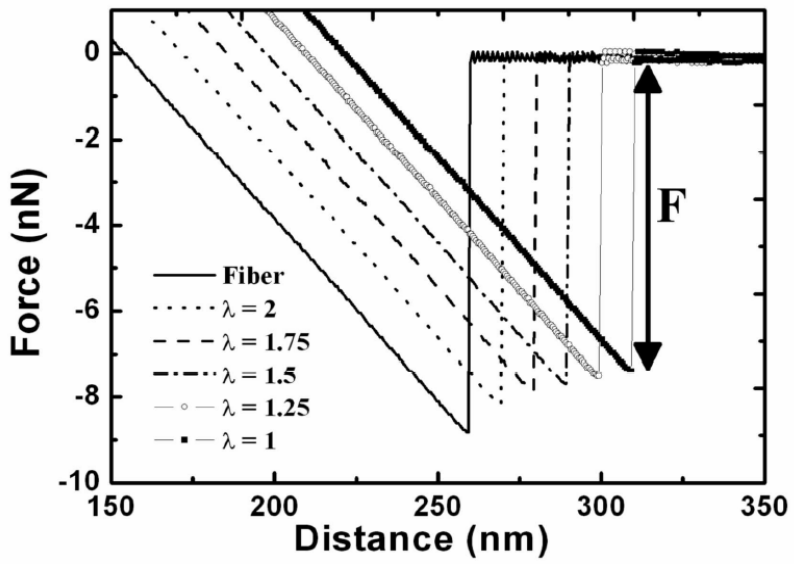

Figure 5.11 Force-distance plot for the separation of an AFM tip from polycarbonate film surfaces with differing draw ratios (λ) and an electrospun fibre surface. The adhesion force F is shown for a film with λ=1 only for clarity.

Figure 5.11 clearly shows that the adhesion force increases for drawn films with increasing λ and electrospun fibre surfaces. The surface free energy of the separated surfaces of the AFM tip and sample surface can be calculated from JKR theory by correlating the maximum pull-off (adhesion) force F by equation 5.3. Figure 5.12

shows the plot of the five different PC films dispersive surface free energy related to their draw ratio.

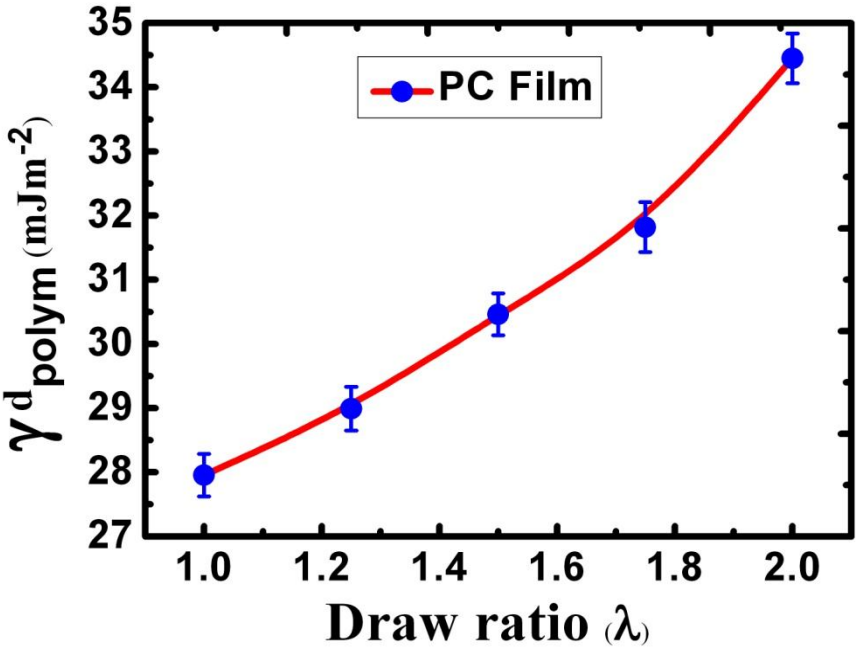

Figure 5.12 Dispersive surface free energy for different draw ratio PC films

Qualitative confirmation of an increase in the dispersive surface free energy with increasing film draw ratio can be shown with contact angle measurements. A droplet of ethylene glycol on a polycarbonate film will be expected to have a lower contact angle if the dispersive surface free energy of the film is increased from drawing. Figure 5.13 demonstrates this contact angle decrease for an increased dispersive surface free energy of the polycarbonate film with a larger draw ratio. However, the evaluation of the liquid contact angle on the electrospun PC fibre is more difficult due to the relatively small length scales involved, emphasizing the applicability of the AFM contact measurements.

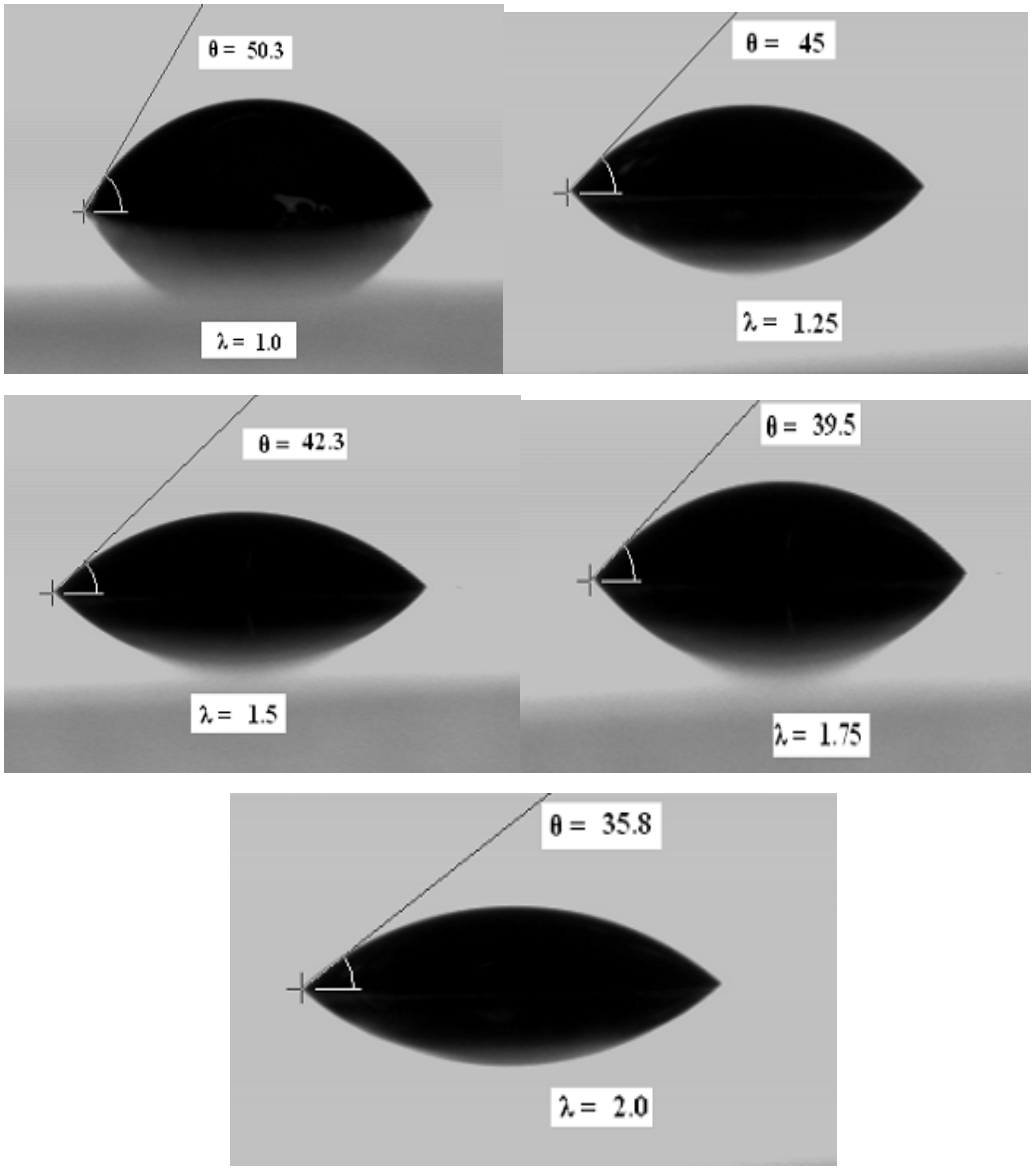

Figure 5.13 Optical micrographs of a polyethylene glycol droplet on polycarbonate films with different draw ratio (λ=1, 1.25, 1.5, 1.75, 2) and smaller droplet contact angle for the higher draw ratio film.

The relationship between the structural organisation in the polymer samples and their surface free energy can be evaluated by considering the density of the polymer samples. The densities of the polymer samples were measured using a pycnometer with Figure 5.14 showing the dependence of dispersive surface free energy on density values for different PC film and fibre samples.

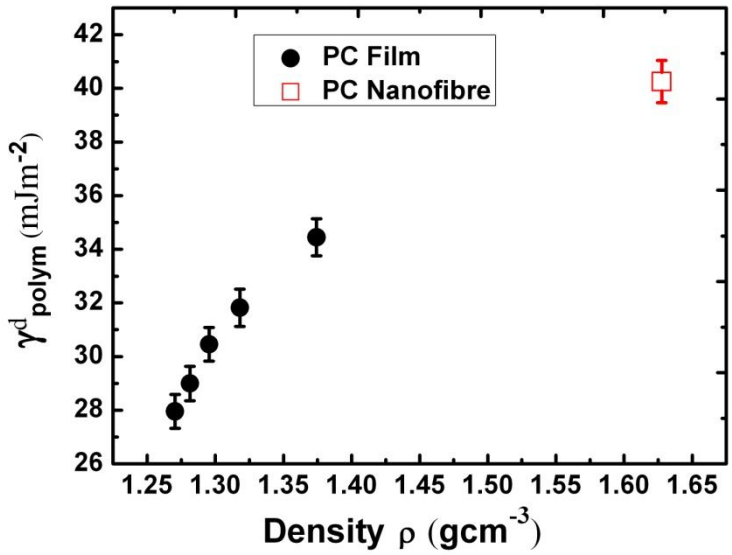

Figure 5.14 Plot of calculated dispersive surface free energy versus polycarbonate density for a variety of drawn films and electrospun fibres.

The density increase with larger draw ratios indicates that alignment of polymer chains cause more effective packing together of these chains. The electrospun fibres have a significantly larger γ^d_{polym} than the largest drawn films which highlights the efficiency in the polymer chain orientation above the mechanical limits of drawing films. Therefore, the polymer dispersive surface free energy is critically dependent on the polymer chain organisation within the material. The origin of the dispersive surface free energy increase must be related to changes in the intermolecular chain distance described by the density measurements. In particular, the dispersive surface free energy is an intermolecular attractive force that arises from a cooperative oscillation of electron clouds on a collection of molecules at relatively close range. The distance between molecules is important as an instantaneous dipole moment of one atom or molecule induces a similar temporary dipole moment in adjacent atoms or molecules. Dispersion forces not only bring molecules together but also tend to mutually align or orient them [229]. Therefore

the interaction between instantaneous and induced dipoles will become stronger and give rise to larger dispersive surface free energy when the intermolecular chain distance between the molecules reduces.

To explore this mechanism further, the relationship between intermolecular spacing and surface free energy is considered. If the energy of interaction of two molecules is given by the Lennard-Jones expression [230]:

$$\varepsilon = -\frac{A}{r^6} + \frac{B}{r^{12}}, \qquad (5.4)$$

Where r is the distance of separation of the molecules, then the force between them is given by [230]:

$$F = \frac{\partial \varepsilon}{\partial r} = \frac{6A}{r^7} - \frac{12B}{r^{13}} \qquad (5.5)$$

If the density of the molecules, ρ, is independent of their position, then the total number in the shaded area in Figure 5.15 is given by M, where [230]:

$$M = 2\pi r \sin\theta (dr / \sin\theta)\rho df \qquad (5.6)$$

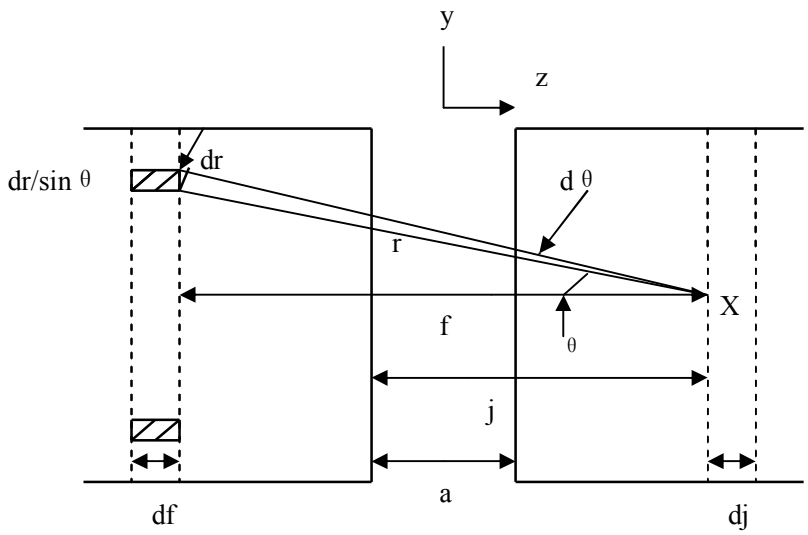

Figure 5.15 Intermolecular forces across an interface [230]

The force in the z-direction exerted on a molecule located at X due to all molecules in the annulus is given by $F_a = MF\cos\theta = MF(f/r)$, and so the force due to all the molecules in the slab of width df is given by F_s where [230]:

$$F_s = 2\pi\rho f df \int_{r=f}^{r=\infty} \left(\frac{6A}{r^7} - \frac{12B}{r^{13}}\right) dr \qquad (5.7)$$

Consequently the force due to all the molecules in the left-hand block acting on the molecules at X is given by $F_b = \int_{f=j}^{f=\infty} F_s df$, and the total force between all the molecules in the left-hand block and the right-hand block is given by F_t, where [230]:

$$F_t = \int_{j=a}^{j=\infty} F_b \rho dj \qquad (5.8)$$

And a is the distance of separation of the two blocks, i.e.

$$F_t = 2\pi\rho^2 \int_{j=a}^{j=\infty} dj \int_{f=j}^{f=\infty} f df \int_{r=f}^{r=\infty} \left(\frac{6A}{r^7} - \frac{12B}{r^{13}}\right) dr = \frac{2\pi\rho^2}{a^3}\left(\frac{A}{12} - \frac{B}{90a^6}\right) \qquad (5.9)$$

If two surfaces are formed by separating the right- and left-hand sides of the material shown in Figure 5.15 then the work done per unit area of the original cross-section should be equal to twice the specific surface energy since two surfaces are formed. The surface energy should therefore be given by [230]:

$$2\gamma = \int_{a=r_{11}}^{a=\infty} F_t da \qquad (5.10)$$

Where r_{11} is the equilibrium distance between the planes. The subscript '11' is introduced to indicate that the planes under consideration each form the surface of a phase [230]. Therefore,

$$\gamma = \frac{\pi\rho^2}{24r_{11}^2}(A - \frac{B}{30r_{11}^6}), \qquad (5.11)$$

However, if r_{11} is the equilibrium distance between the two semi-infinite bodies, the net force between them should be zero. Therefore, from equation 5.9, for the condition $a = r_{11}$ [230]:

$$\frac{A}{12} = \frac{B}{90r_{11}^6} \qquad (5.12)$$

Hence, substituting in equation 5.11

$$\gamma = \frac{\pi\rho^2 A}{32r_{11}^2} \qquad (5.13)$$

Then the surface free energy of a system (γ) and its relation to the density of molecules ρ can be achieved from equation 5.13. Where A is the Hamaker constant and r_{11} is the average equilibrium PC chain intermolecular distance. If assuming all polymer molecules align parallel and linearly in a cubic with same volume, by knowing different density of molecules for different PC films and PC fibres samples, their intermolecular distance can be calculated. Equation 5.13 indicates how a closer packing of polymer chains, described by an increasing ρ value, results in a larger surface free energy. Figure 5.16 shows a plot of γ^d_{polym} with ρ / r_{11} in order to test the validity of equation 5.13.

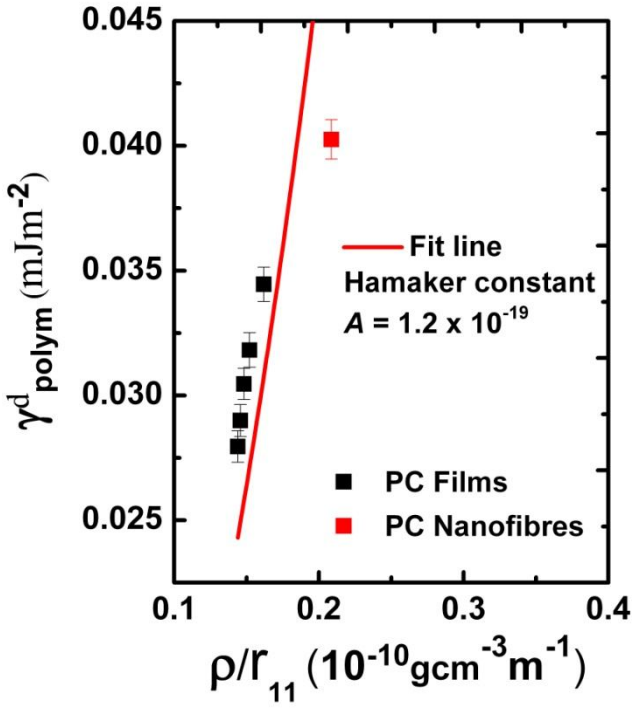

Figure 5.16 Plot of the dispersive free energy γ^{d}_{polym} of various drawn films and electrospun fibre surfaces against the polymer density/average chain distance ρ / r_{11}. The fit line gives πA/32 resulting in a Hamaker constant (A) of 1.2 x 10^{-19}J.

A linear resultant fit line is shown in Figure 5.16, which is equal to πA/32 and gives a calculated Hamaker constant of the PC as 1.2 x 10^{-19} J. This average value for our different polymer samples is similar to other polymer literature values and highlights how equation 5.13 and our proposed mechanism are reasonable for this study.

5.4 Conclusions

The surface free energy of electrospun PVA and PC nanofibres and its relation to molecular ordering using AFM adhesion measurements are investigated.

Comparisons are made with bulk polymer material to show that a high degree of molecular orientation is present at least at the surface of the polymer nanofibre. As a result, the surface free energy of electrospun polymer nanofibres is greater than that of a bulk polymer. This effect indicates that the electrospinning process is effective at polymer alignment, at least at the surface of the fibre.

Density measurements provide supporting evidence for improved packing of polymer chains and, therefore, a smaller average distance between polymer chains. Lennard-Jones interaction potentials show a good fit with collected data and support the relationship between surface free energy and increasing sample density, indicative of decreasing molecular separation. The result of the packing therefore relates molecular alignment to both the density and the dispersive surface free energy of the nanofibres and polymers in general.

Chapter 6

Individual Electrospun Polymer Nanofibre Wetting

6.1 Introduction

The surface of polymer nanofibres plays a significant role in many applications thus measurement of their surface properties is essential but challenging due to their relatively small size. The material surface free energy at the nanoscale can be measured using a Wilhelmy balance method combined with Owens-Wendt theory as discussed in section 2.4.6.3 but has not been previously measured. This chapter details AFM wetting tests for individual electrospun polymer nanofibres in order to measure their polar and dispersive surface free energy components. Individual electrospun PVA nanofibres have been immersed and removed from three different low vapour pressure liquids using AFM. The polymer nanofibre-liquid interactions can be monitored by AFM and accurate measurements of contact angle between liquids and the nanofibre surface made. These wetting data were used to produce Owens-Wendt plot giving the dispersive and polar components of the nanofibre surface. Fourier transform infrared (FTIR) technique and X-ray photoelectron spectroscopy (XPS) are used to provide structural information on electrospun polymer nanofibres. Results are compared with bulk polymer films to

conclude how the surface properties of electrospun polymer nanofibres are different from bulk polymer material.

6.2 Experimental Details

6.2.1 Sample Preparation

Wetting properties of single carbon nanotubes have been measured by immersing and then removing single carbon nanotube from different liquids using AFM as discussed in section 2.4.6. The measurement of the wetting properties of single carbon nanotube was achieved by attachment of the individual nanotube onto an AFM tip. This wetting measurement is also applicable for electrospun polymer nanofibres. Attaching single carbon nanotube onto an AFM tip is relatively easy because single carbon nanotubes have a relatively short length. However, electrospun nanofibres are long and continuous, limiting the use of direct AFM wetting measurements. Therefore short and single electrospun nanofibre with a desired length of a few tens of microns should be obtained in order to characterize the wetting property of electrospun nanofibre. The following sections reviews a variety of experiments carried out in order to prepare single short electrospun polymer nanofibre suitable for attachment to an AFM tip.

6.2.1.1 Short Fibres Formed by Ultrasonic Processor

Electrospun nanofibres have a continuous length hence methods are needed in order to shorten the length of the fibres. Ultrasound was suggested as a possible method to reduce the length of the fibres. Ultrasound is generated by high frequency voltage electricity and this high frequency electricity is then converted

to sound waves or mechanical energy through water, which will make these waves vibrate. At the same time microscopic bubbles form and repeatedly implode upon the given surface. This powerful action was explored in order to break our electropun polymer nanofibres. For this purpose, a high power ultrasonic probe is used in this study. Experiments were initially carried out on electrospun PVA fibres as these are expected to be mechanically weaker than PC, as PVA has a 10.5 MPa tensile strength which is much lower than 75 Mpa tensile strength of PC [231, 232]. In addition, PVA fibres are relatively insoluble in a number of polar solvents whereas previously studied PEO fibres can dissolve rapidly. Electrospun PVA fibres were submerged within a liquid that could be used both as a medium for ultrasonic processing as well as not dissolving the PVA. Propan-2-ol was selected as the medium liquid as the electrospun PVA fibres showed little solubility during the times used. Highly aligned PVA nanofibres were produced for this study. An ultrasonic processor (Sonics&Materials, Inc, USA) as shown in Figure 6.1 was used to break long and continuous PVA nanofibres into short and single fibres within the medium of propan-2-ol.

Figure 6.1 (a) Ultrasonic Processor (Sonics&Materials, Inc, USA) **(b)** Probe of the ultrasonic processor

The ultrasonic processor probe was placed in the nanofibre solution and operated for 3 hours followed by analysis of the fibre length using particle analysis. A Mastersizer 2000 particle analyzer was used to measure the length of short PVA

nanofibres using laser light scattering, as shown in Figure 6.2. Laser light scattering can measure dimensions of materials ranging from 0.02 µm to 2000 µm with an accuracy of ± 1 %. The resultant fibre size distribution after sonication for 3 hours is shown in Figure 6.3. A sharp peak in Figure 6.3 indicates that most electrospun PVA nanofibres are in the 20-30 µm length range. Additional SEM images (Figure 6.4) correlate with the particle analysis results and indicate fibres with lengths of at least 20 µm.

Figure 6.2 Mastersizer 2000 for particle analysis

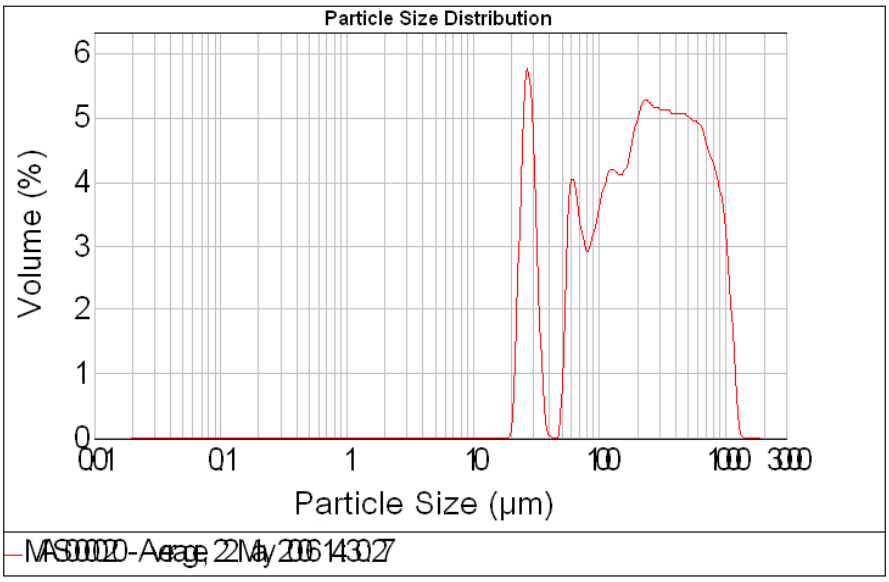

Figure 6.3 Length distribution of short electrospun PVA nanofibres

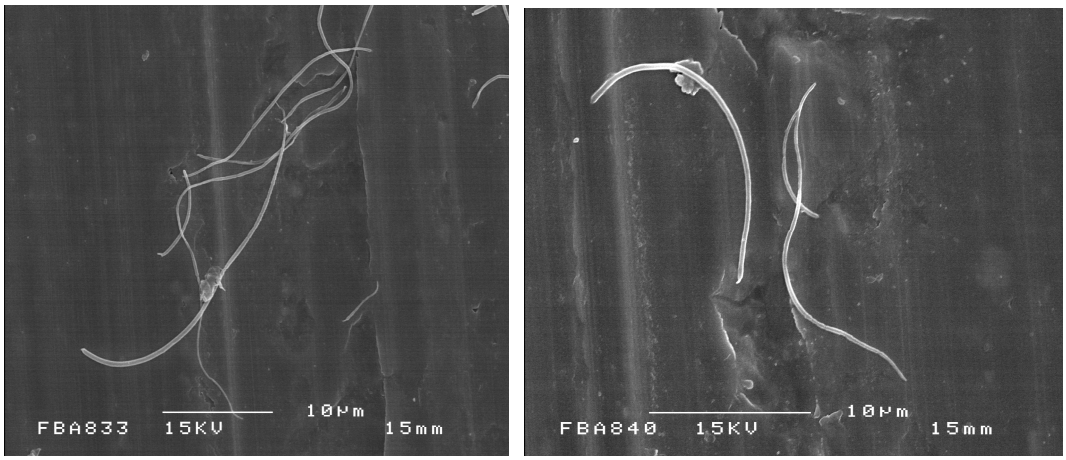

Figure 6.4 SEM images of short PVA nanofibres after sonication

6.2.1.2 Short Fibres Formed by Razor Blade Cutting

Further experimental methods were investigated in order to obtain short electrospun fibre lengths using razor blade cutting. Aligned PVA nanofibres were electrospun onto a piece of aluminium foil and used for this study. This aluminium foil with collected PVA nanofibres was securely held and a cut perpendicular to the nanofibre length made by hand using a sharp razor blade. The results are shown in Figure 6.5. The shortest length of PVA short fibres obtained after cutting is around 20 µm.

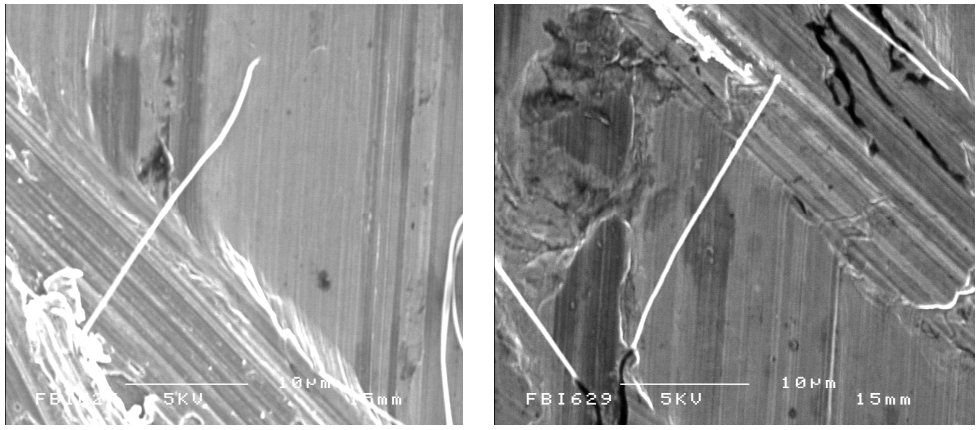

Figure 6.5 Short PVA nanofibres obtained through razor blade cutting

6.2.1.3 Electrospraying Water Droplets onto Nanofibres

PVA is a water soluble polymer, thus micron size water droplets can dissolve away some parts of continuous nanofibres and leave progressively shorter fibre lengths. Electrospraying water droplets onto PVA nanofibres have been carried out for this purpose of dissolving parts of the fibre to produce smaller fibre lengths. In this study, PVA nanofibres were firstly electrospun onto a clean glass slide. A glass slide containing electrospun PVA fibres was placed under an electrospinning needle containing water. Ejection of the water from the needle was achieved using an electrospray process where 5 kV applied voltage and 1 $\mu m.min^{-1}$ flow rate were used. Some of the water droplets electrosprayed onto the PVA nanofibres, and some water droplets electrosprayed onto the glass slide were quickly evaporated. SEM images of electrospun fibres on a glass slide after electrospraying of water indicate that some parts of the PVA nanofibres have dissolved away due to the position of water droplets along their length (Figure 6.6). Therefore short fibres can be achieved from this study but the ends of obtained short fibres adhere onto the glass slide and can not be picked up by tweezers, making removal of the fibres from the slide difficult.

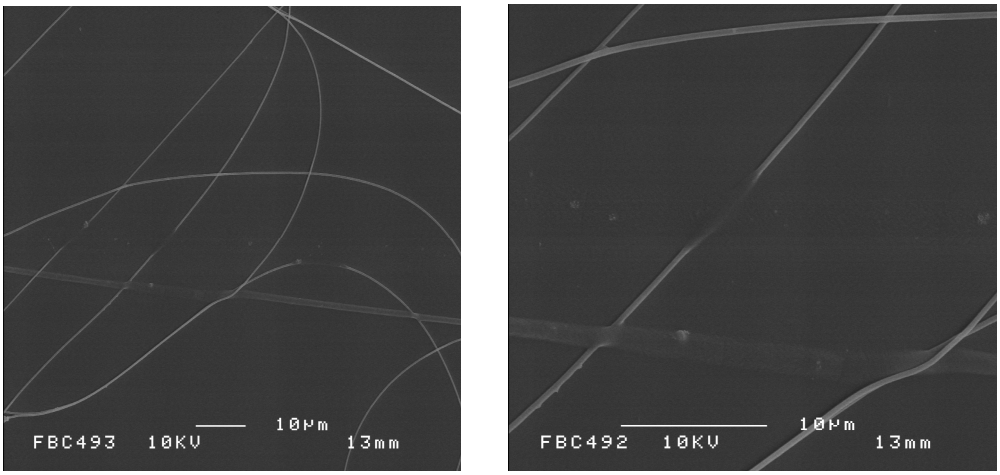

Figure 6.6 Short PVA nanofibres obtained after electrospraying water droplets onto electrospun PVA nanofibres

6.2.1.4 Electrospinning of Nanofibres onto Conductive Metal Particles

Nanofibres can be easily deposited onto sharp edges or conductive points on a grounded electrode due to high electrostatic field strength that develops when applying voltage during the electrospinning process. When conductive metal particles are dispersed onto a substrate, electrospun nanofibres may only deposit between conductive particles to form short fibre lengths between the particles. For this study, copper nanoparticles in the range of 10 nm to 50 nm and aluminium particles in the micrometer size range have been selected due to their good conductivity. These metal particles were dispersed in a water solution and sonicated for 10 minutes using the above mentioned ultrasonic processor. This water solution was then transferred onto a clean silicon substrate using plastic syringe in order to disperse metal particles onto the substrate. This silicon substrate was left to dry in air which leaving well dispersed metal particles on it. Electrospinning of PVA nanofibres was carried out and this silicon substrate was placed on the ground electrode in order to collect the electrospun PVA nanofibres. SEM is used here to see the distribution of the electrospun fibres around the metal particles in order to access whether the electrostatic field strength is high enough to cause the resultant fibres to deposit between the metal particles. Figure 6.7 and Figure 6.8 have shown that those electrospun PVA nanofibres are mainly deposited onto and between these metal particles due to high electrostatic force. However, the fibres are still continuous and do not form short fibre lengths.

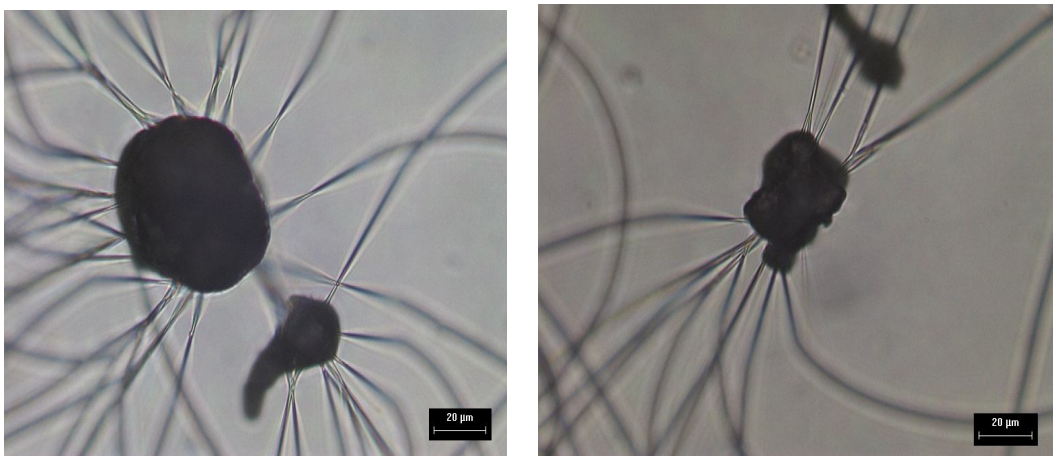

Figure 6.7 Optical images of PVA nanofibres deposited on aluminium particles

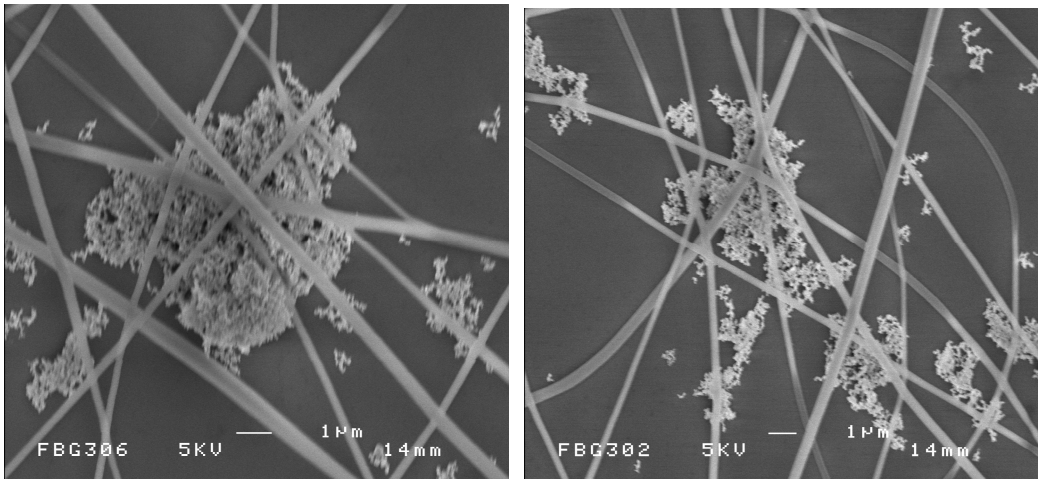

Figure 6.8 SEM images of PVA nanofibres deposited on copper particles

6.2.1.5 Short Fibres Formed by FIB (Focused Ion Beam) Cutting

Direct cutting of materials has been attempted using focussed ion beams (FIB) of relatively heavy ions, typically of Gallium. FIB is used extensively for patterning of samples and preparation of thin samples for transmission electron microscopy. FIB systems operate in a similar manner to SEM except ions of Gallium are focussed onto the sample [233]. Applying an electric field a Gallium source contacting a heated tungsten needle causes the ionisation and field emission of the

gallium atoms. The ions are then accelerated to an energy of 2 – 30 keV and focused onto the sample using magnetic lenses. The Gallium FIB is then raster scanned across the sample surface and the secondary electrons (or ions) that are emitted from the surface are collected and used to build an image. However, FIB differs considerably from SEM as the high energy ion beam will sputter atoms from the sample surface. Therefore FIB is less favourable for imaging, especially for softer samples that have a relatively high sputter rate. However, this sputtering potential is favourable when a material needs to be removed in a controlled manner underneath the ion beam such as for micro and nanomachining tool applications.

Focused ion beam can also be used for the deposition of material onto the sample surface. Beam assisted chemical vapour deposition is when a precursor gas is introduced into the chamber and allowed to chemisorb onto the sample. The FIB is then scanned across the required area and the gas is decomposed into a volatile and non-volatile component; the non-volatile component, for example platinum, is left on the surface during the decomposition process. Ion beams are particularly useful in cutting of electrospun polymer fibres as the beam itself can be positions with high spatial resolution. In addition, the diameter of the beam is around 10 nm, thus allowing accurate milling of samples. In this study, a Quanta 3D FEG system (as shown in Figure 6.9) was used in order to cut through electrospun PVA fibres in order to produce relatively short fibre lengths. The Quanta system consists of an SEM and a Focused Ion Beam (FIB) system. Figure 6.10 (a) shows the electrospun PVA nanofibre attached onto an AFM tip which is ready for FIB cutting, details for the nanofibre attachment will be introduced in the next section 6.2.1.6. A FIB accelerating voltage of 5 keV and beam current of 10 pA was used to cut the PVA nanofibre to a length around 30 μm is shown in Figure 6.10 (b).

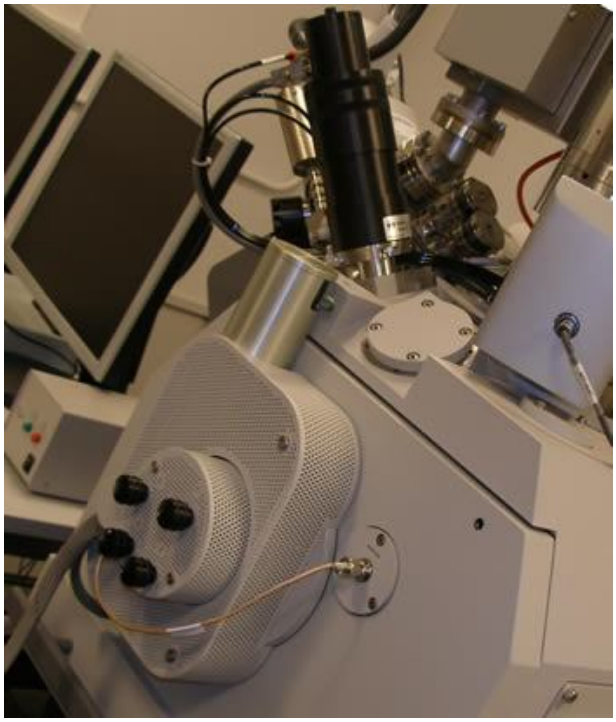

Figure 6.9 Quanta 3D FEG instrument

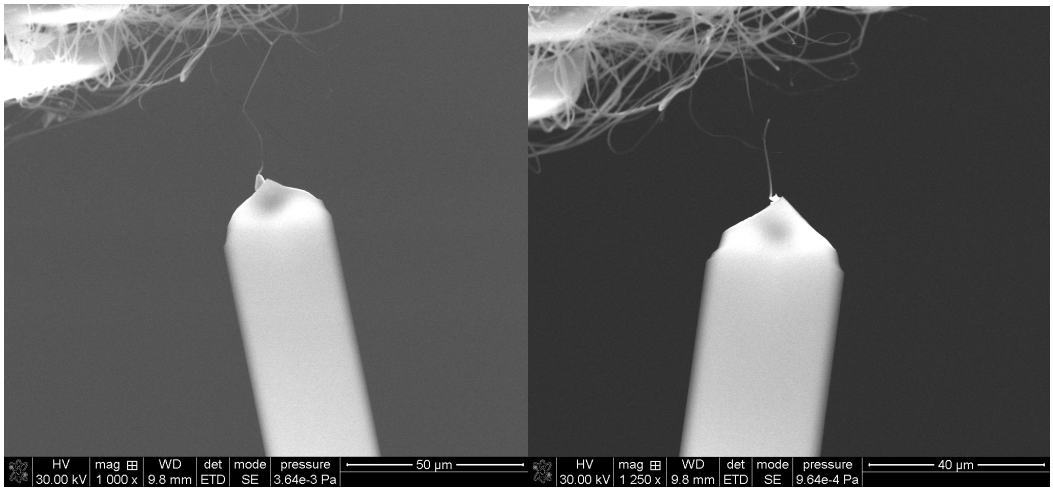

Figure 6.10 (a) Before FIB cutting **(b)** after FIB cutting

In summary, short polymer nanofibres have been prepared by ultrasonic processor, razor blade cutting, electrospraying water droplets onto nanofibres to dissolve parts of nanofibres away, electrospinning of nanofibres onto conductive metal particles and focused ion beam cutting. From the electrospraying water droplets

study, the ends of obtained short fibres adhered onto the glass slide, making removal of the fibres from the slide difficult. Electrospinning of nanofibres onto conductive metal particles was not a successful method to achieve short polymer nanofibres as nanofibres were deposited between metal particles but were still continuous. Ultrasonic processor and razor blade cutting can produce short electrospun fibres but the fibres can not be picked up for the AFM tip attachment. Focused ion beam cutting is deemed to be the most successful method to prepare short electrospun polymer fibres with a desired length. This FIB cutting method to form short fibres is advantageous comparing to other methods because a desired point on the fibre can be selected accurately for cutting.

6.2.1.6 PVA Nanofibre Attachment

Four steps were used in order to attach a short PVA nanofibre, cut using the FIB, onto an AFM tip, which is shown in Figure 6.11. The first step was to use a carbon tape to stick the aligned electrospun PVA nanofibre mats onto a manipulator arm attached within the SEM chamber. In addition, the chip of an AFM cantilever was attached onto the SEM specimen stage using carbon tape. Secondly the electrospun nanofibres attached to the manipulator arm were translated towards the AFM tip until an individual nanofibre contacts the AFM tip driving by the van der Waals attractive force. The third step was to deposit a thin layer of platinum onto the nanofibre contacting the end of the AFM tip in order to secure the nanofibre and the tip together, which is shown in Figure 6.12. The fourth step was to cut the fibre at a length of approximately 20 μm away from the fibre-AFM tip contact point using focused ion beam, as shown in Figure 6.13 (a). This length was selected because wetting force measurement only can be achieved by wetting the portion of this length. Figure 6.13 (b) shows the fibre attached onto the AFM tip from different angle to ensure that the fibre is pointing in the correct

direction. The PVA nanofibre-AFM tip was then deemed to be suitable for wetting tests.

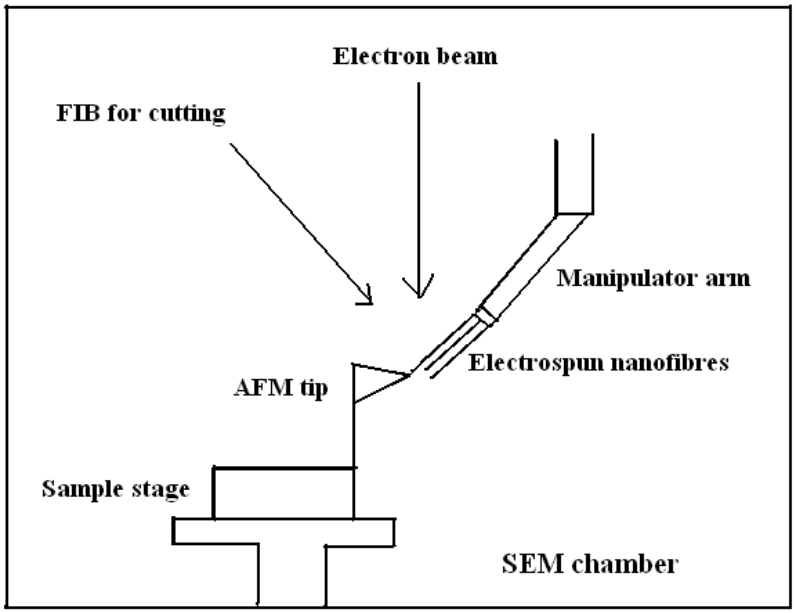

Figure 6.11 PVA nanofibre attachment process.

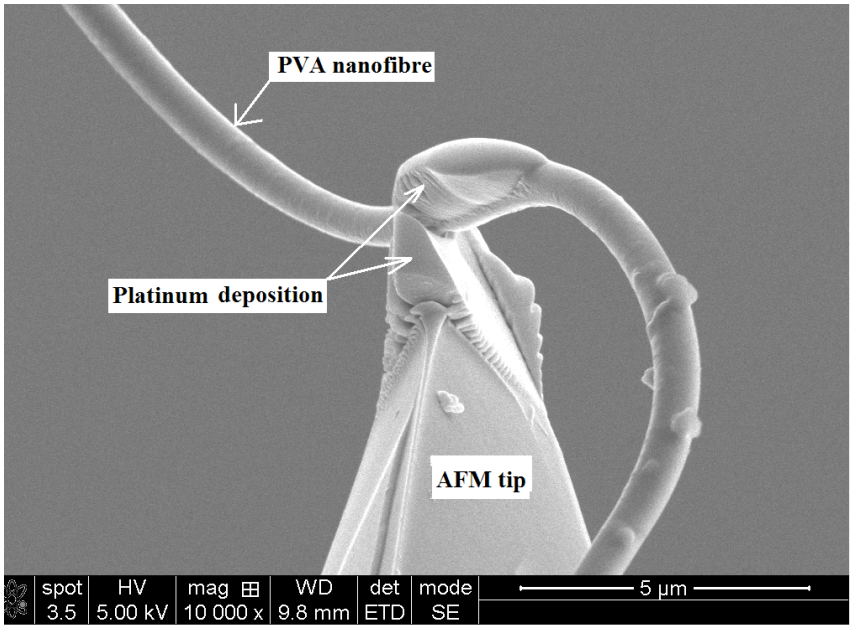

Figure 6.12 Attachment of PVA nanofibre onto an AFM tip before FIB cutting.

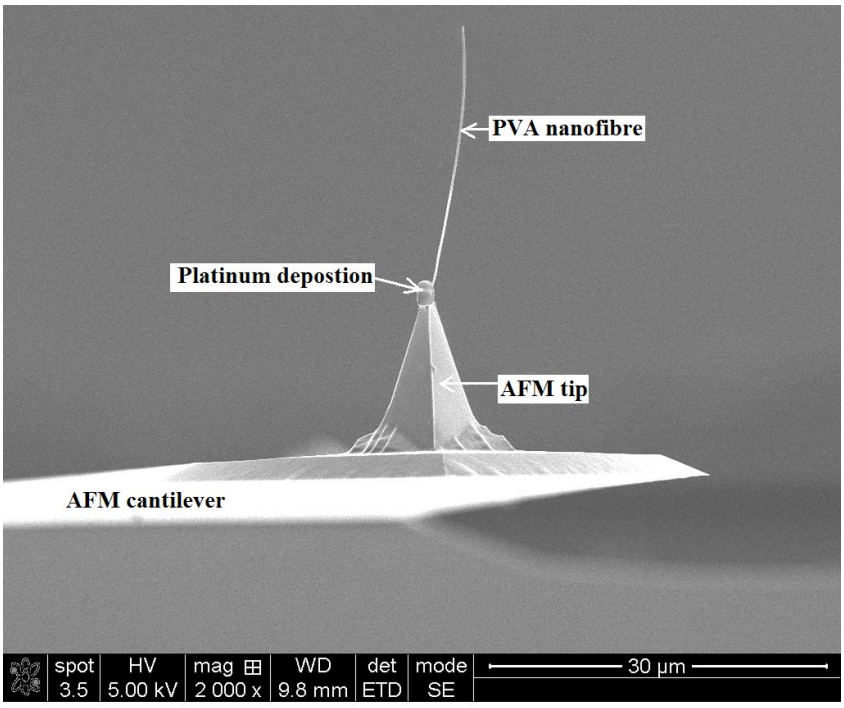

Figure 6.13 (a) Single PVA nanofibre attached onto an AFM tip after FIB cutting.

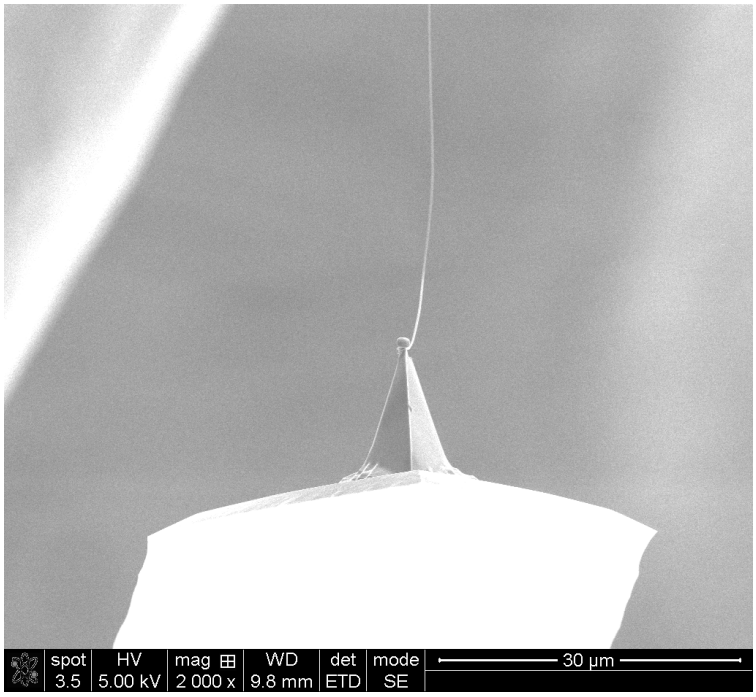

Figure 6.13 (b) Single PVA nanofibre attached onto an AFM tip after FIB cutting.

6.2.2 Methods

6.2.2.1 Wilhelmy Balance Measurements to Measure Capillary Forces using AFM

Owens-Wendt theory described in Section 2.4.4 can be used to calculate the dispersive and polar surface free energy of a solid material. These surface free energy components can be calculated if the contact angle between various probe liquids, of known dispersive and polar surface tension, and a solid material is measured. Measurement of contact angle between liquids of differing surface tensions and an individual electrospun fibre is critical in understanding its surface properties. Qualitative observation of the wetting behaviour between an individual electrospun PVA fibre and various liquids can be achieved using environmental scanning electron microscopy (ESEM). Most of electron microscopes require working in a vacuum condition. Environmental Scanning Electron Microscopy (ESEM) with special detectors can avoid this problem and work by decreasing the specimen temperature and reducing the vacuum to maintain water in a liquid state. The specimen structure can be examined in wet condition or the environment can be varied to detect dynamic changes in the specimen, such as absorption or dehydration processes. The ESEM is therefore a suitable instrument for visualizing the interaction between individual electrospun fibres and a liquid in order to determine the wetting behaviour. A Quanta 3D FEG ESEM was employed to observe the PVA nanofibre wetting behaviour with a number of liquid. The liquids were selected with a relatively low vapour pressure in order to inhibit excessive evaporation within the ESEM chamber. Liquid droplets of glycerol, PEG and formamide were placed onto ESEM sample stage and PVA

nanofibres attached on a manipulator arm were immersed into the liquid as shown in Figure 6.14. However these pictures can not be used to accurately measure the contact angles due to the relatively low resolution of the image but clearly indicate partially wetting between all liquids and the fibre sample. A Wilhelmy balance method is therefore used to measure the capillary forces between the PVA nanofibre attached to the AFM tip in order to further calculate the contact angles and ultimately the PVA nanofibre surface free energy.

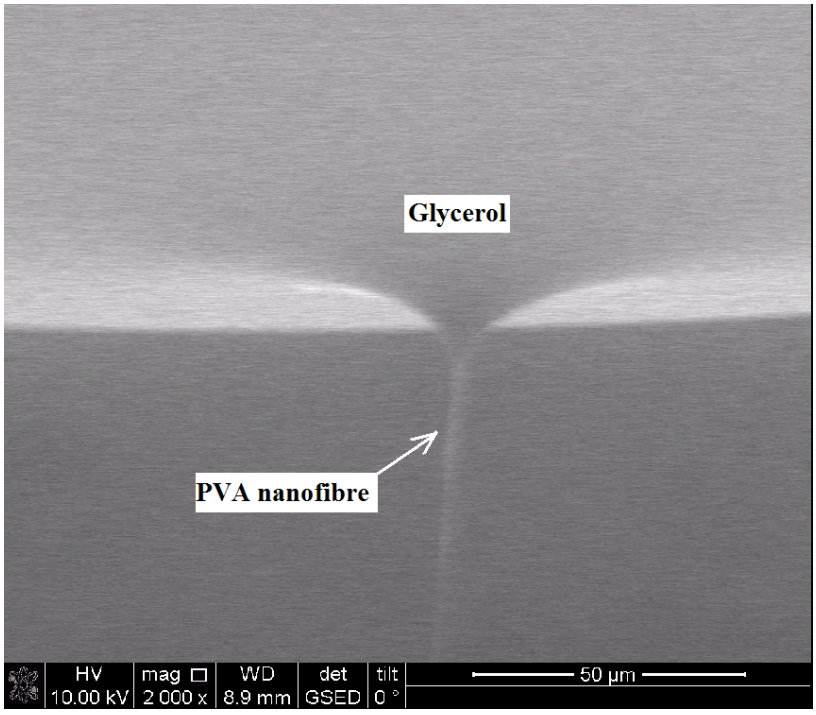

(a)

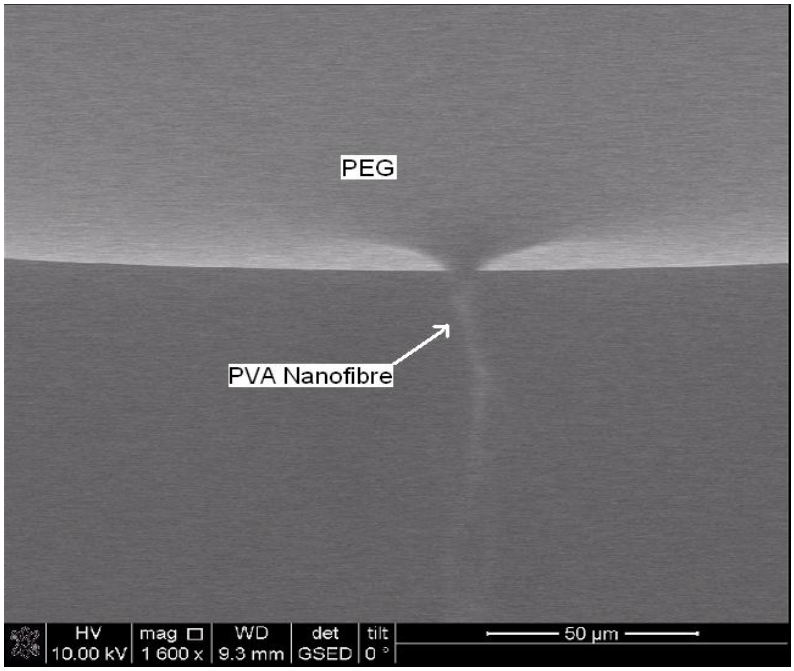

(b)

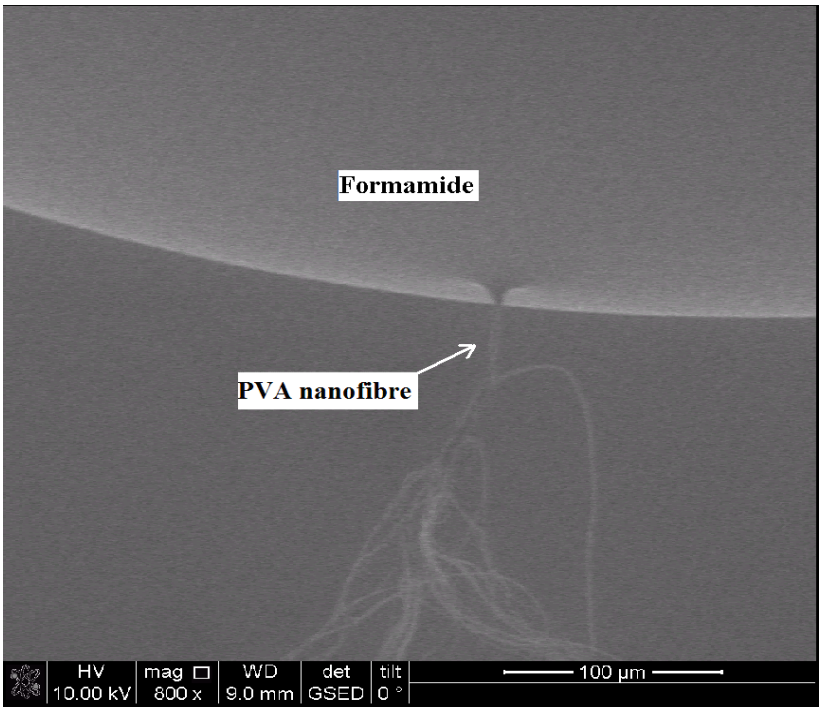

(c)

Figure 6.14 ESEM pictures of PVA nanofibres attached on a manipulator arm was immersed into (a) Glycerol; (b) PEG; and (c) Formamide.

Wilhelmy balance experiments were performed in air using a stand-alone AFM

(NT-MDT NTegra, Rus.) with the electrospun PVA fibre-AFM tips replacing the conventional AFM tips. Liquids of glycerol, polyethylene glycol (PEG) and formamide were placed separately into a liquid cell situated below the nanofibre-AFM tip. The principal of the Wilhelmy experiment was to raise the liquid cell up towards the PVA fibre attached to the AFM tip until contact is achieved. This contact point is accurately determined from bending of the AFM cantilever towards the liquid as partial wetting occurs. The magnitude of the cantilever bending can be converted to force by knowing the spring constant of the cantilever. The AFM was operated in a non-contact mode so that proximity of the liquid surface to the end of the PVA fibre caused the oscillation signal to drop by approximately 20%. The probe modulation was then disabled and the liquid moved slowly toward the nanofibre-AFM probe using the AFM z-piezo while monitoring the cantilever deflection signal. Contact is clearly observable from the cantilever deflection signal as the capillary force will drive the nanofibre to snap into the liquid causing the cantilever bending. The cantilever bending due to the capillary force was illustrated as a sudden drop of cantilever deflection signal for PVA nanofibre-liquid interaction as shown in Figure 6.15. This abrupt change in the deflection signal indicated that the nanofibre had been partially pulled into the liquid due to the capillary forces between the fibre and liquid. This was observed for all of the liquids during contact with PVA nanofibres, which is qualitative proof that electrospun PVA nanofibres are at least partially wetted by the probe liquids and have hydrophilic behaviour due to their contact angles are all less than 90º observed from Figure 6.14. A cantilever deflection signal change Δy_2 related to the time when capillary force acting on the nanofibre was recorded using a digital scope and can be measured. The nanofibre was then fully removed by retracting the sample surface with the *z*-piezo under AFM control. These experiments were repeated for at least ten different PVA nanofibres and for all three liquids.

Figure 6.15 Cantilever deflection signal versus time curve during liquid (glycerol) approaching an individual PVA nanofibre-AFM tip. A sharp drop in the AFM deflection signal indicates bending of the AFM cantilever towards the liquid surface indicating PVA nanofibre jump-in to glycerol probe liquid due to capillary forces.

The change in the deflection signal due to contact of the PVA fibre with each liquid can be used to find the capillary force acting at the fibre's surface. Experiments were repeated for all of the liquids. It is important to note that each liquid is mutually soluble within the other, thus any liquid residues on the nanofibre surface would not affect further wetting experiments when using another liquid.

Calibration of the cantilever is required in order to convert deflection signal to deflection distance. Converting the cantilever deflection signal into cantilever deflection distance is usually achieved by first contacting an AFM probe with a hard sample. Once contact has been achieved, movement of the sample by a

defined amount using the AFM's z-piezo positioner causes a corresponding change in the AFM cantilever bending. However, this method cannot be carried out here as a compliant PVA nanofibre is attached to the end of the AFM tip. Thus, contact of this modified AFM tip with a hard substrate is most likely to cause bending and buckling of the nanofibre itself. It was therefore deemed necessary to remove the PVA nanofibre from the AFM tip in order to carry out the AFM cantilever calibration. To achieve this removal, the liquid cell mounted on the sample stage was replaced by a clean silicon substrate with part of the surface area covered by carbon tape. Secondly, the carbon tape on the substrate was moved up towards the PVA nanofibre attached to the AFM tip using the AFM z-piezo positioner until considerable contact was made, indicated by a large AFM cantilever bending deflection away from the substrate. Retraction of the sample away from the AFM tip was expected to remove the PVA nanofibre from the tip's surface. Figure 6.16 (a) and (b) show the force distance curves from clean silicon substrate with the fibre attached onto the AFM tip and when the fibre has been removed from the AFM tip respectively. The non-linear behaviour when the PVA nanofibre is attached to the AFM tip is indicative of buckling behaviour of a compliant fibre. The force distance curve with the PVA fibre removed is indicative of a hard contact with change in the z-piezo position, indicated as a change in the x-axis value, causes a corresponding change in the cantilever deflection signal. When the fibre is still on the AFM tip, the gradient from the force-distance curve is non-linear due to fibre and silicon tip has different elastic modulus. Cantilever deflection signal versus distance curve was recorded during contact with a hard silicon substrate and the gradient $\frac{\Delta x'}{\Delta y'}$ determined, where $\Delta x'$ is the cantilever moving distance and $\Delta y'$ is the cantilever deflection signal change by moving a distance of $\Delta x'$.

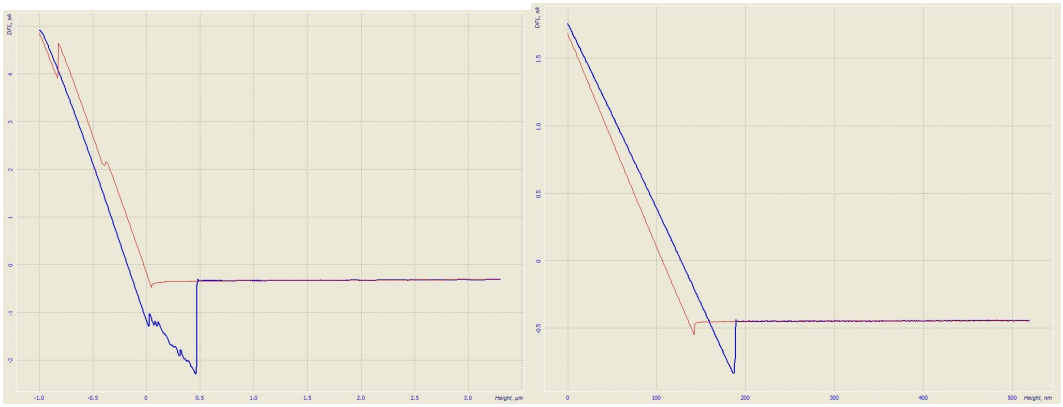

Figure 6.16 (a) Force-distance curve with fibre attached onto the AFM tip **(b)** Force-distance curve of fibre has been removed from the AFM tip

After the determination of both Δy_2 and $\frac{\Delta x'}{\Delta y'}$, the capillary force from Wilhelmy balance method [234] (F_r) can be calculated as $F_r = k \times \frac{\Delta x'}{\Delta y'} \times \Delta y_2$. Equation 2.31 was used to calculate the equilibrium contact angle for each probe liquid. The equilibrium contact angle (θ) can be calculated if the restoring force of the cantilever (F_r), the nanofibre diameter (d) and the probe liquid surface tension (γ_l) were all known. In this study, the nanofibre diameters were characterized from SEM. The probe liquid surface tensions of glycerol, PEG and formamide were taken from the literature [234, 235]. Therefore the equilibrium contact angle for each probe liquid can be calculated after knowing the restoring force of the cantilever. Finally, the dispersive and polar components of the electrospun nanofibre surface free energy can be determined by Owens-Wendt theory as described in section 2.4.6.3.

6.2.2.2 Fourier Transform Infrared (FTIR) Spectroscopy

In this study Fourier transform infrared (FTIR) is used to analyse hydroxyl groups

and hydrogen bonds of electrospun PVA nanofibres and comparative PVA films. FTIR is a measurement technique based on molecular spectroscopy. Its basic principle is that specific molecules of a specimen absorb infrared light energy at specific wavelengths, recognized as their resonance frequencies.

An FTIR spectrometer operates by measuring the wavelength of light absorbed by a sample. The amount of light absorbed is plotted against the wavelength of light, known as an interferogram. A conventional FTIR spectrum is produced by applying a Fourier transform to this interferogram. The light intensity transmitted through the specimen is measured at every wavenumber which allows the amount of light absorbed by the specimen to be determined because of the difference between the light intensity before and after the specimen. In the spectrum's infrared region, the resonance frequencies of a molecule are due to the existence of molecular functional groups particular to the molecule. FTIR spectra of the electrospun PVA nanofibres and bulk PVA film were obtained using a Nicolet 8700 FTIR spectrometer (Thermo Electron Corporation, UK) in our study for comparison, as shown in Figure 6.17.

Figure 6.17 Nicolet 8700 FTIR spectrometer

6.2.2.3 X-ray Photoelectron Spectroscopy (XPS)

X-ray photoelectron spectroscopy (XPS) technique is used to analyse our electrospun PVA nanofibre surfaces. XPS is a quantitative spectroscopic technique which can measure the elemental composition of a material surface in an ultra high vacuum condition. XPS spectra are obtained by irradiating a material with an X-ray beam while at the same time measuring the kinetic energy and number of electrons that escape from the top surface 1 to 10 nm of the material being analyzed. Figure 6.18 shows the Kratos Axis Ultra-DLD system used to analyse our electrospun PVA nanofibre samples combining XPS, micro XPS and imaging XPS together [236]. Electrons ejected from the specimen surface are energy filtered through a hemispherical analyser (HSA) before the intensity for a defined energy is recorded by a detector. As core level electrons in solid-state atoms are quantized, the resulting energy spectra show resonance peaks characteristic of the electronic structure for atoms at the specimen surface. An XPS spectrum is a chart of the number of electrons detected related to the binding energy of the electrons detected. Each element produces a typical set of XPS peaks at typical binding energy values that directly detect each element that exist in or on the material surface being analyzed. These typical peaks correspond to the electron configuration of the electrons within the atoms, e.g., 1s, 2s, 2p, 3s, etc [237].

Electrospun PVA nanofibre samples were mounted using a small amount double sided carbon tape and were analysed using a Kratos Axis Ultra DLD photoelectron spectrometer. All samples were recorded at 40 eV for narrow scans and 160 eV pass energy for survey spectra. The analysis area was 700 x 300 μm.

Figure 6.18 The Kratos Axis Ultra-DLD system at Cardiff University [236]

6.3 Results and Discussion

The forces measured from AFM acting on individual electrospun PVA nanofibres from contact with glycerol, PEG and formamide liquids due to capillary force are shown in Figure 6.19. Any significant bending of electrospun PVA nanofibre at the liquid surface would contribute to the measured cantilever deflection and must be considered together with the wetting force properly interpret the force data. Qualitative observations of the nanofibre wetting in an environmental SEM (Figure 6.9) corroborate the model presumed here of a straight nanofibre, wet by a liquid meniscus.

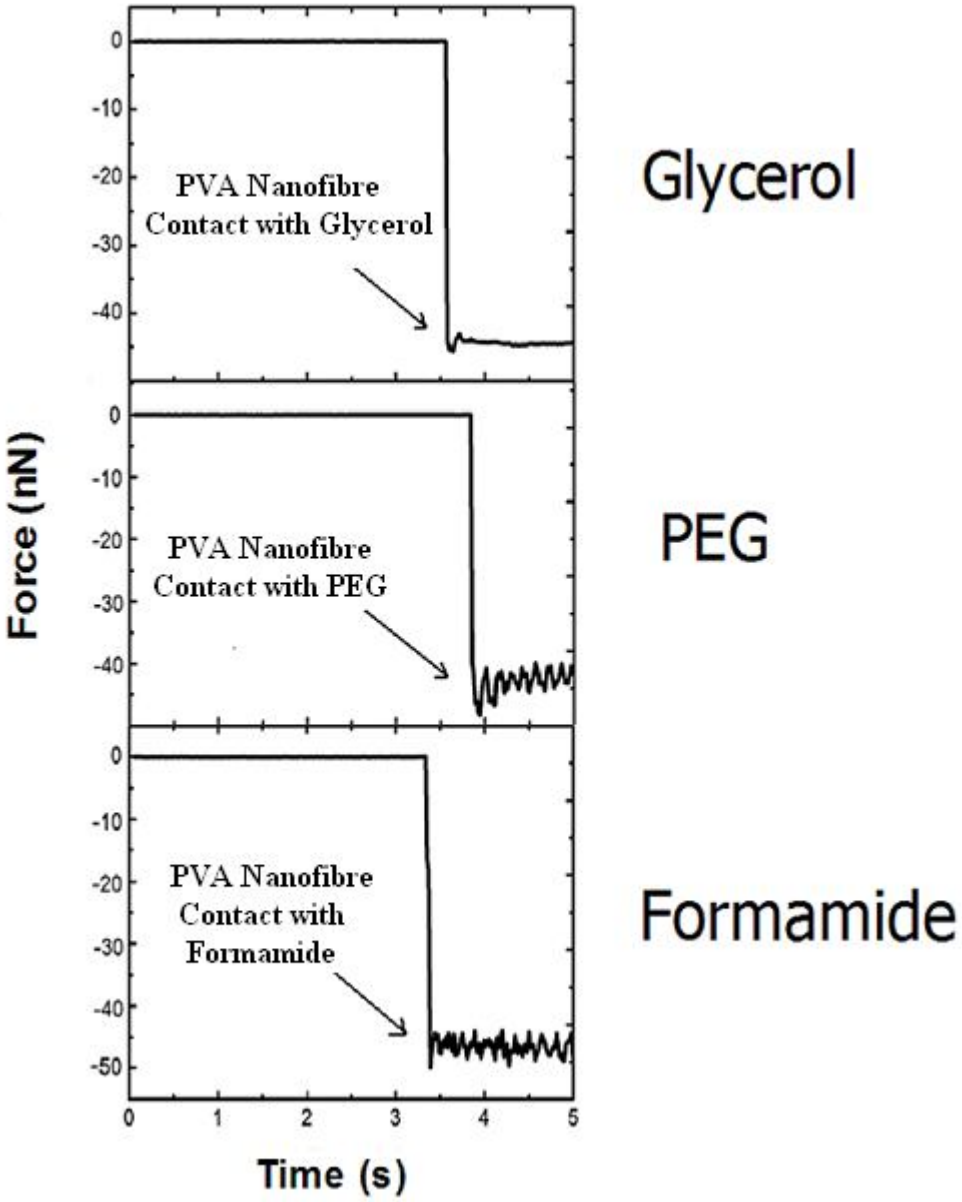

Figure 6.19 Force profiles for individual electrospun PVA nanofibre contacting liquids of glycerol, PEG and formamide. A sudden change in the force with time during the fibre approach to the liquid surface is indicative of the fibre jump-in into the liquid. The negative force represents attraction between the PVA nanofibre and each probe liquid. The small bumps seen at 3.6, 3.9 and 3.3 s, respectively, can be related to environmental noise, and are not reproducible.

Individual electrospun PVA nanofibres with diameters of approximately 400 nm

were attached to AFM tips. The nanofibres were selected in a SEM prior to attaching to the AFM tip thus the diameter of the nanofibre was accurately determined. PEG, glycerol and formamide were used for the probe liquids in this study, with the liquid properties list in Table 6.1. The contact angles are calculated from equation 2.31 as following:

$$F_r = \pi d \gamma_l \cos\theta \qquad (6.1)$$

Table 6.1 Physical parameters for various liquids wetting individual PVA nanofibre [234, 235]

Probe liquid	γ_l **(mJ m^{-2})**	γ_l^d **(mJ m^{-2})**	γ_l^p **(mJ m^{-2})**	**Contact angle (˚)**
Glycerol	64.0	34.0	30.0	58.2 ± 2.9
PEG	48.3	29.3	19.0	36.4 ± 2.6
Formamide	58.2	39.5	18.7	47.1 ± 3.0

The contact angle value increases as the probe liquid surface tension increases, with glycerol exhibiting the largest contact angle (58˚). The dispersive and polar surface free energy of electrospun PVA nanofibre can be calculated from liquid contact angles with the nanofibre surface and the physical properties of each liquid using the Owens-Wendt equation:

$$\frac{\gamma_l(1+\cos\theta)}{2\sqrt{\gamma_l^d}} = \sqrt{\gamma_s^p}\left(\frac{\sqrt{\gamma_l^p}}{\sqrt{\gamma_l^d}}\right) + \sqrt{\gamma_s^d} \qquad (6.2)$$

A plot of Owens-Wendt equation, using the contact angles measured in this study and the literature values of the liquid surface tension components reported in Table 6.1, is shown in Figure 6.20. The linear trend line in the plot supports the validity of Owens-Wendt model here, and allows accurate determination of the PVA nanofibre

diepersive and polar components. The gradient gives $\sqrt{\gamma_s^p}$, and the intercept gives $\sqrt{\gamma_s^d}$, therefore from Figure 6.20, we can get:

$$\gamma_s^d = 38.8 mJm^{-2}$$
$$\gamma_s^p = 5.1 mJm^{-2}$$

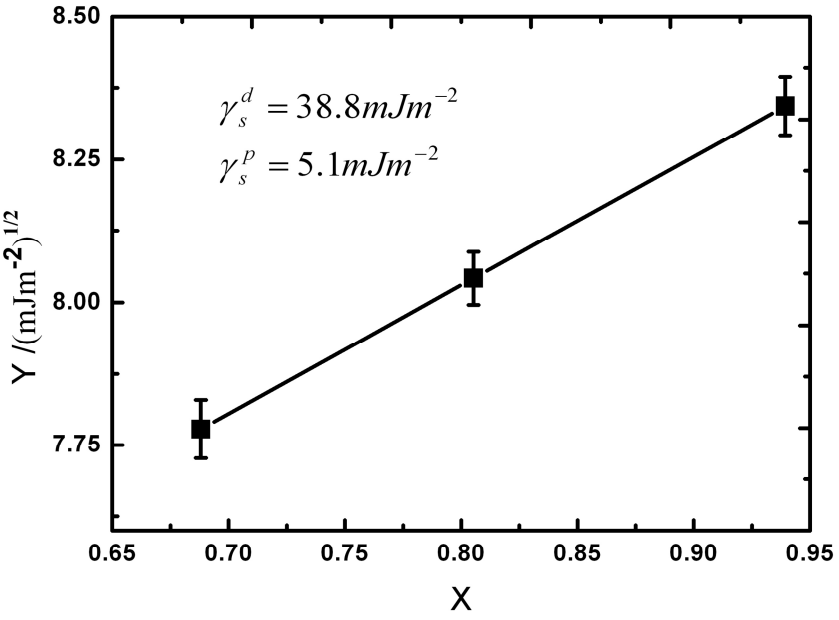

Figure 6.20 Owens and Wendt plot for single PVA nanofibre. The *y* axis value *Y* represents $[\gamma_l(1+\cos\theta)]/2\sqrt{\gamma_l^d}$, and the *x* axis value *X* is $(\sqrt{\gamma_l^p}/\sqrt{\gamma_l^d})$. Each point is an average of at least five measurements.

The dispersive surface free energy value of electrospun PVA nanofibres is in a good agreement with the value measured from contact mechanics JKR theory of about 40 mJm^{-2}. The polar component of PVA nanofibres is less than the bulk PVA polar value of 10.4 mJm^{-2}. This result shows the electrospun PVA nanofibre surface is less polar comparing to the bulk polymer film surface which indicates the hydroxyl group organization for nanofibres is different from bulk polymer

surface. In order to investigate the organization of the chemical groups on PVA nanofibre surface, FTIR and XPS techniques have been used for this study.

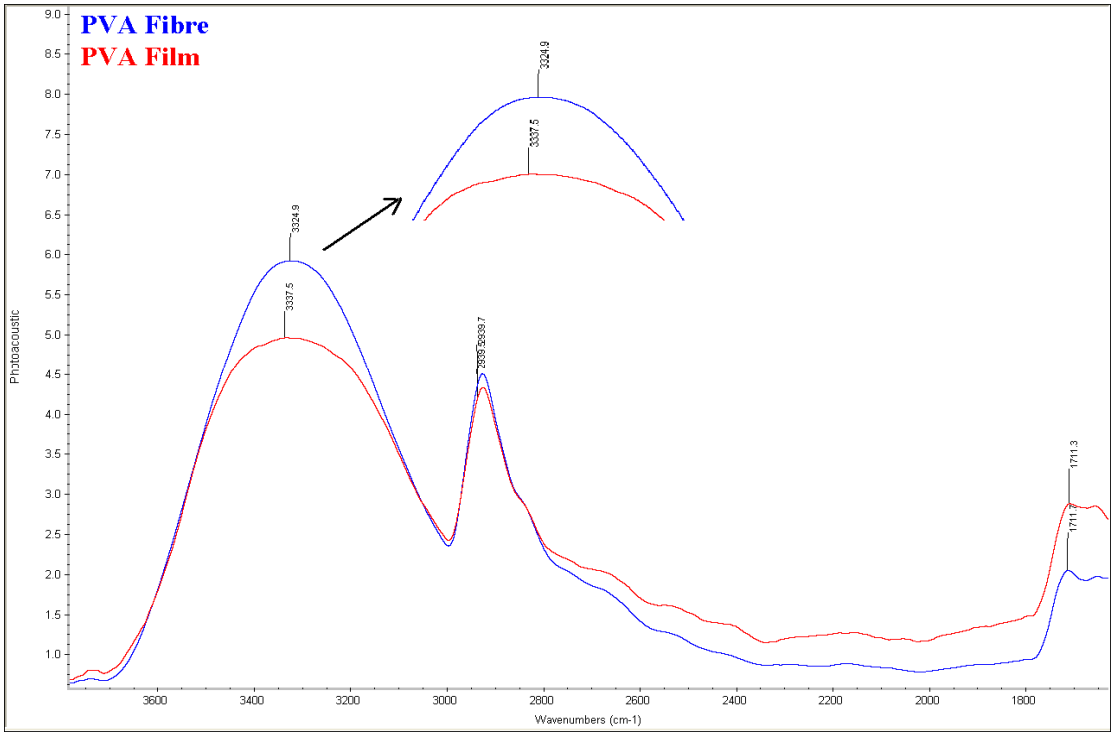

Figure 6.21 FTIR spectrum of PVA nanofibres and bulk PVA film.

PVA is an amphiphilic molecule composed of both hydrophilic (–OH) and hydrophobic (–CH_2) groups. The wetting results and Owens-Wendt plot in Figure 6.20 suggest that the hydrophilic and hydrophobic groups are organized such that the polar contribution of the PVA nanofibre surface is less than bulk values. Previous work has shown the alignment of the PVA chains within a nanoporous template produced nanofibres with hydrophilic groups pointing away from the nanofibre surface [238]. This work therefore provides some potential mechanism to explain the relatively low polar contribution to the electrospun PVA surface free energy values. Figure 6.21 shows the FTIR spectrum of both PVA nanofibres and unaligned bulk PVA film. The first peak at the left of the plot represents the hydroxyl group vibrational mode. Electrospun PVA fibres show a peak at 3325

cm^{-1}, which shifts to 3337 cm^{-1} for the bulk PVA film. The wavenumber is proportional to vibrational frequency, with an increasing wavenumber indicating an increasing vibrational frequency. The origin of the increased vibrational frequency for the –OH group in the PVA film must be due to less restrictions in its movement. Thus, the –OH groups in the electrospun PVA nanofibres should be constrained. An increase in the hydrogen bonding between –OH groups would be expected to provide this contraining effect. This result indicates that the electrospun PVA fibres have more hydrogen bonding comparing to bulk PVA film. As FTIR measures the chemical groups from the surface down to depths of around a few microns, the above result is for the whole nanofibres rather than just their surface. Comparison of the FTIR data to the Owens-Wendt plots showing a less polar PVA fibre surface compared to the film may indicate that the formed hydrogen bonds are within the nanofibres rather than present on the nanofibre surface. Figure 6.22 represents the possible conformation of PVA molecules at the air/solid interface, where $–CH_2–$ groups are present at the surface, and hydrogen bonds are formed in the interior [238]. This model can clearly explain our results. In order to investigate this model, XPS has been used in order to examine the surface of the electrospun PVA fibres only.

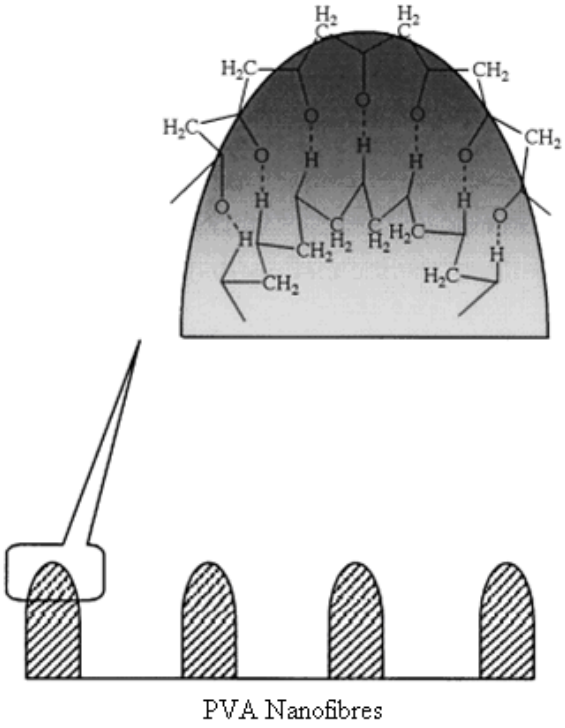

Figure 6.22 Possible conformation modes of the PVA molecules at the air/solid interface, the four columns at the bottom indicating PVA nanofibres [238].

XPS results for electrospun fibre mats were evaluated in terms of incident x-ray beam angle. The difference of the angle for systems where there is a thin outer layer (5 to 50 Å) of material allows signals from the outer layer to be differentiated from that of the substrate. This analysis method is important because the relative distance through the surface travelled by electrons from the substrate and the outer layer varies with this angle. For an actual position at depth *d* below the surface, the real distance travelled by the escaping electrons will be $d\sin\theta$, where θ is the angle. This means that small angles will result in spectra where the relative signal intensity from the outer layer vs. the substrate will be larger. i.e., the spectra will be more surface sensitive [239].

We took a repeat set of spectra at a 45^{o} angle, increasing the surface sensitivity of the XPS further and a similar pattern was observed for O(1s). Figure 6.23 shows

X-ray photoelectron spectra illustrating the dependence of the detection angle of O(1s) for PVA nanofibres. From references [240-243] we know that the binding energy of O(1s) for hydrogen bonds is 532.2 eV and for free hydroxyl groups is 533.5 eV respectively. Therefore the peak of O(1s) can be substituted into two peaks, one represents hydrogen bonds which is at the right of the plot, the other one represents free hydroxyl groups which is at the left of the plot. The intensity of hydrogen bonds for the electrospun PVA fibres with 45^{o} detection angle (more surface sensitive) is 0.72, and the intensity of hydrogen bonds for the electrospun PVA fibres underneath the surface is 0.85. This result indicates that hydrogen bonds are more formed in the nanofibres interior rather than the nanofibre surface, which is in a good agreement with the Owens-Wendt data and the above proposed model in Figure 6.22. Therefore this molecular structure will lower the polar contribution of the electrospun PVA nanofibres surface free energy. An increased hydrogen bonds formed within the PVA nanofibres will further enhance the intermolecular forces between the fibre molecules giving an increased dispersive surface free energy of the electrospun PVA nanofibres.

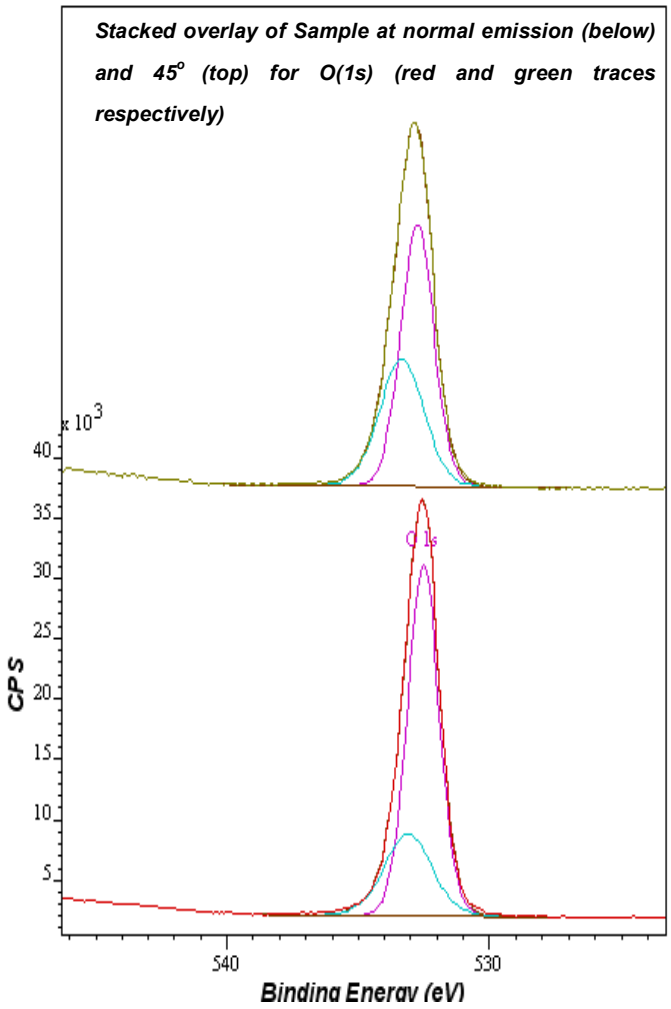

Figure 6.23 X-ray photoelectron spectra illustrating the dependence of the detection angle for O(1s) of PVA nanofibres.

6.4 Conclusions

The wetting behaviour of individual electrospun PVA nanofibres has been investigated in this Chapter using a Wilhelmy based single fibre-AFM method. The resultant calculated contact angles were used to find the dispersive and polar component for the PVA surface free energy using Owens-Wendt theory. The dispersive surface free energy is in a good agreement with the result from Chapter 5 which shows PVA nanofibre has a dispersive surface free energy value of around 40 mJm^{-2} whereas the polar component is lower than a comparable PVA

film of 10.4 mJm^{-2}. Structure information of the electrospun fibre using FTIR and XPS surface techniques explore how an increase in hydrogen bonds formed within nanofibres rather than on the fibre surface enhances the dispersive contribution but lowers the polar contribution. However, the PVA nanofibre total surface free energy value is still larger than bulk polymer film due to nanofibre has a total surface free energy of 43.9 mJm^{-2} whereas bulk PVA only has a total surface free energy of 38.6 mJm^{-2} [244].

Chapter 7

Conclusions and Future Work

7.1 Conclusions

This chapter forms overall conclusions based on previous work in the thesis examining the surface properties of electropun polymer nanofibres.

Polymer films and fibres can be produced by various methods such as gel-spinning or mechanical drawing in order to achieve their alignment and improve their mechanical properties. Electrospinning is a potential fibre fabrication method to improve fibre alignment on the molecular level. Chapter 3 of this thesis has shown that electrospinning is a successful method to produce polymer nanofibres with well controlled morphology. Higher concentration polymer solutions always produce larger average diameter fibres. This can be explained by considering solution viscosity. In general, a higher viscosity results in larger diameter fibres due to the reduction of solvent evaporation rate from the liquid jet. Viscosity of polymer solution can be significantly increased by increasing molecular weight, the resultant fibre morphology can change from beads structure to fibres with small diameters, and further large fibre diameters. Increasing flow rate will deliver more polymer solution to the Taylor cone, which

increases the size of the cone. Thus, the diameter of the liquid jet initiation from the Taylor cone tip was increased, which resulted in larger diameter fibre formation. Increasing surface tension of a spinnable polymer solution results in decreasing fibre diameter. The average electrospun fibre diameters could also be slightly increased with increasing DTC. Increase in the solution conductivity causes higher electric net charges on the liquid jet, resulting in an increase in the force exerted on the jet to allow smaller fibres to be produced. Applied voltage also played a significant role for determining fibre morphology. The average fibre diameters decreased with increasing applied voltage when electrospinning was in a stable cone-jet mode region, since the high electric field strength could favour the formation of thinner liquid jet in this mode. Results further showed that the average fibre diameters can be increased if increasing applied voltage above the cone-jet mode value. This diameter increase is due to the charged liquid jet being ejected from the inside of the needle tip, allowing more liquid to be removed from the needle tip while increasing the applied voltage.

Electrospinning process involves fast stretching of the electrified jet and evaporation of the solvent. Therefore polymer chains will experience a strong shear force during this process and this strong shear force and potentially rapid solidification of the polymer fibres can avoid the polymer chains relaxing back to their equilibrium conformations. Consequently the polymer chain conformation and the alignment of the resultant polymer fibres should be different from products obtained by solution casting or conventional spinning methods. AFM contact mechanics has been used to examine the polymers surfaces of both electrospun nanofibres and larger equivalents related to their chain ordering or molecular alignment. Results have shown dispersive surface free energy of individual electrospun fibres are independent of their fibre diameters produced using different applied voltages. In addition, the surface free energy of electrospun

fibres is higher than their bulk polymer film equivalents achieved from a mechanical drawing method. The dispersive surface free energy is an intermolecular attractive force that arises from a cooperative oscillation of electron clouds on a collection of molecules at relatively close range. The distance between molecules is important as an instantaneous dipole moment of one atom or molecule induces a similar temporary dipole moment in adjacent atoms or molecules. Dispersion forces not only bring molecules together but also tend to mutually align or orient them. Therefore the interaction between instantaneous and induced dipoles will become stronger and give rise to larger dispersive surface free energy when the intermolecular chain distance between the molecules reduces. Results indicate that this dispersive surface free energy is intimately linked to density of the polymer and ultimately the molecular spacing between polymer chains. Drawing of polymer films supports this relationship between polymer density from increased molecular alignment and the dispersive surface free energy. Electrospun fibres follow this trend and show a significantly higher dispersive surface free energy than the largest draw ratio films, indicating that the electrospinning process produces significant molecular orientation at least at the fibre surface. Calculation of dispersive surface free energy for a range of different polymer samples is therefore highly suitable for understanding molecular ordering in amorphous polymer samples. A modified Lennard-Jones model suggested that the proposed physical process is reasonable. Density measurements also provide supporting evidence for improved packing of polymer chains and, therefore, a smaller average distance between polymer chains. Structure information of the electrospun fibre using FTIR and XPS surface techniques explore how an increase in hydrogen bonds formed within nanofibres rather than on the fibre surface enhances this dispersive contribution but lowers the polar contribution. The wetting behaviour of electrospun fibres at length scales above individual fibres highlights how superhydrophobic surfaces can be produced from nanofibre

networks with defined spacing and geometries. This superhydrophobicity was adequately described by a Cassie-Baxter model modified to account for the fibrous geometry.

Surface properties of electrospun polymer fibres have not been sufficiently studied from previous literature, but this thesis explores the surface properties of electrospun polymer fibre at two length scales; that of the fibre itself and the second at the level of networks of many electrospun fibres. Better molecular alignment has been achieved for nanofibres from electrospinning process, this is promising as improved molecular alignment and larger surface free energy of nanofibres can potentially provide better adhesion and good interfacial bonding for the fibres and matrix in a wide composites applications.

7.2 Future Work

7.2.1 Electrospinning Hollow Polymer Fibres

7.2.1.1 Materials

As concluded from the above section, better alignment occurs on the electrospun nanofibre surfaces comparing to their bulk equivalents. Electrospun hollow polymer fibres producing another internal surface could provide more polymer alignment at the internal surface and within the hollow fibres as a whole. Also hollow nanostructures made of polymers, ceramics and other materials have been attractive in many applications such as nanofluidic channels, optical waveguides, energy conversion, gas storage and drug release. Electrospinning has been shown to be an effective method for the production of such nanostructures.

Polyvinylpyrrolidone (PVP) hollow fibres have been produced by Li and Xia [113] in previous literature. Herein we explore the flexibility of electrospinning hollow fibres from Li and Xia's technique and extend to polymers that we have used in this thesis i.e. PVA and PEO. We note that while PVA and PEO are water soluble, showing similarities with PVP, no attempts have been made to electrospin hollow fibres of this polymer despite their popularity in solid fibre electrospinning.

Physical properties of PVA and PEO and their solution preparation have been detailed in Chapter 3. Polyvinylpyrrolidone (PVP) is a water soluble polymer made from monomer *N*-Vinylpyrrolidoneas, shown in Figure 7.1. PVP was originally used as a blood plasma substitute but later on for a wide range of applications such as in industrial production, cosmetics, and medicine. In this study, polyvinylpyrrolidone (PVP) with an average molecular weight 1,300,000 $g.mol^{-1}$ was used for hollow fibre electrospinning and purchased from Sigma-Aldrich, UK. PVP powder has been dissolved in ethanol by continuous stirring for half an hour at room temperature (22-24 ^{o}C) to form 6 wt/v % concentration PVP solutions. PVA polymer solution with M_w of 98,000-143,000 $g.mol^{-1}$ and 8 wt/v % concentration, PEO polymer solution with M_w of 8,000,000 $g.mol^{-1}$ and 0.5 wt/v % concentration and PVP polymer solution with 6 wt/v % described above have been used for the shell solution. Mineral oil was used as the core solution for electrospinning and fabrication of hollow fibres. The selection of a hydrophilic polymer solution as the outer shell component and the inner hydrophobic oil ensures phase separation during the electrospinning process.

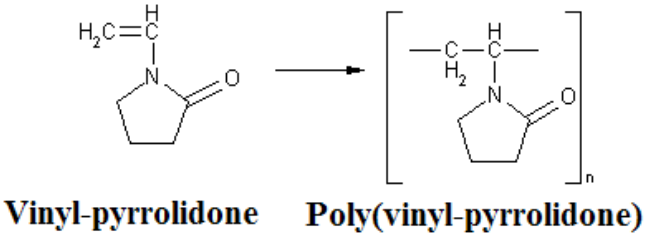

Figure 7.1 Polyvinylpyrrolidone Synthesis

7.2.1.2 Coaxial Needle Electrospinning

Electrospinning with a coaxial needle was used to produce PVA, PEO and PVP hollow fibres. The experimental set-up is similar to the set-up of electrospinning with single needle except that two pumps, two plastic syringes and a coaxial needle were used, as shown in Figure 7.2. The coaxial needle consists of an inner needle and an outer needle. Polymer solution was fed into the outer needle and mineral oil was fed into the inner needle. This experimental procedure followed the work of Li and Xia [113]. Unlike electrospray, electrospinning relies on the stretching of an electrified jet into continuous fibres and any breakup of the jet must be prevented. In particular, the core and shell liquids have to experience the same bending instability and be elongated at the same magnitude throughout the electrospinning process in order to obtain core-shell fibres with continuous, uniform diameters. One pump is used for the feeding rate supply of inner needle and the other one is for the feeding of outer needle. Polymer solution and oil were both fed at a constant flow rate. The flow rates for the PVA, PEO and PVP solutions fed to the outer needle was 10 $\mu l.min^{-1}$, 2 $\mu l.min^{-1}$ and 10 $\mu l.min^{-1}$ respectively. A corresponding feed rate for the oil into the inner needle was 5 $\mu l.min^{-1}$, 1 $\mu l.min^{-1}$ and 5 $\mu l.min^{-1}$ respectively. The applied voltage was selected as 15 kV for PVA, 10 kV for PEO and 9 kV for PVP during the electrospinning process. Clean silicon substrates and carbon coated TEM grids were placed 15 cm below the needle tip in order to collect the electrospun core-shell nanofibres. After electrospinning, octane was used to extract mineral oil to form hollow fibres.

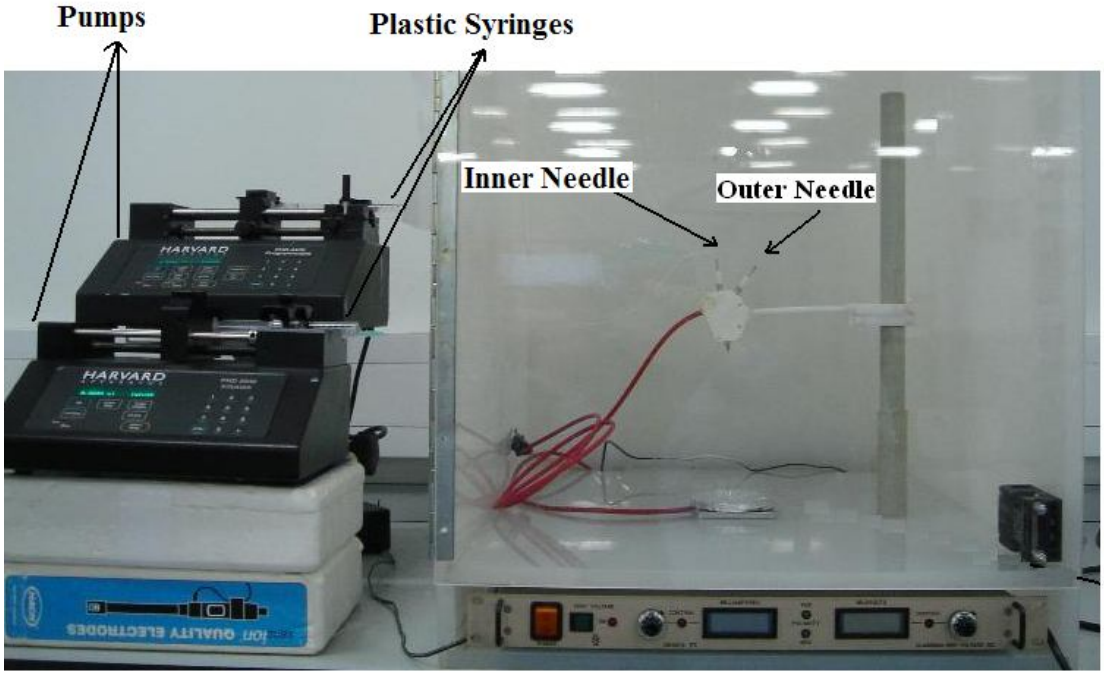

Figure 7.2 Coaxial needle electrospinning experimental set-up.

7.2.1.3 Preliminary Results

All experiments were conducted at room temperature in air, and the as-spun fibres were left in air for about one hour. Mineral oil was extracted by immersing the electrospun PVP fibres in octane for two hours, whereas PVA and PEO fibres required immersion in octane for three hours. TEM was used to image the resultant hollow fibre structure. Figure 7.3 (a) shows PVP nanofibre after electrospinning with mineral oil inside, and Figure 7.3 (b) has shown hollow PVP nanofibre after octane extraction. These images indicate that the mineral oil remains separated from the PVP shell, possibly due to the oil being hydrophobic whereas the PVP is hydrophilic, to give hollow polymer fibres produced from our coaxial needle electrospinning set-up. Figure 7.4 (a) shows electrospun PVA nanofibres after octane extraction but with mineral oil left inside. The remaining oil is shown as dark areas in the image as shown in Figure 7.4 (b). As mineral oil extraction time

for PVP fibres is less than for PVA and PEO fibres, the PVP fibres may have more open ends to allow ingress of octane to allow extraction of the mineral oil whereas PVA and PEO fibres might have closed ends inhibiting the extraction process. However, the small amount of mineral oil remaining in the internal fibre surfaces provides an opportunity to consider the internal wetting behaviour. The mineral oil within the PVA fibres, Figure 7.4 (a), shows an almost dewetting-type condition whereas the mineral oil in the PEO fibres, Figure 7.4 (b), indicates a partially wetting condition. If we consider the bulk surface free energies of PVA and PEO; 38.6 mJm^{-2} and 42.9 mJm^{-2} respectively with a similar polar component of 10.4 mJm^{-2} and 12 mJm^{-2} respectively, then we would expect the less polar PVA to be better wetted by the mineral oil. This increased wetting is observed from the images in Figure 7.4 but the extensive difference in the oil wetting behaviour from PVA to PEO, despite only a small difference in surface tension, is somewhat unexpected. This wetting discrepancy may be due to potentially different internal surface structures in the hollow fibres, indicating the need to understand these internal surfaces further.

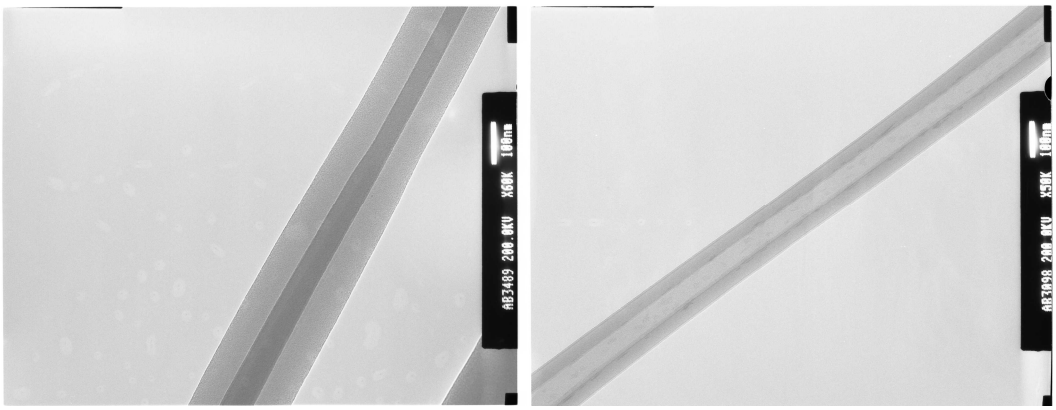

Figure 7.3 (a) Electrospun PVP nanofibre filled with mineral oil **(b)** Hollow PVP nanofibre after octane extraction

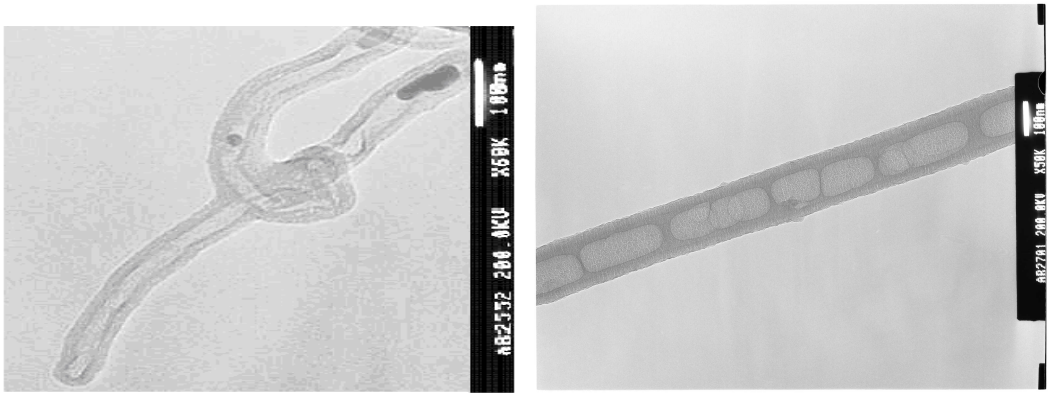

Figure 7.4 (a) PVA hollow fibres with traces of mineral oil left inside **(b)** PEO nanofibre with traces of mineral oil left inside

7.2.1.4 Future Work

PVA, PEO and PVP hollow fibres have been successfully produced from our coaxial needle electrospinning process. This method needs to be improved by using single needle electrospinning set-up rather than the complicated coaxial needle set-up in order to achieve a mass production for industrial applications.

7.2.2 Individual Hollow Fibre Wetting

Individual electrospun polymer nanofibre wetting tests from Chapter 6 only investigated the external surface wetting of polymer nanofibres. Evaluating the wetting behaviour of the internal nanofibre surfaces can also be carried out for the hollow nanofibres produced. The wetting behaviour of a hollow fibre will be a contribution of both the external and internal surface. As the external surface has already being examined in this work, the wetting of internal surfaces can be determined from such experiments. Razor blade cutting method and focused ion beam cutting method have been used to obtain short hollow fibres.

Results from razor blade cutting shown in Figure 7.5 reveal an obvious hollow structure although considerable plastic deformation after cutting gives an irregular end. This provides difficulties in measuring wetting forces directly using individual fibre experiments as described in Chapter 6 due to the complexity in defining the wetted perimeter. Results from FIB cutting in Figure 7.6 shows the the focused ion beam melts the end of the electrospun hollow fibre and the hollow structure is no longer available. Therefore a better solution to cut the electrospun hollow fibres is needed in order to carry out the individual hollow fibre wetting tests.

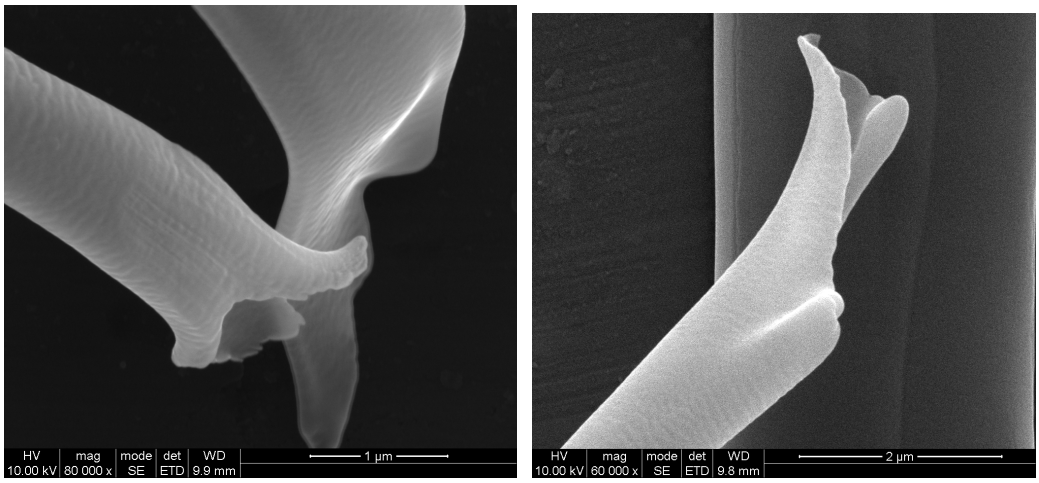

Figure 7.5 PVP hollow fibres with 1 µm diameter after razor blade cutting

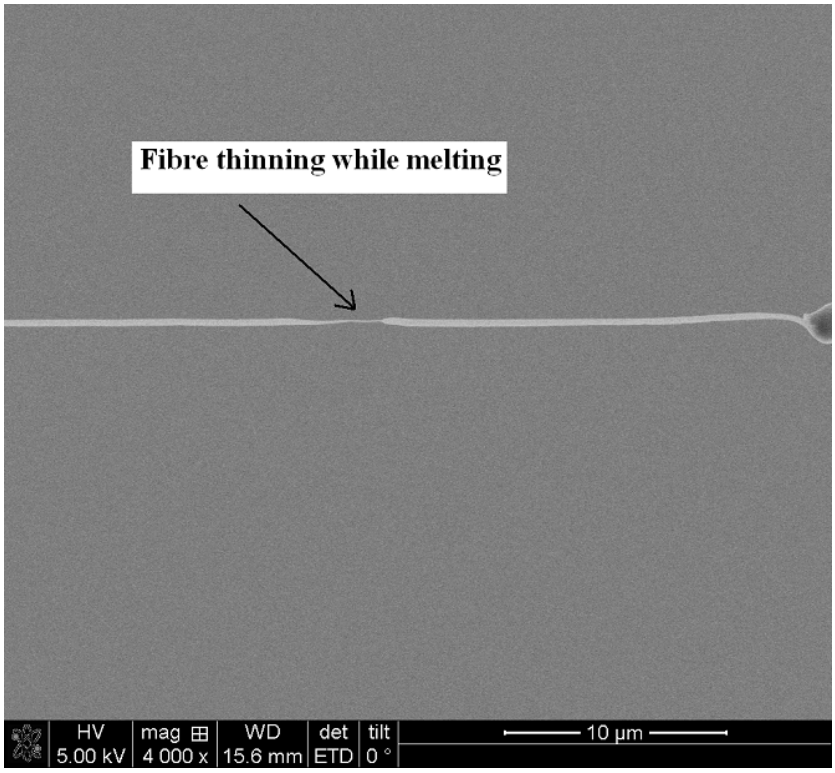

Figure 7.6 FIB melts the end of the electrospun hollow fibre

References

1. Somorjai, G.A., *Introduction to Surface Chemistry and Catalysis*. 1994, New York: Wiley, John & Sons, Inc. 696.
2. Overbury, S., P. Bertrand, and G.A. Somorjai, *The Surface Composition of Binary Systems. Prediction of Surface Phase Diagrams of Solid Solutions.* Chem. Rev, 1975. **75**(547).
3. Adamson, A.W., *Physical Chemistry of Surfaces*. 5th ed. 1990, New York: John Wisley & Sons, Inc.
4. Young, R.J. and P.A. Lovell, *Introduction to Polymers*. Published 1991, London: Chapman & Hall 443.
5. McCrum, N.G., C.P. Buckley, and C.B. Bucknall, eds. *Principles of Polymer Engineering*. 1997, Oxford University Press, USA. 464.
6. Rudin, A., *The Elements of Polymer Science and Engineering*. 2 ed. 1998: Academic Press. Page 24.
7. Rebenfeld, L., ed. *Encyclopedia of Polymer Science and Engineering*. 2nd ed. Vol. 6. 1986, John Wiley&Sons: New York. 662-664.
8. Alcock, B., *"Single polymer composites based on polypropylene: processing and properties."* in *Department of Materials*. 2004, Queen Mary, University of London: London.
9. Dhingra, A.K. and H.G. Lauterbach, eds. *Encyclopedia of Polymer Science and Engineering*. 2nd ed. Vol. 6. 1986, John Wiley&Sons: New York. 762-763.

10. Mallick, P.K., *Fiber-reinforced Composites*. 2 ed. 1993: CRC Press. Page 1.
11. William, J.R. and D. Callister, *Materials Science and Engineering: An Introduction*. 4th ed. 1997: Wiley. 852.
12. Ohta, T., *Review on processing ultra high tenacity fibers from flexible polymer.* Polymer Engineering and Science, 1983. **23**(13): p. 697-703.
13. Smook, J., W. Hamersma, and J.A. Pennings, *The fracture process of ultra-high strength polyethylene fibres* Journal of Materials Science, 1984. **19**(4): p. 1359-1373.
14. Pennings, J.P., et al., Philos MagA 1994. **69**.
15. Wagner, H.D., *Stochastic concepts in the study of size effects in the mechanical strength of highly oriented polymeric materials.* Journal of Polymer Science Part B: Polymer Physics, 2003. **27**(1): p. 115-149.
16. Reynolds, W.N. and J. Sharp, *Crystal shear limit to carbon fibre strength.* Carbon, 1974. **12**(2): p. 103-110.
17. Matsuo, Y., K. Yasuda, and S. Kimura, *Derivation of the Defect Size Distribution Function of the Monofilament in Case of the Coexistence of Several Types of Fracture Origins and an Application to Carbon-Fibers.* Nippon Seramikkusu Kyokai Gakujutsu Ronbunshi-Journal of the Ceramic Society of Japan, 1990. **98**(4): p. 389-395.
18. Griffith, A.A., ed. Vol. Ser A. 1920, Philos Trans R Soc London. 163.
19. Schreuder-Gibson, H., et al., *Protective textile materials based on electrospun nanofibers.* Journal of Advanced Materials, 2002. **34**(3): p. 44-55.
20. Ondarcuhu, T., Joachim, C, *Drawing a single nanofibre over hundreds of microns.* Europhys Lett 1998. **42**(2): p. 215–20.
21. Ma, P.X. and R.Y. Zhang, *Synthetic nano-scale fibrous extracellular matrix.* Journal of Biomedical Materials Research, 1999. **46**(1): p. 60-72.

22. Martin, C., *Membrane-based synthesis of nanomaterials.* . Chem Mater, 1996. **8**: p. 1739-46.

23. Feng, L., et al., *Super-hydrophobic surface of aligned polyacrylonitrile nanofibers.* Angewandte Chemie-International Edition, 2002. **41**(7): p. 1221-+.

24. Whitesides, G.M. and B. Grzybowski, *Self-assembly at all scales.* Science, 2002. **295**(5564): p. 2418-2421.

25. Fong H and R. DH., eds. *Electrospinning and formation of nano-fibers*. Structure formation in polymeric fibers, ed. S. DR. 2001. 225-46.

26. Deitzel, J.M., et al., *Controlled deposition of electrospun poly(ethylene oxide) fibers.* Polymer, 2001. **42**(19): p. 8163-8170.

27. D. Li, Y.X., *Electrospinning of Nanofibers: Reinventing the Wheel?* Advanced Materials, 2004. **16**(14): p. 1151-1170.

28. Reneker, D.H., et al., *Bending instability of electrically charged liquid jets of polymer solutions in electrospinning.* Journal of Applied Physics, 2000. **87**(9): p. 4531-4547.

29. Shin, Y.M., et al., *Electrospinning: A whipping fluid jet generates submicron polymer fibers.* Applied Physics Letters, 2001. **78**(8): p. 1149-1151.

30. Li, S.W., S.N. Jayasinghe, and M.J. Edirisinghe, *Aspirin particle formation by electric-field-assisted release of droplets.* Chemical Engineering Science, 2006. **61**(10): p. 3091-3097.

31. Chronakis, I.S. *Novel nanocomposites and nanoceramics based on polymer nanofibers using electrospinning process - A review.* in *International Forum on the Advances in Materials Processing Technology*. 2005. Glasgow, SCOTLAND: Elsevier Science Sa.

32. Langer, R., *Drug delivery and targeting.* Nature 1998. **392**(Suppl. 6679): p. 5-10.

33. Hendricks, M.H., *Measurement of enzyme laundry product dust levels and characteristics in consumer use.* . Journal of American Oil Chemists' Society 1970. **47**: p. 207-211.

34. Murtomaa, M., et al., *Effect of particle morphology on the triboelectrification in dry powder inhalers.* International Journal of Pharmaceutics, 2004. **282**: p. 107–114.

35. Miller, D.D., et al., *Aerosol delivery and modern mechanical ventilation in vitro/in vivo evaluation.* American Journal of Respiratory and Critical Care Medicine, 2003. **168**: p. 1205-1209.

36. Hermansen, K., et al., *Intensive therapy with inhaled insulin via the AERx insulin diabetes management system: a 12-week proof-of-concept trial in patients with type 2 diabetes.* Diabetes Care 2004. **27**: p. 162-167.

37. McTavish, J., *What's in a name? Aspirin and the American Medical Association.* Bulletin of the History of Medicine, 1987. **61**: p. 364-365.

38. Chen, C.H., et al., *Electrostatic sol-spray deposition of nanostructured ceramic thin films.* Journal of Aerosol Science, 1999. **30**(7): p. 959-967.

39. Cloupeau, M. and B. Prunetfoch, *Electrostatic Spraying of Liquids - Main Functioning Modes.* Journal of Electrostatics, 1990. **25**(2): p. 165-184.

40. GananCalvo, A.M., J. Davila, and A. Barrero, *Current and droplet size in the electrospraying of liquids. Scaling laws.* Journal of Aerosol Science, 1997. **28**(2): p. 249-275.

41. Hartman, R.P.A., et al., *The evolution of electrohydrodynamic sprays produced in the cone-jet mode, a physical model.* Journal of Electrostatics, 1999. **47**(3): p. 143-170.

42. Jaworek, A. and A. Krupa, *Classification of the modes of EHD spraying.* Journal of Aerosol Science, 1999. **30**(7): p. 873-893.

43. Tang, K.Q. and A. Gomez, *Monodisperse electrosprays of low electric conductivity liquids in the cone-jet mode.* Journal of Colloid and Interface

Science, 1996. **184**(2): p. 500-511.

44. Chen, C.H., et al., *Electrostatic sol-spray deposition of nanostructured ceramic thin films.* Journal of Aerosol Science, 1999. **30**: p. 959-967.
45. Fenn, J.B., et al., *Electrospray Ionization for Mass-Spectrometry of Large Biomolecules.* Science, 1989. **246**(4926): p. 64-71.
46. Gomez, A., et al., *Production of protein nanoparticles by electrospray drying.* Journal of Aerosol Science, 1998. **29**(5-6): p. 561-574.
47. Pareta, R., et al., *Electrohydrodynamic atomization of protein (bovine serum albumin).* Journal of Materials Science-Materials in Medicine, 2005. **16**(10): p. 919-925.
48. Gomez, A., et al., *Production of protein nanoparticles by electrospray drying.* Journal of Aerosol Science, 1998. **29**: p. 561–574.
49. Chen, D.R., C.H. Wendt, and D.Y.H. Pui, *A novel approach for introducing bio-materials into cells.* Journal of Nanoparticle Research, 2000(2): p. 133-139.
50. Ijsebaert, J.C., et al., *Electro-hydrodynamic atomization of drug solutions for inhalation purposes.* Journal of Applied Physiology, 2001. **91**: p. 2735.
51. Chen, D.R., D.Y.H. Pui, and S.L. Kaufman, *Electrospraying of Conducting Liquids for Monodisperse Aerosol Generation in the 4 Nm to 1.8 Mu-M Diameter Range.* Journal of Aerosol Science, 1995. **26**(6): p. 963-977.
52. Hartman, R.P.A., et al., *Jet break-up in electrohydrodynamic atomization in the cone-jet mode.* Journal of Aerosol Science, 2000. **31**(1): p. 65-95.
53. Delamora, J.F. and I.G. Loscertales, *The Current Emitted by Highly Conducting Taylor Cones.* Journal of Fluid Mechanics, 1994. **260**: p. 155-184.
54. Kelly, A.J., *On the Statistical, Quantum and Practical Mechanics of Electrostatic Atomization.* Journal of Aerosol Science, 1994. **25**(6): p. 1159-&.

55. Kim, J.S. and D.H. Reneker, *Mechanical properties of composites using ultrafine electrospun fibers.* Polymer Composites, 1999. **20**(1): p. 124-131.

56. Bergshoef, M.M. and G.J. Vancso, *Transparent nanocomposites with ultrathin, electrospun nylon-4,6 fiber reinforcement.* Advanced Materials, 1999. **11**(16): p. 1362-1365.

57. Murugan, R. and S. Ramakrishna, *Nano-featured scaffolds for tissue engineering: A review of spinning methodologies.* Tissue Engineering, 2006. **12**(3): p. 435-447.

58. Kenawy, E.R., et al., *Release of tetracycline hydrochloride from electrospun poly(ethylene-co-vinylacetate), poly(lactic acid), and a blend.* Journal of Controlled Release, 2002. **81**(1-2): p. 57-64.

59. Thakur, R.A., et al., *Electrospun nanofibrous polymeric scaffold with targeted drug release profiles for potential application as wound dressing.* International Journal of Pharmaceutics, 2008. **364**(1): p. 87-93.

60. Khil, M.S., et al., *Electrospun nanofibrous polyurethane membrane as wound dressing.* Journal of Biomedical Materials Research Part B-Applied Biomaterials, 2003. **67B**(2): p. 675-679.

61. Min, B.M., et al., *Electrospinning of silk fibroin nanofibers and its effect on the adhesion and spreading of normal human keratinocytes and fibroblasts in vitro.* Biomaterials, 2004. **25**(7-8): p. 1289-1297.

62. Wang, Z.G., et al., *Enzyme immobilization on electrospun polymer nanofibers: An overview.* Journal of Molecular Catalysis B-Enzymatic, 2009. **56**(4): p. 189-195.

63. Jia, H.F., et al., *Enzyme-carrying polymeric nanofibers prepared via electrospinning for use as unique biocatalysts.* Biotechnology Progress, 2002. **18**(5): p. 1027-1032.

64. Qin, X.H. and S.Y. Wang, *Filtration properties of electrospinning nanofibers.* Journal of Applied Polymer Science, 2006. **102**(2): p.

1285-1290.

65. Barhate, R.S., C.K. Loong, and S. Ramakrishna, *Preparation and characterization of nanofibrous filtering media.* Journal of Membrane Science, 2006. **283**(1-2): p. 209-218.

66. Jones, R.A.L. and R.W. Richards, *Polymers at Surfaces and Interfaces*. 1999: Cambridge University Press.

67. Gennes, P.G.d., F. Brochard-Wyart, and D. Quere, *Capillarity and Wetting Phenomena: Drops, Bubbles, Pearls, Waves* 2003: Springer.

68. Shafrin, E.G. and W.A. Zisman, *Constitutive Relations in the Wetting of Low Energy Surfaces and the Theory of the Retraction Method of Preparing Monolayers 1*. 1960. p. 519-524.

69. Young, T., *An Essay on the Cohesion of Fluids* Journal Philosophical Transactions of the Royal Society of London (1776-1886) **95 - 1805**: p. 65-87.

70. Barber, A.H., H.D. Wagner, and C. S.R., eds. *Investigating Individual Carbon Nanotube/Polymer Interfaces with Scanning Probe Microscopy: Chapter in Applied Scanning Probe Methods VI: Characterization*. 2006, Springer (Ger.) 287.

71. Barber, A.H., S.R. Cohen, and H.D. Wagner, *Static and dynamic wetting measurements of single carbon nanotubes.* Phys. Rev. Lett., selected for Virtual J. Nanosci. Tech, 2004. **92**: p. 186103

72. Barber, A.H., S.R. Cohen, and H.D. Wagner, *External and internal wetting of carbon nanotubes with organic liquids.* Phys. Rev. B., selected for Virtual J. Nanosci. Tech, 2005. **71**: p. 115443.

73. Ramakrishna, S., et al., *An introduction to electrospinning and nanofibers*. 2005: World Scientific Publishing Company. 206.

74. Bognitzki, M., et al., *Nanostructured fibers via electrospinning.* Advanced Materials, 2001. **13**(1): p. 70-72.

75. Ramakrishna, S., K. Fujihara, and W.E. Teo, *An introduction to electrospinning and nanofibers*. 2005: World Scientific Publishing Co Pte Ltd 396.

76. Johnson, K.L., K. Kendall, and A.D. Roberts. Proc.R. Soc. Vol. A. 1971, London: Ser. 301-313.

77. Sun, L., et al., *Modeling the size-dependent elastic properties of polymeric nanofibers.* Nanotechnology, 2008. **19**(45): p. 8.

78. Ondarcuhu, T., Joachim, C, *Drawing a single nanofibre over hundreds of microns.* Europhys Lett 1998. **42**(2): p. 215–20.

79. Ma, P.X. and R.Y. Zhang, *Synthetic nano-scale fibrous extracellular matrix.* Journal of Biomedical Materials Research, 1999. **46**(1): p. 60-72.

80. Martin, C., *Membrane-based synthesis of nanomaterials.* . Chem Mater, 1996. **8**: p. 1739-46.

81. Feng, L., et al., *Super-hydrophobic surface of aligned polyacrylonitrile nanofibers.* Angewandte Chemie-International Edition, 2002. **41**(7): p. 1221-+.

82. Whitesides, G.M. and B. Grzybowski, *Self-assembly at all scales.* Science, 2002. **295**(5564): p. 2418-2421.

83. Fong H and R. DH., eds. *Electrospinning and formation of nano-fibers*. Structure formation in polymeric fibers, ed. S. DR. 2001. 225-46.

84. Deitzel, J.M., et al., *Controlled deposition of electrospun poly(ethylene oxide) fibers.* Polymer, 2001. **42**(19): p. 8163-8170.

85. Ondarcuhu, T. and C. Joachim, *Drawing a single nanofibre over hundreds of microns.* Europhysics Letters, 1998. **42**(2): p. 215-220.

86. Feng, J.J., *The stretching of an electrified non-Newtonian jet: A model for electrospinning.* Physics of Fluids, 2002. **14**(11): p. 3912-3926.

87. Hartgerink, J.D., E. Beniash, and S.I. Stupp, *Self-assembly and mineralization of peptide-amphiphile nanofibers.* Science, 2001.

294(5547): p. 1684-1688.

88. Fong, H., I. Chun, and D.H. Reneker, *Beaded nanofibers formed during electrospinning.* Polymer, 1999. **40**(16): p. 4585-4592.

89. Larrondo, L. and R.S.J. Manley, *Electrostatic Fiber Spinning from Polymer Melts .3. Electrostatic Deformation of a Pendant Drop of Polymer Melt.* Journal of Polymer Science Part B-Polymer Physics, 1981. **19**(6): p. 933-940.

90. Larrondo, L. and R.S.J. Manley, *Electrostatic Fiber Spinning from Polymer Melts .2. Examination of the Flow Field in an Electrically Driven Jet.* Journal of Polymer Science Part B-Polymer Physics, 1981. **19**(6): p. 921-932.

91. Larrondo, L. and R.S.J. Manley, *Electrostatic Fiber Spinning from Polymer Melts .1. Experimental-Observations on Fiber Formation and Properties.* Journal of Polymer Science Part B-Polymer Physics, 1981. **19**(6): p. 909-920.

92. Young, T., *An Essay on the Cohesion of Fluids* Journal Philosophical Transactions of the Royal Society of London (1776-1886) **95 - 1805**: p. 65-87.

93. Ramakrishna, S., et al., *An introduction to electrospinning and nanofibers*. 2005: World Scientific Publishing Company. 396.

94. Baumgart.Pk, *Electrostatic Spinning of Acrylic Microfibers.* Journal of Colloid and Interface Science, 1971. **36**(1): p. 71-&.

95. Reneker, D.H. and I. Chun, *Nanometre diameter fibres of polymer, produced by electrospinning.* Nanotechnology, 1996. **7**(3): p. 216-223.

96. Fong, H. and D.H. Reneker. *Elastomeric nanofibers of styrene-butadiene-styrene triblock copolymer*. in *Meeting of the American-Physical-Society-Division-of-High-Polymer-Physics*. 1999. Atlanta, Georgia: John Wiley & Sons Inc.

97. Reneker, D.H., et al., *Bending instability of electrically charged liquid jets of polymer solutions in electrospinning.* Journal of Applied Physics, 2000. **87**(9): p. 4531-4547.

98. Chen, Z.H., et al., *Structure of poly(ferrocenyldimethylsilane) in electrospun nanofibers.* Macromolecules, 2001. **34**(18): p. 6156-6158.

99. Suthar, A. and G. Chase, *Nanofibres in filter media.* Tce, 2001(726): p. 26-28.

100. Huang, Z.-M., et al., *A review on polymer nanofibers by electrospinning and their applications in nanocomposites.* Composites Science and Technology, 2003. **63**(15): p. 2223-2253.

101. Lim, T.C., et al., *Recent advances in tissue engineering applications of electrospun nanofibers.* Materials Technology, 2004. **19**(1): p. 20-27.

102. Yang, F., et al., *Electrospinning of nano/micro scale poly(L-lactic acid) aligned fibers and their potential in neural tissue engineering.* Biomaterials, 2005. **26**(15): p. 2603-2610.

103. D. Li, Y.X., *Electrospinning of Nanofibers: Reinventing the Wheel?* Advanced Materials, 2004. **16**(14): p. 1151-1170.

104. Qin, X.H., et al., *Effect of LiCl on electrospinning of PAN polymer solution: theoretical analysis and experimental verification.* Polymer, 2004. **45**(18): p. 6409-6413.

105. He, J.H. and Y.Q. Wane, *Allometric scaling for voltage and current in electrospinning.* Polymer, 2004. **45**(19): p. 6731-6734.

106. Shin, Y.M., et al., *Experimental characterization of electrospinning: the electrically forced jet and instabilities.* Polymer, 2001. **42**(25): p. 9955-9967.

107. Yarin, A.L., S. Koombhongse, and D.H. Reneker, *Taylor cone and jetting from liquid droplets in electrospinning of nanofibers.* Journal of Applied Physics, 2001. **90**(9): p. 4836-4846.

108. Yarin, A.L., S. Koombhongse, and D.H. Reneker, *Bending instability in electrospinning of nanofibers.* Journal of Applied Physics, 2001. **89**(5): p. 3018-3026.

109. Loscertales, I.G., et al., *Micro/nano encapsutation via electrified coaxial liquid jets.* Science, 2002. **295**(5560): p. 1695-1698.

110. Obare, S.O., N.R. Jana, and C.J. Murphy, *Preparation of polystyrene- and silica-coated gold nanorods and their use as templates for the synthesis of hollow nanotubes.* Nano Letters, 2001. **1**(11): p. 601-603.

111. Sun, Z.C., et al., *Compound core-shell polymer nanofibers by co-electrospinning.* Advanced Materials, 2003. **15**(22): p. 1929-+.

112. Bazilevsky, A.V., A.L. Yarin, and C.M. Megaridis, *Co-electrospinning of Core−Shell Fibers Using a Single-Nozzle Technique*. 2007. p. 2311-2314.

113. Li, D. and Y. Xia, *Direct Fabrication of Composite and Ceramic Hollow Nanofibers by Electrospinning*. 2004. p. 933-938.

114. Li, D., T. Herricks, and Y.N. Xia, *Magnetic nanofibers of nickel ferrite prepared by electrospinning.* Applied Physics Letters, 2003. **83**(22): p. 4586-4588.

115. Li, D., Y.L. Wang, and Y.N. Xia, *Electrospinning of polymeric and ceramic nanofibers as uniaxially aligned arrays.* Nano Letters, 2003. **3**(8): p. 1167-1171.

116. Doshi, J. and D.H. Reneker, *Electrospinning Process and Applications of Electrospun Fibers.* Journal of Electrostatics, 1995. **35**(2-3): p. 151-160.

117. Koski, A., K. Yim, and S. Shivkumar, *Effect of molecular weight on fibrous PVA produced by electrospinning.* Materials Letters, 2004. **58**(3-4): p. 493-497.

118. M. G. McKee; G. L. Wikes; R. H. Colby; T. E. Long, *"Correlations of solution rheology with electrospun fiber formation of linear and branched*

polyesters." Macromolecules, 2004. **37**: p. 1760.

119. Liu, H.Q. and Y.L. Hsieh, *Ultrafine fibrous cellulose membranes from electrospinning of cellulose acetate.* Journal of Polymer Science Part B-Polymer Physics, 2002. **40**(18): p. 2119-2129.
120. Koombhongse, S., W.X. Liu, and D.H. Reneker, *Flat polymer ribbons and other shapes by electrospinning.* Journal of Polymer Science Part B-Polymer Physics, 2001. **39**(21): p. 2598-2606.
121. Bergshoef, M.M. and G.J. Vancso, *Transparent nanocomposites with ultrathin, electrospun nylon-4,6 fiber reinforcement.* Advanced Materials, 1999. **11**(16): p. 1362-1365.
122. Deitzel, J.M., et al., *The effect of processing variables on the morphology of electrospun nanofibers and textiles.* Polymer, 2001. **42**(1): p. 261-272.
123. Shin, Y.M., et al., *Electrospinning: A whipping fluid jet generates submicron polymer fibers.* Applied Physics Letters, 2001. **78**(8): p. 1149-1151.
124. Hohman, M.M., et al., *Electrospinning and electrically forced jets. I. Stability theory.* Physics of Fluids, 2001. **13**(8): p. 2201-2220.
125. Hohman, M.M., et al., *Electrospinning and electrically forced jets. II. Applications.* Physics of Fluids, 2001. **13**(8): p. 2221-2236.
126. Bognitzki, M., et al., *Nanostructured fibers via electrospinning.* Advanced Materials, 2001. **13**(1): p. 70-+.
127. Demir, M.M., et al., *Electrospinning of polyurethane fibers.* Polymer, 2002. **43**(11): p. 3303-3309.
128. Fong, H. and D.H. Reneker, *Elastomeric nanofibers of styrene-butadiene-styrene triblock copolymer.* Journal of Polymer Science Part B-Polymer Physics, 1999. **37**(24): p. 3488-3493.
129. Magarvey, R.H. and L.E. Outhouse, *Note on the break-up of a charged liquid jet.* Journal of Fluid Mechanics, 1962. **13**: p. 151-157.

130. Megelski, S., et al., *Micro- and nanostructured surface morphology on electrospun polymer fibers.* Macromolecules, 2002. **35**(22): p. 8456-8466.

131. Buchko, C.J., et al., *Processing and microstructural characterization of porous biocompatible protein polymer thin films.* Polymer, 1999. **40**(26): p. 7397-7407.

132. D. Li; Y. Xia, *"Electrospinning of Nanofibers: Reinventing the Wheel?"* Advanced Materials, 2004. **16**: p. 1151.

133. Theron, S.A., E. Zussman, and A.L. Yarin, *Experimental investigation of the governing parameters in the electrospinning of polymer solutions.* Polymer, 2004. **45**(6): p. 2017-2030.

134. Uyar, T. and F. Besenbacher, *Electrospinning of uniform polystyrene fibers: The effect of solvent conductivity.* Polymer, 2008. **49**(24): p. 5336-5343.

135. Zussman, E., A.L. Yarin, and D. Weihs, *A micro-aerodynamic decelerator based on permeable surfaces of nanofiber mats.* Experiments in Fluids, 2002. **33**(2): p. 315-320.

136. Pham, Q.P., U. Sharma, and A.G. Mikos, *Electrospinning of polymeric nanofibers for tissue engineering applications: A review.* Tissue Engineering, 2006. **12**(5): p. 1197-1211.

137. Vollrath, F. and D.T. Edmonds, *Modulation of the Mechanical-Properties of Spider Silk by Coating with Water.* Nature, 1989. **340**(6231): p. 305-307.

138. Fang, X. and D.H. Reneker, *DNA fibers by electrospinning.* Journal of Macromolecular Science-Physics, 1997. **B36**(2): p. 169-173.

139. Yarin, A., *Free liquid jets and films: hydrodynamics and rheology*. 1993, New York:: Wiley.

140. Entov, V. and L. Shmaryan, *Numerical modeling of the capillary breakup of jets of polymer liquids.* Fluid Dynamics, 1997. **32**(5): p. 696-703.

141. Magarvey, R. and L. Outhouse, *Note on the break-up of a charged liquid jet.* Journal of Fluid Mechanics, 1962. **13**: p. 151-157.

142. Huebner, A., *Disintegration of charged liquid jets.* Journal of Fluid Mechanics, 1969. **38**(4): p. 679-688.

143. Jaeger, R., et al., *Electrospinning of ultra-thin polymer fibers.* Macromolecular Symposia, 1998. **127**: p. 141-150.

144. Fridrikh, S.V., et al., *Controlling the fiber diameter during electrospinning.* Phys Rev Lett, 2003. **90**(14): p. 144502.

145. Gibson, P.W., H.L. Schreuder-Gibson, and D. Rivin, *Electrospun fiber mats: Transport properties.* Aiche Journal, 1999. **45**(1): p. 190-195.

146. Angadjivand SA, et al. 2002: US patent.

147. Fertala, A., W.B. Han, and F.K. Ko, *Mapping critical sites in collagen II for rational design of gene-engineered proteins for cell-supporting materials.* Journal of Biomedical Materials Research, 2001. **57**(1): p. 48-58.

148. Jin, H.J., et al., *Electrospinning bombyx mori silk with poly(ethylene oxide).* Abstracts of Papers of the American Chemical Society, 2002. **224**: p. U431-U431.

149. Matthews, J.A., et al., *Electrospinning of collagen nanofibers.* Biomacromolecules, 2002. **3**(2): p. 232-238.

150. Boland, E.D., et al., *Tailoring tissue engineering scaffolds using electrostatic processing techniques: A study of poly(glycolic acid) electrospinning.* Journal of Macromolecular Science-Pure and Applied Chemistry, 2001. **38**(12): p. 1231-1243.

151. Teo, W.E., et al., *Porous tubular structures with controlled fibre orientation using a modified electrospinning method.* Nanotechnology, 2005. **16**(6): p. 918-924.

152. Xu, C.Y., et al., *Aligned biodegradable nanotibrous structure: a potential scaffold for blood vessel engineering.* Biomaterials, 2004. **25**(5): p. 877-886.

153. Theron, A., E. Zussman, and A.L. Yarin, *Electrostatic field-assisted alignment of electrospun nanofibres.* Nanotechnology, 2001. **12**(3): p. 384-390.

154. Li, D., et al., *Collecting electrospun nanofibers with patterned electrodes.* Nano Letters, 2005. **5**(5): p. 913-916.

155. Israelachvili, J., *Intermolecular and Surface Forces, Second Edition: With Applications to Colloidal and Biological Systems (Colloid Science)*. 1992: {Academic Press}.

156. Gennes, P.G.d., F.B. Wyart, and D. Quere, *Capillarity and wetting phenomena*. 2003: Springer. 7.

157. Petrie, E.M., *"Chapter 2: Theories of Adhesion", Handbook of Adhesives and Sealants*. 2nd ed. 2006, New York, : McGraw-Hill,.

158. William, J.R. and D. Callister, *Materials Science and Engineering: An Introduction*. 4th ed. 1997: Wiley. 852.

159. Fowkes, F.M., *Attractive forces at interfaces.* Ind. Eng. Chem, 1964. **56**: p. 40-52.

160. Erbil, H.Y., *Surface chemistry of solid and liquid interfaces*. 1 ed. 2006: Wiley-Blackwell. 332.

161. http://www.surface-tension.de/solid-surface-energy.htm.

162. Mate, C.M., *Tribology on the Small Scale: A Bottom Up Approach to Friction, Lubrication, and Wear*. 2008. p. 479002.

163. K.L. Johnson, K.K., A.D. Roberts, . Vol. A. 1971, London: Proc. R. Soc. . 301-313.

164. Zhang, J.X., et al., *Determination of the surface free energy of crystalline and amorphous lactose by atomic force microscopy adhesion measurement.* Pharmaceutical Research, 2006. **23**(2): p. 401-407.

165. Zhang, J.x., et al., *Determination of the Surface Free Energy of Crystalline and Amorphous Lactose by Atomic Force Microscopy Adhesion*

Measurement Pharmaceutical Research 2006. **23**(2): p. 401-407.

166. Ramakrishna, S., et al., *An introduction to electrospinning and nanofibers*. 2005: World Scientific Publishing Company. 206.

167. Baker, S.C., et al., *Characterisation of electrospun polystyrene scaffolds for three-dimensional in vitro biological studies.* Biomaterials, 2006. **27**(16): p. 3136-3146.

168. Barber, A.H., S.R. Cohen, and H.D. Wagner, *Static and dynamic wetting measurements of single carbon nanotubes.* Phys. Rev. Lett., selected for Virtual J. Nanosci. Tech, 2004. **92**: p. 186103

169. Erbil, H.Y., *Surface chemistry of solid and liquid interfaces*. 1 ed. 2006: Wiley-Blackwell. 239.

170. Barber, A.H., H.D. Wagner, and C. S.R., eds. *Investigating Individual Carbon Nanotube/Polymer Interfaces with Scanning Probe Microscopy: Chapter in Applied Scanning Probe Methods VI: Characterization*. 2006, Springer (Ger.) 287.

171. Nuriel, S., et al., *Direct measurement of multiwall nanotube surface tension.* Chem. Phys. Lett., 2005. **404**: p. 263.

172. Oura, K., et al., *Surface Science: An Introduction (Advanced Texts in Physics)* 2001, Berlin: Springer. 233.

173. Wenzel, R.N., *Resistance of Solid Surfaces to Wetting by Water.* Ind. Eng. Chem, 1936. **28**: p. 988-994.

174. Cassie, A.B.D. and S. Baxter, *Wettability of Porous Surfaces.* Trans Faraday Soc., 1944. **40**: p. 546-551.

175. Nosonovsky, M. and B. Bhushan. *Roughness optimization for biomimetic superhydrophobic surfaces*. in *14th Annual Symposium on Information Storage and Processing Systems*. 2004. Santa Clara, CA: Springer.

176. Nosonovsky, M. and B. Bhushan, *Stochastic model for metastable wetting of roughness-induced superhydrophobic surfaces.* Microsystem

Technologies-Micro-and Nanosystems-Information Storage and Processing Systems, 2006. **12**(3): p. 231-237.

177. Adamson, A.W., *Physical Chemistry of Surfaces*. 5th ed. 1990, New York: John Wisley & Sons, Inc.

178. Yost, F.G., J.R. Michael, and E.T. Eisenmann, *Extensive Wetting Due to Roughness.* Acta Metallurgica Et Materialia, 1995. **43**(1): p. 299-305.

179. Shibuichi, S., et al., *Super water-repellent surfaces resulting from fractal structure.* Journal of Physical Chemistry, 1996. **100**(50): p. 19512-19517.

180. Erbil, H.Y., et al., *Transformation of a simple plastic into a superhydrophobic surface.* Science, 2003. **299**(5611): p. 1377-1380.

181. Johnson, R.E., R.H. Dettre, and D.A. Brandreth, *Dynamic Contact Angles and Contact-Angle Hysteresis.* Journal of Colloid and Interface Science, 1977. **62**(2): p. 205-212.

182. Marmur, A., *Wetting on hydrophobic rough surfaces: To be heterogeneous or not to be?* Langmuir, 2003. **19**(20): p. 8343-8348.

183. Patankar, N.A., *On the modeling of hydrophobic contact angles on rough surfaces.* Langmuir, 2003. **19**(4): p. 1249-1253.

184. Neinhuis, C. and W. Barthlott, *Characterization and distribution of water-repellent, self-cleaning plant surfaces.* Annals of Botany, 1997. **79**(6): p. 667-677.

185. Wagner, P., et al., *Quantitative assessment to the structural basis of water repellency in natural and technical surfaces.* Journal of Experimental Botany, 2003. **54**(385): p. 1295-1303.

186. Bhushan, B. and Y.C. Jung, *Micro- and nanoscale characterization of hydrophobic and hydrophilic leaf surfaces.* Nanotechnology, 2006. **17**(11): p. 2758-2772.

187. Burton, Z. and B. Bhushan, *Hydrophobicity, adhesion, and friction properties of nanopatterned polymers and scale dependence for micro-*

and nanoelectromechanical systems. Nano Letters, 2005. **5**(8): p. 1607-1613.

188. Yarin, A.L., Koombhongse, S., Reneker, D. H., *Bending instability in electrospinning of nanofibers.* J. Appl. Phys., 2001. **89**(5): p. 3018-26.

189. Reneker, D.H., Yarin, A.L., Fong, H., Koombhongse, S., *Bending instability of electrically charged liquid jets of polymer solutions in electrospinning.* J. Appl. Phys., 2000. **87**(9): p. 4531-47.

190. Shin, Y.M., Hohman, M.M., Brenner, M.P., Rutledge, G.C., *Experimental characterization of electrospinning: the electrically forced jet and instabilities.* Polymer, 2001. **42**: p. 9955-67.

191. Li, D. and Y. Xia, *Direct Fabrication of Composite and Ceramic Hollow Nanofibers by Electrospinning*. 2004. p. 933-938.

192. Li, S.W., S.N. Jayasinghe, and M.J. Edirisinghe, *Aspirin particle formation by electric-field-assisted release of droplets.* Chemical Engineering Science, 2006. **61**(10): p. 3091-3097.

193. Inoguchi, H., et al., *Mechanical responses of a compliant electrospun poly(l-lactide-co-[epsilon]-caprolactone) small-diameter vascular graft.* Biomaterials, 2006. **27**(8): p. 1470-1478.

194. Ayres, C., et al., *Modulation of anisotropy in electrospun tissue-engineering scaffolds: Analysis of fiber alignment by the fast Fourier transform.* Biomaterials, 2006. **27**(32): p. 5524-5534.

195. LeGrand, D.G. and J.T. Bendler, *Handbook of Polycarbonate Science and Technology*. 2000, New York: Marcel Dekker. 1-3.

196. Lau, K.K.S., et al., *Superhydrophobic carbon nanotube forests.* Nano Letters, 2003. **3**(12): p. 1701-1705.

197. Huang, L., et al., *Stable Superhydrophobic Surface via Carbon Nanotubes Coated with a ZnO Thin Film.* The Journal of Physical Chemistry B, 2005. **109**(16): p. 7746-7748.

198. Han, D. and A.J. Steckl, *Superhydrophobic and Oleophobic Fibers by Coaxial Electrospinning*. Langmuir, 2009.

199. Feng, L., et al., *Creation of a superhydrophobic surface from an amphiphilic polymer.* Angewandte Chemie-International Edition, 2003. **42**(7): p. 800-802.

200. Theron, S.A., E. Zussman, and A.L. Yarin, *Experimental investigation of the governing parameters in the electrospinning of polymer solutions.* Polymer, 2004. **45**(6): p. 2017-2030.

201. Rucker, V.C., et al., *Functional antibody immobilization on 3-dimensional polymeric surfaces generated by reactive ion etching.* Langmuir, 2005. **21**(17): p. 7621-7625.

202. Kang, M., et al. *Preparation of superhydrophobic polystyrene membranes by electrospinning*. in *Asian Conference on Nanoscience and Nanotechnology (AsiaNANO 2006)*. 2006. Busan, SOUTH KOREA: Elsevier Science Bv.

203. Massardier, V., et al., *Molecular orientation in cold-stretched poly(phenylene vinylene) films.* Synthetic Metals, 1995. **75**(3): p. 169-173.

204. Gonzalez-Martin, M.L., et al., *Analysis of the silica surface free energy by the imbibition technique.* Journal of Colloid and Interface Science, 2001. **240**(2): p. 467-472.

205. Binnig, G., C.F. Quate, and C. Gerber, *Atomic Force Microscope.* Physical Review Letters, 1986. **56**(9): p. 930-933.

206. Young, R., J. Ward, and F. Scire, *Topografiner - Instrument for Measuring Surface Microtopography.* Review of Scientific Instruments, 1972. **43**(7): p. 999-&.

207. D'Costa, N.P. and J.H. Hoh, *Review of Scientific Instruments.* 1995. **66**(10): p. 5096.

208. Moheimani, S.O.R., *Review of Scientific Instruments.* 2008. **79**(7): p.

071101.

209. Moreno-Baron, L., A. Merkoci, and S. Alegret, *Graphite-epoxy composite as an alternative material to design mercury free working electrodes for stripping voltammetry.* Electrochimica Acta, 2003. **48**(18): p. 2599-2605.

210. Wilson, N.R., et al., *Impact of grain-dependent boron uptake on the electrochemical and electrical properties of polycrystalline boron doped diamond electrodes.* Journal of Physical Chemistry B, 2006. **110**(11): p. 5639-5646.

211. Butt, H.J., B. Cappella, and M. Kappl, *Force measurements with the atomic force microscope: Technique, interpretation and applications*. Surface Science Reports. Vol. 59. 2005: Elsevier. 1-152.

212. Giessibl, F.J., *Advances in atomic force microscopy.* Reviews of Modern Physics, 2003. **75**(3): p. 949.

213. Martin, Y. and H.K. Wickramasinghe, *Magnetic imaging by ``force microscopy'' with 1000 [A-ring] resolution.* Applied Physics Letters, 1987. **50**(20): p. 1455-1457.

214. http://www.ntmdt.com/spm-principles/view/kelvin-probe-microscopy.

215. Eaton, P., et al., *Combined Nanoindentation and Adhesion Force Mapping Using the Atomic Force Microscope: Investigations of a Filled Polysiloxane Coating.* Langmuir, 2002. **18**(25): p. 10011-10015.

216. Drelich, J., G.W. Tormoen, and E.R. Beach, *Determination of solid surface tension from particle-substrate pull-off forces measured with the atomic force microscope.* Journal of Colloid and Interface Science, 2004. **280**(2): p. 484-497.

217. Sader, J.E., J.W.M. Chon, and P. Mulvaney, *Calibration of rectangular atomic force microscope cantilevers.* Review of Scientific Instruments, 1999. **70**(10): p. 3967-3969.

218. Zhang, J.X., et al., *Determination of the surface free energy of crystalline*

and amorphous lactose by atomic force microscopy adhesion measurement. Pharmaceutical Research, 2006. **23**(2): p. 401-407.

219. Zhang, J.x., et al., *Determination of the Surface Free Energy of Crystalline and Amorphous Lactose by Atomic Force Microscopy Adhesion Measurement* Pharmaceutical Research 2006. **23**(2): p. 401-407.
220. Barber, A.H., H.D. Wagner, and C. S.R., eds. *Investigating Individual Carbon Nanotube/Polymer Interfaces with Scanning Probe Microscopy: Chapter in Applied Scanning Probe Methods VI: Characterization*. 2006, Springer (Ger.) 287.
221. Barber, A.H., S.R. Cohen, and H.D. Wagner, *Static and dynamic wetting measurements of single carbon nanotubes.* Phys. Rev. Lett., selected for Virtual J. Nanosci. Tech, 2004. **92**: p. 186103
222. Barber, A.H., S.R. Cohen, and H.D. Wagner, *External and internal wetting of carbon nanotubes with organic liquids.* Phys. Rev. B., selected for Virtual J. Nanosci. Tech, 2005. **71**: p. 115443.
223. Israelachvili, J.N., *Intermolecular and Surface Forces, Academic Press*. 1985, London.
224. Cooper, C.A., S.R. Cohen, and A.H. Barber, *Detachment of nanotubes from a polymer matrix.* Appl. Phys. Lett, 2002. **80**: p. 3873.
225. *Zisman, W.A.*, *Adv. Chem. Ser.* , *1964*. **43**(1).
226. Tan, E. and C. Lim, *Mechanical characterization of nanofibers – A review.* Composites Science and Technology, 2006. **66**: p. 1102-1111.
227. Jaeger, R., H. Schonherr, and G.J. Vancso, *Chain packing in electro-spun poly(ethylene oxide) visualized by atomic force microscopy.* Macromolecules, 1996. **29**(23): p. 7634-7636.
228. Bianco, A., et al., *Strong orientation of polymer chains and small photochromic molecules in polyamide 6 electrospun fibers.* Chemphyschem, 2007. **8**(4): p. 510-514.

229. Israelachvili, J., *Intermolecular and Surface Forces, Second Edition: With Applications to Colloidal and Biological Systems (Colloid Science)*. 1992: {Academic Press}.

230. Cherry, B.W., *Polymer Surfaces* 1981: Cambridge University Press. 16.

231. Mondino, A.V., et al., *Physical properties of gamma irradiated poly(vinyl alcohol) hydrogel preparations.* Radiation Physics and Chemistry, 1999. **55**(5-6): p. 723-726.

232. http://www.nationmaster.com/encyclopedia/Polycarbonate.

233. Seliger, R.L., et al., *High-Intensity Scanning Ion Probe with Submicrometer Spot Size.* Applied Physics Letters, 1979. **34**(5): p. 310-312.

234. Barber, A.H., S.R. Cohen, and H.D. Wagner, *Static and dynamic wetting measurements of single carbon nanotubes.* Phys. Rev. Lett., selected for Virtual J. Nanosci. Tech, 2004. **92**: p. 186103

235. Yan, X.B., et al., *Water-repellency and surface free energy of a-C:H films prepared by heat-treatment of polymer precursor.* Diamond and Related Materials, 2005. **14**(8): p. 1342-1347.

236. http://www.cardiff.ac.uk/chemy/staffinfo/xpsaccess/analysis.html.

237. Wagner, C.D., et al., *Handbook of X-ray Photoelectron Spectroscopy*. 1992, Eden Prairie, MN, USA Perkin-Elmer Corp.

238. Feng, L., et al., *Creation of a superhydrophobic surface from an amphiphilic polymer.* Angewandte Chemie-International Edition, 2003. **42**(7): p. 800-802.

239. Somasundaran, P. and A. Hubbard, eds. *Encyclopedia of Surface and Colloid Science*. 2006, Taylor & Francis.

240. Dziembaj, R., et al., *XPS study of polyaniline supported dodecatungstosilicic acid catalyst.* Journal of Molecular Catalysis a-Chemical, 1996. **112**(3): p. 423-430.

241. Schindler, M., et al., *XPS spectra of uranyl minerals and synthetic uranyl compounds. II: The O 1s spectrum.* Geochimica et Cosmochimica Acta, 2009. **73**(9): p. 2488-2509.

242. Adadi, R., et al., *Phosphonate-anchored thin films on titanium and niobium oxide surfaces: Fabrication and characterization.* Thin Solid Films. **In Press, Corrected Proof**.

243. O'Shea, J.N., et al., *Hydrogen-bond induced surface core-level shift in pyridine carboxylic acids.* Surface Science, 2001. **486**(3): p. 157-166.

244. Sionkowska, A., et al., *Surface properties of UV-irradiated poly(vinyl alcohol) films containing small amount of collagen.* Applied Surface Science, 2009. **255**(7): p. 4135-4139.